2012

Analysis and Design of Test Setup and Loading Fixture for Horizontally Curved Tubular Flange Girder Test Specimen

Kayla Marie Hampe
Lehigh University

Analysis and Design of Test Setup and Loading Fixture for Horizontally Curved Tubular Flange Girder Test Specimen

by

Kayla Marie Hampe

Presented to the Graduate and Research Committee
of Lehigh University
in Candidacy for the Degree of
Master of Science

in

Structural Engineering

Lehigh University

September 2012

This thesis is accepted and approved in partial fulfillment of the requirements for the Master of Science.

_____
Date

_____
Dr. Richard Sause
Thesis Advisor

_____
Dr. Sibel Pamukcu
Department of Civil & Environmental Engineering

ACKNOWLEDGEMENTS

This research was conducted at the Advanced Technology for Large Structural Systems (ATLSS) Research Center at Lehigh University in Bethlehem, PA, USA. Research funding and financial support provided by the Federal Highway Administration (FHWA) and the Pennsylvania Department of Community and Economic Development through the Pennsylvania Infrastructure Technology Alliance (PITA) is gratefully acknowledged.

I would like to thank my thesis advisor, Dr. Richard Sause, for his guidance and support during my research. His insight and intelligence provided much understanding. I would also like to thank Darrick Fritchman, the Laboratory Operations Manager at ATLSS, for the many hours he spent providing insight and suggestions on how to improve the designs for my research. The support and help from John Hoffner and all of the ATLSS laboratory staff is appreciated. The technical assistance and advice from Peter Bryant was always welcomed and valued. Thank you to Eric Putnam for providing calculation files and drawings for the test setup, which were often modified and used in my thesis. I would like to extend a thank you to my peers, especially Haiying Ma, for their academic and nonacademic assistance during my time at Lehigh University.

Finally, I want to express my sincerest gratitude for the love and support of my family and friends. Their encouragement and faith in me through the years is deeply cherished and much appreciated.

TABLE OF CONTENTS

LIST OF TABLES

LIST OF FIGURES

ABSTRACT

A curved tubular flange girder (TFG) is an innovative curved steel I-shaped girder for highway bridges. The cross section of a TFG combines the flexurally-efficient open cross section of an I-girder with the closed cross section of a tube. A TFG has a steel tube as the top flange and either a steel tube or a flat steel plate as the bottom flange. TFGs are easy to fabricate and have a much greater torsional stiffness and strength than conventional curved I-girders.

The curved TFGs studied here have a hollow-structural-section as the top flange and a flat steel plate as the bottom flange. A 2/3-scale test specimen with two curved TFGs braced by diaphragms has been designed, fabricated, and erected. Finite element (FE) models of the test specimen were developed by Ma and the FE results from these models were used in the present study.

This thesis presents the test setup, and the FE analyses of the loading and the kinematics of the test specimen response. The thesis also describes how the FE results were used to design the loading fixtures for the tests. The test setup includes the test specimen, the bearings and the footings, the ground anchor rods used to react the loads, and the loading fixtures. A description of the location and layout of test setup is included and the design of the test specimen is explained. Information on the TFGs, the stiffeners, the diaphragms, and the diaphragm to TFG connections is presented. The bearings and the footings are described, followed by information on the ground anchor rods.

The design of the loading fixtures, explained in this thesis, attempts to minimize the restraint of the test specimen and maintain stability of the loads as the test specimen displaces. Four different types of loading fixtures were designed to accommodate the geometry of the test specimen and the expected displacements of the test specimen based on the FE results. Seven loading fixtures are required to load the test specimen with 14 concentrated loads that produce load effects at mid-span similar to those of an idealized uniformly distributed load over the span. The idealized uniformly distributed load was selected to simulate actual loading conditions for a curved steel girder bridge.

With each loading fixture, two assemblies, each comprised of a hydraulic jack and a series of steel plates, half-rounds, and steel rods, will pull down on a wide flange beam above the test specimen, and pull up on a pair of laced channels below the test specimen. The wide flange beam will bear down on the test specimen through two assemblies consisting of steel components, which include plates, half-rounds, and hollow-structural-sections. The channels will be anchored by the ground anchor rods that will resist the upward force.

CHAPTER 1: INTRODUCTION

1.1. Overview

Horizontally curved bridges with steel girders are frequently used in highway systems. The horizontal curvature produces significant torsional effects in the bridge girder system. The steel girders are often I-shaped steel plate girders (I-girders) although box-shaped girders are also used. I-girders are effective in a curved bridge system when they are connected by diaphragms or cross-frames. However, due to the open cross section, an individual curved I-girder is torsionally flexible and weak, which makes transportation and erection of individual curved I-girders challenging. For example, temporary supports may be required during erection to stabilize the I-girders until the diaphragms (or cross-frames) are installed and the I-girder framing system is established. After the I-girder framing system is established, the diaphragms (or cross-frames) and the I-girders work together to resist the torsional effects.

Fan (2007) and Dong and Sause (2010a, b) proposed an innovative curved steel I-shaped girder, which has a tube-shaped flange, to take advantage of the torsional stiffness and strength of a closed cross section (the tube). This girder is called a curved tubular flange girder (TFG). The cross section of a TFG combines the flexurally-efficient open cross section of an I-girder with the closed cross section of a tube. An I-shaped TFG has a steel tube as the top flange and either a steel tube or a flat steel plate as the bottom flange. TFGs are easy to fabricate and have a much greater torsional stiffness and strength than conventional I-girders.

The curved TFGs studied here have a cross section with a hollow rectangular steel tube (i.e., a hollow-structural-section or HSS) as the top flange and a flat steel plate as the bottom flange. A 2/3-scale test specimen with two curved TFGs braced by three internal diaphragms and two end diaphragms has been designed, fabricated, and erected. The design of the test specimen was completed by Ma (2012) and Putnam (2011). The design used the American Association of State Highway and Transportation Officials (AASHTO) Load and Resistance Factor Design (LRFD) Bridge Design Specifications (2005) and design recommendations by Dong (2008). Finite element (FE) models of the test specimen were developed by Ma (2012) and the FE results from these models were used in the present study. This thesis explains the tests to be conducted on this test specimen and the test setup.

The test setup includes the test specimen, the bearings and the footings, the ground anchor rods used to react the loads, and the loading fixtures. The bearings were designed by Putnam (2011) and the footings are from previous tests on straight TFGs. The design and installation of the ground anchor rods in the test area were managed by Putnam (2011). The requirements of the loading fixtures and the design of the loading fixtures are explained in Chapter 4 and Chapter 5 of this thesis, respectively.

The loading fixture design used specifications from the American Institute of Steel Construction (AISC) Steel Construction Manual (2005) and AASHTO LRFD Bridge Design Specifications (2005). Four different types of loading fixtures were designed to accommodate the geometry and expected displacements of the test specimen. The design of the loading fixtures attempts to minimize the restraint of the test specimen

and maintain stability of the loads as the test specimen deforms. Seven loading fixtures are required to load the test specimen with 14 concentrated loads that produce load effects at mid-span similar to those of an idealized uniformly distributed load over the span. The idealized uniformly distributed load was selected to simulate actual loading conditions for a curved steel girder bridge.

1.2. Research Objectives

The overall goal of this research is to synthesize information on the test specimen, the test setup, and the required loading conditions, and to develop and design the method of loading the test specimen. To do this, the following objectives are established:

1. To gather and synthesize information on the test specimen and the test setup
2. To study the effects of different possible load patterns on the response of the test specimen using FE model results
3. To study the displacements of the test specimen under loads using FE model results
4. To develop the method of loading the test specimen and design the loading fixtures

1.3. Report Scope

To achieve these objectives, information on the test specimen, the expected test specimen behavior, and the test setup was gathered from previous work done by Dong

(2008), Putnam (2010, 2011), and Ma (2012), and other sources. Different loading cases were studied using FE results to determine if multiple concentrated loads could produce the required load effects. The FE displacement results for the test specimen were examined. The load and kinematic results were used to design the loading fixtures.

1.4. Organization of Thesis

This thesis consists of six chapters:

Chapter 1 introduces the research with a general overview, the research objectives, and the organization of the thesis.

Chapter 2 presents background information on previous and current research involving straight and curved TFGs.

Chapter 3 presents an explanation of the test setup including information on the design of the test specimen, the TFGs, the TFG stiffeners, the diaphragms, the connections of the diaphragms to the TFGs, the bearings and the footings, and the ground anchor rods.

Chapter 4 presents FE study results for the test specimen under different load patterns and the resulting loads and displacements. The basis for the selected test loading condition for the test specimen is explained. The displacements of the test specimen from the FE analyses, the effect of boundary conditions on the FE results, and the displacements used to design the loading fixtures are discussed.

Chapter 5 presents the design of the loading fixtures. It includes an explanation of the design loads, the stability concerns taken into consideration, and the designs of the components of the loading fixtures, including the demands and the capacities for each component.

Chapter 6 presents a summary of the thesis, conclusions, and possible future work.

CHAPTER 2: BACKGROUND

2.1. Introduction

Tubular flange girders (TFG) with different cross sections (shown in Figure 2.1) have been studied and compared with conventional steel I-girders. The previous studies involved theoretical, analytical, and experimental research. TFGs for straight bridges are discussed in Section 2.2. TFGs for curved bridges are discussed in Section 2.3 through Section 2.6: Section 2.3 presents the theoretical studies; Section 2.4 presents the studies on individual curved TFGs with two hollow steel tube flanges; Section 2.5 presents the studies on systems of curved TFGs with two hollow steel tube flanges; and Section 2.6 presents the studies on systems of curved TFGs with a hollow steel tube as the top flange and a flat steel plate as the bottom flange.

2.2. Straight TFGs

Steel girders with tubular flanges filled with concrete were first proposed by Wassef et al. (1997) for straight highway bridges. Increased local buckling resistance, large torsional stiffness, and reduced web slenderness were identified as potential advantages of these girders. A study of straight concrete-filled TFGs was conducted by Wimer and Sause (2004). The two-TFG test specimen studied is shown in Figure 2.2. The straight concrete-filled TFGs had a rectangular steel tube as the top (compression) flange and a flat steel plate as the bottom (tension) flange. The large torsional stiffness of the straight concrete-filled TFG allows for large unbraced lengths and fewer diaphragms (or cross-frames) in a TFG bridge framing system.

The test specimen (Wimer and Sause, 2004) was fabricated and tested at a 0.45 scale. The tests were conducted at the Advanced Technology for Large Structural Systems (ATLSS) Engineering Research Center at Lehigh University in Bethlehem, PA. The location of the test setup of the present research is the same as the location of the test setup for the test specimen studied by Wimer and Sause (2004). The tests by Wimer and Sause (2004) examined the test specimen for two conditions: (1) TFGs non-composite with a concrete deck when the lateral-torsional buckling (LTB) strength controls the flexural capacity and (2) TFGs composite with a concrete deck when the TFG cross section flexural strength controls the flexural capacity. The test specimen was loaded with precast concrete deck panels and additional concrete blocks (see Figure 2.3) to reach the factored design loads based on the 1998 AASHTO Load and Resistance Factor Design (LRFD) Bridge Design Specifications. The straight concrete-filled TFGs carried their design loads. The maximum load capacity of the test specimen could not be validated because the test specimen could not safely be loaded to the maximum load capacity.

Kim and Sause (2005a, b) studied straight concrete-filled TFGs with a round steel tube as the top flange and a flat steel plate as the bottom flange (Figure 2.4). A four-girder, simply supported bridge prototype was designed to develop design flexural strength formulas for TFGs considering LTB and cross section yielding. These equations were calibrated to finite element (FE) analysis results. The details are summarized in Sause (2012). The prototype bridge was designed for strength, stability, service, and fatigue design criteria. Compared with corresponding minimum weight conventional steel

I-girders, the straight concrete-filled TFGs require less steel and fewer diaphragms, which reduces fabrication and erection efforts.

Kim and Sause (2005a, b) designed a 0.45-scale test specimen with two straight TFGs with round concrete-filled steel tubes as the top flanges. The test specimen with non-composite TFGs (see Figure 2.5) was tested for two conditions: (1) construction conditions when the LTB strength controls the flexural capacity and (2) service conditions when the TFG cross section flexural strength controls the flexural capacity. The test specimen was loaded with a concrete deck and additional concrete and steel blocks. For the construction conditions, the TFGs were not braced by the concrete deck, but for the service conditions, the TFGs were braced by the concrete deck. The test specimen carried loads exceeding the factored design loads for both conditions. No unexpected lateral or vertical displacements occurred. The experimental results were compared with FE analysis results, which indicated that the behavior of the test specimen could be estimated accurately with FE models.

Dong and Sause (2009) studied straight TFGs with hollow, rectangular steel tubes for both flanges. An FE parametric study was conducted. The study showed the effects of stiffeners, cross section dimensions, residual stresses, initial geometric imperfections, and bending moment distribution on the LTB flexural strength of straight TFGs. The study was used to validate the flexural strength formulas developed by Kim and Sause (2005a, b).

2.3. Theoretical Work on Curved TFGs

Fan (2007) extended the work on single curved girders with either an open cross section or a closed cross section by Dabrowski (1968) to curved TFGs. Linear elastic theoretical analysis methods for single curved TFGs and multiple curved TFGs braced by cross-frames were developed. A parametric study of the tube width and depth, the cross section depth, and the girder curvature on individual curved TFGs and on curved TFG systems was completed. A parametric study of the number of cross-frames in curved TFG systems was also done. The behavior of curved TFG systems was compared with the behavior of corresponding curved I-girder systems.

FE models were developed (Fan, 2007) to verify the theoretical analysis methods. FE analyses of a curved TFG bridge framing system (girders and cross-frames) under dead load and FE analyses of a curved TFG bridge framing system with a composite concrete deck under dead load and live load was conducted. Curved TFGs have smaller warping normal stress and cross section rotation than corresponding curved I-girders, especially for individual girders. The cross-frames in a curved TFG system can be lighter than the cross-frames in a corresponding curved I-girder system because the cross-frame forces are smaller. A curved TFG system and corresponding curved I-girder system, both with a composite concrete deck, have similar behavior. However, fewer cross-frames are required in the curved TFG system than the corresponding curved I-girder system.

2.4. Individual Curved TFGs with Two Hollow Tube Flanges

Dong and Sause (2010a, b) studied curved TFGs with hollow rectangular steel tubes for both flanges. FE studies were done on individual girders and simply supported three-girder systems of curved hollow TFGs and conventional I-girders. For the comparative studies, the curved hollow TFGs and I-girders had the same weight, depth, and flange width. The span, L, was held constant and the radius of curvature, R, was varied to produce different L/R ratios between 0.1 and 0.45 to study torsional effects.

A study of an individual curved hollow TFG was done to determine the effects of cross section distortion, stiffeners, tube diaphragms, and cross section dimensions on the load capacity (Dong and Sause, 2010a). The FE model is shown in Figure 2.6. Cross section distortion reduces the load capacity, but the use of stiffeners and diaphragms in the tubes mitigate the cross section distortion. In addition, second-order effects, initial geometric imperfections, and residual stresses were considered. Initial geometric imperfections and residual stresses did not have a large effect on the load capacity.

A comparative study (Dong and Sause, 2010a) of individual girders under self-weight demonstrated that the curved hollow TFG develops less warping normal stress due to the larger torsional rigidity, smaller vertical displacements, and smaller cross section rotations than a corresponding I-girder. The I-girder has less primary bending stress due to the slightly larger flexural rigidity. However, the curved hollow TFG has a smaller maximum total longitudinal normal stress than the I-girder because the I-girder has much larger warping normal stress. The study showed that while individual curved I-

girders would require temporary support during erection, individual curved hollow TFGs may not.

Putnam (2010) studied a 1/2-scale individual curved hollow TFG test specimen (see Figure 2.7). Putnam used the test results to validate FE models. The behavior of the curved hollow TFG under vertical loads was examined and the results showed that an FE model can accurately predict vertical displacements, cross section rotations, normal strains, and shear strains away from the ends of the curved hollow TFG. A parametric study of the end conditions and the shear strains near the ends of the curved hollow TFG was conducted considering internal steel tube diaphragms and concrete infill. The end conditions had a significant effect on the shear strains and the values depended on the method of stiffening used, the location of the internal diaphragm, and the extent to which the concrete infill extended. The results were compared to the theoretical analysis methods developed by Fan (2007).

2.5. Curved Systems of TFGs with Two Hollow Tube Flanges

FE analyses were conducted by Dong and Sause (2010b) on three-girder systems of curved hollow TFGs (Figure 2.8). The systems were compared with three-girder systems of curved I-girders. The horizontal curvature, cross section dimensions, number of cross-frames, and inclusion of composite action with the concrete deck were varied. The small reduction in load capacity due to initial geometric imperfections and residual stresses was neglected. The three-girder systems were loaded with a vertical, uniformly distributed load over the span. Two main loading conditions were considered. The first

loading condition was loading of the girder system (without a composite concrete deck) during construction of the deck. The second loading condition was loading of the girder system with a composite deck in its final constructed condition.

The curved hollow TFGs in the three-TFG system had a smaller maximum total normal stress than the corresponding I-girders in the three-I-girder system (Dong and Sause, 2010b). The vertical displacements of both three-girder systems were similar. The maximum cross-frame force in the I-girder system was much greater than the maximum cross-frame force in the TFG system. The three-girder systems with a composite concrete deck had an increased stiffness and load capacity, and a decreased maximum normal stress, vertical displacement, and maximum cross-frame force. The load capacity of the TFG system was similar to the load capacity of the I-girder system.

Dong (2008) adapted the design criteria from the 2004 AASHTO LRFD Bridge Design Specifications for conventional curved I-girders to curved hollow TFGs. Constructability, Service II, and Strength I limit states were considered. The FE results showed that these equations could be used to safely design curved hollow TFGs for highway bridges.

The advantages of a curved hollow TFG system in comparison to a corresponding curved I-girder system are summarized by Sause (2012) as follows:

- Under the same load, the TFGs develop less total normal stress than the corresponding curved I-girders.

- The forces in the cross-frames of the TFG systems are smaller than in the corresponding I-girder systems, and thus lighter cross-frame members could be used for the TFG systems.
- Fewer cross-frames are needed for the TFG systems.
- The TFG systems can carry their own weight (plus the weight of a concrete deck) without any support within the span and without interior cross-frames, and, therefore, temporary support for the TFG systems during construction (before the concrete deck is composite with the girders) may not be needed, which makes bridge erection faster and less expensive.

2.6. Test Specimen for Curved TFGs with Single Hollow Tube Top Flange

Tests on a large-scale test specimen were needed to validate the FE results and design criteria equations developed by Dong (2008). The bottom tubular flange in the TFGs studied by Dong (2008) was eliminated because concrete infill or internal diaphragms would be required to resist bearing from the reactions. In addition, Dong (2008) found that available hollow-structural-sections (HSS) were not adequate for the bottom flange and a cover plate might be needed to increase the flexural strength of the section. Therefore, curved TFGs with a rectangular hollow steel tube as the top flange and a flat steel plate as the bottom flange were developed by Ma (2012).

A 2/3-scale test specimen with two curved hollow TFGs braced by three intermediate diaphragms was designed (Ma, 2012; Putnam, 2011), fabricated, and erected

(see Figure 2.9). FE models of the test specimen were developed (Ma, 2012) to validate the design criteria developed by Dong (2008) for Constructability, Service II, and Strength I limit states (AASHTO, 2005), and to determine the load capacity of the test specimen. The test specimen and the corresponding test setup are described in Chapters 3, 4, and 5 of this thesis.

Further research on curved hollow TFGs and curved hollow TFG systems is underway (Ma, 2012). Additional curved hollow TFG systems are being designed and studied with FE models. The FE models are being used to conduct parametric studies on the erection process of the TFG systems, which includes installation of the diaphragms or cross-frames.

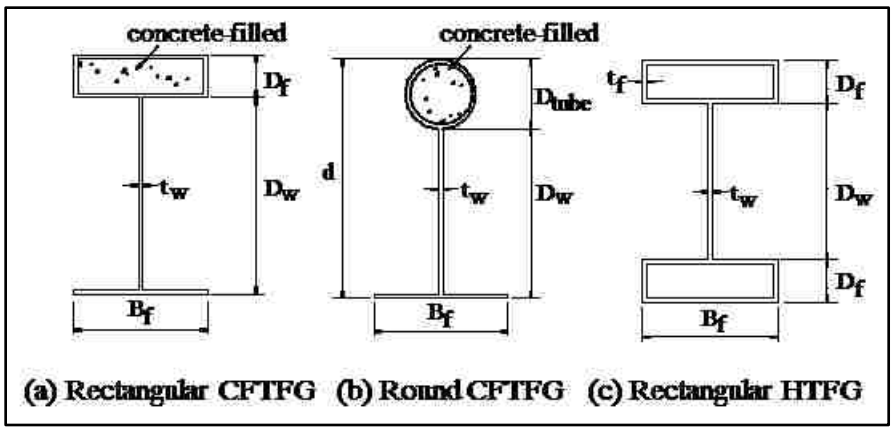

Figure 2.1: Tubular flange girders (Sause, 2012)

Figure 2.2: Straight TFGs with concrete-filled rectangular steel tube top flange (Wimer and Sause, 2004)

Figure 2.3: Straight concrete-filled rectangular steel tube TFG test specimen with concrete deck and loading blocks during testing (Sause, 2012)

Figure 2.4: Straight TFGs with concrete-filled round steel tube top flange (Kim and Sause, 2005a, b)

Figure 2.5: Straight concrete-filled round steel tube TFG test specimen with concrete deck and loading blocks during testing (Kim, 2005)

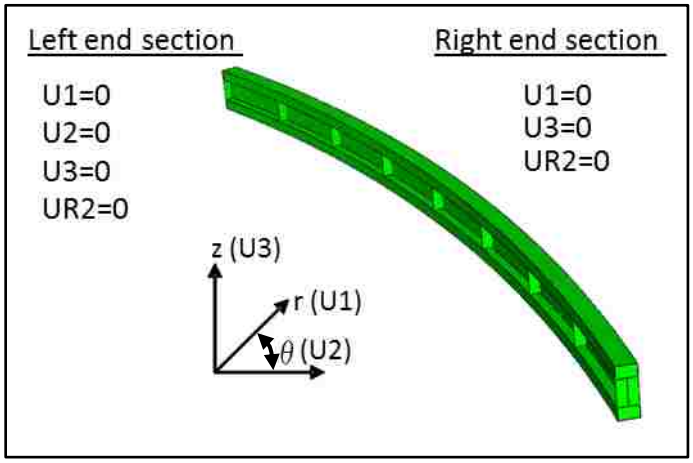

Figure 2.6: FE model of individual curved TFG with two hollow tube flanges (Sause, 2012)

Figure 2.7: Curved TFG with hollow steel tube flanges and concrete infilled ends (Putnam, 2010)

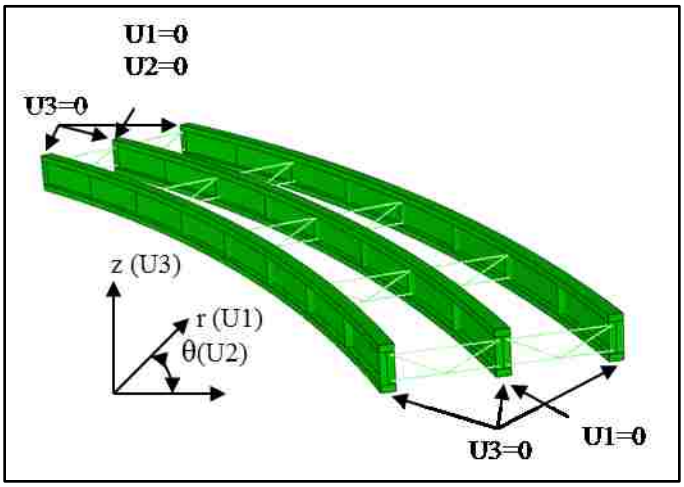

Figure 2.8: FE model of curved system of TFGs with two hollow tube flanges (Sause, 2012)

Figure 2.9: Curved TFG with hollow steel tube top flange (Sause et al., 2009)

CHAPTER 3: TEST SETUP AND TFG TEST SPECIMEN DESIGN

3.1. Introduction

This chapter provides an overview of the test setup and the 2/3-scale TFG test specimen design. It discusses the geometry and layout of the test setup, the design of the test specimen, the components of the test specimen including the girders, stiffeners, and diaphragms, the bearing and the footings, and the ground anchor rods that will be used to react the applied loads.

3.2. Test Setup Location and Layout

The location for the tests is at the Advanced Technology for Large Structural Systems (ATLSS) Engineering Research Center at Lehigh University in Bethlehem, PA. The location of the test setup, shown in Figure 3.1, is outside, directly north of the building. The area used by the test setup is approximately 80 ft long and 35 ft wide and encompasses the girders, bearings, footings, and ground anchor rods. Figure 3.2 is a plan view of the test setup area showing the test setup.

The test setup is singly symmetric about the mid-span of the test specimen. Seven parallel cross sections of four types divide up the test specimen. Section A is located at mid-span, Section B is 7.5 ft away from mid-span, Section C is 15 ft away from mid-span, and Section D is 22.5 ft away from mid-span. Section B, Section C, and Section D are each used at two cross sections located symmetrically about mid-span: one is to the east of Section A and one is to the west of Section A. To differentiate between the two

locations, a subscript of "E" or "W" has been added to denote the east cross section and west cross section, respectively.

Two coordinate systems are used to describe the test setup. The first coordinate system is a cylindrical coordinate system, which corresponds to the geometry of the test specimen. The curved test specimen can be described in terms of a circumferential plane along the centerline of the test specimen, and radial planes perpendicular to the circumferential plane. The second coordinate system is a Cartesian coordinate system, which corresponds to the test setup area. The parallel planes of the test setup area are in the north-south direction and the longitudinal planes of the test setup area are in the east-west direction. The vertical direction is the same for both coordinate systems and is parallel to the direction of gravity.

Section D has the largest angular difference between the parallel plane and the radial plane. Figure 3.3 shows an enlarged plan view of Section D_E. This figure shows linear dimensions between the centerline of the individual TFGs, the centerline of the test specimen, and the centerlines of the ground anchor rods, as well as the angle and the arc length along the TFG centerlines between the two planes.

3.3. TFG Test Specimen Design

The test specimen is 2/3-scale, and is based on a full-scale TFG bridge designed by Haiying Ma and Eric Putnam in 2009. The TFG bridge design was based on recommendations by Dong (2008) and used the AASHTO Load and Resistance Factor Design (LRFD) Bridge Design Specifications Customary U.S. Units, 2005 Interim

Revisions (AASHTO, 2005) as well as information from the American Welding Society (AWS) Bridge Welding Code D1.5 (AWS, 1988) and the American Institute of Steel Construction (AISC) Steel Construction Manual (AISC, 2005). Ma and Putnam used the following steps to design the 2/3-scale test specimen:

1. Design a full-scale two-girder curved TFG bridge using AASHTO LRFD Specifications (AASHTO, 2005) with recommendations by Dong (2008) for the design of the TFGs including the tube, flange, web, and length of the TFGs
2. Scale the dimensions of the full-scale TFG bridge down to obtain a 2/3-scale TFG bridge design
3. Adjust the original 2/3-scale TFG bridge design dimensions to practical dimensions based on available steel plate thickness and tube sizes
4. Load the practical 2/3-scale TFG bridge with scaled loads to check compliance of the responses with the AASHTO LRFD Specifications (2005) and recommendations by Dong (2008)
5. Scale up the dimensions of the practical 2/3-scale TFG bridge by 3/2 to get a new full-scale TFG bridge design
6. Develop an FE model for the new full-scale TFG bridge in ABAQUS, apply the full-scale loads to the model, and check compliance of the full-scale TFG bridge responses with the AASHTO LRFD Specifications (2005) and recommendations by Dong (2008)

7. Model the practical 2/3-scale TFG bridge in ABAQUS, apply scaled loads to the model, and compare the practical 2/3-scale TFG bridge responses with the full-scale TFG bridge responses

The responses of the practical 2/3-scale TFG bridge were similar to the responses of the full-scale TFG bridge as intended. Therefore, the practical 2/3-scale TFG bridge design was considered to be acceptable and used for the test specimen design.

Proper scale factors and associated loading were used to ensure that the stress in the reduced-scaled specimen would be equal to the stress in a full-scale specimen. Putnam conducted an analysis on an arbitrary beam under its self-weight to study the correct scale factors. This process is explained in Section 3.4 of Putnam (2010). The scale factors for the properties of a beam are given in Table 3.1 where λ is the scale factor for the reduced-scale model. The analysis results for a scaled beam with the same stresses under a uniform self-weight load are given in Table 3.2. As explained by Putnam (2010):

> "Column 2 of [Table 3.2] shows the ratio of the reduced-scale to full-scale analysis results for self-weight per unit length, shear force, moment, stress, strain, shear flow, and displacement for the arbitrary scaled beam loaded with a single increment of self-weight… Column 3 of [Table 3.2] shows the ratio of the reduced-scale to full-scale analysis results for the arbitrary scaled beam loaded to $1/\lambda$ increments of self-weight. For a specimen loaded to $1/\lambda$ increments of self-weight, the ratio of the reduced-scale stress and strains to the full-scale stresses and strains is 1.0."

Therefore, the 2/3-scale TFG specimen has to be loaded with $1/\lambda = 3/2$ of the 2/3-scale self-weight to have the same stresses as the full-scale TFG specimen under the full-scale self-weight.

The results from Table 3.2 were used to scale down the design loads of the full-scale TFG bridge to appropriate values for the 2/3-scale TFG bridge. A summary of the applied loads for the full-scale TFG bridge and 2/3-scale TFG bridge is given in Table 3.3. This table includes a description of the loads from the AASHTO LRFD Bridge Design Specifications (2005) considered in the design process; a description of the values for the loads applied to the full-scale TFG bridge; and a description of the values for the scaled loads applied to the 2/3-scale TFG bridge.

Figure 3.4 is a cross section view of the full-scale TFG bridge designed by Ma and Putnam. The design took into consideration the limit states for Constructability, Service II, and Strength I; Section 4.2 describes the loading for these limit states in more detail. The two-girder bridge was assumed to be a single-lane highway ramp with one lane of traffic. A two-girder bridge was chosen to simplify the fabrication and testing of the test specimen. The notation G1 and G2 is used to denote the inside girder and outside girder, respectively. The spacing between the centerlines of the girders is 12 ft at full-scale, which is the width of a typical traffic lane (AASHTO, 2005). The depth of the full-scale girders is 4.5 ft. Each overhang is 3.75 ft. The concrete deck is 8 in thick and 19.5 ft wide. A 3 in thick deck haunch was assumed. The span is 90 ft and the curved bridge has a span length to radius of curvature (L/R) ratio of 0.45. This L/R ratio was selected to produce the largest torsional effects compared to the other L/R ratios of 0.1, 0.2, and 0.3 that were studied by Dong (2008) and Putnam (2010).

Figure 3.5 is a cross section view of the 2/3-scale TFG bridge. The test specimen is a 2/3-scale model of the full-scale TFG bridge. The scale was chosen to accommodate

the available test setup area and to reduce cost. The 2/3 scale factor also satisfies practical considerations. For example, a 2/3-scale model of a 90 ft bridge has the same length as a 1/2-scale model for a 120 ft bridge. However, it is more practical to fabricate the test specimen from plates with the required thickness for the 2/3-scale model than from (thinner) plates with the required thickness for the 1/2-scale model.

3.4. Test Specimen TFGs

A TFG with only one tube as the top flange was chosen instead of a TFG with two tubular flanges, as studied by Dong (2008), for multiple reasons. The first reason is that local deformations may occur in the bottom tube at the bearings due to the compressive force from the reactions. To prevent these deformations, the tube would need an internal steel diaphragm or concrete infill. The second reason is that when the girder is composite with a concrete deck (in the final constructed condition), a larger girder flexural strength can be achieved using a plate rather than a tube as the bottom flange. The nominal yield stress of an ASTM A500 steel tube is 46 ksi, but an ASTM A709 plate can have a nominal yield stress of 50 ksi or larger. In addition, a steel plate bottom flange can have an area larger than the area of the largest available tube, which permits the flexural strength of a composite TFG to be larger when the bottom flange is a plate. The third reason is that the unit cost of steel plates is less than the unit cost of steel tubes.

The top flanges of the test specimen girders are HSS12x8x3/8 tube sections fabricated from ASTM A500-B steel with a nominal yield stress of 46 ksi and nominal

ultimate tensile stress of 58 ksi (AISC, 2005). The actual yield stress of the material is expected to vary from the nominal value. According to the mill report, the tubes of the TFGs have a yield stress of 52.6 ksi and an ultimate tensile stress of 71.4 ksi (ITC, 2008). The tubes were cold bent into the required curvature. The cold bending process for the tubes led to distortions in the cross sections. Table 3.4 gives the nominal and actual dimensions of the 2/3-scale TFG tubes after cold bending.

The webs and bottom flanges are fabricated from ASTM A709 grade 50 steel plates with a nominal yield stress of 50 ksi and a nominal ultimate tensile stress of 65 ksi (AASHTO, 2005). The actual yield stress and actual ultimate tensile stress of the plates of the TFGs are larger than the nominal values. The actual values from the mill reports (Nucor, 2009) are given in Table 3.5.

Figure 3.6 shows a radial cross section view of G1 and of G2 at the bearings, at Section A, and at Section C. Figure 3.7 shows a radial cross section view of G1 and of G2 at Section B and at Section D. The nominal dimensions of the girders are given in the figures. The two sets of radial cross section views show the differences in the stiffener designs. At the bearings, at Section A, and at Section C, the stiffeners are wider than at Section B and at Section D, and they have bolt holes for attaching the diaphragms. Quarter-inch fillet welds made with E70XX electrodes using shielded metal arc welding (SMAW) joined the plates and tubes together to create the TFG sections. High Steel Structures, Inc. in Lancaster, PA, fabricated the girders in 2009.

The TFGs have a span length to radius ratio of 0.45 as explained in Section 3.3. The arc length of the span and radius along the centerline of the test specimen are 60 ft and 133.3 ft, respectively.

Table 3.6 gives the arc length of the span and radius along the centerlines of G1, the test specimen, and G2. The distance between the girder centerlines is 8 ft. Table 3.7 provides a summary of the nominal dimensions of the TFGs.

The horizontal curvature of the TFGs can be described by the horizontal sweep. Figure 3.8 is a plan view showing eleven points along G1 and G2 where the horizontal sweep was taken from. The sweep is described as the lateral distance between a point of reference and a point on the centerline of the TFG. The point of reference is on a straight line between the centerline locations of the TFG at the bearings. The nominal lateral position (sweep) in the parallel plane between the reference points and eleven points along the TFG centerline is given in Table 3.8 for G1 and G2. These values apply to the centerlines of the tube, web, and bottom flange.

The TFGs had a specified camber to offset the vertical deflection due to self-weight. Figure 3.9 is an elevation view showing the eleven locations along G1 and G2 where the camber was specified. Table 3.9 gives the specified camber for the TFGs for the eleven locations.

The as-built condition of the location of the TFGs of the test specimen deviated slightly from the specified values on the drawings. The lateral distance in the parallel plane from the centerline of the ground anchor rods (Section 3.9) to the edge of the

bottom flange of the closest TFG was measured to the nearest half inch. The measured distances, the specified distances given on the drawings, and the difference between the two distances for the fourteen ground anchor rods are given in Table 3.10. The distances given on the drawing were used for calculations requiring this distance for the design of the loading fixtures.

3.5. TFG Stiffeners

To reduce web and tube distortions in the TFGs, pairs of transverse and bearing stiffeners are fillet welded to the tube, web, and flange at multiple locations along the length of the TFGs (Dong, 2008). A plan view of the locations is given in Figure 3.10. The stiffeners for the test specimen were designed using AASHTO LRFD Bridge Design Specifications (2005).

A pair of bearing stiffeners is located at each end of the span of each TFG, which is 6 in away from actual end of each TFG. Figure 3.11 gives the nominal dimensions for these stiffeners. These were milled to bear against the bottom flange of the TFGs. Four of the bearing stiffeners have bolt holes for the connections to the diaphragms, as explained further in Section 3.7.

Seven pairs of intermediate transverse stiffeners are located along the lengths of the TFGs. For G1, these stiffeners are spaced at 7.28 ft. For G2, these stiffeners are spaced at 7.72 ft. There are four different transverse stiffener designs. Figure 3.11 provides the dimensions of the stiffeners for G1 and G2 at the bearings, at Section A, and at Section C. Figure 3.12 provides the dimensions of the stiffeners for G1 and G2 at

Section B and at Section D. The stiffeners at the bearings, at Section A, and at Section C have larger widths to accommodate the connections to the diaphragms.

Dong (2008) found that as the number of pairs of intermediate transverse stiffeners increased, the load capacity of a curved TFG with distortions in the FE model approached the load capacity of a curved TFG without distortions in the FE model; that is, with a sufficient number of stiffeners, cross section distortion does not affect the load capacity of a TFG. The results for seven pairs of intermediate transverse stiffeners along the length of each TFG were similar to the results for nine pairs of intermediate transverse stiffeners (Dong, 2008). Therefore, the TFGs of the test specimen included seven pairs of intermediate transverse stiffeners and two pairs of bearing stiffeners. All stiffeners were fabricated from ASTM A709 steel with a nominal yield stress of 50 ksi and a nominal ultimate tensile stress of 65 ksi.

3.6. Test Specimen Diaphragms

Diaphragms connect G1 and G2 together and brace the TFGs. The diaphragms transmit forces between the TFGs that are necessary to maintain equilibrium of a curved girder system. For this reason, the diaphragms are considered primary members in the design of a curved girder bridge. The diaphragms influence the flange lateral bending stresses in curved girders (AASHTO, 2003). Although the term cross-frame is occasionally used synonymously with the term diaphragm, technically they are different. A cross-frame is a “transverse truss framework” whereas a diaphragm is a “vertically

oriented solid transverse member" (AASHTO, 2005). The test specimen uses diaphragms made from rolled wide flange beam sections.

Five diaphragms brace the TFGs together as shown in Figure 3.10. The diaphragms are located at the bearings, at Section A, and at Section C, and are evenly spaced at 15 ft in the circumferential plane of the test specimen. According to AASHTO Section 6.7.4.2, "intermediate diaphragms or cross-frames should be provided at nearly uniform spacing in most cases, for efficiency of the structural design, for constructability, and/or to allow the use of simplified methods of analysis for calculation of flange lateral bending stress" (AASHTO, 2005).

Dong (2008) studied the effect of the number of intermediate cross-frames on primary bending normal stress, warping normal stress, cross-frame forces, and girder displacements and rotations at mid-span of a curved TFG system. As the number of cross-frames increased, the stresses, forces, displacements, and rotations decreased and the load capacity of the curved TFG system increased. Figure 3.13 and Figure 3.14 show results from Dong (2008) for the maximum force in the cross-frames and the maximum normalized load, respectively, as the number of cross-frames in a curved three-girder system is varied. The plots include two types of systems: one is for a curved hollow TFG (CHTFG) system and one is for a curved I-girder system. Both plots are for the case where the concrete deck is non-composite with the girders. Dong (2008) observed that the differences in the results were relatively large between one cross-frame and three cross-frames, but the differences were not very large between three cross-frames and five

cross-frames. Therefore, the test specimen design incorporated three intermediate cross-frames or diaphragms.

To simplify the design and to reduce the cost of the reduced-scale test specimen, diaphragms were used instead of cross-frames. Figure 3.10 is a plan view of the test specimen including the diaphragm locations. Wide flange beam diaphragms were used to enable simpler connection details to be used. Putnam designed the diaphragms based on AASHTO Section 6.7.4 (2005) using scaled diaphragm forces from the full-scale TFG bridge as described in Section 3.3. A W24x62 section was found to be adequate. The 6.84 ft long diaphragms were fabricated from ASTM A992 steel with a nominal yield stress of 50 ksi and a nominal ultimate tensile stress of 65 ksi. The average actual yield stress is 56 ksi and the average actual ultimate tensile stress is 71.5 ksi according to the mill report (SDI, 2008).

3.7. Diaphragm to TFG Connections

The diaphragms are connected to the stiffeners of the TFGs with bolted connection plates. Figure 3.15 shows a typical test specimen cross section view in the radial plane at Section A and at Section C, where the intermediate diaphragms are located. Figure 3.16 provides the connection details of the diaphragm, the connection plates, and the stiffener. Figure 3.17 (a) shows a cross section view in the circumferential plane of the connection plates attached to the diaphragm with a filler plate. Figure 3.17 (b) shows a cross section view in the circumferential plane of the connection plates attached to the stiffener.

The connection plates are 20 in long, 11 in wide, 1/2 in thick, and fabricated from ASTM A709 steel. Two connection plates are used at each connection between a diaphragm and a TFG stiffener. Fourteen 3/4 in diameter ASTM A325 bolts fasten the diaphragm to the connection plates and another fourteen 3/4 in diameter ASTM A325 bolts fasten the connection plates to the stiffener. A 5/16 in thick fill plate was used on the diaphragm side of the connection to adjust for the differences in thickness between the web of the diaphragm, 7/16 in, and the stiffener, 3/4 in. These plates were also fabricated from ASTM A709 steel.

3.8. Bearings and Footings

Figure 3.18 is a plan view of the west bearing and footing. The footings are approximately 10 in thick, 8 ft by 13 ft concrete slabs. The depth varies to accommodate the uneven asphalt pavement of the test area and produce a level surface for the bearings. The compressive strength of the concrete is 5 ksi and the nominal yield stress of the steel reinforcement is 60 ksi. A W14x233 reaction beam with a nominal yield stress of 36 ksi is tied into the middle of the footing and runs in the parallel plane. The footings and the reaction beams were built for previous tests of straight TFGs. The design of the footings is presented in Kim (2005). During the previous tests (Kim, 2005), each footing was subjected to 305 kip. Two 3.67 ft long W14x176 pieces have been added to the reaction beam to accommodate the locations of the bearings of the curved test specimen. There are two pairs of stiffeners along the length of the W14x233 and added pairs of stiffeners along the lengths of the W14x176 pieces.

As shown in the photo of Figure 3.19, above the reaction beams, a bearing plate overlaps the two wide flange sections. A 1 in square steel bar on top of this bearing plate acts as a "roller" support for the TFG. A square bar will not be a perfect "roller" because the friction between the square bar and the girder will resist lateral displacement. However, the square bar provides more stability than a true roller during erection. Figure 3.20 is a photograph of the bearings and the footings during the erection of the test specimen.

3.9. Ground Anchor Rods

The ground anchor rods were drilled and grouted into underlying bedrock at the test setup location. The rods are 1.25 in diameter galvanized grade 150 Dywidag threaded bar with a modulus of elasticity of 29,700 ksi, an ultimate stress of 150 ksi, and a design load of 112.5 kips. The ground anchor rods are located in pairs, 18 ft apart, in the parallel plane. Figure 3.21 shows a plan view of the location of the ground anchor rods labeled as "tiedown anchor." The ground anchor rods were located in the parallel plane rather than the radial plane to allow more opportunity for future use of the ground anchor rods for tests with girders having different geometry. Section 4.2.3 provides a more in-depth discussion of loading in parallel planes instead of radial planes. The heights of the ground anchor rods above the ground vary. Table 3.11 lists the measured height of each ground anchor rod, rounded to the nearest half inch. These measurements were taken in October of 2011 and include a small mound of grout where the ground anchor rod enters the ground.

Peirce Engineering, Inc. (PE) designed the ground anchor rods, and Earthcore Services, LLC (ES) installed the 14 ground anchor rods in the test setup area. Figure 3.21 and Figure 3.22 contain the design drawings by PE for the ground anchor rods. Figure 3.21 includes a plan view of the test setup with the numbered ground anchor rods, a preliminary cross section view of the loading fixture for a curved TFG test specimen, a detailed explanation of the installation and testing procedures, the test acceptance criteria, and the material details. Figure 3.22 provides additional schematic drawings for the ground anchor rods and installation procedure as well as a cross section view of a typical ground anchor rod aligned with the results of a boring log. ES took one boring located approximately at the center of the 14 ground anchor rods. Figure 3.23 is a copy of the boring log.

To check the quality of the ground anchor rods, PE observed and assisted ES in the ground anchor rod proof testing procedure on July 27, 2009. The proof tests were completed to check that the design capacity of the ground anchor rods can be safely carried. ES and PE tested each ground anchor rod according to the testing procedures shown in Figure 3.21. The load on the ground anchor rod was gradually increased until a load of 133% of the design load (DL), 150 kips, was reached. PE recorded the load, pressure, and movement at increments 0.25xDL, 0.50xDL, 0.75xDL, 1.00xDL, 1.20DL, and 1.33xDL. These three parameters were also measured each minute, for 10 minutes total, after the 1.33xDL load was reached. All of the ground anchor rods met the required acceptable deflection criteria of less than or equal to 0.04 in of movement during the one 10 minute hold period. Table 3.12 provides the total movement for each ground anchor

rod. At the end of each hold, ES released the tension from the ground anchor rod. The ground anchor rods were covered with a plastic pipe for protection until they are needed for tests. Figure 3.24 is a photograph of the covered ground anchor rods in the test setup area.

Table 3.1: Beam property scale factors (Putnam, 2010)

Component	Scale Factor
Width, b (in)	λ
Depth, d (in)	λ
Thickness, t (in)	λ
Area, A (in^2)	λ^2
Volume, V (in^3)	λ^3
Torsional Rigidity, J (in^3)	λ^3
Moment of Inertia, I (in^4)	λ^4

Table 3.2: Analysis results scale factors for applied uniform self-weight (Putnam, 2010)

Component	Self-Weight	1/λ Increment of Self-Weight
Self-Weight per unit Length, w (kip/in)	λ^2	λ
Shear Force, V (kip)	λ^3	λ^2
Moment, M (kip-in)	λ^4	λ^3
Stress, σ (ksi)	λ	1.0
Strain, ε	λ	1.0
Shear Flow, q (kip/in)	λ^2	λ
Displacement, u (in)	λ^2	λ

Table 3.3: Applied loads for full-scale TFG bridge design and 2/3-scale TFG bridge design (Ma, 2012)

Design Load	AASHTO (2005) and Guide Design Specifications for Bridge Temporary Works (AASHTO, 1995)	Full-Scale TFG Bridge	2/3-Scale TFG Bridge
Dead Load	Dead load of the (steel) structural components	Dead load of the girders and stiffeners with a unit weight of 490 lb/ft^3	Dead load of the scaled girders and stiffeners with a unit weight of 490 lb/ft^3 and an additional load that is equal to 1/2 of the dead load of the scaled girders and stiffeners
	Dead load of the (concrete) structural components	Uniform pressure load of the 8 in thick concrete deck with a unit weight of 150 lb/ft^3 distributed over a 19.5 ft deck width along the 90 ft span	Uniform pressure load of the scaled (5.33 in thick) concrete deck with a unit weight of 150 lb/ft^3 and an additional uniform pressure load equal to 1/2 of the uniform pressure load of the scaled concrete deck distributed over a 13 ft deck width along the 60 ft span
	Dead load of the nonstructural components	Uniform pressure load of the deck forms with a weight of 16 lb/ft^2 distributed over a 19.5 ft deck width along the 90 ft span	Uniform pressure load of the deck forms with a weight of 16 lb/ft^2 distributed over a 13 ft deck width along the 60 ft span
	Dead load of the wearing surfaces	Uniform pressure load with a weight of 30 lb/ft^2 distributed over a 19.5 ft deck width along the 90 ft span	Uniform pressure load with a weight of 30 lb/ft^2 distributed over a 13 ft deck width along the 60 ft span
	Dead load of the utilities	Uniform line load with a weight of 275 lb/ft at the edges of the deck along the 90 ft span	Uniform line load with a weight of 183.3 lb/ft at the edges of the deck along the 60 ft span

Table 3.3 (cont'd): Applied loads for full-scale TFG bridge design and 2/3-scale TFG bridge design (Ma, 2012)

Design Load	AASHTO (2005) and Guide Design Specifications for Bridge Temporary Works (AASHTO, 1995)	Full-Scale TFG Bridge	2/3-Scale TFG Bridge
Construction Live Load	Construction live load	Uniform pressure load with a weight 20 lb/ft^2 distributed over a 19.5 ft deck width along the 90 ft span	Uniform pressure load with a weight 20 lb/ft^2 distributed over a 13 ft deck width along the 60 ft span
Live Load	HS20 truck load with 8 kip, 32 kip, and 32 kip loads for the three axles, and a spacing of 14 ft between the two 32 kip axles to produce the maximum load effects	Concentrated load with the same force and the same spacing as the axle loads	Concentrated load with $(2/3)^2$ of the force and 2/3 of the spacing as the axle loads
	The lane load with a pressure of 640 plf uniformly distributed over a 10 ft width for a design lane	Uniform pressure load with a weight of 64 lb/ft^2 distributed over a 10 ft width along the 90 ft span	Uniform pressure load with a weight 64 lb/ft^2 distributed over a (2/3)*10 ft = 6.67 ft width along the 60 ft span

Table 3.4: Tube distortion from cold curving process (Sause et al., 2009)

Location	Nominal Dimensions (in)	Actual Dimensions After Curving					
		G1			G2		
		Inside Depth (in)	Outside Depth (in)	Tube Width (in)	Inside Depth (in)	Outside Depth (in)	Tube Width (in)
East End	12 x 8	8.450	8.116	11.708	8.328	8.160	11.746
Section A		8.506	8.157	11.642	8.499	8.123	11.678
West End		8.325	8.157	11.689	8.501	8.124	11.633

Table 3.5: Actual material properties of TFGs (Nucor, 2009)

TFG Component		Yield Stress (ksi)	Ultimate Tensile Stress (ksi)
Tube (G1 & G2)		52.6	71.4
Web (G1 & G2)	Test 1	59.5	82.0
	Test 2	51.9	77.0
	Avg.	55.7	79.5
G1 bottom flange	Test 1	53.2	79.6
	Test 2	64.3	81.5
	Avg.	58.8	80.6
G2 bottom flange		Not Available	

Table 3.6: Test specimen radii and arc lengths

Location	Radius		Arc Length	
	in	ft	in	ft
G1	1552.0	129.3	698.4	58.2
CL Test Specimen	1600.0	133.3	720.0	60.0
G2	1648.0	137.3	741.6	61.8

Table 3.7: TFG cross section and geometry summary (Sause et al., 2009)

Girder	Depth (in)	Tube (in)	Plate (in)	Web (in)	Area (in^2)	L (ft)	L/R
G1	36	12x8x0.349	12x0.75	27.25x0.375	32.7	60	0.45
G2	36	12x8x0.349	12x1.5	26.5x0.375	41.4	60	0.45

Table 3.8: Nominal horizontal sweep values (Putnam, 2011)

Location	Sweep (in)	
	G1	G2
0	0.000	0.000
0.1	14.693	15.571
0.2	26.023	25.579
0.3	34.066	36.102
0.4	38.871	41.195
0.5	40.469	42.889
0.6	38.871	41.195
0.7	34.066	36.102
0.8	26.023	25.579
0.9	14.693	15.571
1	0.000	0.000

Table 3.9: Specified camber values (Putnam, 2011)

Location	Camber (in)	
	G1	G2
CL BRG.	0.00	0.00
0.1	0.06	0.14
0.2	0.11	0.27
0.3	0.15	0.37
0.4	0.17	0.43
0.5	0.18	0.45
0.6	0.17	0.43
0.7	0.15	0.37
0.8	0.11	0.27
0.9	0.06	0.14
CL BRG.	0.00	0.00

Table 3.10: Lateral distance in parallel plane from edge of TFGs to centerline of ground anchor rods

Anchor Rod	Section	Measured Distance (in)	Drawing Distance (in)	Difference (in)
1	D_W	53.0	53.8	-0.8
2	C_W	41.5	41.5	0.0
3	B_W	34.0	34.1	-0.1
4	A	31.0	31.7	-0.7
5	B_E	32.5	34.1	-1.6
6	C_E	41.5	41.5	0.0
7	D_E	53.5	53.8	-0.3
8	D_W	52.0	52.6	-0.6
9	C_W	65.5	65.8	-0.3
10	B_W	72.5	73.7	-1.2
11	A	75.0	76.3	-1.3
12	B_E	72.5	73.7	-1.2
13	C_E	65.5	65.8	-0.3
14	D_E	52.0	52.6	-0.6

Table 3.11: Measured ground anchor rod heights

Ground Anchor Rod	Height (in)
1	51.0
2	49.5
3	48.0
4	51.5
5	50.5
6	51.0
7	49.0
8	51.5
9	53.5
10	54.5
11	48.5
12	52.5
13	53.5
14	56.0

Table 3.12: Ground anchor rod proof test summary (PE, 2009b)

Ground Anchor Rod	Total Movement (in)	Allowable Movement (in)	Actual / Allowable
1	0.016	0.04	0.400
2	0.023	0.04	0.575
3	0.010	0.04	0.250
4	0.007	0.04	0.175
5	0.015	0.04	0.375
6	0.021	0.04	0.525
7	0.007	0.04	0.175
8	0.020	0.04	0.500
9	0.010	0.04	0.250
10	0.028	0.04	0.700
11	0.005	0.04	0.125
12	0.012	0.04	0.300
13	0.022	0.04	0.550
14	0.015	0.04	0.375

Figure 3.1: Test location (Google, 2012)

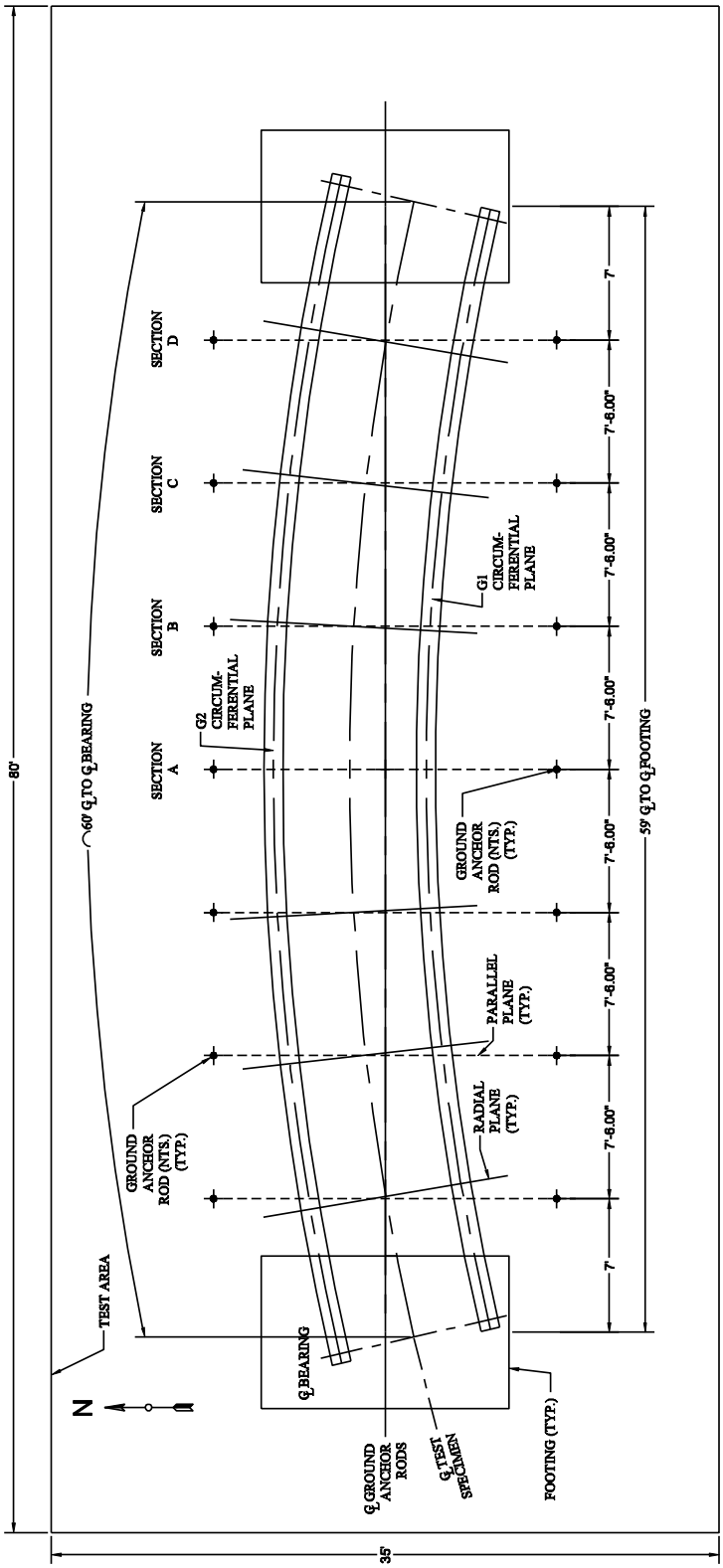

Figure 3.2: Plan view of test setup area

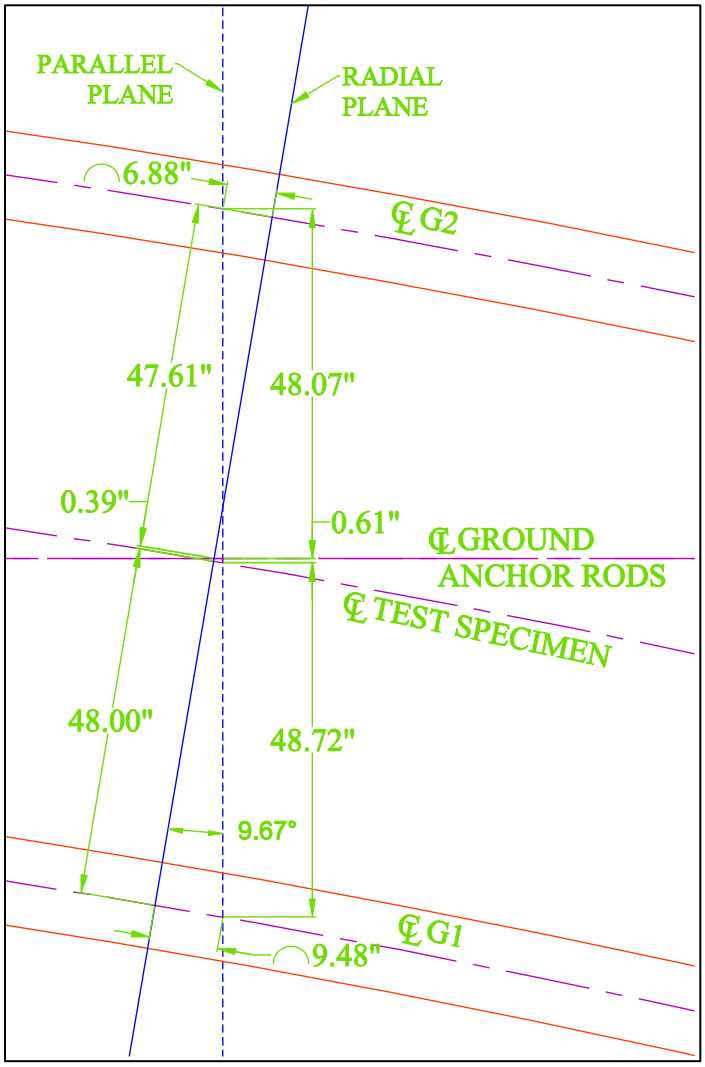

Figure 3.3: Plan view at Section D_E

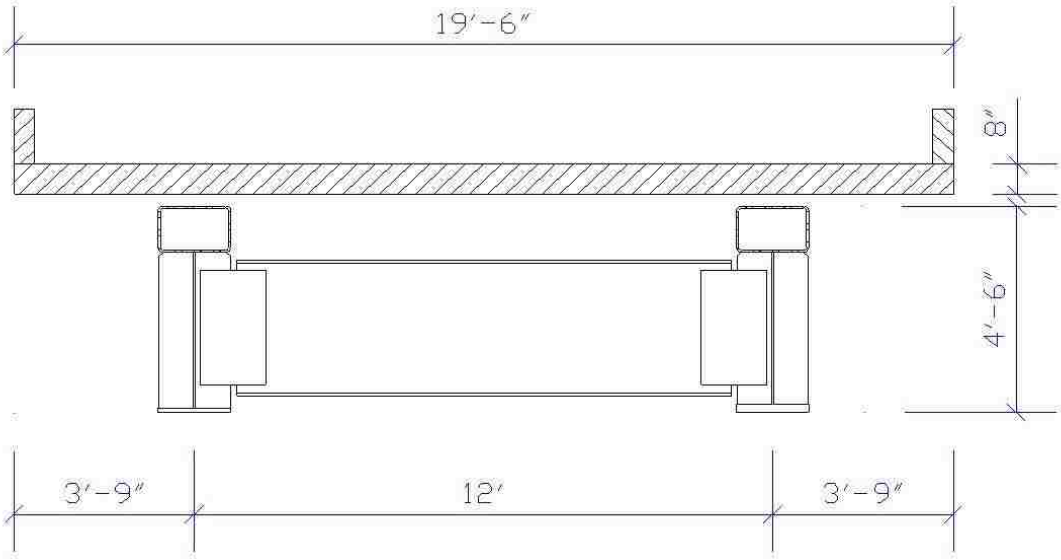

Figure 3.4: Cross section view of full-scale TFG bridge (Sause et al., 2009)

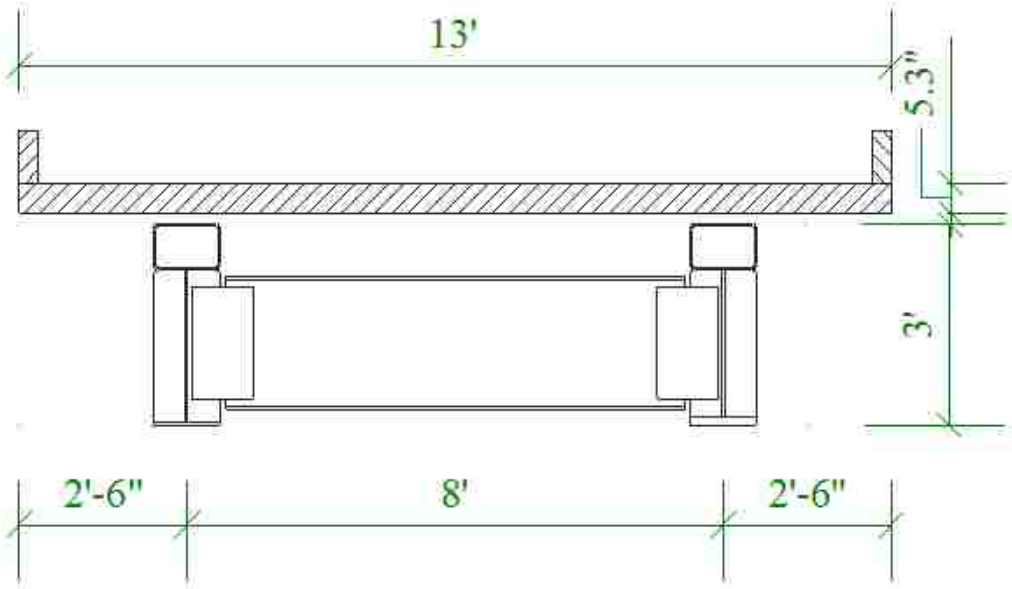

Figure 3.5: Cross section view of 2/3-scale TFG bridge (Sause et al., 2009)

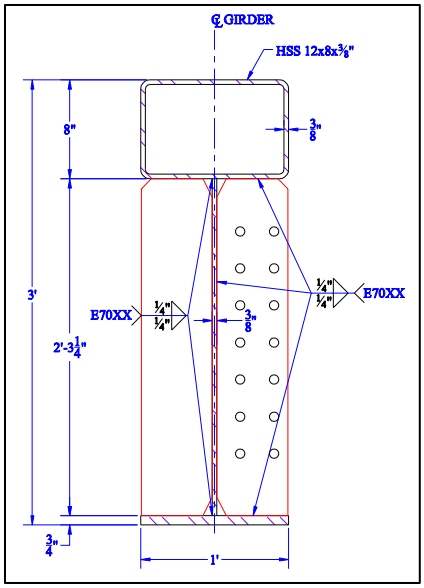

(a) G1

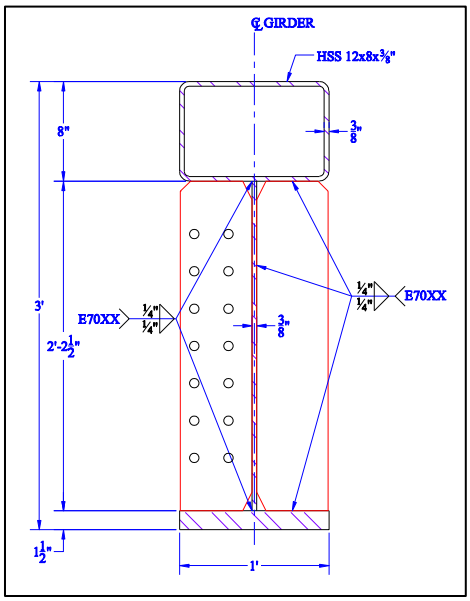

(b) G2

Figure 3.6: Radial cross section view of TFG at the bearings, at Section A, and at Section C (Putnam, 2011)

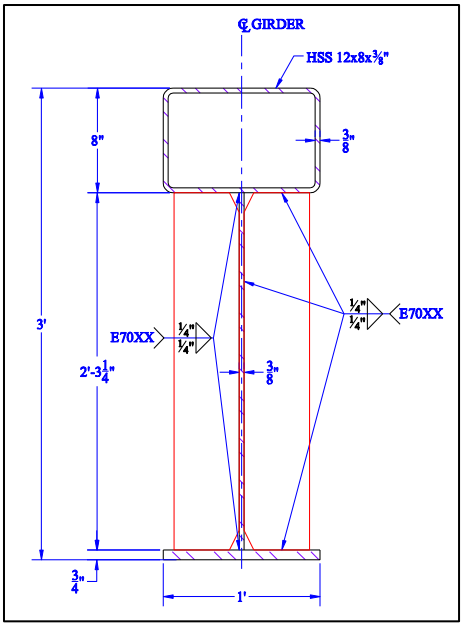

(a) G1

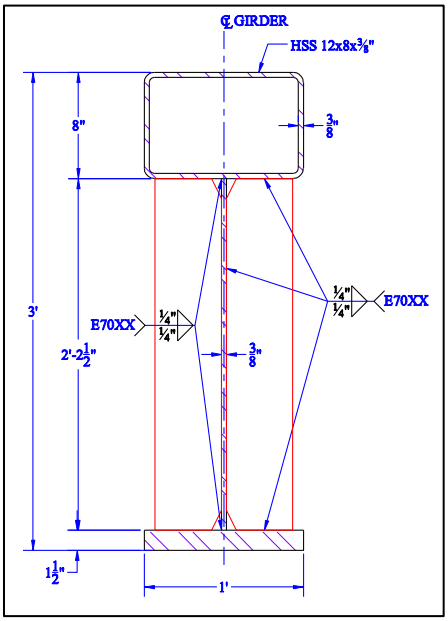

(b) G2

Figure 3.7: Radial cross section view of TFG at Section B and at Section D (Putnam, 2011)

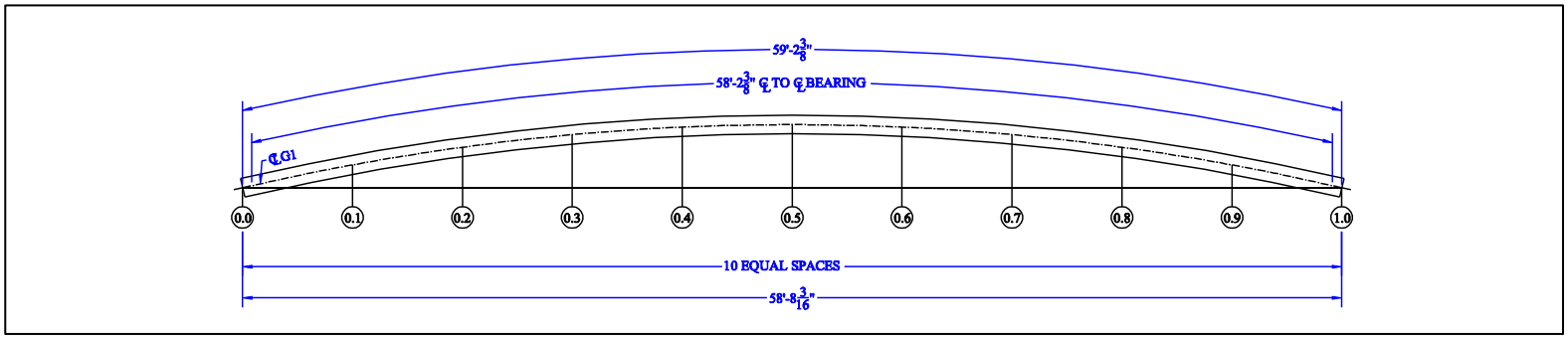

(a) G1

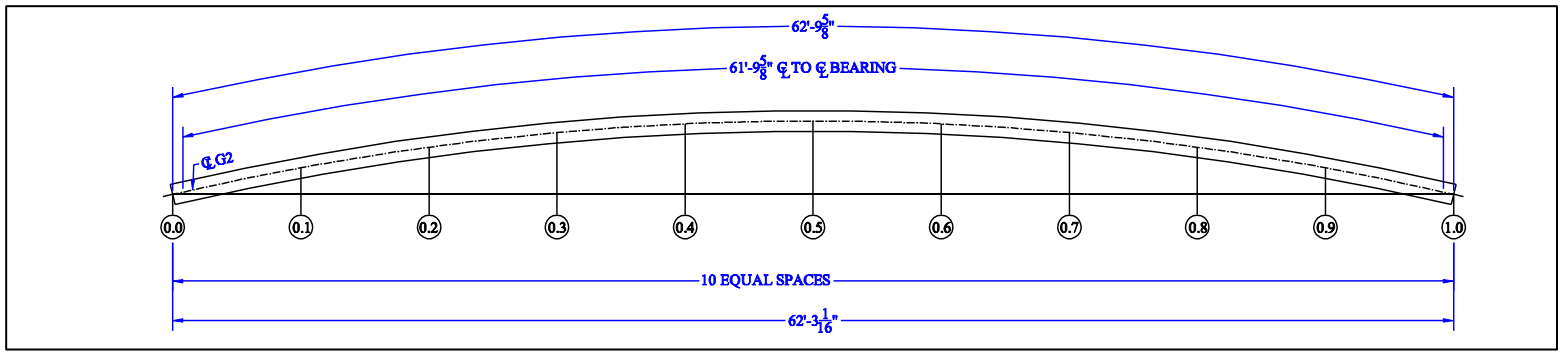

(b) G2

Figure 3.8: TFG horizontal sweep diagram (Putnam, 2011)

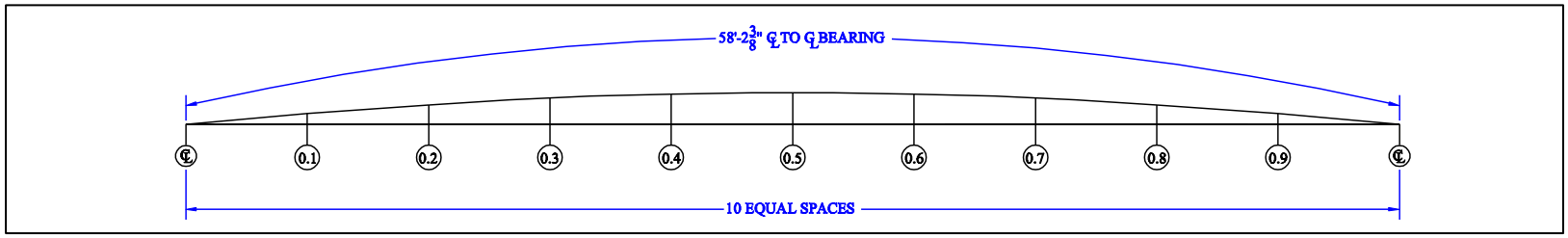

(a) G1

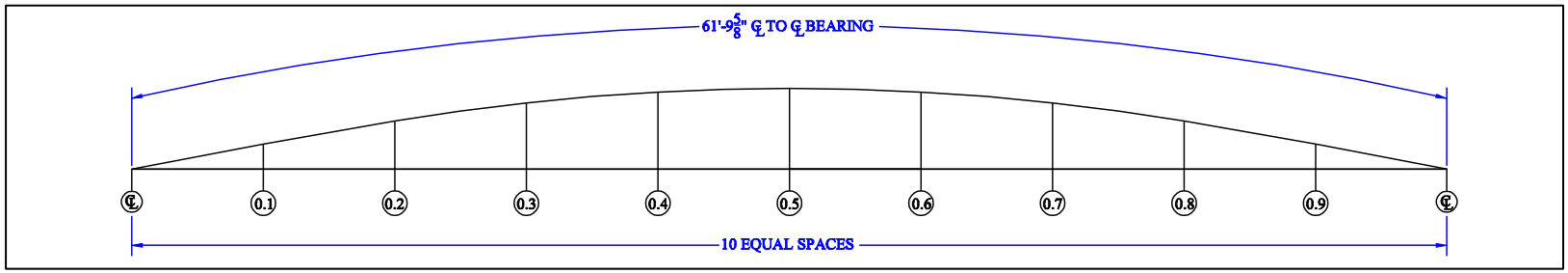

(b) G2

Figure 3.9: TFG camber diagram (Putnam, 2011)

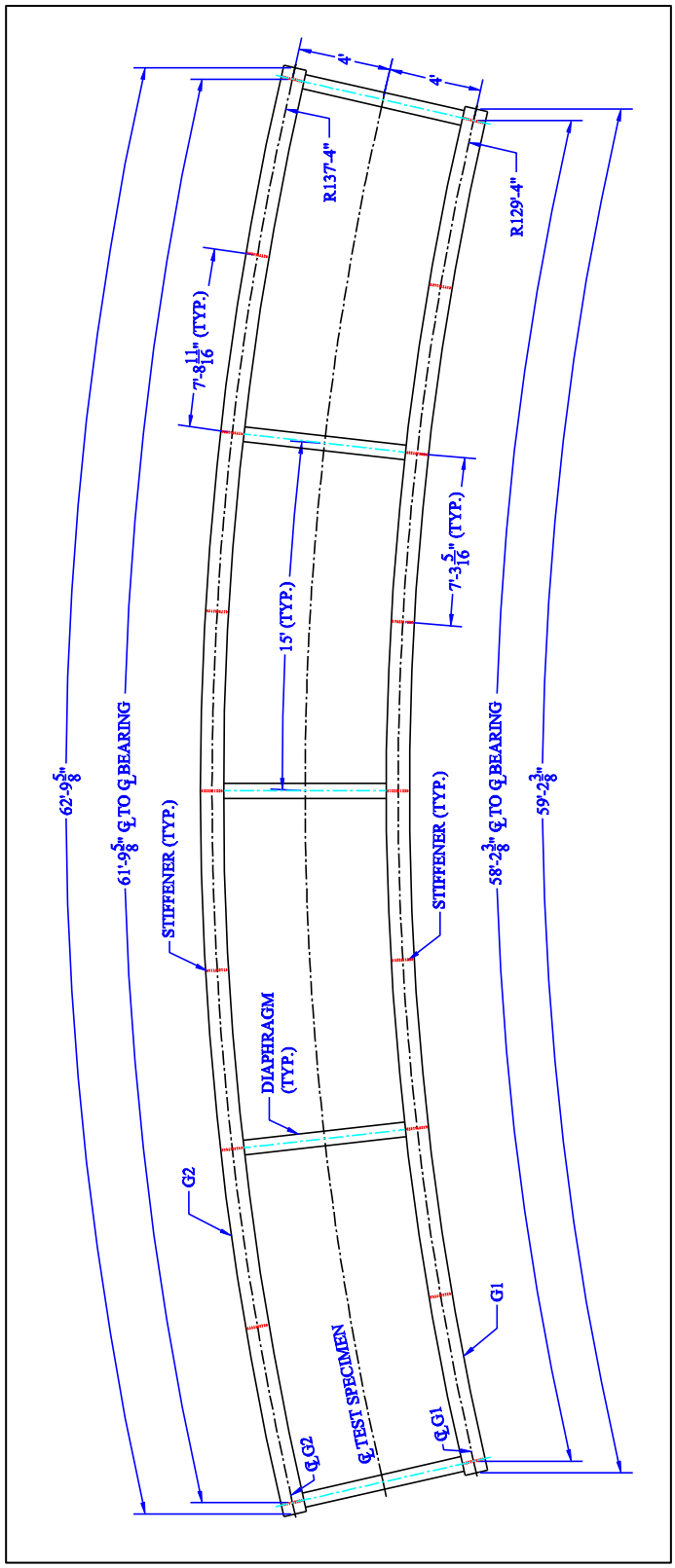

Figure 3.10: Test specimen plan view including diaphragms and stiffeners (Putnam, 2011)

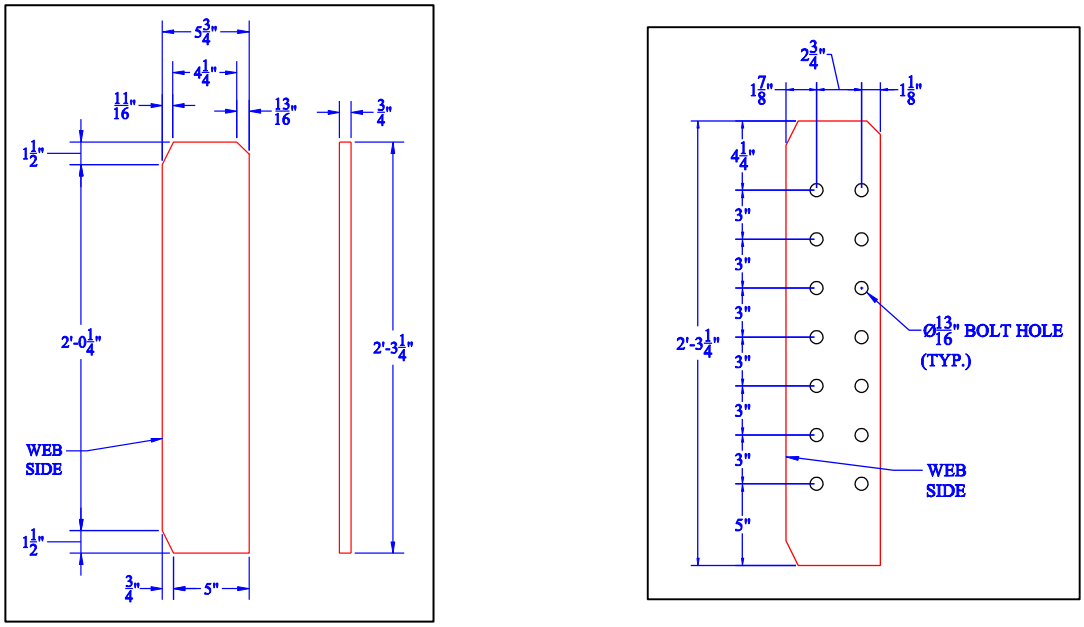

(a) G1

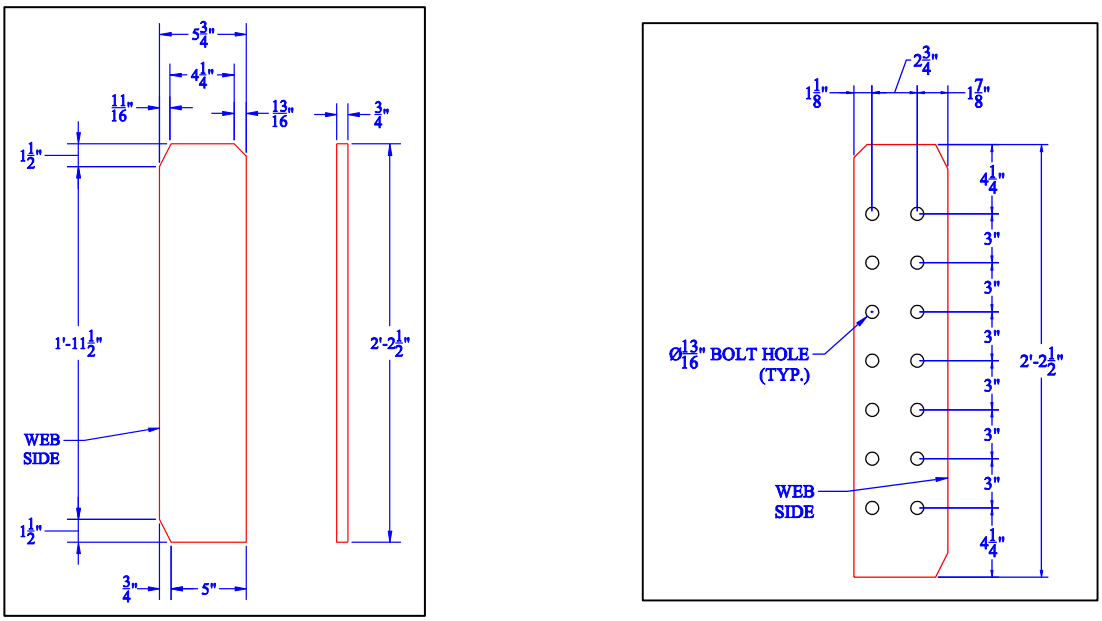

(b) G2

Figure 3.11: Bearing stiffeners and transverse stiffeners at Section A and at Section C (Putnam, 2011)

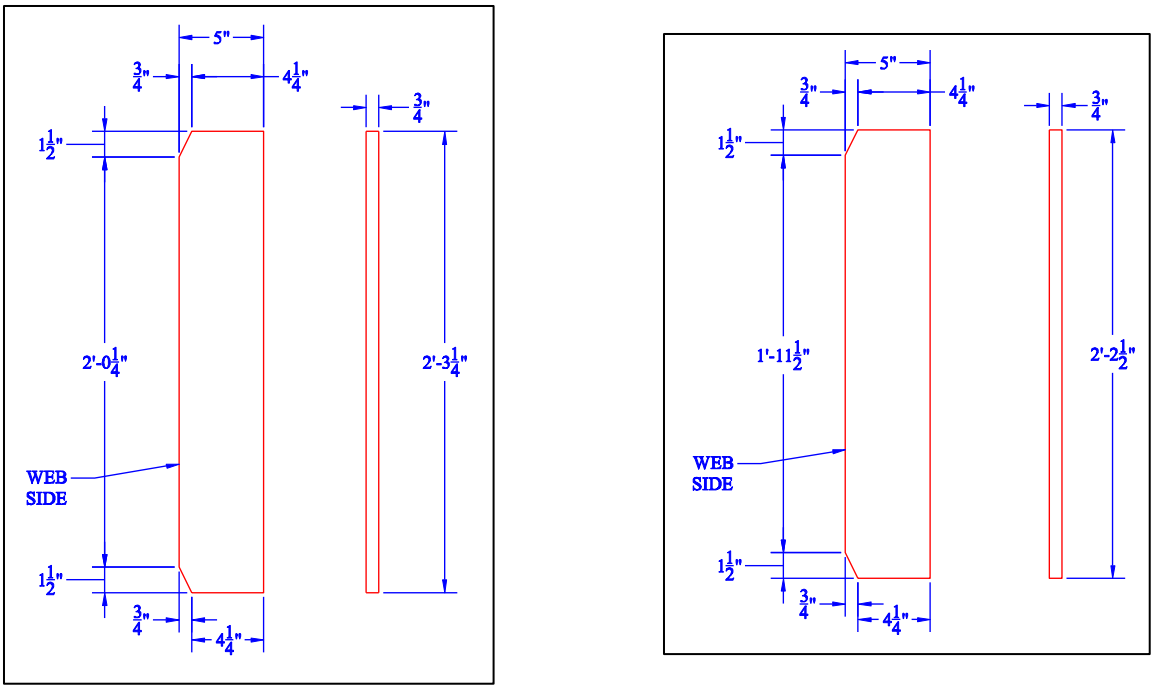

(a) G1 (b) G2

Figure 3.12: Transverse stiffeners at Section B and at Section D (Putnam, 2011)

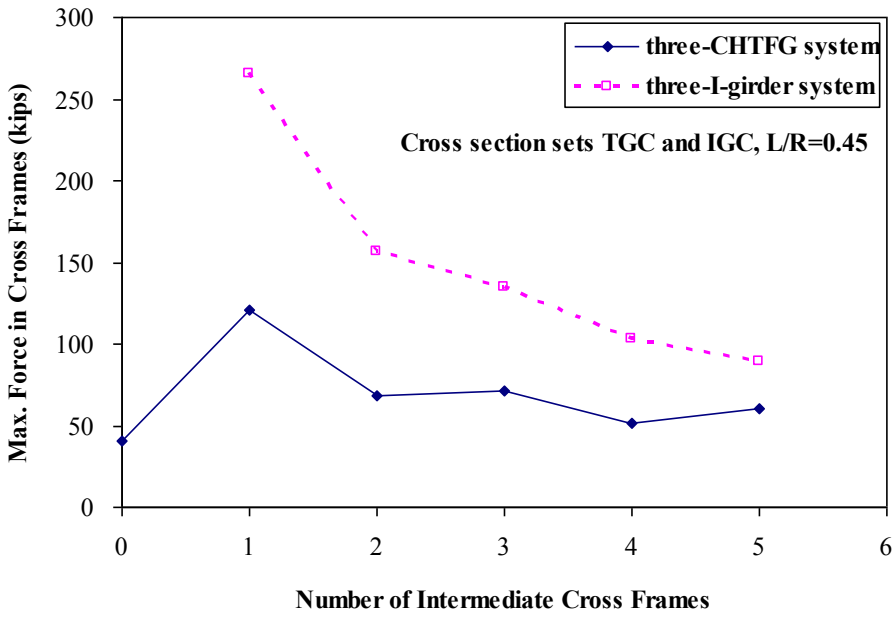

Figure 3.13: Variation of maximum force in cross-frames with number of cross-frames for systems without a composite deck (Dong, 2008)

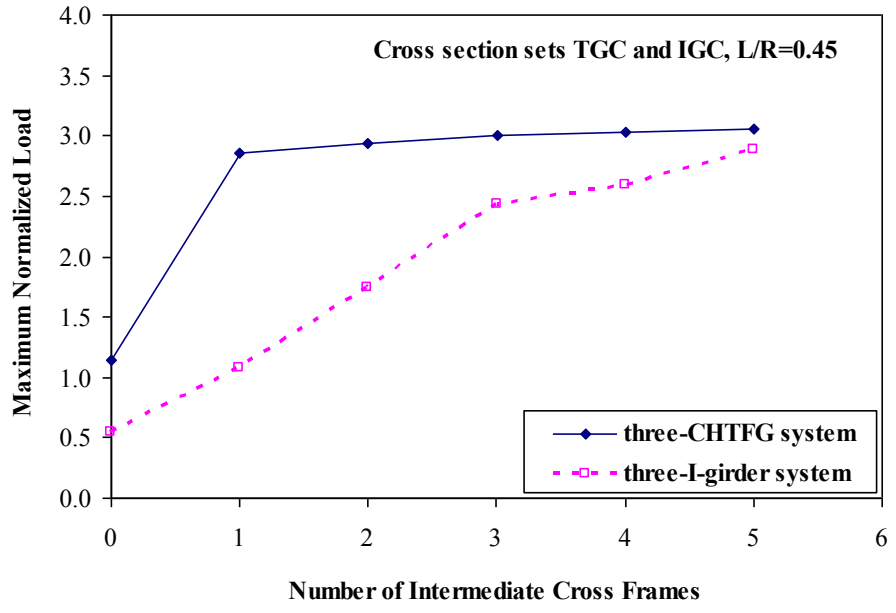

Figure 3.14: Variation of load capacity with number of cross-frames for systems without a composite deck (Dong, 2008)

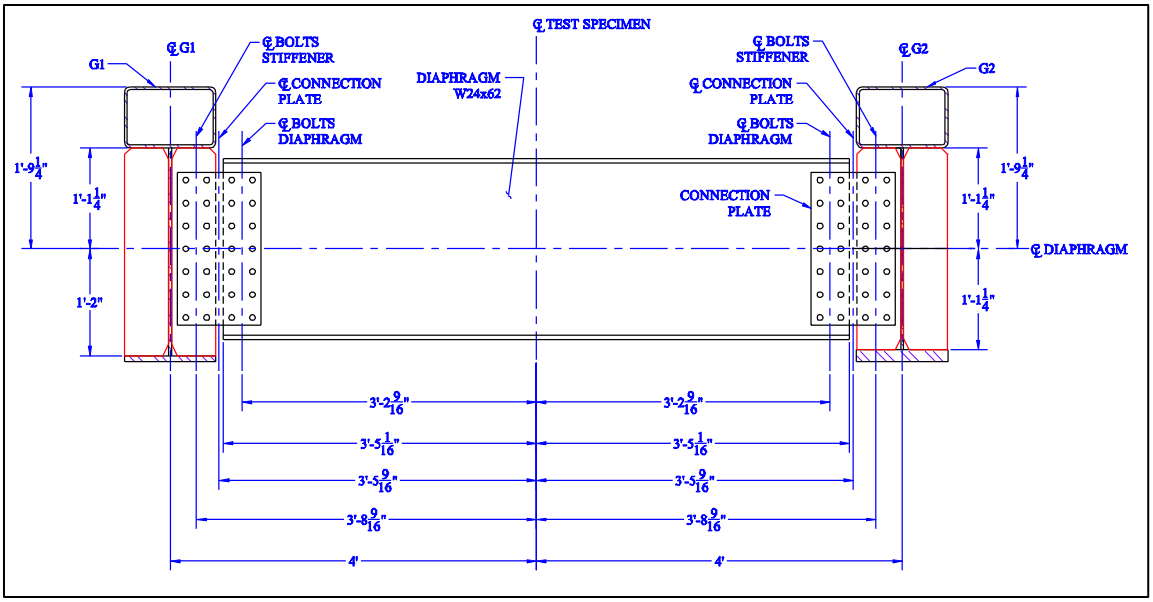

Figure 3.15: Test specimen radial cross section view at diaphragm location (Putnam, 2011)

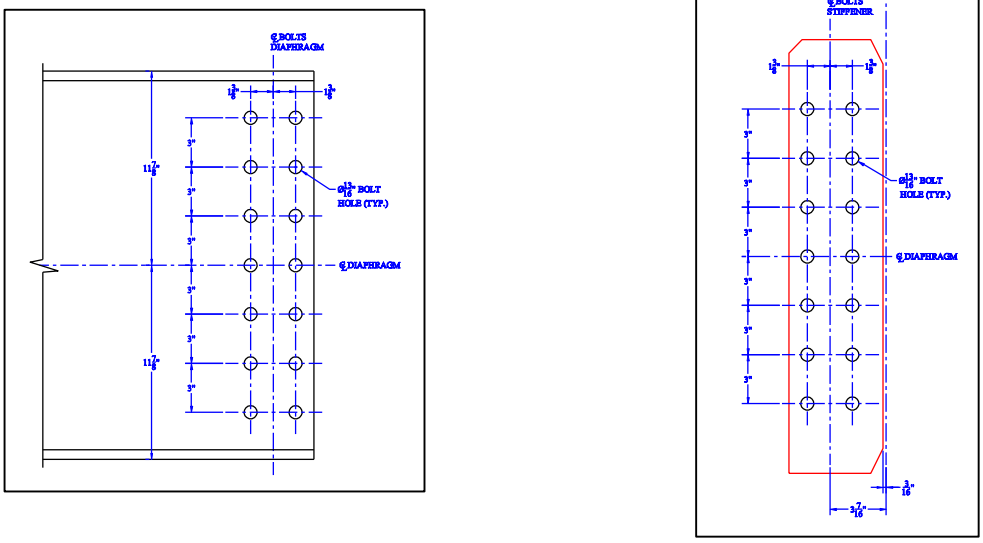

(a) Bolt holes in diaphragm

(b) Bolt holes in G2 stiffener

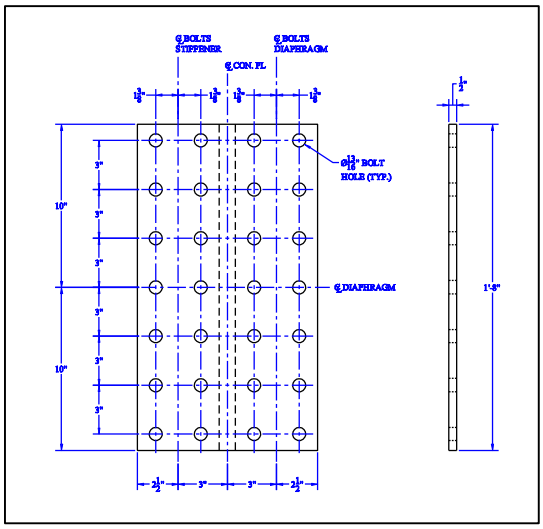

(c) Bolt holes in connection plate

Figure 3.16: Diaphragm to TFG connection detail in radial plane (Putnam, 2011)

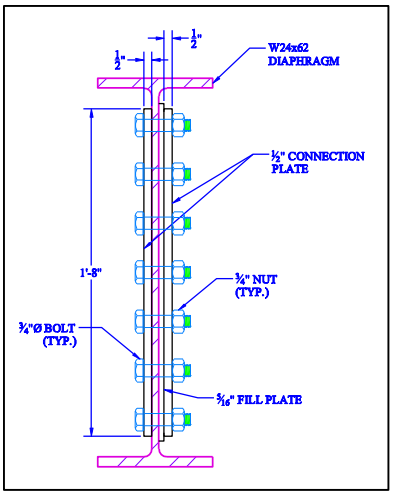

(a) Connection to diaphragm

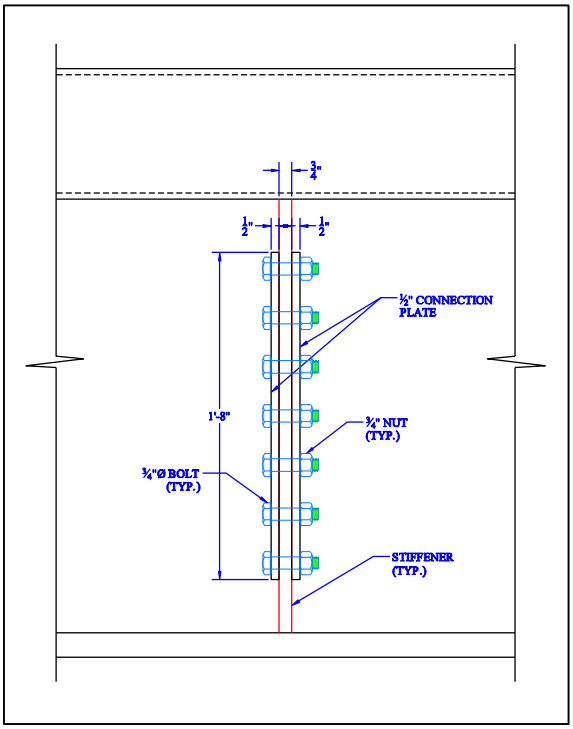

(b) Connection to stiffener

Figure 3.17: Diaphragm to TFG connection detail in circumferential plane (Putnam, 2011)

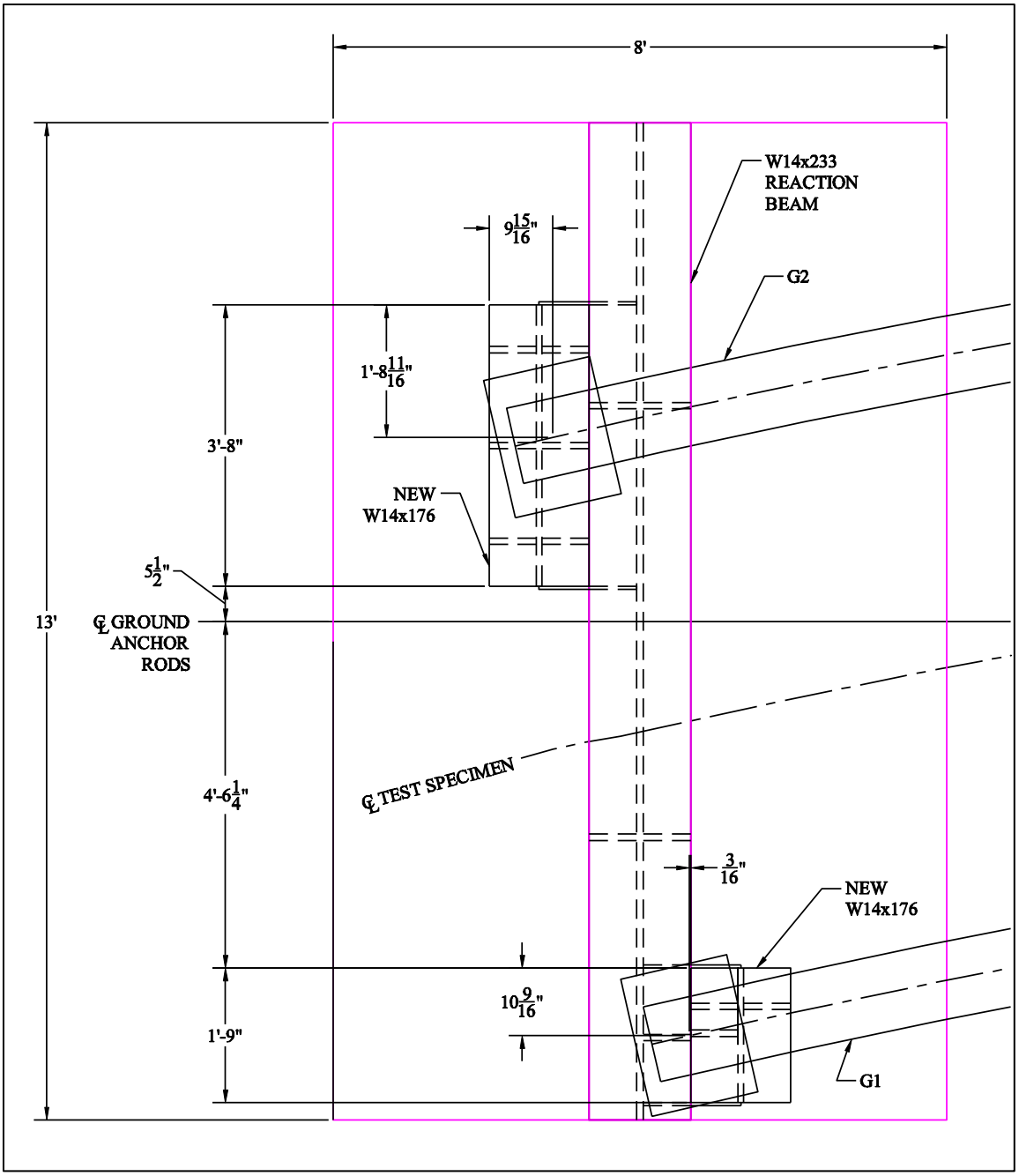

Figure 3.18: Plan view of west bearing and footing (Putnam, 2011)

Figure 3.19: East bearing of test setup (Sause et al., 2009)

Figure 3.20: Erection of test specimen (Sause et al., 2009)

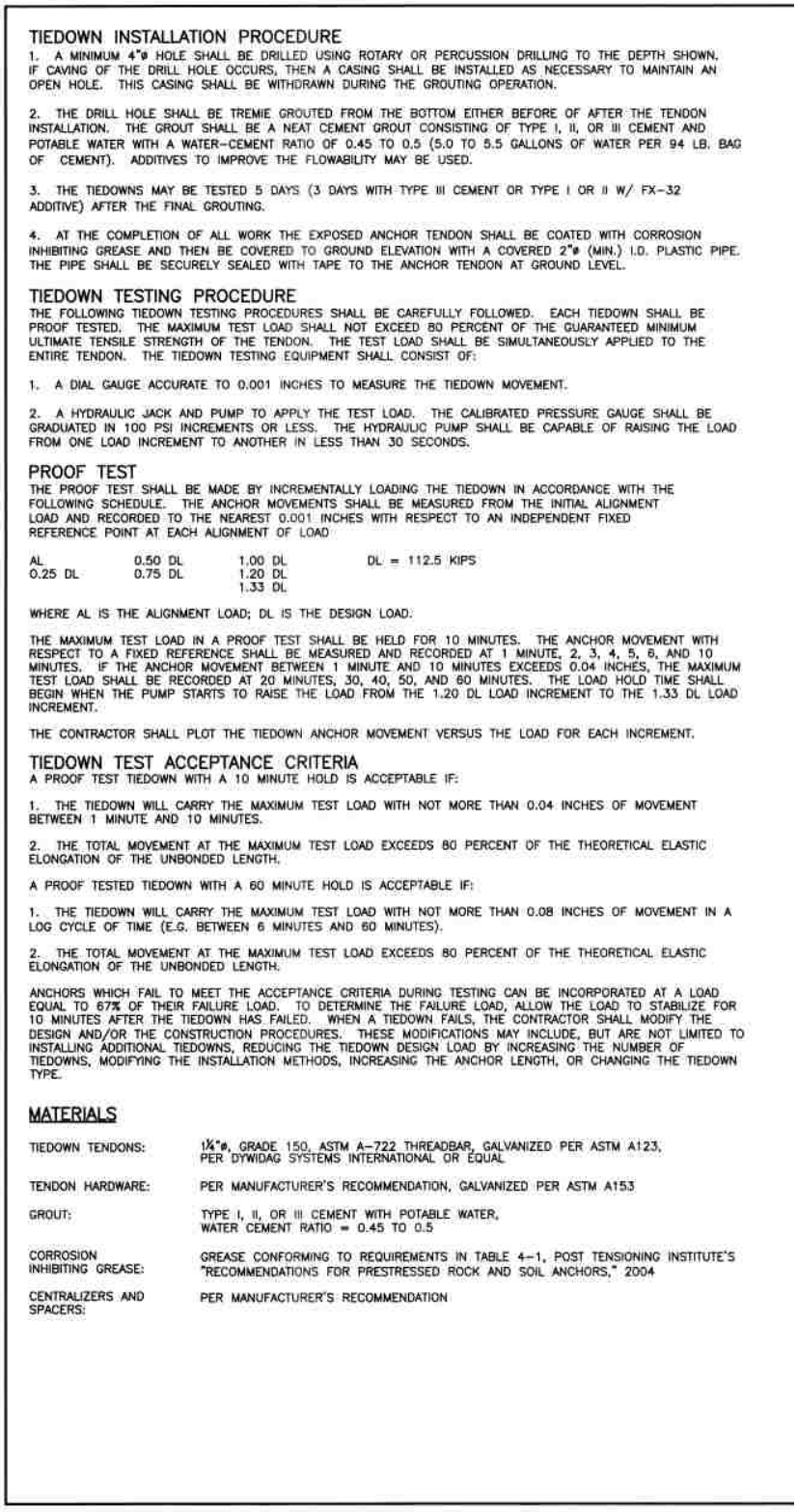

TIEDOWN INSTALLATION PROCEDURE

1. A MINIMUM 4"ø HOLE SHALL BE DRILLED USING ROTARY OR PERCUSSION DRILLING TO THE DEPTH SHOWN. IF CAVING OF THE DRILL HOLE OCCURS, THEN A CASING SHALL BE INSTALLED AS NECESSARY TO MAINTAIN AN OPEN HOLE. THIS CASING SHALL BE WITHDRAWN DURING THE GROUTING OPERATION.

2. THE DRILL HOLE SHALL BE TREMIE GROUTED FROM THE BOTTOM EITHER BEFORE OF AFTER THE TENDON INSTALLATION. THE GROUT SHALL BE A NEAT CEMENT GROUT CONSISTING OF TYPE I, II, OR III CEMENT AND POTABLE WATER WITH A WATER-CEMENT RATIO OF 0.45 TO 0.5 (5.0 TO 5.5 GALLONS OF WATER PER 94 LB. BAG OF CEMENT). ADDITIVES TO IMPROVE THE FLOWABILITY MAY BE USED.

3. THE TIEDOWNS MAY BE TESTED 5 DAYS (3 DAYS WITH TYPE III CEMENT OR TYPE I OR II W/ FX-32 ADDITIVE) AFTER THE FINAL GROUTING.

4. AT THE COMPLETION OF ALL WORK THE EXPOSED ANCHOR TENDON SHALL BE COATED WITH CORROSION INHIBITING GREASE AND THEN BE COVERED TO GROUND ELEVATION WITH A COVERED 2"ø (MIN.) I.D. PLASTIC PIPE. THE PIPE SHALL BE SECURELY SEALED WITH TAPE TO THE ANCHOR TENDON AT GROUND LEVEL.

TIEDOWN TESTING PROCEDURE

THE FOLLOWING TIEDOWN TESTING PROCEDURES SHALL BE CAREFULLY FOLLOWED. EACH TIEDOWN SHALL BE PROOF TESTED. THE MAXIMUM TEST LOAD SHALL NOT EXCEED 80 PERCENT OF THE GUARANTEED MINIMUM ULTIMATE TENSILE STRENGTH OF THE TENDON. THE TEST LOAD SHALL BE SIMULTANEOUSLY APPLIED TO THE ENTIRE TENDON. THE TIEDOWN TESTING EQUIPMENT SHALL CONSIST OF:

1. A DIAL GAUGE ACCURATE TO 0.001 INCHES TO MEASURE THE TIEDOWN MOVEMENT.

2. A HYDRAULIC JACK AND PUMP TO APPLY THE TEST LOAD. THE CALIBRATED PRESSURE GAUGE SHALL BE GRADUATED IN 100 PSI INCREMENTS OR LESS. THE HYDRAULIC PUMP SHALL BE CAPABLE OF RAISING THE LOAD FROM ONE LOAD INCREMENT TO ANOTHER IN LESS THAN 30 SECONDS.

PROOF TEST

THE PROOF TEST SHALL BE MADE BY INCREMENTALLY LOADING THE TIEDOWN IN ACCORDANCE WITH THE FOLLOWING SCHEDULE. THE ANCHOR MOVEMENTS SHALL BE MEASURED FROM THE INITIAL ALIGNMENT LOAD AND RECORDED TO THE NEAREST 0.001 INCHES WITH RESPECT TO AN INDEPENDENT FIXED REFERENCE POINT AT EACH ALIGNMENT OF LOAD

AL	0.50 DL	1.00 DL	DL = 112.5 KIPS
0.25 DL	0.75 DL	1.20 DL	
		1.33 DL	

WHERE AL IS THE ALIGNMENT LOAD; DL IS THE DESIGN LOAD.

THE MAXIMUM TEST LOAD IN A PROOF TEST SHALL BE HELD FOR 10 MINUTES. THE ANCHOR MOVEMENT WITH RESPECT TO A FIXED REFERENCE SHALL BE MEASURED AND RECORDED AT 1 MINUTE, 2, 3, 4, 5, 6, AND 10 MINUTES. IF THE ANCHOR MOVEMENT BETWEEN 1 MINUTE AND 10 MINUTES EXCEEDS 0.04 INCHES, THE MAXIMUM TEST LOAD SHALL BE RECORDED AT 20 MINUTES, 30, 40, 50, AND 60 MINUTES. THE LOAD HOLD TIME SHALL BEGIN WHEN THE PUMP STARTS TO RAISE THE LOAD FROM THE 1.20 DL LOAD INCREMENT TO THE 1.33 DL LOAD INCREMENT.

THE CONTRACTOR SHALL PLOT THE TIEDOWN ANCHOR MOVEMENT VERSUS THE LOAD FOR EACH INCREMENT.

TIEDOWN TEST ACCEPTANCE CRITERIA

A PROOF TEST TIEDOWN WITH A 10 MINUTE HOLD IS ACCEPTABLE IF:

1. THE TIEDOWN WILL CARRY THE MAXIMUM TEST LOAD WITH NOT MORE THAN 0.04 INCHES OF MOVEMENT BETWEEN 1 MINUTE AND 10 MINUTES.

2. THE TOTAL MOVEMENT AT THE MAXIMUM TEST LOAD EXCEEDS 80 PERCENT OF THE THEORETICAL ELASTIC ELONGATION OF THE UNBONDED LENGTH.

A PROOF TESTED TIEDOWN WITH A 60 MINUTE HOLD IS ACCEPTABLE IF:

1. THE TIEDOWN WILL CARRY THE MAXIMUM TEST LOAD WITH NOT MORE THAN 0.08 INCHES OF MOVEMENT IN A LOG CYCLE OF TIME (E.G. BETWEEN 6 MINUTES AND 60 MINUTES).

2. THE TOTAL MOVEMENT AT THE MAXIMUM TEST LOAD EXCEEDS 80 PERCENT OF THE THEORETICAL ELASTIC ELONGATION OF THE UNBONDED LENGTH.

ANCHORS WHICH FAIL TO MEET THE ACCEPTANCE CRITERIA DURING TESTING CAN BE INCORPORATED AT A LOAD EQUAL TO 67% OF THEIR FAILURE LOAD. TO DETERMINE THE FAILURE LOAD, ALLOW THE LOAD TO STABILIZE FOR 10 MINUTES AFTER THE TIEDOWN HAS FAILED. WHEN A TIEDOWN FAILS, THE CONTRACTOR SHALL MODIFY THE DESIGN AND/OR THE CONSTRUCTION PROCEDURES. THESE MODIFICATIONS MAY INCLUDE, BUT ARE NOT LIMITED TO INSTALLING ADDITIONAL TIEDOWNS, REDUCING THE TIEDOWN DESIGN LOAD BY INCREASING THE NUMBER OF TIEDOWNS, MODIFYING THE INSTALLATION METHODS, INCREASING THE ANCHOR LENGTH, OR CHANGING THE TIEDOWN TYPE.

MATERIALS

TIEDOWN TENDONS:	1¼"ø, GRADE 150, ASTM A-722 THREADBAR, GALVANIZED PER ASTM A123, PER DYWIDAG SYSTEMS INTERNATIONAL OR EQUAL
TENDON HARDWARE:	PER MANUFACTURER'S RECOMMENDATION, GALVANIZED PER ASTM A153
GROUT:	TYPE I, II, OR III CEMENT WITH POTABLE WATER, WATER CEMENT RATIO = 0.45 TO 0.5
CORROSION INHIBITING GREASE:	GREASE CONFORMING TO REQUIREMENTS IN TABLE 4-1, POST TENSIONING INSTITUTE'S "RECOMMENDATIONS FOR PRESTRESSED ROCK AND SOIL ANCHORS," 2004
CENTRALIZERS AND SPACERS:	PER MANUFACTURER'S RECOMMENDATION

Figure 3.21: PE ground anchor rod drawing, sheet 1 of 2 (PE, 2009a)

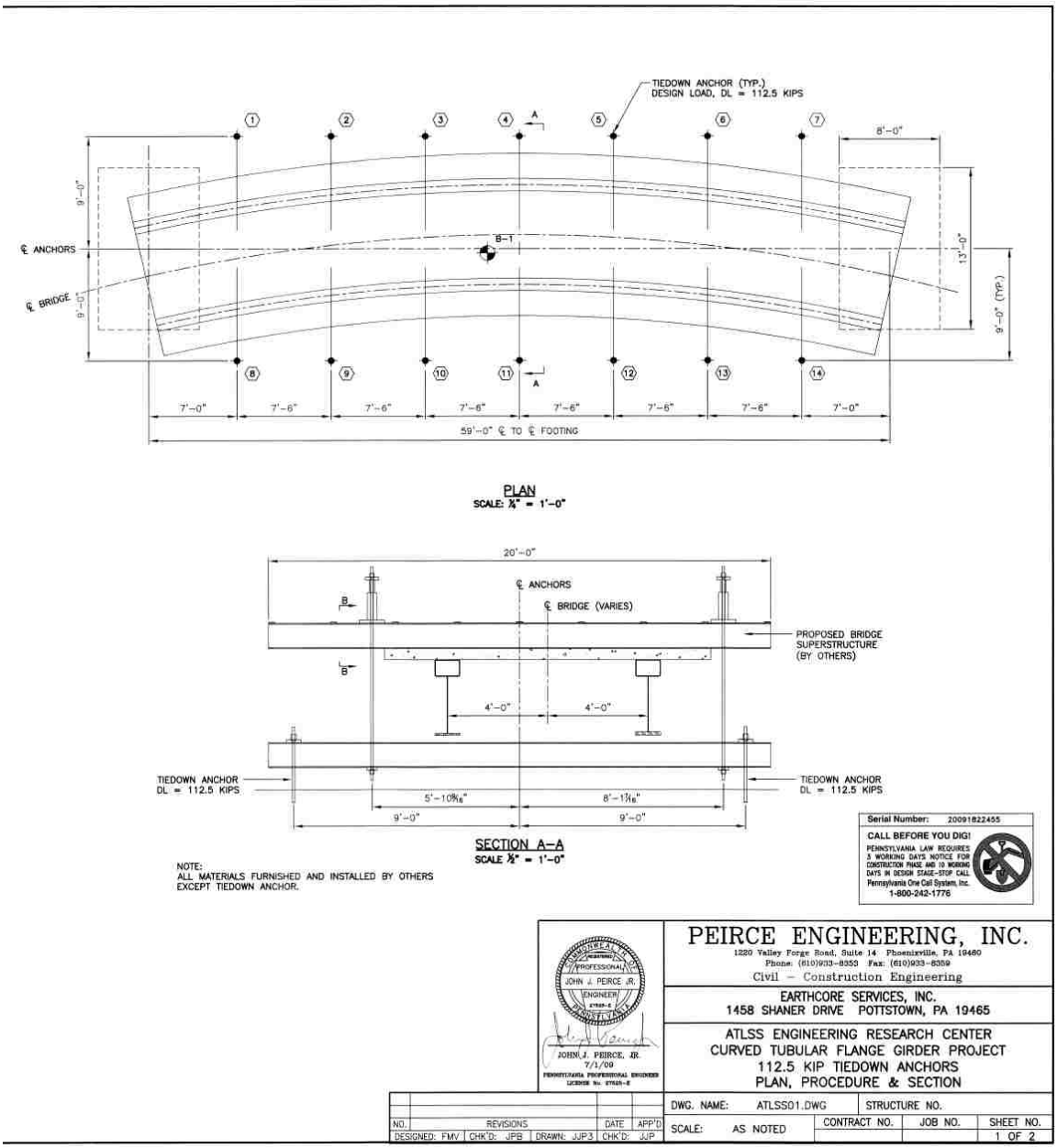

Figure 3.21 (cont'd.): PE ground anchor rod drawing, sheet 1 of 2 (PE, 2009a)

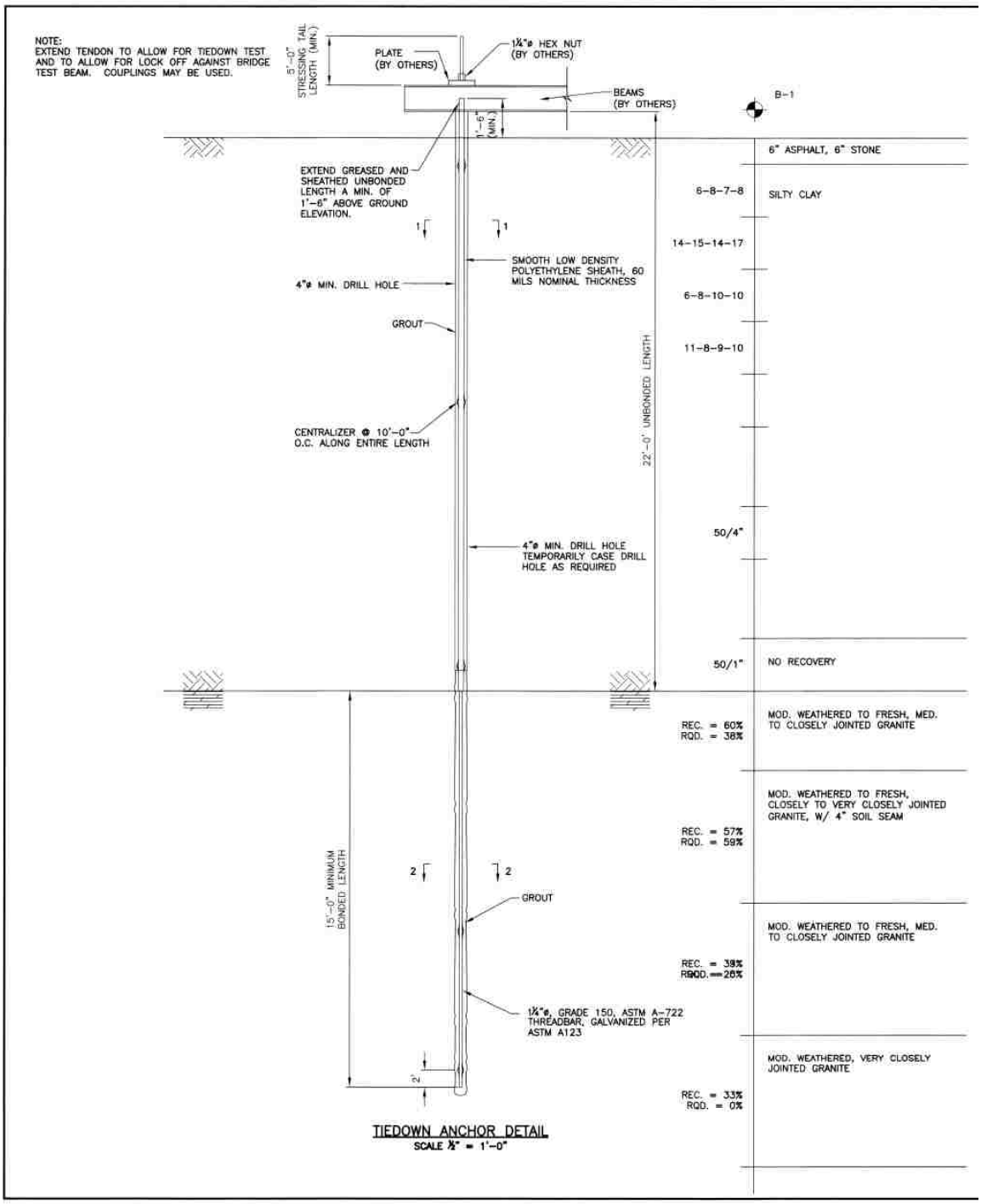

Figure 3.22: PE ground anchor rod drawing, sheet 2 of 2 (PE, 2009a)

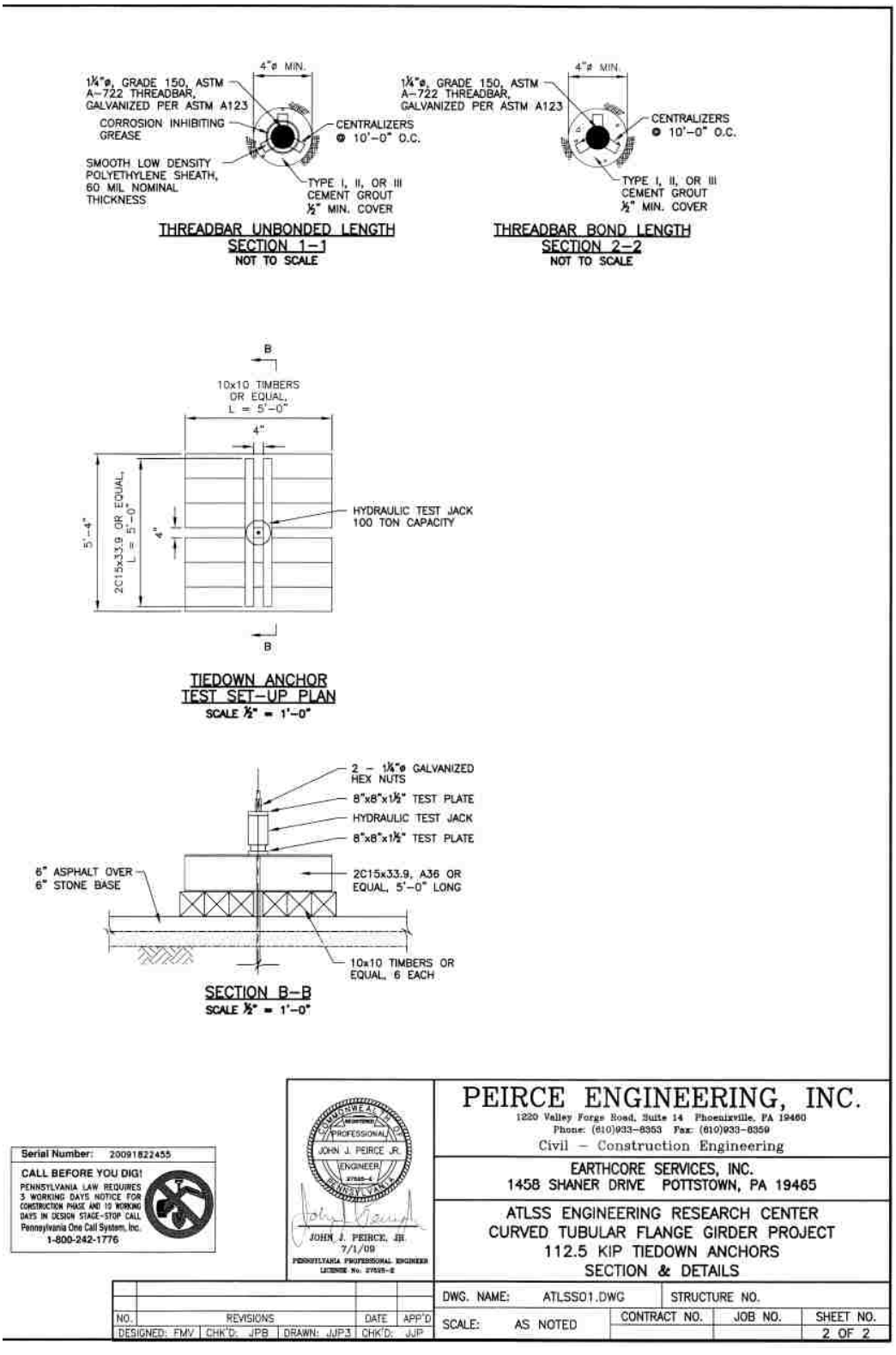

Figure 3.22 (cont'd.): PE ground anchor rod drawing, sheet 2 of 2 (PE, 2009a)

Earthcore Services Boring Log

Client: Lehigh University | Client Rep: N/A | Project: Lehigh University

BORING NO. B-1 | Date Started: 6/19/2009 | Date Completed: 6/19/2009

Driller: Tim Wilson | Drill Make/Model: Acker Soilmax

Auger: 4 ¼" HSA | Sampler: 2" Split Spoon | Shelby Tube: N/A | Rock Coring: NQ 2

* Earthcore Services, LLC assumes no responsibility for interpretations made by any party relying on information provided on this test boring log. Only an experienced Geotechnical Engineer can interpret and determine the results of the information provided below.

Depth Below Surface	Blows per 6" 140# / 30" Safety Hammer	Soil/Rock Classification	Auger Refusal	Rock Coring Start/Stop (Recovery)	Water Depth	Remarks
0-1'	N/A	6" Asphalt, 6" Stone				
1-3'	6-8-7-8	Gray-brown Silty clay				6" Recovery Fill
3-5'	14-15-14-17	Orange-yellow Silty clay				6" Recovery Fill
5-7'	6-8-10-10	Gray-brown Silty clay				6" Recovery Fill
7-9'	11-8-9-10	Brown-dark yellow, Silty clay				4" Recovery 10-12' cobbles
14-16'	50/4"	Brown-yellow, Silty clay				4" Recovery 14-17' cobbles
19-21'	50/1	No recovery	19'		18'	
19-24'		Gray, dark gray and olive brown moderately weathered to fresh, med to closely jointed granite		60" recovery 38% RQD		18 minutes cut time
24-29'		Olive brown and gray mod weathered to fresh, closely to very closely jtd granite with 4" soil seam		57" recovery 59% RQD		21 minutes cut time
29-34'		Dark gray and yellow-brown mod weathered to fresh, med to closely jointed granite		39" recovery 25% RQD		19 minutes cut time
34-39'		Dark gray, mod weathered, very closely jointed granite		33" recovery 0% RQD		21 minutes cut time
39-43'		Gray and dark gray, mod weathered to fresh, v closely to closely jointed, granite		48" recovery 29% RQD		18 minutes cut time
43'						Boring/coring terminated

* While coring, experienced core barrel jamming due to fractured and weathered rock. Actual rock recovered may not be indicative of true recovery value. Numerous attempts were made to retrieve rock samples. The last 3 runs were drilled in competent rock with steady drill times and no indication of soil seams.

Figure 3.23: Test setup area boring log (ES, 2009)

Figure 3.24: Installed ground anchor rods covered by plastic pipes (Sause et al., 2009)

CHAPTER 4: LOADING AND KINEMATICS OF TEST SPECIMEN AND LOADING FIXTURES

4.1. Introduction

This chapter describes the loading and the kinematics of the test specimen and the loading fixtures. Section 4.2 explains the test specimen loading and then Section 4.3 discusses the kinematic response of the test specimen and loading fixtures under load.

4.2. Test Specimen Loading

This section explains the basis for the loads applied to the test specimen. The loads are based on the loads and limit states considered by the AASHTO Load and Resistance Factor Design (LRFD) Bridge Design Specifications (AASHTO, 2005). Section 4.2.1 describes the aspects of the AASHTO LRFD Specifications (2005) related to the tests. Section 4.2.2 describes the loads that will be applied to the test specimen and Section 4.2.3 presents results from an FE model that was used to plan the tests.

4.2.1. LRFD Loading and Limit States for Bridge Design

The AASHTO LRFD Specifications (2005) require an examination of all structural components and connections of a bridge considering all critical stages of its life, including handling, transportation, and construction (Dong, 2008). The factored load effect (demand) on a structural component or connection must be less than the factored resistance of the component or connection. The material, geometry, and resistance factors affect the calculated factored resistance values (Putnam, 2010). The resistance factors, ϕ,

specified in AASHTO Section 6.5.4.2 depend on resistance type (e.g., flexure, shear, and axial compression). All resistance factors are less than or equal to 1.0. The load factors, γ, given in AASHTO Section 3.4.1 depend on the type of load (e.g., dead load and live load) and the limit state being examined. AASHTO Table 3.4.1-1 provides various load combinations to be considered. The load factors can be less than, equal to, or greater than 1.0. If the factored resistances are less than or equal to the factored load effects, the bridge design is deemed to be adequate (AASHTO, 2005).

Dong (2008) considered three limit states in developing design guidelines for curved hollow TFGs: Constructability, Service II, and Strength I. Constructability limit states are considered to ensure that yielding or buckling will not occur during construction. This consideration includes controlling stresses and deflections that occur during erection. Service II limit states are considered to ensure that under normal service conditions, yielding and permanent deflections do not occur in bridge girders. Strength I limit states are considered to establish safety under the maximum loading of the bridge under normal use; global and local strength and stability are ensured (Dong, 2008). Constructability limits are checked for two conditions: (1) a single girder during erection and (2) multiple non-composite girders connected by cross-frames (or diaphragms) during deck placement. Service II and Strength I limits are checked for the final constructed condition of the bridge. In this condition, the bridge girders are composite with the bridge deck.

For the three limit states studied by Dong (2008), different combinations of loads are considered. For an individual, non-composite steel girder during erection, the only

design load considered for Constructability is the self-weight of the steel girder, SW, which is based on a unit weight of 490 lb/ft^3 for the steel. For a system of non-composite girders connected by cross-frames during construction, the design loads considered for Constructability include the applied dead load, D_C, and the applied live load, LL_C, during deck placement. D_C includes the weight of the structural components and attachments (including SW) and the weight of the concrete deck, which is based on a unit weight of 150 lb/ft^3 for reinforced, normal weight concrete. D_C also includes a weight of 16 lb/ft^3 for the stay-in-place deck forms and an estimated weight of 10% of the steel girder weight to account for stiffeners and cross-frames. The construction live load (LL_C) is assumed to be a uniform pressure of 20 lb/ft^2 over the bridge deck area; this value was taken from the Guide Design Specifications for Bridge Temporary Works (AASHTO, 1995). Table 4.1 lists the load combinations for the Constructability limit states.

For Service II and Strength I limit states, the same types of loads are used, but the load factors are different. Table 4.2 gives the load factors. The loads include dead loads, D_C and D_W, and live loads, LL. D_C is explained previously. D_W is the superimposed dead load, including the weight of the utilities attached to the bridge and the weight of the future wearing surfaces applied in the final constructed condition of the bridge. The superimposed dead load also includes components, such as lights and parapets, and is estimated to be 275 lb/ft applied along the centerline of the curb. The future wearing surface has a weight of 30 lb/ft^2. The live load is based on the design lane load and the HS20 design truck given in AASHTO (2005). These two loads are arranged to produce the maximum load effects on each girder.

The AASHTO LRFD Specifications (2005) provide different design criteria for each limit state. Dong (2008) explains how the criteria apply to curved TFGs. Constructability limit states during deck placement are the main focus of the tests on the test specimen. The design criteria for Constructability during deck placement are included here. The following two equations must be satisfied:

$$f_{bu} + f_l \leq \phi_f R_h F_{yc} \quad \textbf{(4.1)}$$

$$f_{bu} + \frac{1}{3} f_l \leq \phi_f F_{nc} \quad \textbf{(4.2)}$$

The variables as defined in AASHTO Section 6.3 (2005) are,

f_{bu} is the largest value of the compressive stress throughout the unbraced length in the flange under consideration, calculated without consideration of flange lateral bending (ksi)

f_l is the flange lateral bending stress (ksi)

ϕ_f is the resistance factor for flexure

R_h is the hybrid factor to account for different material strengths for the web and flanges

F_{yc} is the specified minimum yield stress of the compression flange (ksi)

F_{nc} is the nominal flexural resistance of the compression flange (ksi)

Equation (4.1) requires that the maximum combined stress in the compression flange does not exceed the minimum yield stress of the flange. Equation (4.2) requires that the flange has sufficient strength with regard to flange local buckling and member lateral-torsional buckling. For TFGs, F_{nc} is based on the lateral-torsional buckling resistance of the compression flange. Local buckling is not considered for the tubular flange as long as the tubular flange is compact and satisfies the following limit:

$$\frac{b}{t} \leq 1.7\sqrt{\frac{E}{F_y}} \qquad \textbf{(4.3)}$$

where,

b is the horizontal width of the tube (in)

t is the thickness of the tube (in)

E is Young's modulus (ksi)

F_y is the specified minimum yield stress of the tube (ksi)

The lateral-torsional buckling resistance, F_{nc}, equals the design flexural strength, M_d, divided by the elastic section modulus of the compression flange taken about the major axis of the cross section, S_{xc}. The calculation of M_d is explained further by Dong (2008) and is based on prior work by Kim and Sause (2005a, b).

4.2.2. Load Condition of Test Specimen

Two load conditions will be applied to the test specimen. The first load condition is the Constructability limit state design load, based on the deck placement condition. The total load on the test specimen for this condition is 181 kip. This total load is the 2/3-scaled value (i.e., 4/9 of the total full-scale load) for the deck placement condition design load used to design the full-scale TFG bridge. The TFG test specimen design and scaling process is explained in Section 3.3. This load condition may be applied multiple times. The second load condition for the test specimen will take it to its maximum load capacity. The expected failure mode is yielding in the top tube flanges where the stress is expected to be dominated by bending normal stress (Dong, 2008). Under both load conditions, the responses of the test specimen, including reactions at the bearings, deflections, and strains, will be measured.

The test specimen will be loaded using seven loading fixtures. Each loading fixture will apply two concentrated loads to the test specimen. The loading fixtures will be located at the seven parallel sections explained in Section 3.2. Figure 4.1 is a parallel plane cross section view of the test specimen and a loading fixture. At each loading fixture, two "loading rod assemblies" will pull down on a wide flange beam (the "loading beam") above the test specimen. Each loading rod assembly is comprised of a hydraulic jack and a series of steel plates, half-rounds (steel round bars cut in half lengthwise), and steel rods. The loading beam will bear down on the test specimen through two "load bearing assemblies." Each load bearing assembly is a series of steel components including plates, half-rounds, and a hollow-structural-section (HSS). The loading rod

assemblies will also pull up on a pair of laced channels (the "load transfer channels") below the test specimen. The load transfer channels will be anchored by the "ground anchor rods" that will resist the upward force of the loading rod assemblies. The design of the loading fixtures and its components is presented in Chapter 5.

4.2.3. Idealization and Modeling of Loads

Deck placement loads are dominated by uniformly distributed loads. The primary exception is the load from deck finishing machines. For the tests, the deck placement loads are initially idealized as a uniformly distributed load, which is constant over the deck area. This distributed load will be simulated in the tests with 14 discrete concentrated loads applied by the seven loading fixtures. An FE study was completed using FE models developed by Ma (2012) to show that the concentrated loads would produce test specimen responses similar to those from a distributed load. The study, explained in this section, considered multiple load cases, each with a different simulation of the idealized uniformly distributed load. As discussed later, the responses were found to be similar enough to use concentrated loads in the tests.

During deck placement, the non-composite girders support the weight of the concrete deck, the construction live load, and the formwork required to cast the deck, as described previously. The formwork supports the deck and the construction live load, and transfers this load as a pressure to the top of the girder flanges. In the tests, it is not possible to apply a uniformly distributed load representing the concrete deck, formwork, and construction live loads. The tests require the load to be applied and removed multiple

times. In addition, constructing an actual deck would be expensive. In the final test, the test specimen will be loaded beyond its maximum load capacity, and safety would be a concern.

The test specimen will be loaded with concentrated loads instead of a uniformly distributed load. For a simply supported straight girder, the same mid-span moment can be developed by a uniformly distributed load or a set of concentrated loads. For a simply supported curved girder, this may not be true because of the torsional load effects caused by the horizontal curvature of the girder. Therefore, FE models of the test specimen were developed in ABAQUS (2011) to determine if concentrated loads on the test specimen could produce similar load effects as a uniformly distributed load on the test specimen.

To help determine the number and locations of the concentrated loads on the test specimen, a preliminary analysis was conducted of a simply supported straight girder under a uniformly distributed load, and then under concentrated loads. Figure 4.2 (a), (b), and (c) shows the free body diagram and corresponding moment diagram for a uniformly distributed load, a concentrated load simulation with an even number of segments (N is even), and a concentrated load simulation with an odd number of segments (N is odd), respectively. The concentrated loads used to simulate the uniformly distributed load are evenly spaced between the supports, creating N segments with the same length. Each concentrated load simulates a portion of the uniformly distributed load. The mid-span moment for the concentrated load simulation can be calculated based on N.

For a uniformly distributed load, ω, acting along a beam of length, L, the maximum moment is:

$$M_{max\_distr} = \frac{\omega L^2}{8} \tag{4.4}$$

For the concentrated load simulation, each intermediate concentrated load is equal to:

$$P = \frac{\omega L}{N} \tag{4.5}$$

The concentrated load applied at each support is equal to P/2.

When N is an even number, the maximum moment can be calculated from the following equation:

$$M_{max\_even} - \frac{\omega L^2}{4} + \frac{\omega L^2}{4N} + \sum_{i=0}^{\frac{N}{2}-1} \left(\frac{\omega L^2}{N^2} i \right) = 0 \tag{4.6}$$

When simplified, M_{max_even} equals M_{max_distr}.

When N is an odd number, the maximum moment can be calculated from the following equation:

$$M_{max\_odd} - \frac{\omega L^2}{4} + \frac{\omega L^2}{4N} + \sum_{i=0}^{\frac{N-1}{2}-1} \left[\frac{\omega L^2}{N^2} \left(i + \frac{1}{2} \right) \right] = 0 \tag{4.7}$$

Simplifying this equation results in a maximum moment of:

$$M_{max\_odd} = \frac{\omega L^2}{8}\left(\frac{N^2 - 1}{N^2}\right) \quad \textbf{(4.8)}$$

M_{max_odd} is always less than M_{max_distr}. Therefore, the load effects at mid-span due to a uniformly distributed load are well-simulated by equally-spaced concentrated loads that divide the span into an even number of segments, where the number of intermediate concentrated loads is odd.

The tests will use seven concentrated loads along each curved TFG between the bearings to simulate the idealized uniformly distributed load. Figure 4.3 shows a radial plane cross section view of the 2/3-scale test specimen with idealized loads. For the curved girder test specimen, it was not assumed that the load effects at mid-span produced by concentrated loads would be the same as the load effects at mid-span produced by a uniformly distributed load. FE analyses were used to compare the idealized load condition with the test load condition to ensure that the concentrated loads on the curved TFGs would produce similar responses at mid-span as the idealized uniformly distributed load.

Several load cases were studied using ABAQUS FE software (ABAQUS, 2011). An FE model of the test specimen was developed using shell elements for the TFGs and the stiffeners, and beam elements for the diaphragms and connection plates (Ma, 2012). The FE model used the boundary condition combination bc2 with two pins and two rollers, explained in Section 4.3.2. For each load case, the FE model was loaded until the

TFG system reached its maximum load capacity. The load was applied to the TFGs in increments. The load for each increment was proportional to a reference load. The reference load used for the FE analysis was equal to the weight of the concrete deck. The responses of the FE model, such as the displacements, were provided at each increment, or "load step", during loading (Ma, 2012).

The maximum load capacity of the FE model for each load case was used to verify the similarity in the responses of the test specimen to the different load cases. Six load cases are presented next. The six load cases evolve from the idealized load condition to the test load condition. Case 1 is the most accurate simulation of the idealized uniformly distributed load for the deck placement condition and Case 6 is the most accurate simulation of the concentrated loads for the test load condition.

Case 1, shown in Figure 4.4 (a) and Figure 4.5 (a), models the idealized uniformly distributed load as distributed line loads and distributed pressure loads on the TFGs over the span. The distributed line loads simulate the loads that would be carried to the TFGs by formwork. The line loads correspond to the idealized uniformly distributed load from bridge deck segments a and c in Figure 4.3. The distributed pressure loads simulate the loads applied directly to the TFGs, which corresponds to the uniformly distributed load from bridge deck segments b in Figure 4.3.

In the FE model, the loads are applied to the tops of the TFG tubes. The line loads are applied at the centerline of the sides of the tubes and the pressure loads are applied between the line loads. Figure 4.4 (a) shows a cross section view and Figure 4.5 (a)

shows an elevation view of the test specimen with these loads. In Figure 4.5 (a), for load Case 1, ω represents ω_{1_1} or ω_{1_2}. The line load, ω_{1_1}, is applied to the south side of the tube of G1 and the north side of the tube of G2. This load simulates the weight of the concrete deck over a 2 ft width from the edge of the bridge deck to the centerline of the side of the closest tube (segment a in Figure 4.3). The line load, ω_{1_2}, is applied to the north side of the tube of G1 and the south side of the tube of G2. This load simulates the weight of the concrete deck over an 8 ft width from the centerline of the side of the tube where the line load is applied to the centerline of the bridge (segment c in Figure 4.3). The uniform pressure, f_1, is applied to the top of the tubes. This load simulates the weight of the concrete deck directly above the tubes (segment b in Figure 4.3).

Case 2 models the idealized distributed load using distributed line loads applied to the centerlines of the sides of the tubes. Figure 4.4 (b) shows a cross section view and Figure 4.5 (a) shows an elevation view of the test specimen with these applied loads. In Figure 4.5 (a), f_1 is not applied for load Case 2, and ω represents ω_{2_1} or ω_{2_2}.The line loads, ω_{2_1} and ω_{2_2}, combine the loads from Case 1 as follows:

$$\omega_{2\_1} = \omega_{1\_1} + \frac{f_1}{2} b \qquad \textbf{(4.9)}$$

$$\omega_{2\_2} = \omega_{1\_2} + \frac{f_1}{2} b \qquad \textbf{(4.10)}$$

These loads are applied over the span of the TFGs.

Case 3 and Case 4 model the idealized uniformly distributed load as 14 concentrated patch loads, with one load applied over a 12 in by 12 in bearing plate at each of the seven locations along the length of each TFG. Figure 4.4 (c) shows a cross section view at Section B and Section D and Figure 4.5 (b) shows an elevation view of the test specimen with these applied loads. In Figure 4.5 (b), p represents p_{3_1}, p_{4_1}, p_{3_2}, or p_{4_2}. Cross section views at Section A and at Section C differ from the view shown in Figure 4.4 (c) in that these cross section views would include a diaphragm. The difference between Case 3 and Case 4 is the location of the patch loads. The patches of Case 3 are located in radial planes, but the patches of Case 4 are located in parallel planes. Section 3.2 describes these planes.

Ideally, the loading fixture would load the test specimen in the radial planes because each patch load for one TFG would represent an idealized tributary area of the bridge deck. However, the ground anchor rods are located in parallel planes as discussed in Section 3.9. The loading fixtures (Figure 4.1), introduced in Section 4.2.2 and described more completely in Chapter 5, use the ground anchor rods to react the load that is applied to the test specimen. Sketches of a loading beam and load transfer channels are shown in Figure 4.6 and Figure 4.7. Figure 4.6 shows a perspective view, cross section view, and plan view for radial loading of the test specimen. Figure 4.7 provides the same views for parallel loading of the test specimen. When the loading beam is in the radial plane and the load transfer channels are in the parallel plane with the ground anchor rods, there are significant eccentricities in the loading fixture. Therefore, parallel plane loading (Figure 4.7) was selected for the loading fixtures.

In the parallel plane loading condition, the loads are applied at seven parallel sections between the ends of the test specimen. An odd number of sections was chosen so that one load is applied at mid-span to maximize the primary bending moment at mid-span. In addition, as shown earlier, a uniformly distributed load and an odd number of evenly-spaced concentrated loads produces the same mid-span moment (per unit total applied load) in a straight beam. For seven concentrated loads (and three internal diaphragms), the loads are applied at the sections with a diaphragm and at the sections halfway between the diaphragms. In the test setup, sufficient space is needed to work around the loading fixtures and using seven uniformly spaced loading fixtures allows for 7.5 ft spacing between adjacent loading fixtures.

For Case 3, the radial loading case, the patch loads along G2 are the same and the patch loads along G1 are the same. However, the G2 patch loads are larger than the G1 patch loads because the G2 patch loads simulate the load on a larger bridge deck area as shown in Figure 4.8 (a). The difference is caused by the curvature of the test specimen and the resulting bridge deck area that each TFG supports. Assuming that each TFG supports half of the width of the deck, G2 supports a total area of 399.5 ft^2 and G1 supports a total area of 380.5 ft^2. The outside patch loads are each equal to $1/8^{th}$ of the total load supported by G2 and the inside patch loads are each equal to $1/8^{th}$ of the total load supported by G1.

The parallel loading patch load tributary areas are different from the radial loading patch load tributary areas because the areas are divided by parallel planes and not radial planes. Figure 4.8 compares the bridge deck divided into tributary areas for the

radial loading case and the parallel loading case. The differences between the corresponding areas for the two cases are small. Therefore, the patch load values based on the radial loading tributary areas were used for both Case 3 and Case 4.

Case 5 is the same as Case 4 except that at mid-span, concentrated point loads replace the patch loads. Figure 4.4 (d) shows a cross section view of the test specimen with the applied loads at Section A. The diaphragm is modeled as a beam element (as in the FE model). Figure 4.5 (c) shows an elevation view of the test specimen with the applied loads where p represents p_{5_1} or p_{5_2}, and P represents P_{5_1} or P_{5_2}. Each point load equals the patch pressure load multiplied by the patch area it replaces. The point loads, $P_{5\text{-}1}$ and P_{5_2}, are applied to the inside top edge of the stiffeners. The load is applied to the stiffener because loading directly on the tube at mid-span, where failure due to flexural yielding of the tube is expected, might affect the test specimen capacity. Therefore, the loads at mid-span will be applied to the mid-span diaphragm or stiffeners instead of the tubes. The exact location was unknown before the loading fixtures were designed, so the location was approximated. The loading fixtures were designed using Case 5 results.

Case 6 is the same as Case 5 except the mid-span point loads are located where the loading fixture will apply the loads to the mid-span diaphragm. Figure 4.4 (e) shows a cross section view at Section A with the actual location of the point loads. The elevation view is similar to Case 5 (Figure 4.5 (c) where p represents p_{6_1} or p_{6_2}, and P represents P_{6_1} or P_{6_2}). Case 6 closely simulates the loading of the test specimen by the loading fixtures.

Figure 4.9 and Figure 4.10 are force-vertical displacement plots provided by Ma (2012) from the FE analyses of the test specimen under the six different load cases simulating the idealized uniformly distributed load. Figure 4.9 shows results for G1 and Figure 4.10 shows results for G2. The vertical axis is the normalized total load calculated by dividing the total load by the reference load. The horizontal axis is the vertical deflection of the node at the center of the web at Section A (mid-span). The plots show that the force-displacement responses are similar between load cases. Each load case has approximately the same maximum load and corresponding displacements up to the load step of the maximum load. There is more variation between the different load cases after the maximum load during unloading. Using concentrated loads for the tests should closely simulate the load effects at mid-span that would be caused by the idealized uniformly distributed load on the test specimen.

4.3. Kinematic Conditions of Test Specimen and Loading Fixtures

A study of the kinematics of the test specimen and loading fixtures was conducted to design the loading fixtures. The design of the loading fixtures attempts to minimize the restraint of the test specimen and maintain stability of the loads as the test specimen deforms under loads. Section 4.3.1 explains the displacements obtained from the FE analysis of the test specimen. Section 4.3.2 discusses how boundary conditions in the FE model affected the kinematic results. Lastly, Section 4.3.3 describes how the displacements of the FE analysis were used to visualize the kinematics of the test specimen and loading fixtures, and to estimate the displacements needed to design the loading fixtures.

4.3.1. Displacements from FE Analysis

The loading fixtures are designed to minimize the restraint of the test specimen as it deforms under loads. Differences in the initial position and a displaced position of the test specimen were used to define the required movements of the loading fixtures. Displacement values for the test specimen under load Case 5 were obtained from the FE analysis. Some values were used directly, and other values were used in calculations and/or sketches to approximate the required displacements of the loading fixtures. FE responses were obtained at the nodes of the FE model. Results needed at a location without a node were estimated.

Displacements were obtained in the FE model coordinate system, which coincides with the cylindrical coordinate system based on the geometry of the test specimen. Displacements in the Cartesian coordinate system were estimated from these results. Section 3.2 explains the two coordinate systems. Positive displacements in the cylindrical coordinate system are up for the vertical direction, away from the center of curvature of the test specimen in the radial direction, and counterclockwise in the circumferential direction. Positive displacements in the Cartesian coordinate system are up for the vertical direction, towards the north in the "parallel plane," and towards the west in the "longitudinal plane."

FE displacement results were taken at nodes on the top of the tubes and the mid-height of the web for both G1 and G2. Figure 4.11 shows the node locations on a TFG. Displacements of the TFGs near the position of the loading fixtures were of interest. The

nodes on the north and south edges of a patch load are arranged in a radial plane, but were often treated as being in a parallel plane. The nodes on the east and west edges of a patch load are arranged in a circumferential plane, but were often treated as being in a longitudinal plane.

Displacements for the test specimen were obtained at the seven parallel cross sections where the loading fixtures are located. In theory, displacements from only four cross sections should have been needed because of the symmetry of the test setup. However, the displacements of the test specimen were not symmetric in the FE model because of the boundary conditions used in the FE model (Section 4.3.2). The loading fixture designs at Section B, at Section C, and at Section D used the largest displacements from the FE analysis for either the corresponding east section or the corresponding west section.

The loading fixtures were designed for displacements from a load step in the FE results after the maximum load capacity was reached. Even though the load was less than the maximum load, the displacements were larger due to yielding and failure of the TFGs. For example, Figure 4.12 and Figure 4.13 are force-vertical displacement plots for G1 and G2, respectively, under load Case 5 (Ma, 2012). Figure 4.14 and Figure 4.15 are corresponding force-radial displacement plots for G1 and G2, respectively (Ma, 2012). The displacements are given for the top, center node (node C in Figure 4.11 (b)) at Section A, at Section B_E, at Section C_E and at Section D_E. These plots show how the FE model continues to displace after the maximum load capacity is reached. The loading fixtures are designed so the movements of the loading fixtures do not limit the

displacement of the test specimen as it displaces beyond the displacements at the predicted maximum load.

4.3.2. Effect of Boundary Conditions on Kinematics

One parameter that affected the FE kinematic results was the boundary conditions, which are intended to simulate the test specimen support conditions for the tests. FE models were used to study how different combinations of pins and rollers changed the FE kinematic results (Ma, 2012). The results were then compared and a set of boundary conditions was chosen for the FE analysis used to provide the displacements needed to design the loading fixtures.

In the test setup, the test specimen bears on square, steel bars. The TFGs are not attached to the bars. The bars restrain vertical displacement in the downward direction at each bearing. The test specimen is free to rotate about a radial axis at the edges of the bars. The radial displacements and circumferential displacements are partially restrained by friction. The supports should not move radially or circumferentially as long as the radial and circumferential reactions are less than the maximum static frictional force that can be developed, which is equal to:

$$f_{s\,max} = \mu_s N \tag{4.11}$$

In this equation, μ_s is the static coefficient of friction for steel on steel, approximately 0.3 (AASHTO, 2005), and N is the force normal to the contact surface, which would be equal to the vertical reaction. The static friction developed is only as large as it needs to be to

prevent motion, but cannot be larger than $f_{s\ max}$. Slip should occur if the radial and circumferential reactions become larger than $f_{s\ max}$.

The FE models used to study the effects of the different boundary condition combinations used two types of supports. The first type of support was a roller support that allowed circumferential displacements and rotations about all axes, and prevented radial displacements and vertical displacements. The second type of support was a pin support that allowed rotations about all axes, and prevented circumferential displacements, radial displacements, and vertical displacements.

Figure 4.16 shows a schematic of the two boundary condition combinations studied. For both FE models, the west end of G1 and G2 was supported by a roller and the east end of G1 was supported by a pin. For the first FE model, with boundary condition combination bc1, a roller supported the east end of G2. For the second FE model, with boundary condition combination bc2, a pin supported the east end of G2.

To obtain a better comparison of displacements from the two FE models, the displacements were taken at a load step when the total load was equal to 325 kip in both FE models. For bc1, this load occurs at load step 33 in the FE results, and for bc2, this load occurs at load step 32 in the FE results. This load was near the maximum applied load on the FE model for both boundary conditions.

Table 4.3 and Table 4.4 present some of the displacements that were compared. These tables contain displacements for G1 and G2 at all seven parallel cross sections. Table 4.3 provides vertical, radial, and circumferential displacements obtained directly

from the center node of each patch load. Table 4.4 gives rotations about the radial axis (in the circumferential plane) obtained directly from the center node of each patch load. Table 4.4 also gives estimated rotations about the circumferential axis (in the radial plane) of the TFG at each patch load. The estimation of the rotations in the radial plane is explained in Section 4.3.3.

Most of the displacements were similar between the two FE models, but those for the FE model with the boundary condition combination bc2 were usually slightly smaller, because the additional pin support of G2 restrained the test specimen more. The main exception is the circumferential displacements of the east side of the test specimen, which are smaller for boundary condition combination bc1. The roller at the east end of G2 for bc1 can displace circumferentially away from the mid-span. Therefore, the circumferential displacements of the TFGs near this support were reduced.

It was decided to use the kinematic results from the FE model with boundary condition combination bc2 for the design of the loading fixtures. Boundary condition combination bc2 was chosen because the kinematic results are similar for bc1 and bc2, and bc2 better simulates the boundary conditions of the test specimen since G1 and G2 have similar bearings as described in Section 3.8.

4.3.3. Kinematics Used to Design Loading Fixtures

The displacements of the test specimen from the FE model were used to estimate the displacements of the loading fixtures during the tests. Estimated displacements from

the FE model with boundary condition combination bc2 under load Case 5 were used to design the loading fixtures.

Sketches and calculations were used to visualize and quantify the displacements of the test specimen and loading fixtures under loading. For example, Figure 4.17 is an AutoCAD drawing of a radial plane cross section view of the TFGs. The sketch was produced using vertical and radial displacements, and rotations in the radial plane, from the top center nodes of the TFGs, assuming the TFG cross sections displace as rigid bodies. This sketch can be used to visualize how the test specimen displaces under loading.

The displaced positions of the test specimen were used to estimate the displaced positions of the loading fixtures, which were also visualized with sketches. Figure 4.18 presents a parallel plane cross section view of a preliminary design of the loading fixture in its initial position and an estimated displaced position after the test specimen reaches the maximum load. The sketch shows that the loading fixture may collide with the north ground anchor rod, so the positions of the loading rod assemblies were changed. Figure 4.19 shows a parallel plane cross section view at Section A of the final design of the loading fixture in its initial position and an estimated displaced position after the test specimen reaches the maximum load. The sketch shows that the final loading fixture design should not collide with the north ground anchor rod. In this figure, the diaphragm in the displaced position is not shown for clarity.

The kinematics of the test specimen and loading fixtures were estimated from the displacements of the top of the TFG tubes from the FE analysis. The rotation of the top of each tube in the parallel plane, which is the rotation about the longitudinal axis, was approximated by the calculated rotation in the radial plane. The rotation in the radial plane was not taken directly from the rotation of the center node (C) because of the potential for local deformation of the top tube wall. Figure 4.20 (a) shows a radial plane cross section schematic view of a TFG in the initial position and a displaced position with the corresponding north and south nodes of the patch on the top of the tube (shown in Figure 4.11). Figure 4.20 (b) shows the nodes with the variables used to calculate the rotation in the radial plane of the tube, θ_{pp}. θ_{pp} is the angle from a horizontal line in the radial plane to a straight line drawn through the displaced north (N') and south (S') nodes. θ_{pp} was calculated as follows:

$$\theta_{pp} = tan^{-1}\left(\frac{\Delta_{\delta v}}{L_{hf}}\right) \quad \textbf{(4.12)}$$

Where:

$$\Delta_{\delta v} = \delta_{vN} - \delta_{vS} \quad \textbf{(4.13)}$$

$$L_{hf} = L_{hi} + \delta_{hN} - \delta_{hS} \quad \textbf{(4.14)}$$

δ_{vN} is the vertical displacement of the north node (positive downward)

δ_{vS} is the vertical displacement of the south node (positive downward)

δ_{hN} is the radial displacement of the north node (positive outward)

δ_{hS} is the radial displacement of the south node (positive outward)

L_{hi} is the initial radial distance between the north and south nodes

The rotation of the top of each tube in the longitudinal plane, which is the rotation about the parallel axis, was approximated by the calculated rotation in the circumferential plane. The vertical displacements and circumferential displacements of the east node and the west node of the patch of the top of the tube (shown in Figure 4.11) were used to calculate the rotation in the circumferential plane. The calculation was similar to the calculation of the rotation in the radial plane in Equation (4.12). The results are given in Table 4.5. The rotation in the longitudinal plane given in Table 4.5 is the calculated rotation of the top of the tubes in the circumferential plane. The values of the east sections are negative indicating the TFG cross sections are rotating counterclockwise towards mid-span.

The rotation of the loading beam of the loading fixture in the parallel plane was estimated using the displacements of the center node of the patch on top of G1 (C_{G1}) and the center node of the patch on top of G2 (C_{G2}). Figure 4.21 (a) shows a parallel plane cross section schematic of the two TFGs in the initial position and an estimated displaced position based on the center nodes. The rotation of the loading beam in the parallel plane, θ_{LB}, was calculated in a similar manner as θ_{pp}, but using the vertical displacements and the radial displacements of C_{G1} and C_{G2}, where the radial displacements were used to approximate the parallel displacements.

For each section (Section A, Section B_E, Section B_W, etc.), the plane of the predominant rotation was determined. The difference between the estimated rotation of the top of the tubes, θ_{pp}, and the loading beam, θ_{LB}, in the parallel plane was calculated, termed the relative rotation, θ_{rel}, and listed in Table 4.5 for load step 50 of the FE analysis. Table 4.5 compares θ_{rel} with the calculated rotation in the longitudinal plane. The loading fixture was designed to accommodate the larger rotation, at each section type, using half-rounds in the load bearing assemblies, which are discussed in Section 5.9. The half-rounds were aligned to minimize the restraint of the test specimen, and they were aligned with the axis of the larger rotation in Table 4.5. For section types with east and west sections, the larger values from these two sections were considered in the loading fixture design.

In Table 4.5, as noted above:

$$\theta_{rel} = \theta_{LB} - \theta_{pp} \qquad \textbf{(4.15)}$$

A negative value indicates that the rotation of the top of the tube is larger than the rotation of the loading beam. The relative rotation in the parallel plane for G2 of Section B_W is much larger than at the other locations. There is no diaphragm at Section B to restrain the rotation, and B_W is on the side closest to the two roller supports in the FE model.

The vertical displacements and lateral displacements in the parallel plane of the loading rod assemblies were estimated using the vertical displacements, δ_{vG1} and δ_{vG2},

and the lateral displacements in the parallel plane (approximated by the radial displacements), δ_{hG1} and δ_{hG2}, of the center nodes of the top of the TFG tubes, and calculated rotations of the loading beam in the parallel plane, θ_{LB}. Figure 4.21 (a) shows a schematic with the center nodes of the tops of the tubes and the locations of the loading rod assemblies (represented by the squares labeled J_S for the south loading rod assembly and J_N for the north loading rod assembly). The schematic shows the initial position and an estimated displaced position. Figure 4.21 (b) and (c) show schematics with the variables used to estimate the displacements of the loading rod assemblies. The location of J_S is shown in a longitudinal plane cross section view of the loading rod assembly, corresponding to section A-A in Figure 4.1, given in Figure 4.22. The location of J_N is similar. J_S in Figure 4.22 is the same location of J_S shown in the parallel plane cross section view of the TFGs shown in Figure 4.21 (a) and (b).

The vertical displacement of the south and north loading rod assemblies were estimated as follows:

$$\delta_{vJS} = \delta_{vG1} - L_S \sin\theta_{LB} \quad \textbf{(4.16)}$$

$$\delta_{vJN} = \delta_{vG2} + L_N \sin\theta_{LB} \quad \textbf{(4.17)}$$

L_S and L_N are the initial lateral distance in the parallel plane between the centerline of the given loading rod assembly and the center node of G1 or G2, respectively.

The lateral displacement in the parallel plane of the south and north loading rod assemblies were estimated as follows:

$$\delta_{hJS} = \delta_{hG1} + L_S(1 - cos\,\theta_{LB}) \quad \textbf{(4.18)}$$

$$\delta_{hJN} = \delta_{hG2} - L_N(1 - cos\,\theta_{LB}) \quad \textbf{(4.19)}$$

The vertical displacements and lateral displacements in the parallel plane of the loading rod assemblies at Section A, at Section B, at Section C, and at Section D are given in Table 4.6 for load step 50 of the FE model with boundary condition combination bc2 under load Case 5. Figure 4.23 is a force-vertical displacement plot for the estimated vertical displacements at the north loading rod assembly at Section A during loading. Figure 4.24 shows a plan view of the west half of the test setup that shows the lateral displacements in the parallel plane of the loading rod assemblies for load step 50. This view corresponds to section D-D of the loading fixture shown in Figure 4.1. The location of the loading rod assemblies is represented by Plate E (Figure 4.22), which would be the first part of the loading rod assembly to collide with the north ground anchor rod. Plate E is discussed in Section 5.8. Figure 4.24 shows that the north loading rod assemblies will not collide with the north ground anchor rods.

The estimated vertical displacements of the loading rod assemblies are the displacements of the top part of the loading rod assemblies (nodes J_S and J_N). The bottom of the loading rod assemblies should not displace vertically, so the vertical displacements of the loading rod assembly are the total required stroke of the jacks. The jacks have a stroke capacity of 6.13 in (ENERPAC, 2011). When the vertical displacements of the loading rod assemblies are larger than 6.13 in, the jacks will have to be reset. After resetting, the jacks can be re-stroked and the jacks can continue to be used to load the test

specimen. Loading the test specimen to the Constructability deck placement load of 181 kip should not require resetting the jacks. However, loading the test specimen beyond the maximum load capacity will require resetting the north jacks. A resetting plan was created using the estimated vertical displacements of the loading rod assemblies to determine when the jacks may need to be reset.

Table 4.7 presents the resetting plan for the north jacks at Section A, at Section B, at Section C, and at Section D for the test to load the test specimen beyond its maximum capacity. The load steps of the FE analysis that correspond to the resetting points of the jack during the test are shown graphically in Figure 4.23. This figure shows the estimated vertical displacement of the north loading rod assembly at Section A and the corresponding total load for each load step. For each resetting point, the plan in Table 4.7 lists the "Current Δ", which is the incremental vertical displacement since the previous load step, and "ΣΔ", which is the total estimated vertical displacement at that resetting point. ΣΔ is equal to δ_{vJ} for a given load step. To reduce the number of times the loading has to be paused to reset the jacks, multiple jacks will be reset at once. The north jacks at Section A, at Section B, and at Section C should be reset twice and the north jacks at Section D should be reset once before the expected maximum load is reached. The bolded values in the table indicate that the jack should be reset. An additional resetting of the jacks at Section A, at Section B, and at Section C may be necessary to reach displacements larger than the displacements from load step 50.

The vertical displacements and circumferential displacements for C_{G1} and C_{G2}, as shown in Figure 4.25, were used to estimate the lateral displacement in the longitudinal

plane and the rotation in the longitudinal plane that may develop in the loading rod assemblies. Figure 4.25 is a longitudinal plane cross section view of the load bearing assembly on G2 corresponding to section C-C in Figure 4.1 (Figure 4.25 is discussed in more detail later).

The displacements of the loading rod assemblies were estimated, not precisely calculated, because of uncertainties in the kinematics of the test specimen and the loading fixtures in the circumferential plane, as explained next. Table 4.8 gives a summary of the estimated displacements for load step 50 of the FE analysis. It was assumed that the centerline of the loading rod assembly remains half way between the two load transfer channels (the centerline of the loading rod assembly is aligned with the centerline of the loading beam shown in Figure 4.25 (a)). Table 4.8 includes the following variables:

δ_c is the circumferential displacement of the center node of the TFG (see Figure 4.25 (d))

δ_{vJ} is the estimated vertical displacement of the loading rod assembly (see Equations (4.16) and (4.17), and Figure 4.21)

h_i is the initial height equal to the vertical distance from the bottom of the load transfer channels to the mid-thickness of the top wall of the tubes of the TFGs (see Figure 4.22 and Figure 4.25)

h_f is the estimated final height

α_l is the estimated rotation of the loading rod assembly in the longitudinal plane

δ_l is the estimated longitudinal displacement of the loading rod assembly at the top of the load transfer channels

The final height, the rotation in the longitudinal plane, and the longitudinal displacement were estimated as follows:

$$h_f = h_i + \delta_{vJ} \tag{4.20}$$

$$\alpha_l = -arctan\left(\frac{\delta_c}{h_f}\right) \tag{4.21}$$

$$\delta_l = d * tan(\alpha_l) \tag{4.22}$$

Here, d is the depth of the load transfer channels. Values are provided for all seven sections where the loading fixtures are located.

The estimated longitudinal displacements and rotations in the longitudinal plane of the loading rod assembly are not as reliable as the other displacements. There is uncertainty in the vertical displacements and circumferential displacements from the FE analysis that could significantly change the estimated longitudinal displacements and rotations in the longitudinal plane. For example, small changes in the vertical displacements and circumferential displacements could cause large changes in the estimated rotations of the loading rod assembly in the longitudinal plane.

There is also uncertainty in the kinematics of the loading fixtures. Teflon will be placed between the bottom of the load transfer channels and Plate F of the loading rod assembly (see Figure 4.22; this is explained further in Section 5.8). The Teflon should enable the loading rod assemblies to slip and displace laterally in the parallel plane. However, the Teflon may also allow the loading rod assemblies to displace laterally in the longitudinal plane.

Figure 4.25 is a longitudinal plane cross section view of the load bearing assembly on G2 at Section D_W. This location has the largest longitudinal displacement and rotation in the longitudinal plane. The sketch shows the initial position and an estimated displaced position of the load bearing assembly and loading beam for load step 12 (approximately the Constructability limit state load), load step 35 (the maximum load), and load step 50 (beyond the maximum load). The loading beam and the top plates of the load bearing assembly would ideally remain vertical and are therefore, shown without a rotation in the longitudinal plane. The loading rod assembly would ideally remain vertical (Figure 4.22). The vertical centerline of the loading beam indicates that for this to be true, the loading beam and everything attached to it would have to displace laterally in the longitudinal plane. This displacement may be larger than the available distance between the edge of the main rod of the loading rod assembly and the load transfer channels. Therefore, the loading beam, the load bearing assembly plates attached to the loading beam, and the loading rod assembly may rotate in the longitudinal plane at Section D_W.

In the tests, the lateral displacements in the longitudinal plane and the rotations in the longitudinal plane will probably be smaller than estimated for Section D_W because this section is closest to the rollers used in the FE model (Section 4.3.2). The friction between the test specimen and the bearings of the test specimen should prevent some of the lateral displacements that the rollers in the FE model allow. In addition, the main rod of the loading rod assembly will bend as it bears against the load transfer channels, and the loading rod assembly may not remain vertical. Based on the estimated displacements in Table 4.8 for load step 50 of the FE analysis, the main rod of the north loading rod assembly at D_W may bear against the top of the load transfer channel. The calculated longitudinal displacement is 0.51 in, but there is only 0.50 in clearance between the main rod and the load transfer channels (Figure 4.22).

Table 4.1: Load combinations for Constructability limit states

Limit State	SW	D_C	LL_C
Constructability (girder erection)	1.25	-	-
Constructability (deck placement)	-	1.25	1.75

Table 4.2: Load combinations for Service II and Strength I limit states

Limit State	D_C	D_W	LL
Service II	1.00	1.00	1.30
Strength I	1.25	1.50	1.75

Table 4.3: Displacements of top center nodes of TFGs for bc1 (for load step 33) and bc2 (for load step 32)

Section	Vertical Displacement (in)				Radial Displacement (in)				Circumferential Displacement (in)			
	G1		G2		G1		G2		G1		G2	
	bc1	bc2	bc1	bc2	bc1	bc2	bc1	bc2	bc1	bc2	bc1	bc2
A	-4.347	-4.297	-11.3	-11.15	4.742	4.443	4.898	4.601	-0.181	-0.138	-0.145	-0.05
B_E	-4.031	-3.984	-10.52	-10.38	4.198	3.904	5.092	4.793	0.149	0.174	0.468	0.543
B_W	-4.034	-3.99	-10.58	-10.43	4.312	4.058	5.297	5.013	-0.514	-0.454	-0.774	-0.656
C_E	-3.035	-2.999	-8.095	-7.996	2.967	2.737	3.323	3.086	0.421	0.430	0.948	1.003
C_W	-3.035	-3.003	-8.137	-8.03	3.148	2.968	3.516	3.324	-0.794	-0.721	-1.27	-1.135
D_E	-1.553	-1.534	-4.452	-4.402	1.422	1.309	1.685	1.539	0.610	0.607	1.302	1.343
D_W	-1.548	-1.532	-4.474	-4.418	1.563	1.477	1.795	1.699	-0.994	-0.911	-1.635	-1.486

Table 4.4: Rotations of top of TFGs for bc1 (for load step 33) and bc2 (for load step 32)

Section	Estimated Rotation in Radial Plane (radians)				Rotation in Circumferential Plane of Top Center Node (radians)			
	G1		G2		G1		G2	
	bc1	bc2	bc1	bc2	bc1	bc2	bc1	bc2
A	0.0702	0.0691	0.0702	0.0694	0.0000	0.0000	-0.0002	-0.0003
B_E	0.0632	0.0624	0.1006	0.0989	-0.0073	-0.0073	-0.0207	-0.0204
B_W	0.0636	0.0627	0.103	0.1009	0.0074	0.0074	0.0208	0.0205
C_E	0.0463	0.0456	0.0526	0.052	-0.0134	-0.0133	-0.0329	-0.0324
C_W	0.0465	0.0458	0.0528	0.0522	0.0134	0.0133	0.0330	0.0326
D_E	0.0282	0.0272	0.0331	0.034	-0.0177	-0.0175	-0.0419	-0.0414
D_W	0.0257	0.0252	0.0331	0.0327	0.0177	0.0175	0.0422	0.0416

Table 4.5: Rotations at load fixture sections for load step 50

Section	Relative Rotation in Parallel Plane (θ_{rel})		Rotation in Longitudinal Plane		Plane with Largest Rotation	
	G1	G2	G1	G2	G1	G2
A	0.0036	0.0073	-0.0006	-0.0024	P	P
B_E	0.0047	-0.0232	-0.0106	-0.0324	P	P
B_W	0.0149	-0.0617	0.0097	0.0470		
C_E	0.0073	0.0015	-0.0176	-0.0441	L	L
C_W	0.0098	0.0048	0.0178	0.0505		
D_E	0.0026	-0.0042	-0.0222	-0.0532	L	L
D_W	0.0054	0.0044	0.0232	0.0592		

Table 4.6: Estimated displacements in parallel plane of loading rod assemblies for load step 50

Section	Vertical Displacement, δ_{vJ} (in)		Lateral Displacement in Parallel Plane, δ_{hJ} (in)	
	South	North	South	North
A	-3.606	-17.348	6.88	6.61
B	-3.365	-17.481	6.51	8.86
C	-2.470	-12.945	4.88	5.21
D	-1.176	-6.977	2.45	2.42

Table 4.7: Jack resetting plan

Section	Reset 1 Load Step 14		Reset 2 Load Step 29		Maximum Load Load Step 35		Reset 3 Load Step 48		Limit	
	Current Δ	ΣΔ	Current Δ	ΣΔ	Current Δ	ΣΔ	Current Δ	ΣΔ	Current Δ	ΣΔ
A	**-5.67**	-5.67	**-5.78**	-11.45	-1.78	-13.23	**-5.13**	-16.58	-6.13	-22.71
B	**-5.50**	-5.50	**-5.22**	-10.72	-1.73	-12.45	**-5.81**	-16.54	-6.13	-22.67
C	**-4.38**	-4.38	**-3.93**	-8.31	-1.27	-9.57	**-4.00**	-12.31	-6.13	-18.44
D	-2.39	-2.39	**-4.61**	-4.61	-0.67	-5.28	-2.04	-6.65	-6.13	-12.78

Table 4.8: Estimated longitudinal displacements and rotations in longitudinal plane of loading rod assemblies for load step 50

Section	δ_c (in)		δ_{vJ} (in)		h_i (in)		h_f (in)		α_l (rad)		δ_l (in)	
	G1	G2	South	North	South	North	South	North	South	North	South	North
A	-0.28	-0.02	-3.61	-17.35	69.9	69.9	66.3	52.6	0.0043	0.0004	0.051	0.004
B_E	0.16	0.71	-3.36	-15.33	69.9	69.9	66.5	54.6	-0.0024	-0.013	-0.029	-0.156
B_W	-0.75	-1.42	-3.19	-17.48	69.9	69.9	66.7	52.4	0.0112	0.0271	0.135	0.326
C_E	0.51	1.24	-2.47	-11.51	69.9	69.9	67.4	58.4	-0.0075	-0.0213	-0.09	-0.255
C_W	-1.15	-2.16	-2.41	-12.95	69.9	69.9	67.5	57.0	0.0171	0.0378	0.205	0.454
D_E	0.74	1.66	-1.18	-6.26	69.9	69.9	68.7	63.6	-0.0107	-0.0260	-0.129	-0.312
D_W	-1.46	-2.69	-1.15	-6.98	69.9	69.9	68.7	62.9	0.0212	0.0427	0.254	0.513

δ_c = Circumferential displacement of center node of TFG (Figure 4.25 (d))

δ_{vJ} = Estimated vertical displacement of loading rod assembly (see Equations (4.16) and (4.17), and Figure 4.21)

h_i = Initial height equal to vertical distance from bottom of load transfer channels to mid-thickness of top wall of tubes of TFGs (see Figure 4.22 and Figure 4.25)

h_f = Estimated final height

α_l = Estimated rotation of loading rod assembly in longitudinal plane

δ_l = Estimated longitudinal displacement of loading rod assembly at top of load transfer channels

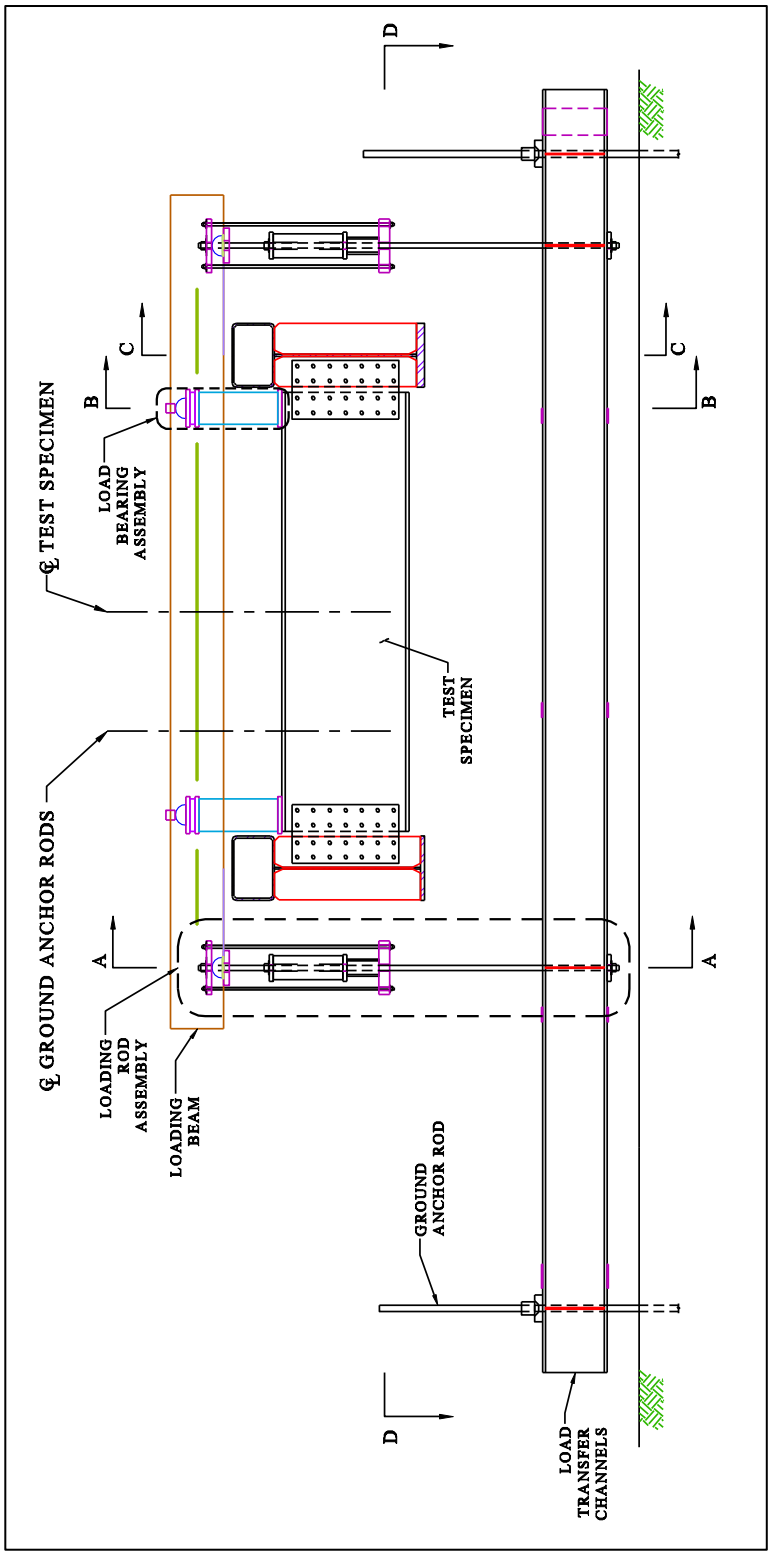

Figure 4.1: Parallel plane cross section view of test specimen and loading fixture at Section A

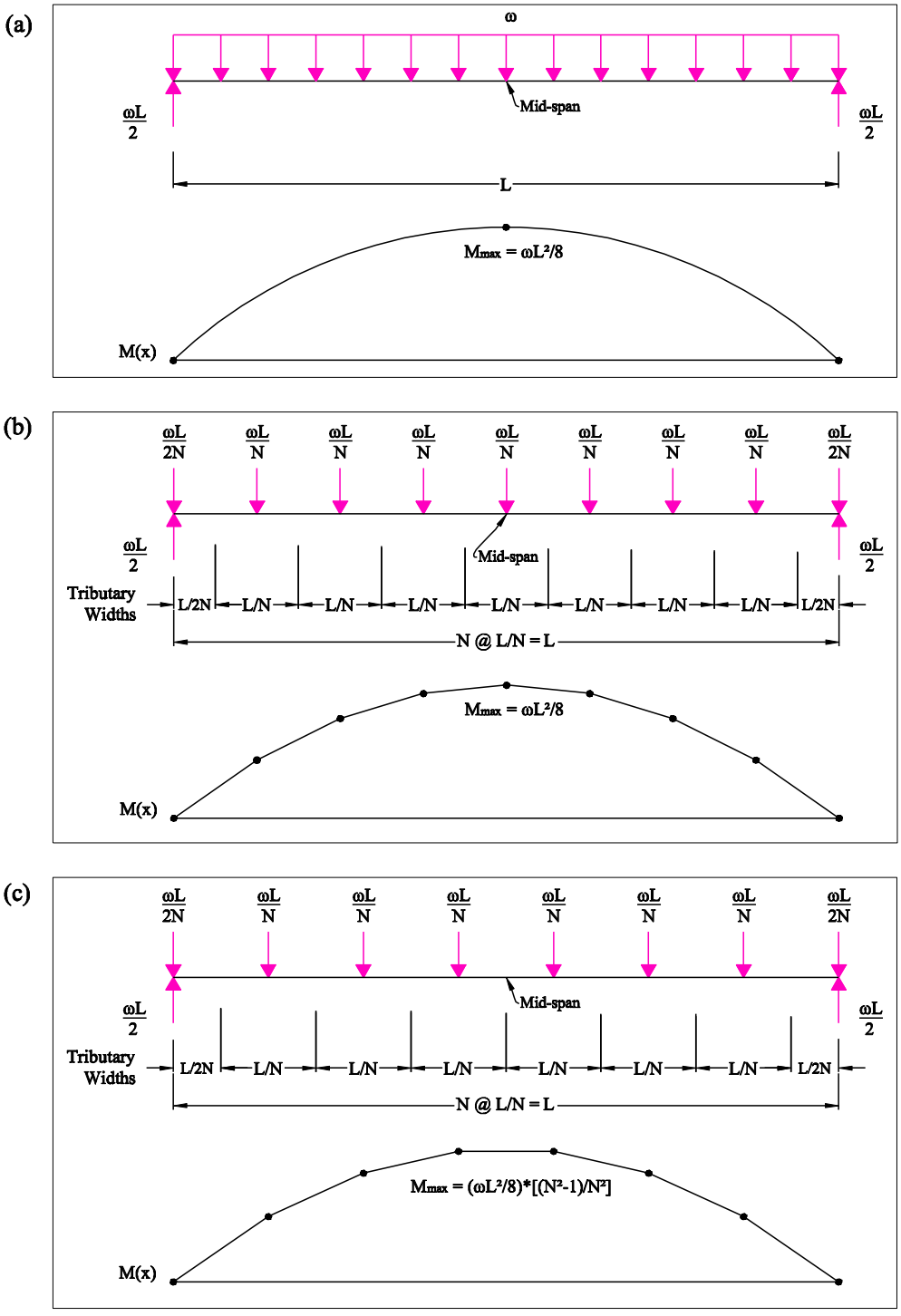

Figure 4.2: Free body diagram and corresponding moment diagram for (a) idealized uniformly distributed load, (b) concentrated load simulation with even number of segments, and (c) concentrated load simulation with odd number of segments

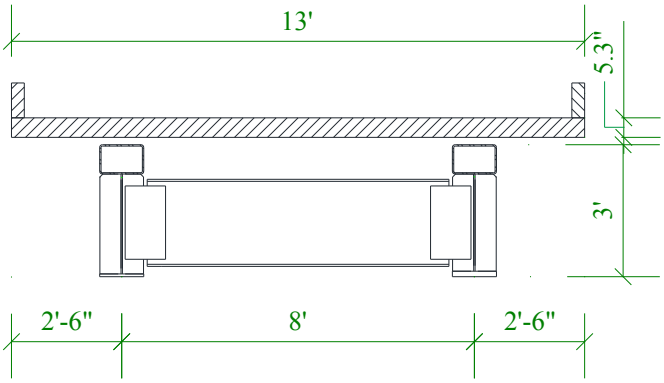

(a) Ideal 2/3-scale TFG test specimen

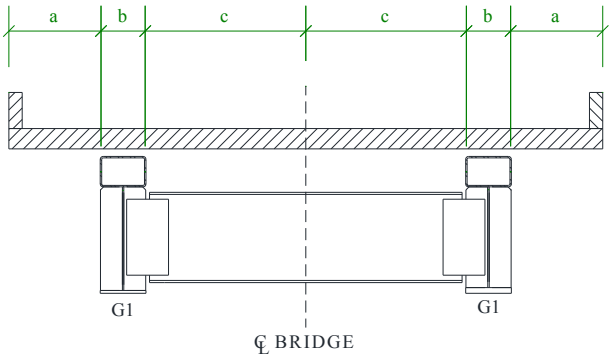

(b) Bridge deck cross section segments

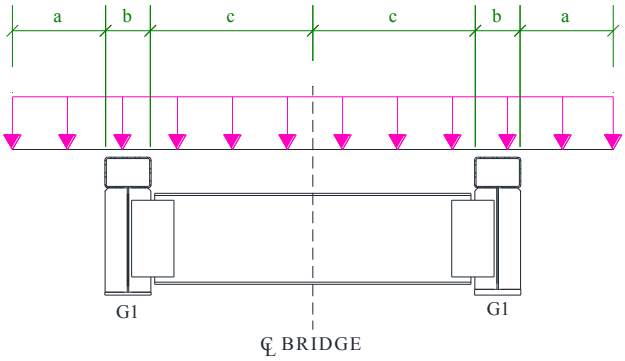

(c) Idealized load (assumed constant over the span)

Figure 4.3: Radial plane cross section view of TFG bridge

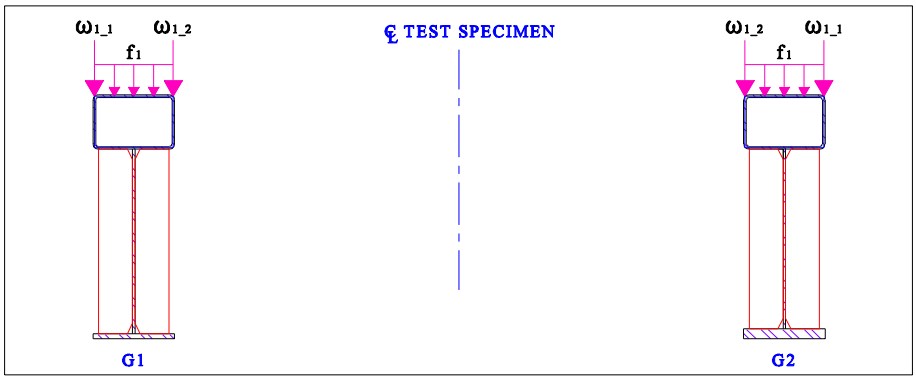

(a) Case 1

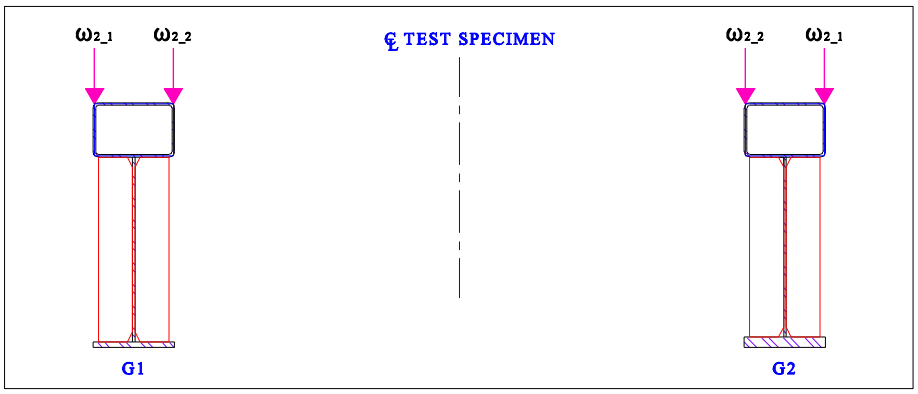

(b) Case 2

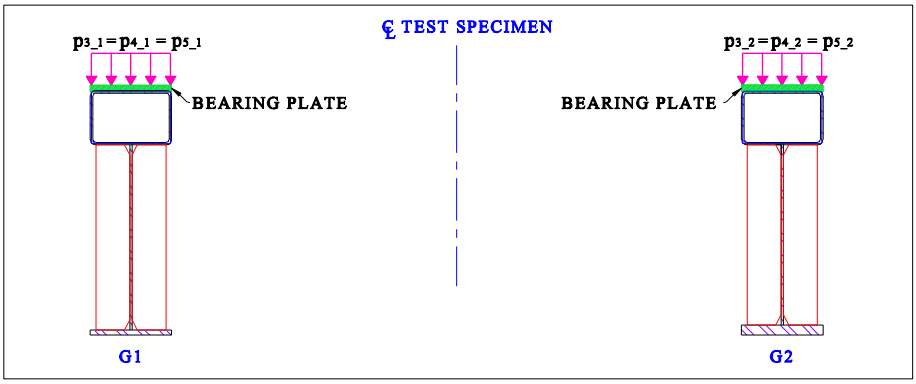

(c) Case 3 and Case 4

Figure 4.4: Radial plane cross section views of load cases

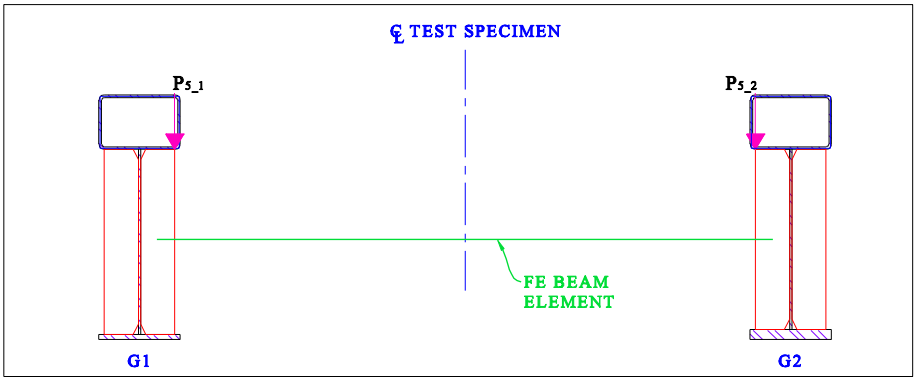

(d) Case 5

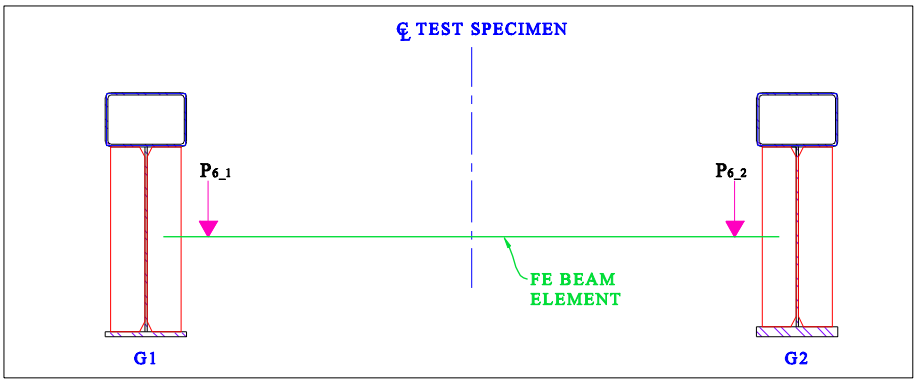

(e) Case 6

Figure 4.4 (cont'd): Radial plane cross section views of load cases

Figure 4.5: Elevation views of load cases

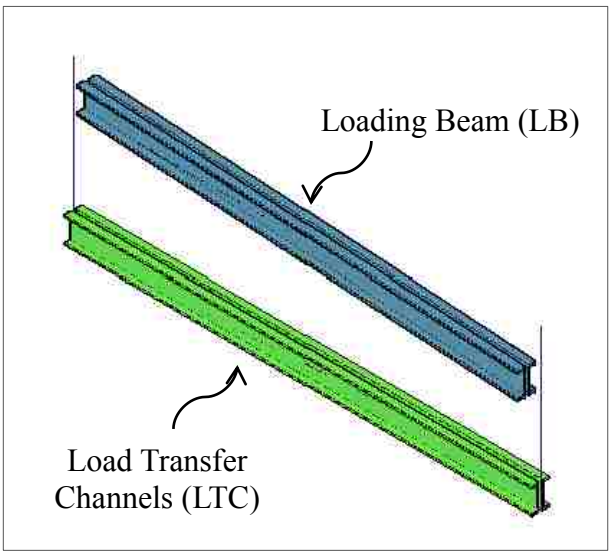

(a) 3-D perspective view

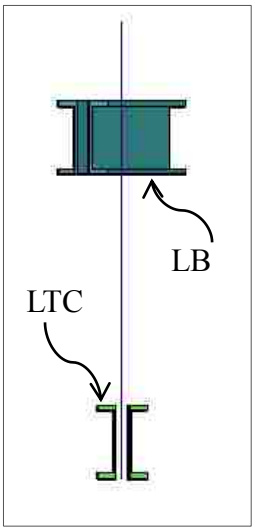

(b) Cross section view

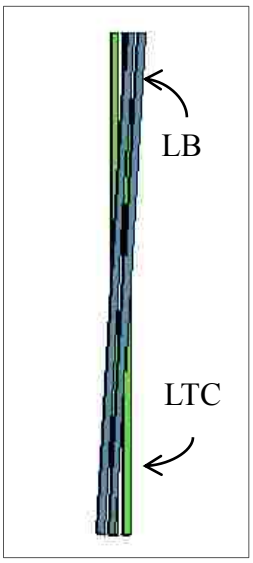

(c) Plan view

Figure 4.6: Preliminary sketches of loading beam and load transfer channels of loading fixture - radial loading

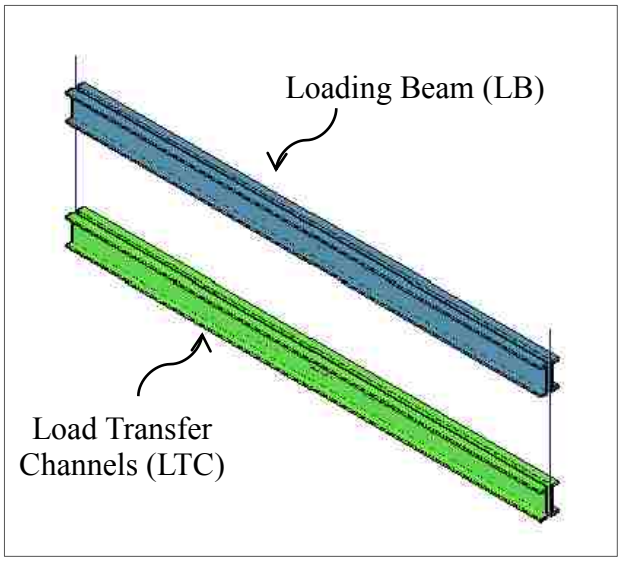

(a) 3-D perspective view

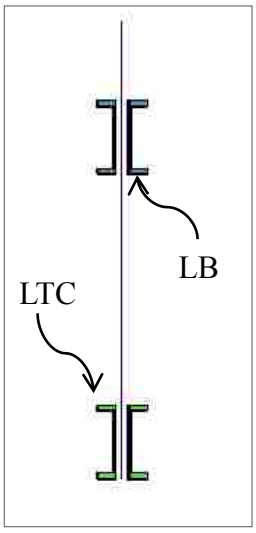

(b) Cross section view

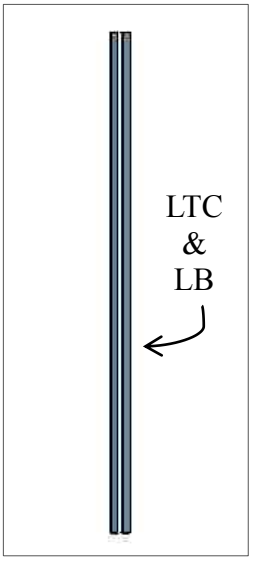

(c) Plan view

Figure 4.7: Preliminary sketches of loading beam and load transfer channels of loading fixture - parallel loading

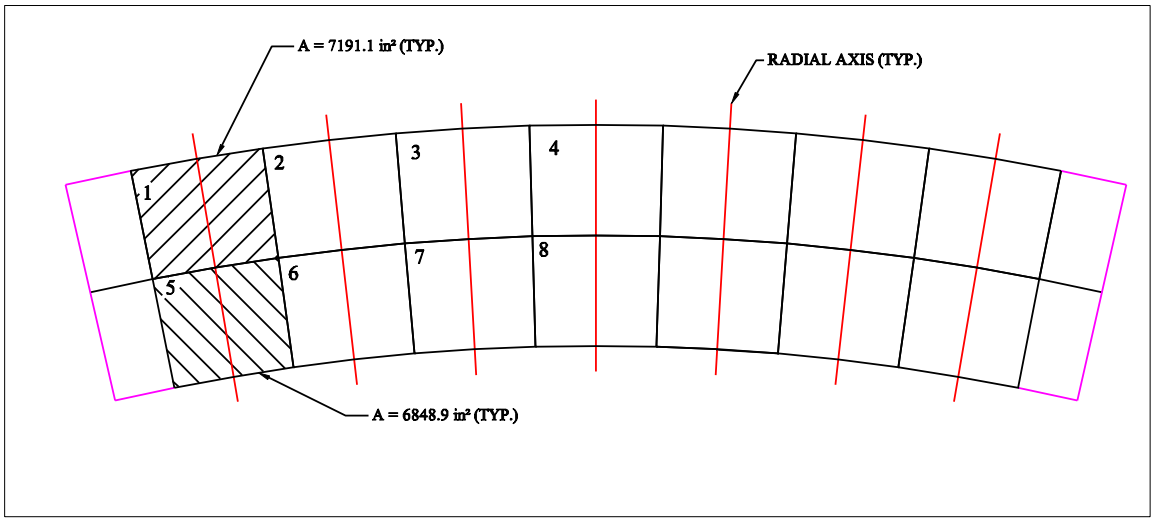

(a) Areas divided by radial planes

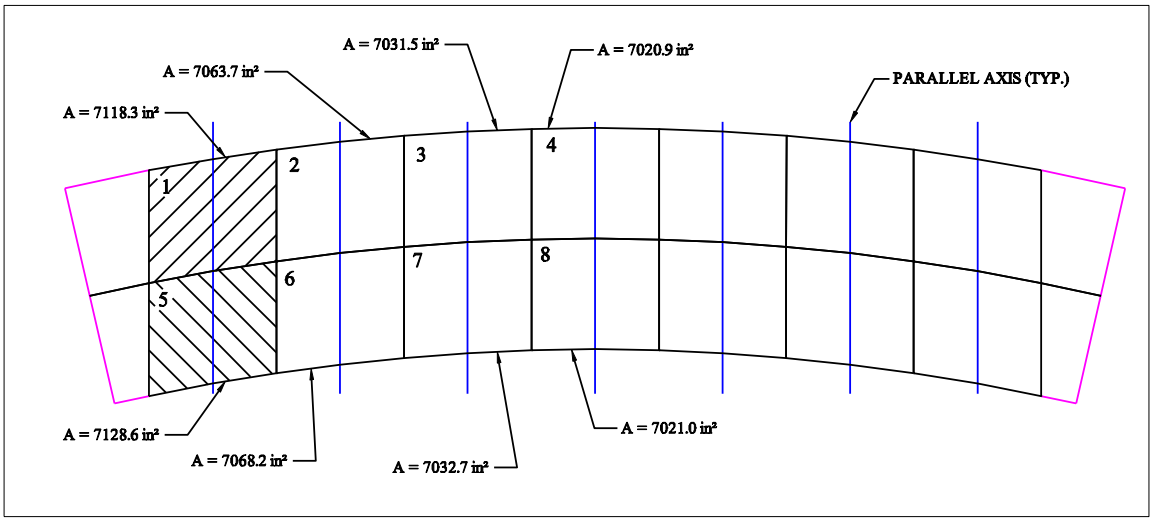

(b) Areas divided by parallel planes

Figure 4.8: Areas for patch loads

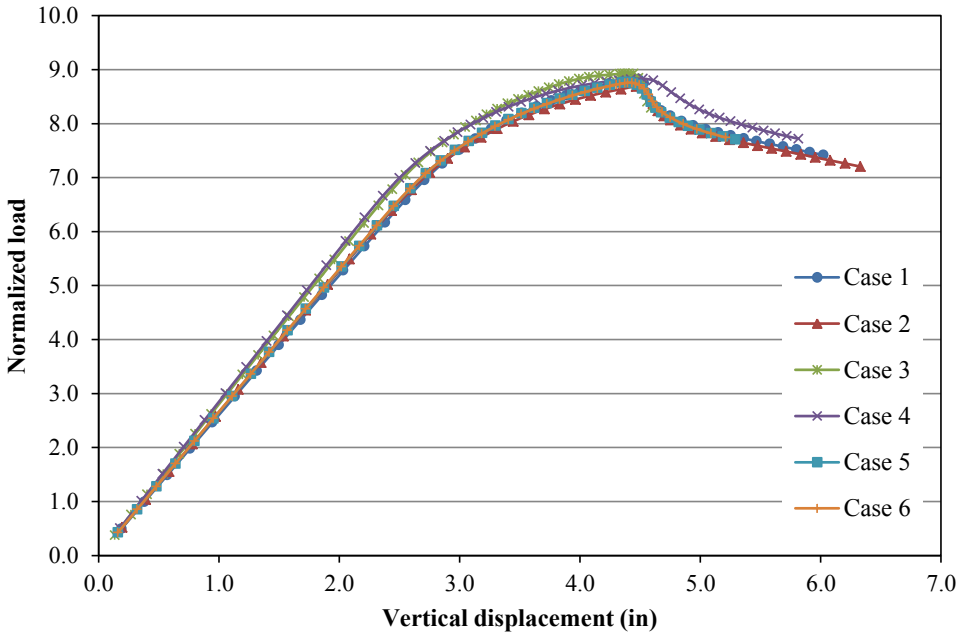

Figure 4.9: Force-vertical displacement response from web node of G1 for load cases (Ma, 2012)

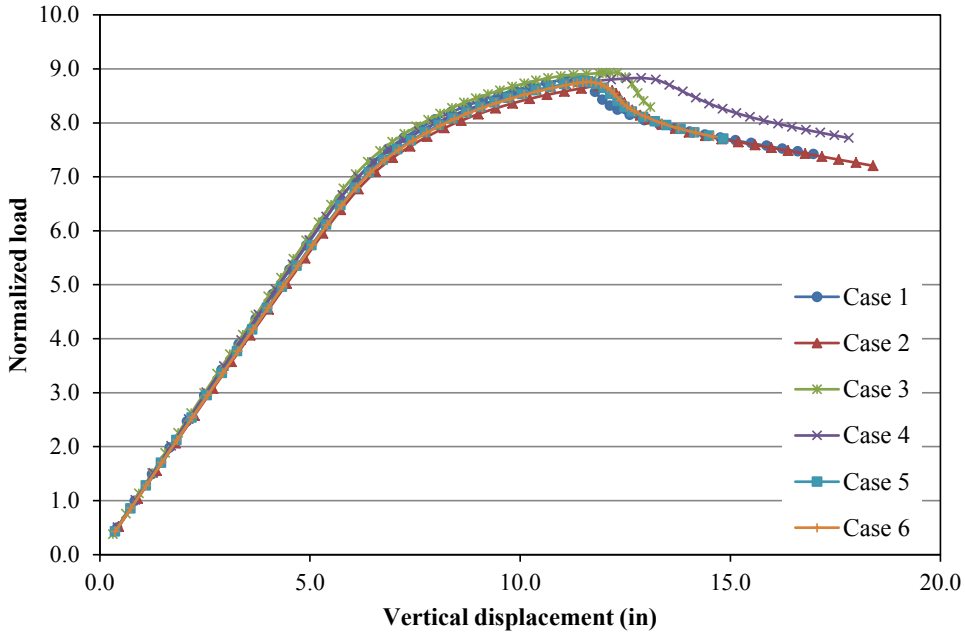

Figure 4.10: Force-vertical displacement response from web node of G2 for load cases (Ma, 2012)

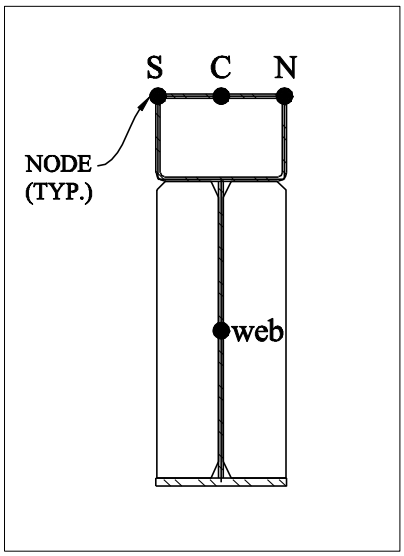

(a) Radial plane cross section view

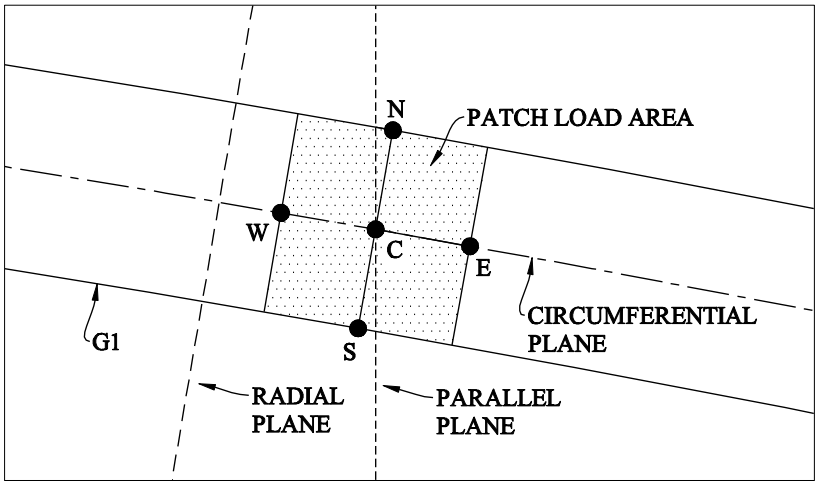

(b) Plan view of G1 at Section D_E

Figure 4.11: Node locations on TFGs

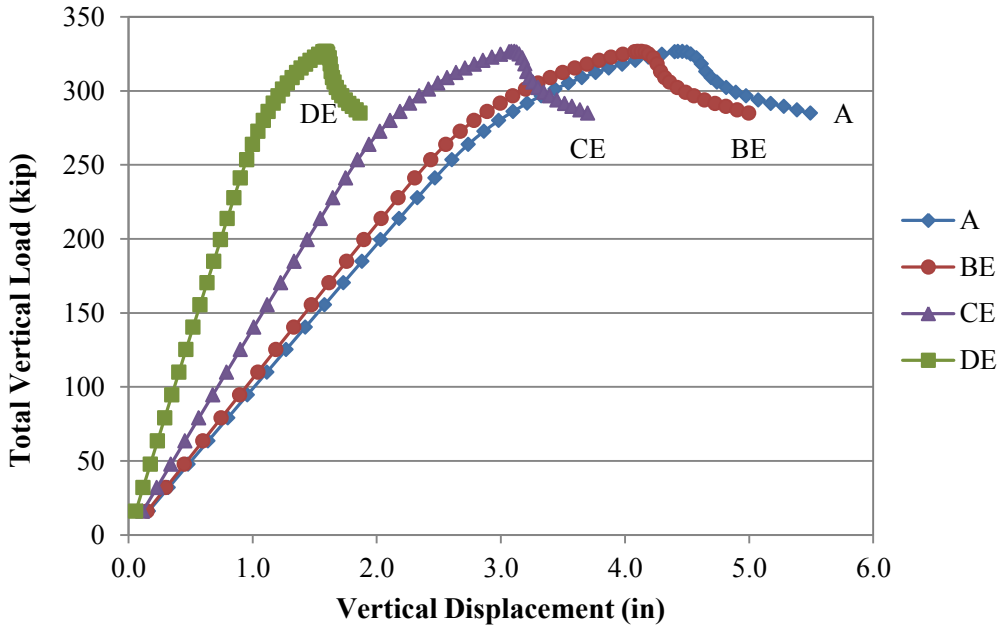

Figure 4.12: Force-vertical displacement response of top center node of G1 (Ma, 2012)

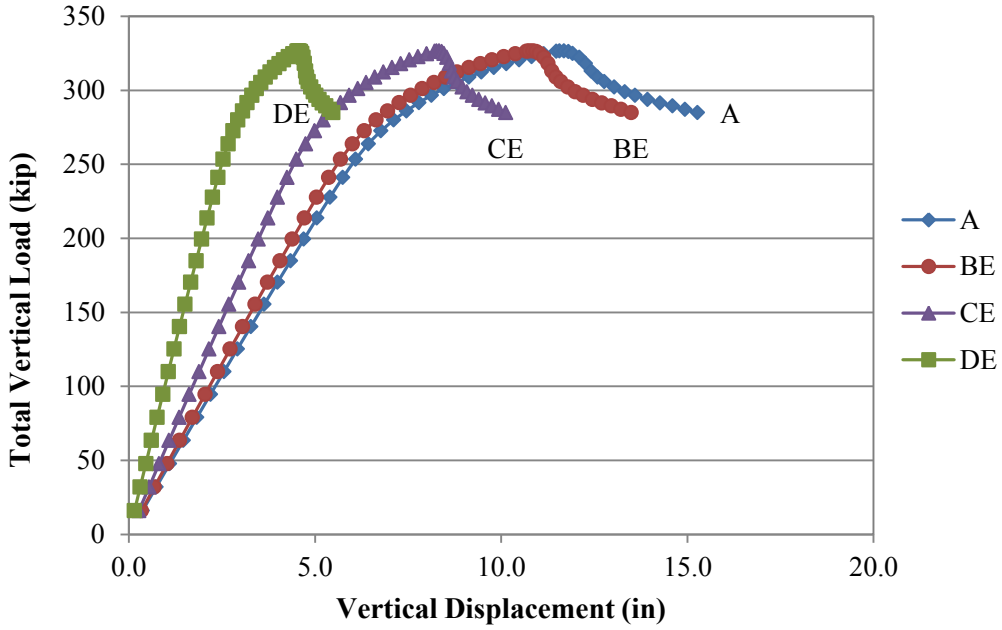

Figure 4.13: Force-vertical displacement response of top center node of G2 (Ma, 2012)

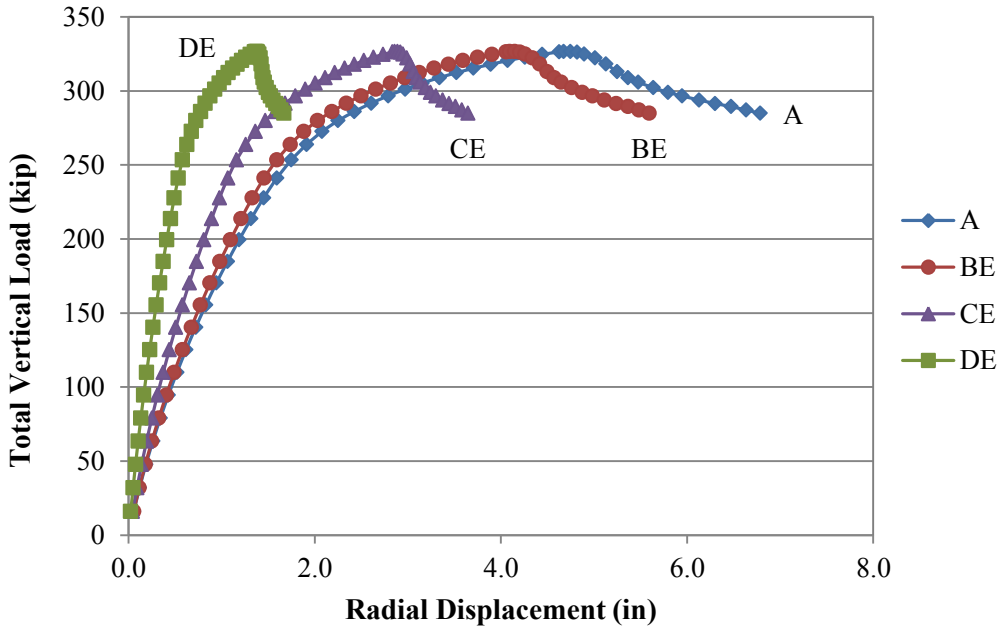

Figure 4.14: Force-radial displacement response of top center node of G1 (Ma, 2012)

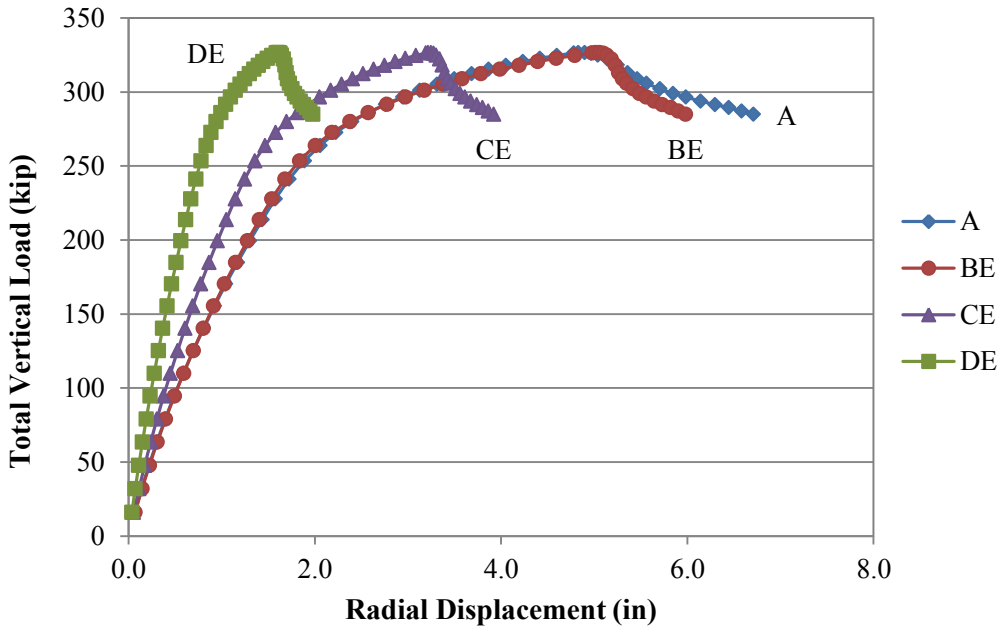

Figure 4.15: Force-radial displacement response of top center node of G2 (Ma, 2012)

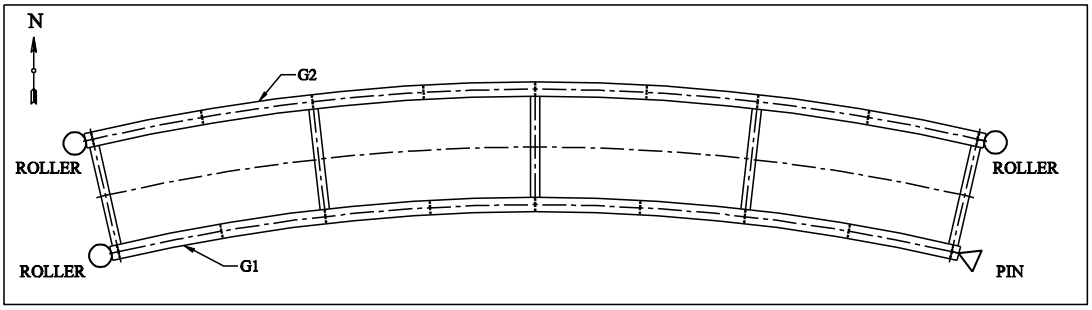

(a) bc1

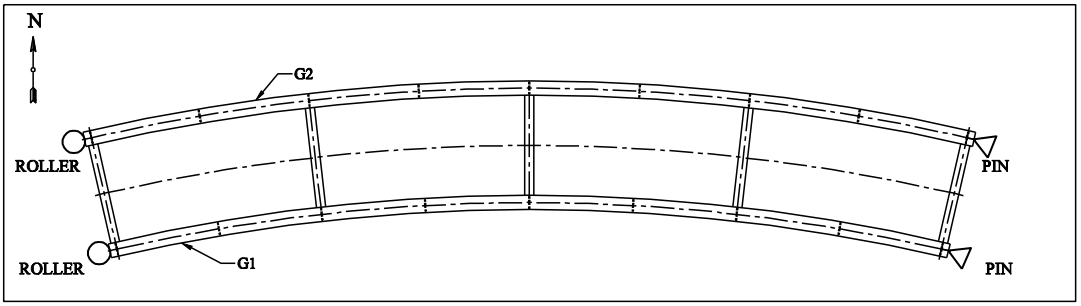

(b) bc2

Figure 4.16: Boundary condition combinations studied with FE models

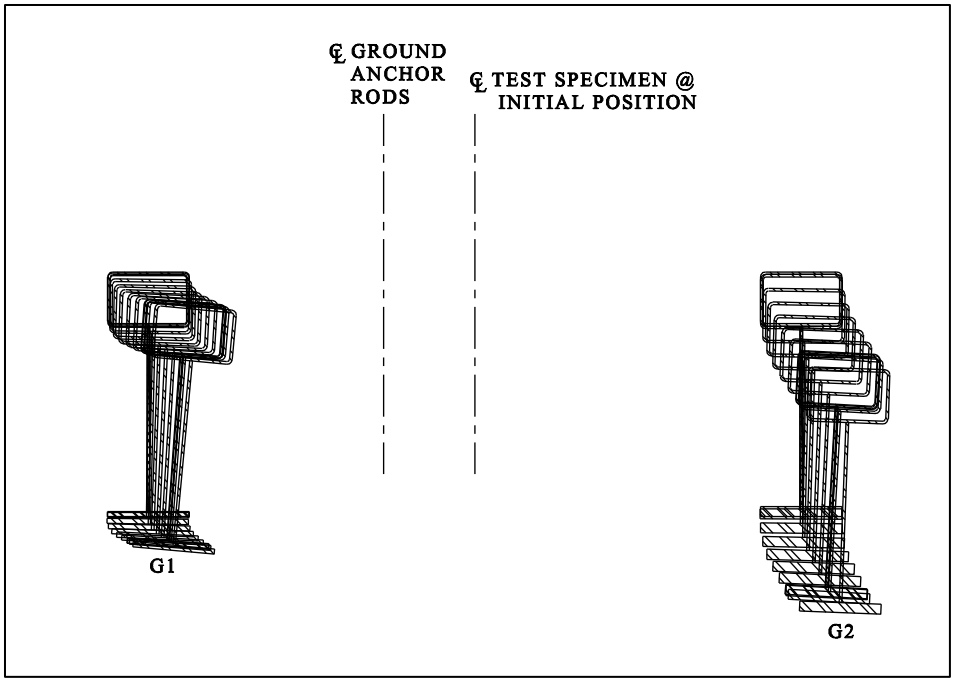

Figure 4.17: Radial plane cross section view of TFG displacements

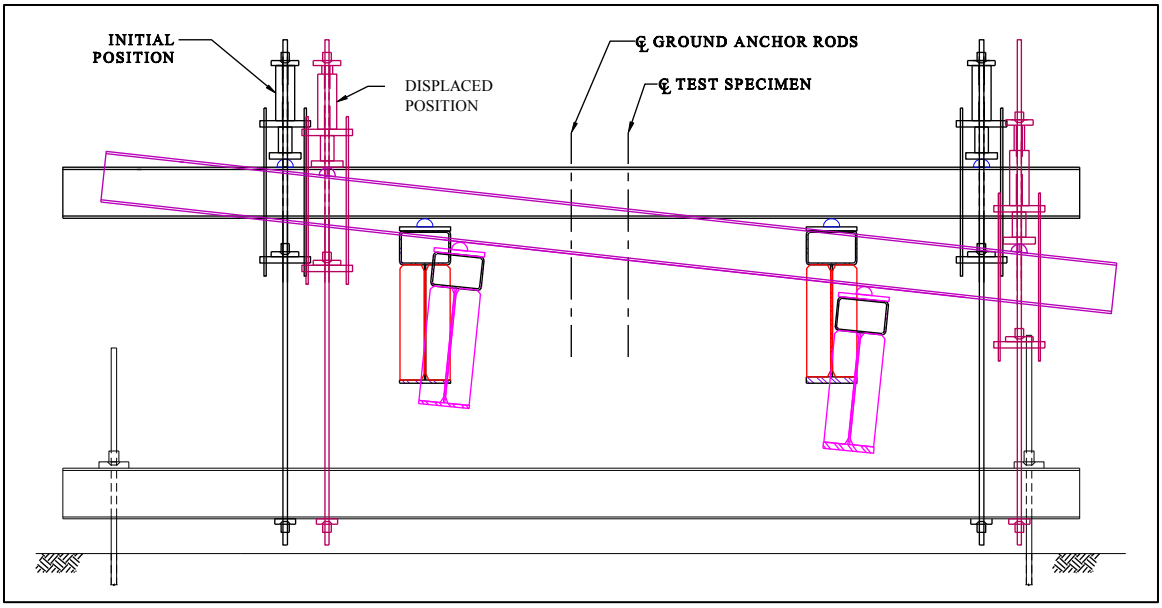

Figure 4.18: Parallel plane cross section view of initial and estimated displaced position of preliminary loading fixture design

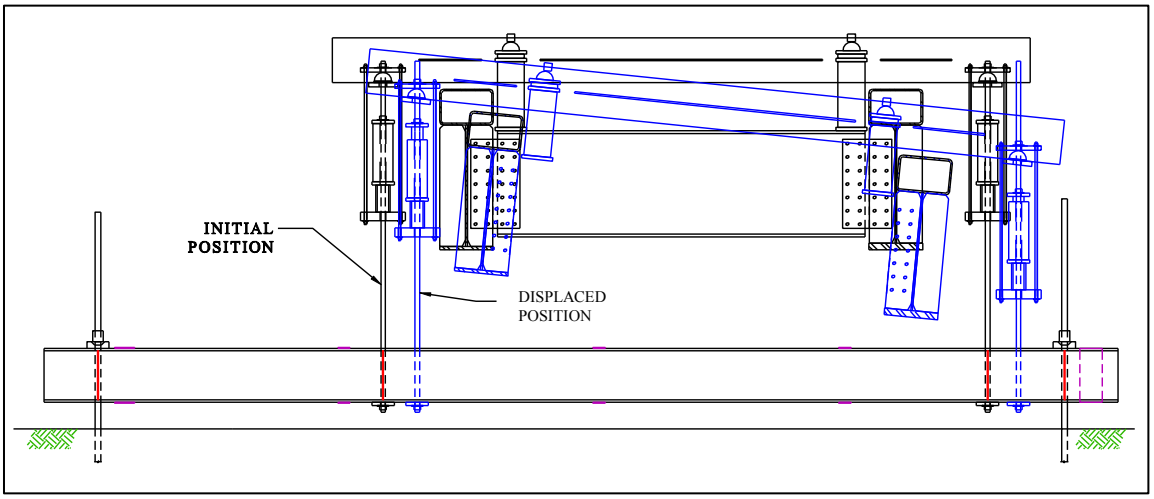

Figure 4.19: Parallel plane cross section view at Section A of initial and estimated displaced position of final loading fixture design

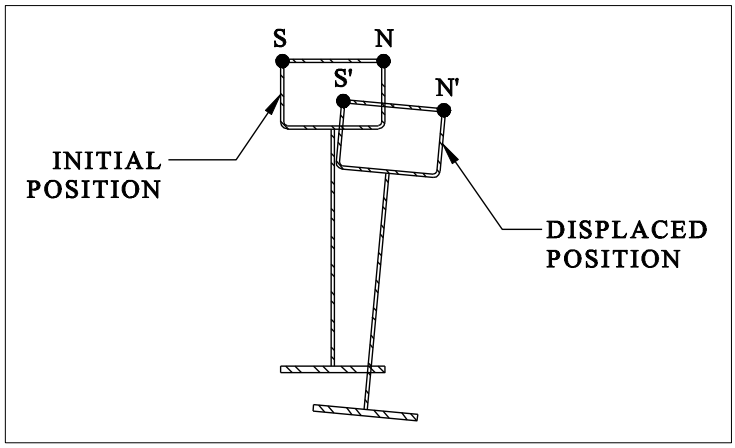

(a) Nodes on TFG

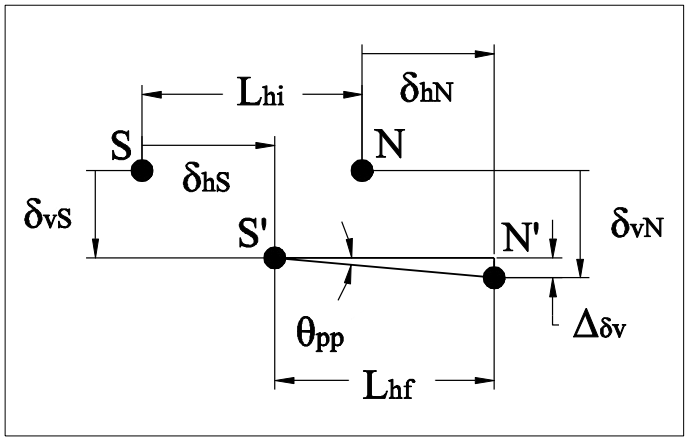

(b) Variables used for calculations

Figure 4.20: Schematics used to calculate rotations of top of tubes in radial plane

(a) Initial and estimated displaced TFGs used to calculate rotation of loading beam in parallel plane

Figure 4.21: Schematics used to calculate displacements of loading fixtures

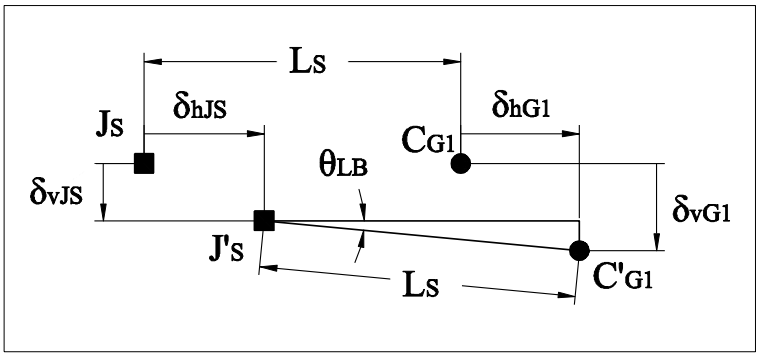

(b) Variables used for south loading rod assembly

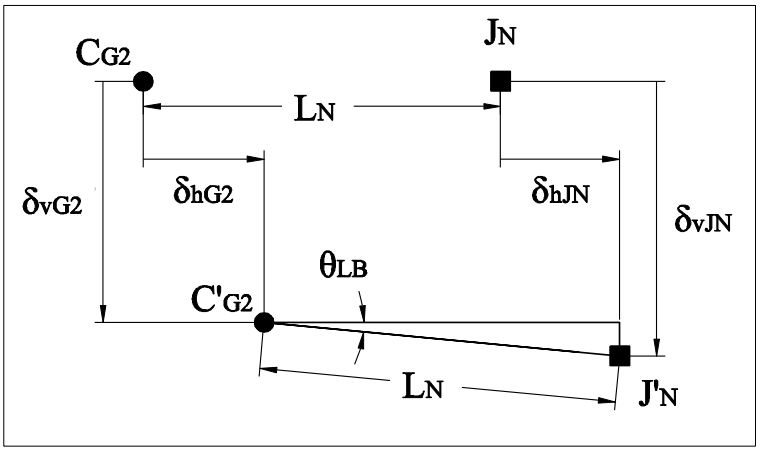

(c) Variables used for north loading rod assembly

Figure 4.21 (cont'd): Schematics used to calculate displacements of loading fixtures

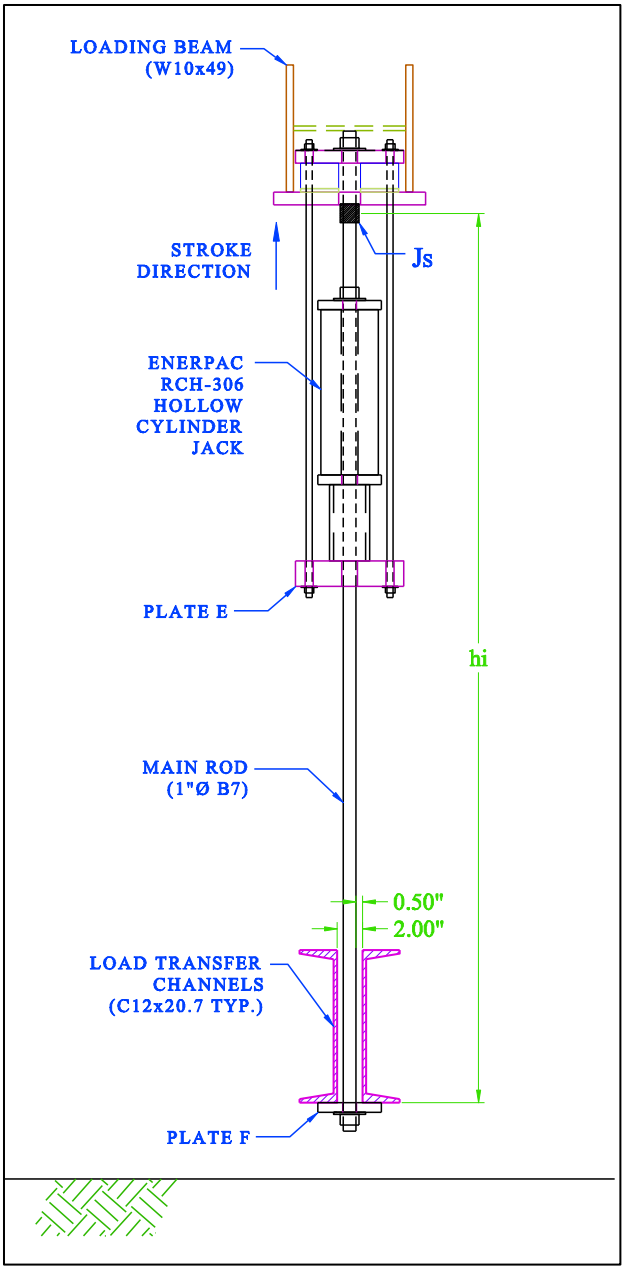

Figure 4.22: Longitudinal plane cross section view of loading rod assembly

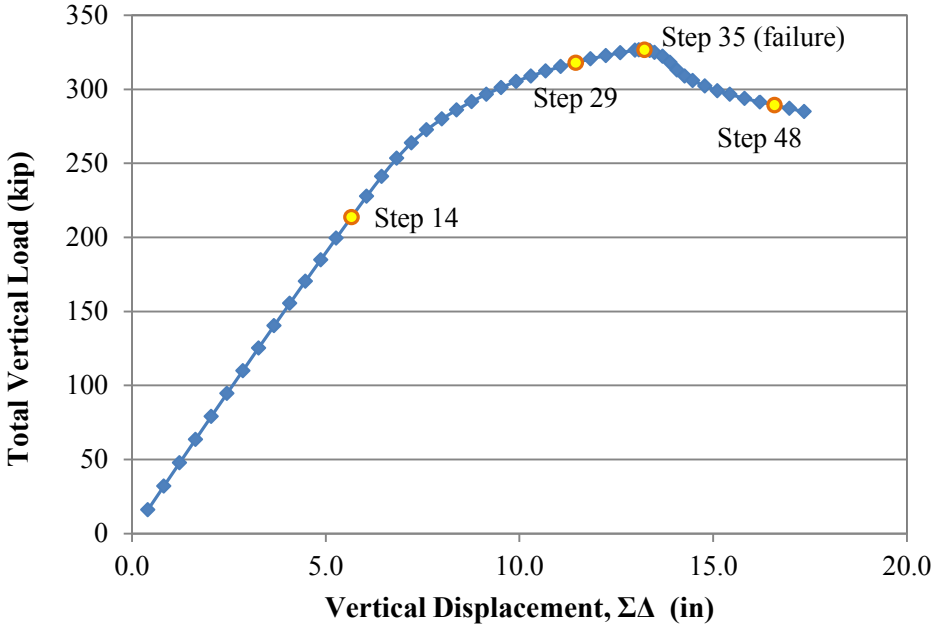

Figure 4.23: Force-displacement plot for north loading rod assembly at Section A

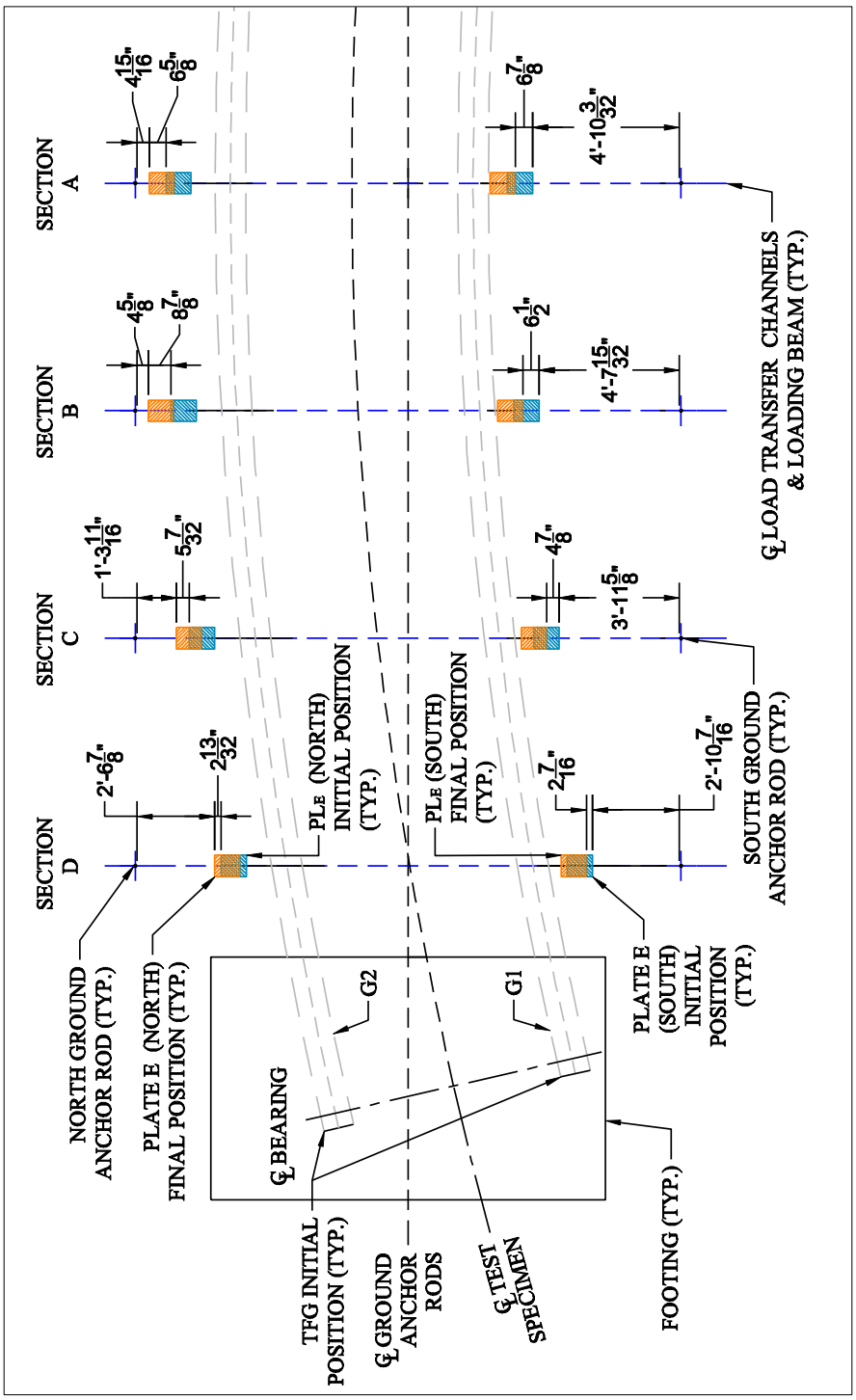

Figure 4.24: Lateral displacement in parallel plane of loading rod assemblies for load step 50

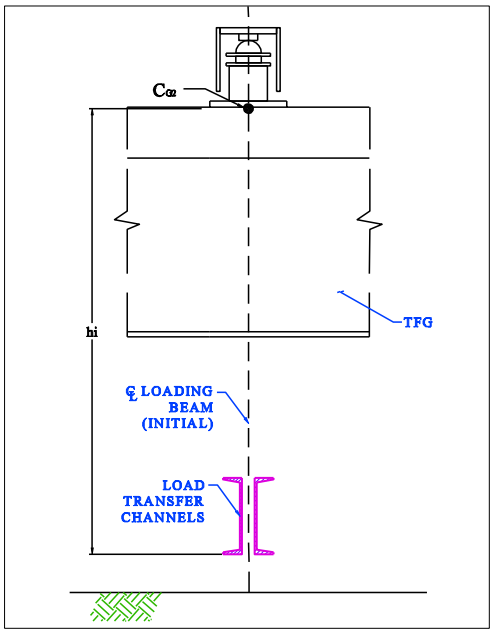

(a) Initial position

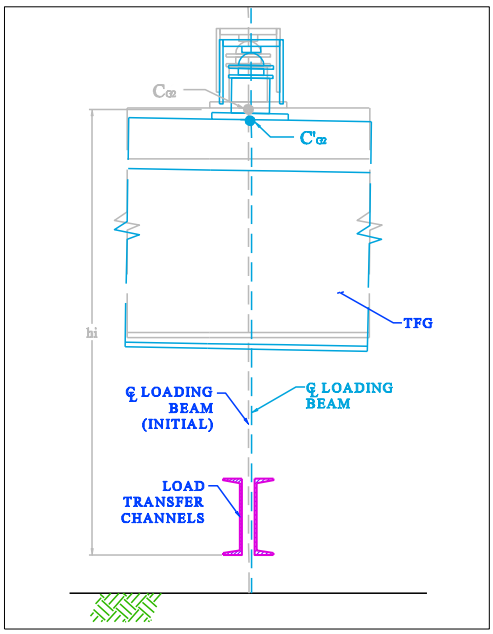

(b) Load step 12 (Constructability)

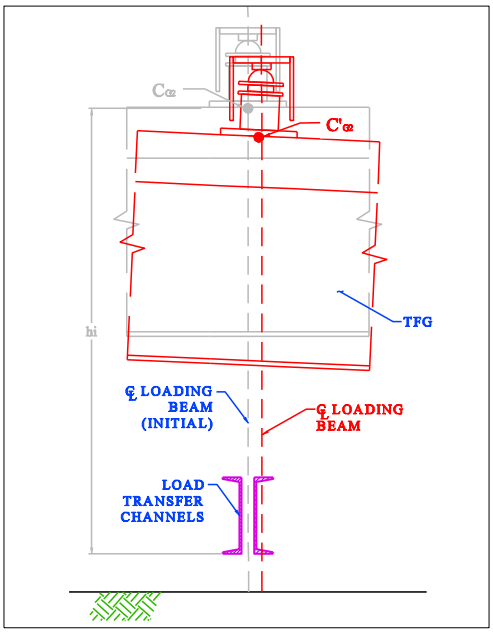

(c) Load step 35 (maximum load)

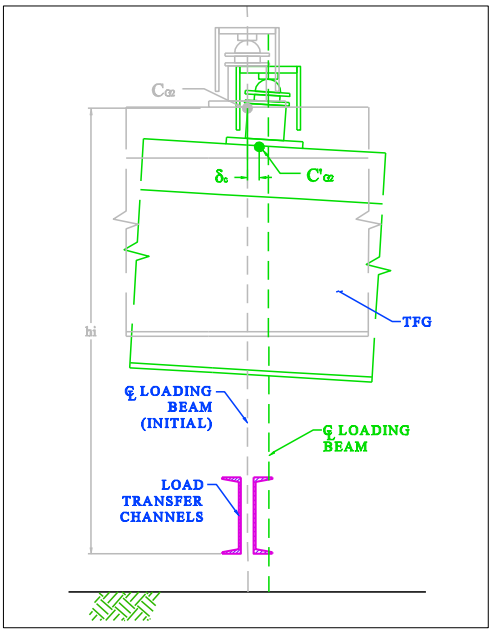

(d) Load step 50
(beyond maximum load)

Figure 4.25: Longitudinal plane cross section view of G2 at Section D_W

CHAPTER 5: DESIGN OF TEST LOADING FIXTURES

5.1. Introduction

This chapter explains the design of the loading fixtures for the tests. Figure 5.1 is a parallel plane cross section view of the test specimen and a loading fixture where the main parts of the loading fixture are given. Section 5.2 provides an overview of the loading fixtures. The loads used for the designs are then discussed in Section 5.3. Four different loading fixture designs are required, as explained in Section 5.4. Stability of the loading fixtures is explained in Section 5.5. The designs of the load transfer channels are explained in Section 5.6 and the loading beam is explained in Section 5.7. The design of the loading rod assemblies is explained in Section 5.8. The design of the load bearing assemblies that apply the load to the test specimen is explained in Section 5.9. At Section A, the loads are applied to the diaphragm instead of directly on the TFGs. The capacities of the connections between the diaphragms and TFGs were evaluated for this load, as explained in Section 5.10.

5.2. Overview of Loading Fixtures

The design of the loading fixtures for the tests has four main goals. The first goal is to allow loading and unloading of the test specimen multiple times. The second goal is to be able to load the test specimen safely beyond its maximum load capacity. The third goal is to allow the test specimen to respond without restraint from the loading fixtures so that the loading fixtures do not influence the response to the loads. The fourth goal is to keep the applied loads vertical.

The test specimen is loaded using seven loading fixtures. Figure 5.1 is a parallel plane cross section view of the test specimen with a loading fixture. Each loading fixture applies one concentrated load to each TFG. The loading fixtures are located at the seven parallel cross sections explained in Section 3.2. At each loading fixture, two "loading rod assemblies" pull down on a wide flange beam (the "loading beam") above the test specimen. Each loading rod assembly is comprised of one hydraulic jack and a series of steel rods, steel plates, and half-rounds (steel round bars cut in half lengthwise). The loading beam bears on the test specimen through two "load bearing assemblies." Each load bearing assembly is comprised of a series of steel components including plates, half-rounds, and a hollow-structural-section (HSS). The loading rod assemblies also pull up on a pair of laced channels (the "load transfer channels") below the test specimen. The load transfer channels are anchored by the "ground anchor rods" that provide reactions to the force of the loading rod assemblies.

Parallel plane cross section views of the loading fixtures are shown in Figure 5.2, Figure 5.3, Figure 5.4, and Figure 5.5, at Section A, at Section B, at Section C, and at Section D, respectively. As shown, for each of these section types, there is a corresponding loading fixture.

Figure 5.6 is a parallel plane cross section view at Section A corresponding to Detail A of Figure 5.2. Figure 5.7 is a parallel plane cross section view at Section B corresponding to Detail B of Figure 5.3. Figure 5.8 is a parallel plane cross section view at Sections C and D corresponding to Detail C of Figure 5.4 and Detail D of Figure 5.5.

Figure 5.9 is a longitudinal plane cross section view at Section A corresponding to section A-A of Figure 5.2. Figure 5.10 is a longitudinal plane cross section view at Section B corresponding to section B-B of Figure 5.3. Figure 5.11 is a longitudinal plane cross section view at Sections C and D corresponding to section C-C of Figure 5.4 and section D-D of Figure 5.5.

A longitudinal plane cross section view of the loading rod assembly is shown in Figure 5.12, which corresponds to section A-A in Figure 5.1. Full length longitudinal plane cross section views of the load bearing assembly at Section A, at Section B, and at Sections C and D are shown in Figure 5.13, Figure 5.14, and Figure 5.15, respectively. Figure 5.13 corresponds to section B-B in Figure 5.1. Figure 5.14 and Figure 5.15 correspond to section C-C in Figure 5.1.

The designs of the components of the loading fixtures are explained in Section 5.3 through Section 5.9. For the designs of the components, the term "width" refers to the dimension in the longitudinal plane, the term "length" refers to the dimension in the parallel plane, and the term "thickness" refers to the dimension in the vertical direction. A summary of the dimensions of the plates and bars of the loading fixtures is given in Table 5.1. A summary of the lengths of the HSS, the load transfer channels, the loading beam, and the half-rounds is given in Table 5.2.

5.3. Design Loads for Loading Fixtures

The loading fixtures load the test specimen with concentrated loads to simulate the idealized uniformly distributed load (as described in Section 4.2). From the FE model

with boundary condition combination bc2 under load Case 5, the nominal total load of the test specimen when it reaches its maximum load capacity is expected to be 327 kip. Note that the total reaction at each end of the test specimen is 163.5 kip, which is much less than the total reaction applied to the bearings and the footings during the previous tests by Kim (Kim, 2005; see Section 3.8). The loading fixture designs are based on the applied loads when the test specimen reaches its maximum load capacity, multiplied by a factor of safety (FS) of 1.3. The factored total load when the test specimen reaches its load capacity is expected to be 425 kip. Fourteen hydraulic jacks will provide the load for the tests. Each jack provides the same load. The expected maximum load at each jack is 20.4 kip and the factored load is 26.6 kip. These values are $1/16^{th}$ of the total load. The values were calculated using the concentrated load simulation explained in Section 4.2.

The jacks are Enerpac RCH-326 hollow plunger cylinders with a 30 ton capacity and maximum operating pressure of 10 ksi (ENERPAC, 2012). Figure 5.16 is a photograph of a fully retracted jack, which is 13 in tall. When fully extended, the jack has a stroke of 6.13 in. The outer diameter is 4.5 in and the center hole diameter is 1.31 in. A port at the bottom connects to a hydraulic hose that provides oil. In the tests, a single pump will supply oil to all of the jacks. A series of hydraulic hoses and manifolds will connect the pump to the jacks. Gauges will measure the oil pressure during the tests. Load cells will be used measure the force at the loading rod assemblies (explained in Section 5.8).

One jack is located within each loading rod assembly. Each loading fixture has two loading rod assemblies. The loading rod assemblies are arranged on the loading beam

to produce a load on G2 that is 1.05 times the load on G1. This difference accounts for the different deck area supported by each TFG, as discussed in Section 4.2.3. Figure 5.17 (a) shows a sketch of a simply supported beam used to find the relative positions of the two loading rod assemblies of each loading fixture. The figure also includes the corresponding moment diagram. In the analysis, the loading beam was simulated by the simply supported beam, the load bearing assembly at G1 was simulated by a pin, the load bearing assembly at G2 was simulated by a roller, and the loading rod assemblies were simulated as concentrated loads on the simply supported beam. One loading rod assembly position was chosen and the other was determined to produce a 1.05 load ratio at the load bearing assemblies.

The loading rod assembly positions are designed to accommodate the expected displacement of the test specimen and the expected displacement of the loading fixtures determined from the kinematic studies described in Section 4.3.3. The south loading rod assemblies are located 18.625 in away from the centerline of G1. The north loading rod assemblies at Section B, at Section C, and at Section D are located 21 in away from the centerline of G2. The north loading rod assembly at Section A is located 20.5 in away from the centerline of G2. Section A is different to accommodate loading on the mid-span diaphragm, instead of on the TFGs, while providing the 1.05 load ratio.

The nominal loads at the load bearing assemblies on G1 and G2 when the test specimen reaches its maximum load are expected to be 19.9 kip and 20.9 kip, respectively, and the corresponding factored loads are 25.9 kip and 27.2 kip. Although the actual distance between the TFGs is different at each parallel section, the difference is

small and does not have a significant effect on the loads on the test specimen. Table 5.3 lists the nominal and factored maximum moments in the loading beam for the four different parallel sections.

The reactions in the ground anchor rods and the maximum moment in the load transfer channels were determined from statics based on the position of the loading rod assemblies and ground anchor rods. Figure 5.17 (b) is a sketch of a simplified beam and corresponding moment diagram used to determine the load effects. The analysis treats the load transfer channels as a simply supported beam with the south ground anchor rod as a pin, the north ground anchor rod as a roller, and the two loading rod assembly loads as upward concentrated loads. The distances between the loading rod assemblies and the ground anchor rods are different at each parallel section due to the horizontal curvature of the test specimen (Section 5.8). Table 5.3 lists the nominal and factored maximum moments in the load transfer channels for the four different types of loading fixtures and Table 5.4 lists the ground anchor rod reactions for the four different types of loading fixtures.

Table 5.4 includes the demand-to-capacity ratios (DCRs) for the ground anchor rods of each section. A DCR is the ratio of the factored demand divided by the factored capacity. The demand is multiplied by a load factor (in this case, FS equal to 1.3) and the capacity is multiplied by an appropriate ϕ factor. The DCRs of the ground anchor rods use the design load of 112.5 kip as the factored capacity. As discussed in Section 3.9, the ground anchor rods were tested for 1.33 times the design load indicating that the design

load is a reduced (factored) capacity. All of the DCRs are less than 1.0, which means that the ground anchor rods will not be overloaded.

5.4. Differences Between Loading Fixture Types

Although the overall schematic of the loading fixtures is the same, four types of loading fixtures are needed (Figure 5.2 through Figure 5.15). The lateral distance in the parallel plane between the centerline of the ground anchor rods and the centerline of the test specimen is different at each section type. The distances between the centerlines affect the maximum moment in the load transfer channels (see Section 5.3 and Section 5.6) and the lateral distance in the parallel plane between the north loading rod assembly and the north ground anchor rod. In addition, the distance between the TFGs in the parallel plane changes at each section due to the curvature of the test specimen. Section A has the smallest distance, 96.0 in, and Section D has the largest distance, 97.4 in. The differences have a small effect on the estimated rotation in the parallel plane of the loading beams. However, the differences affect the location of the loading rod assemblies on the loading beam. The four loading fixtures have different locations in order to achieve the 1.05 load ratio at each section.

Another difference between the types of loading fixtures is due to the diaphragms at Section A and at Section C, but not at Section B and at Section D. The diaphragms influence the kinematics of the test specimen, such as the relative displacement and relative rotation between the two TFGs.

At Section A, the loads are applied to the diaphragm rather than the TFGs, so that a concentrated load is not applied to the top of the tube. Yielding of the tubes and, ultimately, failure of the tubes is expected at Section A (mid-span) and applying the load on the tubes would affect yielding and failure of the tubes. As shown in Figure 5.6, the centerlines of the load bearing assemblies at Section A are located 3 in toward the centerline of the test specimen from the ends of the diaphragm.

5.5. Stability of Loading Fixture

Certain aspects of the loading fixtures are designed to provide stability. This section explains the stability concerns. There are three stability conditions related to the forces within the loading fixture that are discussed. First, for Stability Condition 1, stability from the load-height effect is discussed. To provide stability of the loading beam, the loading rod assemblies *pull down* at the *bottom* of the loading beam, and the load bearing assemblies *push up* at the *top* of the loading beam. Second, for Stability Condition 2, stability related to Plate B bearing on the half-rounds of the loading rod assemblies is discussed. Third, for Stability Condition 3, stability of the HSS within the load bearing assemblies is discussed.

There are three different half-round loading cases to consider for stability. The first half-round loading case is the loading beam bearing on the load bearing assembly half-rounds at Section A (see Figure 5.2 and Figure 5.6) and at Section B (see Figure 5.3 and Figure 5.7). The load bearing assembly half-rounds are aligned in the longitudinal plane. In this orientation, the loading beam is simply supported and therefore, inherently

stable. The second half-round loading case, which is Stability Condition 1, is the loading beam bearing on the load bearing assembly half-rounds at Section C (see Figure 5.4 and Figure 5.11) and at Section D (see Figure 5.5 and Figure 5.11). At these sections, the load bearing assembly half-rounds are aligned in the parallel plane. In this orientation, the load-height effect is used to provide stability. The third half-round loading case, which is Stability Condition 2, is Plate B bearing on the loading rod assembly half-rounds (Figure 5.12).

5.5.1. Stability Condition 1: Load-Height Effects

The first stability concern, Stability Condition 1, is stability/instability due to the load-height effect. The load-height effect can be seen by examining Figure 5.18. Figure 5.18 shows simplified models of (a) a short rectangle (square) and (b) a tall rectangle, acted on by a pair of forces assumed to be eccentric to the vertical centerline of the rectangle. The eccentricity simulates the actual unintentional eccentricities in the loading fixtures. Three orientations are shown. The first orientation is the case where the forces put the rectangle into tension in an unstable position. The second orientation is the case where the forces put the rectangle into tension in a stable position. The third orientation is the case where the forces put the rectangle into compression in an unstable position.

For the rectangles in tension in an unstable position, the rectangle will rotate clockwise until the forces are aligned and it becomes stable. For the rectangle in compression in an unstable position, the rectangle must rotate much farther until the rectangle is in tension rather than compression to be stable. A comparison of the two

different size rectangles shows that when the eccentricity is small compared to the height (simulated by the tall rectangle), the tall rectangle has to rotate less than the short rectangle to achieve a stable position. The larger vertical distance between the tension forces increases the stability.

Figure 5.19 shows Stability Condition 1 for the loading beam from the loading fixture design for Section C and Section D. When the force from the load bearing assembly is eccentric to the centerline of the loading beam, the loading beam will try to rotate in the longitudinal plane until the force from the load bearing assemblies align with the resultant vertical forces from the loading rod assemblies. A larger vertical distance between the forces of the load bearing assemblies and the forces of the loading rod assemblies on the loading beam increases the stability of the loading beam. For the loading fixtures, the HSS in the load bearing assemblies increase the upward vertical distance to the location of the force on the loading beam from the load bearing assemblies. The HSS were checked for stability and this check is discussed later as Stability Condition 3.

5.5.2. Stability Condition 2: Bearing on Half-Round

A second stability concern, Stability Condition 2, is bearing on the cylindrical half-rounds at the loading rod assemblies. Figure 5.20 and Figure 5.21 is a series of simplified sketches from a stability analysis with two different sized plates bearing on a half-round. The thin plate in Figure 5.20 has a height (thickness) $H = 0.5r_{HR}$, where r_{HR} is the radius of the half-round, and the thick plate in Figure 5.21 has a height $H = 1.5r_{HR}$. A

vertical force, P, is applied to the top of the plate and the reaction, R, acts perpendicular to the half-round at the contact point. Figure 5.20 (a) and Figure 5.21 (a) show stable initial positions when P and R are aligned.

One stability consideration for Stability Condition 2 is the effect of applying P eccentrically by an amount e_{acc} as shown in Figure 5.20 (b) and Figure 5.21 (b). The plate will rotate because the forces are misaligned. As shown in Figure 5.20 (c), if the applied force remains vertical, the plate will rotate by θ_{acc}, which is equal to (using small angle theory):

$$\theta_{acc} = \frac{e_{acc}}{r_{HR} - H} \qquad \textbf{(5.1)}$$

Where H is the height (thickness) of the plate. Since the plate has rotated, the normal force at the contact point is not vertical. It is assumed, however, that the frictional force plus the normal force at the contact point provide a vertical reaction, R.

The height (thickness) of the plate is another stability consideration for Stability Condition 2. Only a plate with a height less than the radius of the half-round will be stable when it rotates due to e_{acc} (note alignment of P and R in Figure 5.18 (c)).

Note that Figure 5.20 and Figure 5.21 show the plate rotated, but during the tests, the half-round will rotate as depicted in Figure 5.22, which shows the initial position and an estimated final position at the top of the loading rod assembly for load step 50 of the FE analysis.

Figure 5.20 (d) shows the thin plate rotated by θ. P has an eccentricity of e_{total}, and R has an eccentricity of e at the contact point. For this analysis, we assume θ equals θ_{LB} for load step 50 from the FE results. Figure 5.20 (e) shows the location of R (at the contact point), P (eccentric from the centerline of the plate by e_{acc}), the half-round, and the plate (eccentric from the centerline of the half-round by e_{add}). Assuming an initial accidental eccentricity, the total eccentricity between P and the centerline of the half-round is equal to:

$$e_{total} = e_{add} + e_{acc} \tag{5.2}$$

In this equation, e_{add} is the additional eccentricity of P due to θ, which is equal to:

$$e_{add} = \theta H \tag{5.3}$$

To be stable, e_{total} has to be less than the arc length that the plate rolls along, which is equal to:

$$arc = \theta r_{HR} \tag{5.4}$$

A stable position is possible only if the height is less than the radius, as follows:

$$e_{total} < arc \tag{5.5}$$

$$\theta H + e_{acc} < \theta r_{HR} \tag{5.6}$$

$$e_{acc} < \theta(r_{HR} - H) \quad \textbf{(5.7)}$$

$$r_{HR} > H \quad \textbf{(5.8)}$$

Since e_{acc} is positive, the inequality of Equation (5.8) must be satisfied for the inequality of Equation (5.7) to be satisfied. When this condition is met, the eccentricity of P with respect to R (at the contact point), called e_{force}, is such that the moment resists the rotation and tends to return the plate towards its initial position.

Figure 5.21 is similar to Figure 5.20, but the plate is thicker and H > r_{HR}. An eccentricity makes the thick plate unstable. Figure 5.21 (d) and (e) show the rotated thick plate and vertical load corresponding to θ_{LB} from load step 50 of the FE analysis. In this case, r_{HR} < H, so the inequality of Equation (5.7) cannot be satisfied, even if e_{acc} is zero. The eccentricity of P with respect to R produces a moment that tends to increase the eccentricity and the place can rotate off the half-round. Therefore, the thickness of Plate B has to be less than the radius of the half-round at the loading rod assembly (see Figure 5.22).

5.5.3. Stability Condition 3: HSS Stability

The stability analysis for the HSS at Section A is shown schematically in Figure 5.23. The HSS at Section A was analyzed because it is taller than the HSS at the other sections. Figure 5.23 (a) shows a parallel plane cross section view of the load bearing assembly at Section A in its initial position. The initial height, H_i, is the distance from the bottom of the HSS to the top of the half-round in contact with Plate J ("PL_J", explained in

Section 5.9). Figure 5.23 (b) shows the displaced position of the load bearing assembly at load step 50 from the FE analysis (after the test specimen reaches its maximum load capacity). PL_J has rotated by θ_{PLJ}, which is equal to the rotation in the parallel plane of the loading beam (θ_{LB}, explained in Section 4.3.3). The HSS and other parts of the load bearing assembly (assumed rigid) have rotated by θ_{TFG}, which is equal to the rotation in the parallel plane of the closest tube (θ_{pp}, explained in Section 4.3.3). The relative rotation, θ_{rel}, between θ_{LB} and θ_{pp} causes PL_J to have a different contact point on the half-round in the displaced position than in the initial position. However, this effect is small and is neglected.

Figure 5.23 (c) shows the displaced position of the load bearing assembly with PL_J replaced with a vertical force at the contact point. There is an eccentricity, e, between the centerline of the HSS and the centerline of the force. The final vertical height is H_f. The change in height from H_i to H_f is small and H_i was used for the calculations in the displaced position.

The eccentric force produces a moment at the base of the HSS. A stress analysis at the base of the displaced HSS is depicted in Figure 5.23 (d) (the base is shown as horizontal for convenience). The total stress is equal to the uniform compression stress caused by the applied load plus the stress caused by the moment due to the eccentricity of the applied load. The uniform compression stress was calculated as the vertical force divided by the cross sectional area of the HSS. The bending moment stress was calculated as the vertical force multiplied by the eccentricity divided by the elastic section modulus of the HSS.

If the total stress at the base of the HSS is compressive everywhere, the HSS is stable. If the left side of the HSS is in tension, the HSS may start to tip. The HSS at Section B, at Section C, and at Section D are short enough and the rotation is small enough so that the total stress is in compression. The south edge of the HSS at Section A may be in tension due to the larger HSS height. Therefore, to prevent tipping, welds between the HSS and the bearing plate (Section 5.9) are arranged to be in the longitudinal plane and the bearing plate is made wider than the HSS.

5.6. Load Transfer Channels and Attachments

The test setup, test loads, kinematics of the test specimen and the loading fixtures, and stability conditions all influenced the design of the loading fixtures. The factored demand loads from the analysis of the FE model with bc2 supports under load Case 5 (Section 4.2.3 and Section 4.3.2) were used for the design. The AISC Steel Construction Manual (2005) was used to calculate the capacities of the loading fixture components. At each loading fixture, as shown in Figure 5.1, the loading rod assemblies pull down on the loading beam above the test specimen. The loading beam bears on the test specimen through the load bearing assemblies. The loading rod assemblies also pull up on the load transfer channels below the test specimen, which are anchored by the ground anchor rods. The designs of the load transfer channels and the attachments (stiffeners, tie plates, and bracing) to support the load transfer channels are explained in this section.

The load transfer channels are back-to-back C12x20.7 ASTM A992 grade 50 steel channels. The load transfer channels are 2 in apart, and are laced together with steel tie

plates. The ground anchor rods and the main rods of the loading rod assemblies fit in the gap between the backs of the channels.

The load transfer channels were treated as a simply supported beam with two concentrated loads at the location of the loading rod assemblies (Figure 5.17 (b)). The beam was analyzed for the forces at load step 35, and for the loading rod assembly displacements at load steps 35 and 50. The factored concentrated loads each equal 26.6 kip. The shear and moment results in the load transfer channels at Section A were the largest demands, which were used to design the load transfer channels. The maximum factored shear is 34.0 kip and the maximum factored moment is 1355 kip-in. It was assumed that one load transfer channel carries half of the shear, and initially it was assumed that one load transfer channel carries half of the moment. The deflections of the load transfer channels were determined at the locations of the concentrated loads. These locations correspond to the estimated locations of the north and south loading rod assemblies (Section 4.3.3) for load step 35 (when the test specimen reaches its maximum load capacity) and load step 50 (after the test specimen reaches its maximum load capacity). The deflections are given in Table 5.5.

The shear capacity of one load transfer channel based on AISC Equation (G2-1) is 102 kip. AISC Chapter F was used to determine the flexural capacity of an individual load transfer channel. The web and flanges are compact based on AISC Table B4.1. AISC Section F2 for channels with a compact web and flanges bent about their major axis was used. Equations (F2-5) and (F2-6) were used to calculate L_p and L_r, respectively. L_r is 114 in, less than the unbraced length, L_b, of 216 in, which is the parallel distance

between the ground anchor rods. The lateral-torsional buckling capacity was calculated using Equation (F2-4) with C_b conservatively taken as 1.0 in Equation (F2-3). The capacity of a single load transfer channel is 303 kip-in, much less than half of the maximum moment demand. Therefore, the flexural capacity of two individual C12x20.7 was not adequate.

The two load transfer channels were, therefore, designed as a built-up member to create a larger flexural capacity. The two load transfer channels were laced together with tie plates. Figure 5.24 shows the cross section dimensions of the built-up load transfer channels. The area, polar moment of inertia, warping product of inertia, nominal plastic moment (M_p), and nominal yield moment (M_y) were estimated to be twice the corresponding value for a single load transfer channel. The moment of inertia about the weak axis (I_y) was calculated using the centerline dimensions and the parallel axis theorem. The calculated I_y is 48.4 in^4, much larger than twice the I_y = 3.86 in^4 of each channel.

A larger I_y and corresponding r_y increases L_p and L_r. L_p was re-calculated using Equation (F2-5) and equals 84.5 in. L_r was calculated by setting the elastic buckling moment limit of the built-up member equal to 70% of the nominal yield moment of the built-up member. The elastic buckling moment limit was set equal to the stress from Equation (C-F2-2) multiplied by S_x, and the result was solved for L_b. The resulting L_b is L_r, which equals 239 in.

The nominal flexural strength of the built-up load transfer channels as a function of unbraced length is shown in Figure 5.25. Linear interpolation between the points (L_p, M_p) and (L_r, $0.7M_y$) was used to find the nominal flexural strength of the built-up load transfer channels with an L_b of 216 in. The nominal flexural strength of the built-up load transfer channels was determined to be 1665 kip-in, which results in a factored flexural strength of 1500 kip-in. For the built-up load transfer channels, the flexural DCR is 0.90.

The shear DCR was calculated assuming each load transfer channel carries half of the shear. The resulting DCR is 0.17.

The two load transfer channels are laced together with steel tie plates. Figure 5.26 shows the tie plate arrangement along the load transfer channels at each section type. Figure 5.26 shows that the south end tie plates and intermediate tie plates are between the ground anchor rods, and the north end tie plate is beyond the north ground anchor rod. Figure 5.27 shows cross section views and plan views of the three types of tie plates. The tie plates are fabricated from ASTM A572 grade 50 steel. The south end tie plates and the intermediate tie plates consist of a pair of plates (Figure 5.27 (a), (c), and (d)). For the pair of south end tie plates and the three pairs of intermediate tie plates, one tie plate is welded to the top of the load transfer channels and one tie plate is welded to the bottom of the load transfer channels. The south end tie plates are 4.5 in wide, 4.5 in long, and 0.25 in thick. The intermediate tie plates are 4.5 in wide, 2.75 in long, and 0.25 in thick. The north end tie plate is a single tie plate bolted between the load transfer channels (Figure 5.27 (b), (e), and (f)) to make the assembly of the loading fixture easier. The north end tie plate is 2 in wide, 5 in long, and 12 in thick (deep).

As suggested by AISC Section F13.4, AISC Section E6.2 for built-up compression members was used to design the tie plate spacing. The spacing of the tie plates is shown in Figure 5.26 for the west half of the test specimen. The maximum allowed spacing between the tie plates is 64.75 in. This spacing is controlled by the effective slenderness ratio, Ka/r_i, of a single load transfer channel between the tie plates, which cannot exceed three-fourths the governing slenderness ratio of the built-up load transfer channels, where the spacing between the tie plates is a. The largest spacing used in the loading fixtures is 59 in at Section C.

AISC (2005) also provides dimensional limits for the tie plates. AISC Section E6.2 stipulates that for end tie plates, the length of the tie plate, L_{TIE} in Figure 5.28, has to be larger than or equal to the distance between the lines of welds connecting the tie plate to the load transfer channels of the built-up member, which is equal to W_{TIE} in Figure 5.28. For intermediate tie plates, L_{TIE} has to be larger than or equal to half of W_{TIE}. In addition, the thickness of the tie plate has to be larger than or equal to $0.02W_{TIE}$. All of the welded tie plate sizes meet these requirements.

Tie plates are designed "to provide a shearing strength normal to the axis of the member equal to two percent of the available compressive strength of the member" according to AISC Section E6.2 (2005). The available compressive strength (i.e., the factored capacity) of the built-up load transfer channels was computed using AISC Section E7 and using $(KL/r)_m$ from Equation (E6-2) equal to 124. Section E7 was used because the webs of the load transfer channels are slender based on AISC Table B4.1. The flanges are noncompact based on AISC Table B4.1. The critical stress, F_{cr}, was

calculated from Equation (E7-3). In this equation, Q_a was calculated from Equation (E7-16), and b_e was calculated from Equation (E7-17). The nominal compressive strength of the built-up load transfer channels is 189 kip, which was calculated using Equation (E7-1). The available compressive strength (i.e., factored capacity) of the built-up load transfer channels is 170 kip.

Two percent of the available compressive strength of the built-up load transfer channels is 3.4 kip. This is the demand on the tie plates required by AISC (2005). However, it was decided to use two percent of the resultant compressive force in the built-up load transfer channels due to the factored maximum moment in the load transfer channels. The moment produces a flexural stress in the built-up load transfer channels equal to the moment divided by the elastic section modulus about the strong axis of the member. The elastic section modulus was taken as twice the $S_x = 21.5$ in^3 of each load transfer channel. The resultant compressive force was estimated by multiplying the flexural stress in the built-up load transfer channels by the total area of the built-up load transfer channels. Two percent of the resultant compressive force is 7.7 kip, which is conservative compared with the specified AISC demand.

The shear strength capacity of the tie plates was calculated using AISC Equation (G2-1). The shear strength of the south end tie plates and intermediate tie plates is 33.8 kip. The shear strength of the north end tie plate is 720 kip, which is much larger because the cross section area of the north end tie plate in the longitudinal plane is large (see Figure 5.27(b)). The corresponding DCRs are 0.23 and 0.01, respectively. The demands,

capacities, DCRs, and AISC equations used to calculate the capacities are given in Table 5.6.

The south end tie plates and the intermediate tie plates are welded to the load transfer channels. The welds are shown in Figure 5.27. The weld lengths for the tie plates are designed using AISC Section E2 requirements and are based on the IS 800:2007 guidelines (taken from Sai, 2008) shown in Figure 5.29. The size and strength of the welds were determined using AISC Section J2. The welds are 1/8 in fillet welds.

The demand on the tie plate welds was taken as 7.7 kip. The capacity of the welds was calculated using AISC Equation (J2-3). The capacity of the south end tie plate welds is 36.2 kip. The capacity of the intermediate tie plate welds is 19.5 kip. The south end tie plate welds have a DCR of 0.21 and the intermediate tie plate welds have a DCR of 0.39.

The north end tie plate will be installed in the field for easier assembly and disassembly of the loading fixtures. The north end tie plate is bolted to the load transfer channels with two 0.75 in diameter ASTM A325 bolts as shown in Figure 5.27. The demand on the connection was taken as 7.7 kip. The connection was evaluated as a slip-critical connection using AISC Section J3.8. The design slip resistance (i.e., the factored capacity) equals 9.4 kip, calculated using Equation (J3-4). The resulting DCR is 0.82. The bolt spacing, as shown in Figure 5.27 (f), meets the requirements in AISC Section J3.

The loading rod assemblies pull up on the built-up load transfer channels and the loads are resisted by ground anchor rods. A standard Dywidag nut and plate, PL_A,

transfer the load to each ground anchor rod, as shown in Figure 5.1. A plan view of PL_A is shown in Figure 5.30 (a). PL_A is 8 in wide, 5 in long, and 1.5 in thick.

The flexural demand on PL_A was taken as the maximum moment determined by treating PL_A as a simply supported beam. This beam has a 2.28 in length, equal to the distance between the centerlines of the webs of the load transfer channels (Figure 5.24). The assumed simply supported beam is loaded at mid-span by a concentrated load equal to the maximum factored ground anchor rod reaction (34.0 kip). The maximum moment is 19.4 kip-in. The shear demand on PL_A was taken as half of the 34.0 kip load. The bearing demand on PL_A was taken as 34.0 kip.

The flexural capacity of PL_A was calculated with AISC Equation (F11-1). The plastic section modulus was calculated using the parallel plane cross section at section A-A shown in Figure 5.30 (a). The flexural capacity is 93.3 kip-in, which results in a DCR of 0.21. The capacities, DCRs, and the AISC equations used to calculate the capacities for shear and bearing are listed in Table 5.6. PL_A is adequate for shear and bearing.

At the ground anchor rods and the loading rod assemblies, AISC Section J10 for "Flanges and Webs with Concentrated Forces" applies to the load transfer channels. For single, compressive concentrated loads, the pertinent limit states are web local yielding, web crippling, and web sidesway buckling. Table 5.7 lists the demand, capacity, DCR, and AISC equation used to calculate the capacity for each limit state.

Assuming the web of each load transfer channel carries half of the load, the demand on the web of each load transfer channel for the limit states is half of the applied

factored load: either 13.3 kip at the loading rod assemblies or 17.0 kip at the ground anchor rods. The capacity calculations for web local yielding and web crippling used N = zero. Web sidesway buckling when the compression flange is not restrained against rotation was a concern. This failure mode is shown in Figure 5.31. The web sidesway buckling DCRs were much greater than 1.0 when the web was unrestrained, so stiffeners were added to prevent web sidesway buckling. With the compression flange restrained by stiffeners, the web sidesway buckling DCRs are less than 0.20.

A pair of stiffeners, shown in Figure 5.32, is located at the locations of the ground anchor rods and at the initial position of the loading rod assemblies. In addition to preventing web sidesway buckling, the stiffeners at the location of the ground anchor rods are required per AISC J10.7 for unframed ends of beams. The stiffeners are 0.25 in thick ("long"), 2.25 in wide, extend the depth of the load transfer channel, and are fabricated from ASTM A572 grade 50 steel.

Each stiffener pair is designed to support the factored load of 34.0 kip. They were designed as bearing stiffeners following AISC Section J10.8 and Section 11.11 of Salmon et al. (2009). The slenderness ratio of the effective cross section shown in Figure 5.32 (a) is less than 25, therefore, AISC Equation (J4-6) was used for the limit states of yielding and buckling. AISC Equation (J7-1) was used for the limit state of bearing. The demands, capacities, and DCRs are summarized in Table 5.6.

The stiffeners are welded to the load transfer channels. The welds are the minimum size fillet weld of 1/8 in per AISC Table J2.4. The flange welds are provided

on both sizes of each stiffener and the welds extend the full length of the flanges. The web welds are required on only one side of each stiffener and are 7 in long. The demand on the flange welds of one stiffener was taken as 17 kip. The web weld was designed to carry the difference between the demand on the load transfer channel (17 kip) and the capacity of the load transfer channel for web sidesway buckling when the web is not restrained (4 kip). The demand on the web weld is 13 kip. The demands, capacities, and DCRs are summarized in Table 5.6.

The load transfer channels are braced at the end by concrete blocks (and wooden wedges as needed). Figure 5.33 shows a plan view and Figure 5.34 shows elevation views of the bracing (without the wooden wedges). The concrete blocks are 72 in wide, 24 in long, and 24 in tall ("thick"), and were chosen from available material at ATLSS.

For torsional bracing requirements of the load transfer channels, the required strength of the braces was calculated using AISC Equation (A-6-9). The modification factor, C_b, was conservatively taken as 1.0, and the required flexural strength was taken as the factored moment of 1355 kip-in. The required bracing strength is 16.3 kip-in. The provided strength was calculated as the moment that would cause zero stress at the edge of the concrete block due to overturning. The provided strength is 41.8 kip-in, which results in a DCR of 0.39.

Sliding of the concrete blocks was checked by treating the braces as lateral nodal braces. The required strength for lateral nodal bracing was calculated using AISC Equation (A-6-7) and is 2.4 kip based on the maximum moment in the load transfer

channels at Section A. The provided strength was taken as the maximum frictional force between the concrete block and the asphalt pavement of the test area. The static coefficient of friction was estimated to be 0.6 based on ACI 318-11 (ACI, 2011). The normal force was calculated as the estimated weight of the concrete block of 3.5 kip using the density for normal weight concrete of 145 lb/ft^3. The provided strength is 2.1 kip, which results in a DCR of 1.13. However, because the concrete blocks run continuously between the individual loading fixtures at each end, several blocks can be mobilized to resist the bracing force. This condition may not be true for the end concrete blocks at Section D. Using the maximum moment of the load transfer channels at Section D, the required strength for the lateral nodal bracing is 1.9 kip, which results in a DCR of 0.92.

The friction between the concrete block braces and the load transfer channels is the only restraint on the displacement of the load transfer channels in the parallel plane direction. During the tests, displacement in the parallel plane direction should be checked. The load transfer channels may displace in this direction if the applied loads from the loading rod assemblies do not remain vertical.

5.7. Loading Beam and Attachments

The loading rod assemblies pull down on the loading beam, which transfers the load to the load bearing assemblies on the test specimen. The loading beam is a W10x49 fabricated from ASTM A992 grade 50 steel. The loading beam is 13 ft long and the mid-

length is aligned with the centerline of the test specimen. The loading beam is oriented to bend about the weak-axis, so lateral-torsional buckling is not a concern.

The loading beam was treated as a simply supported beam with two concentrated loads at the location of the loading rod assemblies and two reactions at the locations of the load bearing assemblies (Figure 5.17 (a)). The beam was analyzed for the forces at load steps 35, and in the initial positions of the test specimen and loading rod assemblies. The factored load in the loading rod assemblies equals 26.6 kip. The shear and moment results at Section A were the largest demands, which were used to design the loading beam. The maximum factored shear is 26.6 kip and the maximum factored moment is 809 kip-in. The deflections of the loading beam were determined at the locations of the concentrated loads, which corresponded to the initial position of the loading rod assemblies. The initial position is used because θ_{LB} would cause negligible changes in the parallel distances between the loading rod assemblies and the load bearing assemblies. The deflections are given in Table 5.5.

The flexural capacity of the loading beam was determined using AISC Section F6 for I-shaped members bent about their minor axis. The shear capacity was calculated according to AISC Section G7, which used Equation (G2-1) with the modifications:

$$A_w = b_f t_f \tag{5.9}$$

$$k_v = 1.2 \tag{5.10}$$

Portions of the web of the loading beam are cut out so the load bearing assemblies will push up near the top of the loading beam to increase stability (see Section 5.5.1). The capacities of the loading beam should not be affected by removing the web because the flexural and shear capacity is supplied by the flanges. In Figure 5.2 through Figure 5.5, the remaining web is shown by the dashed lines along the length of the loading beam. The cuts in the web are at the ends of the loading beam and at the locations of the load bearing assemblies. The demands, capacities, DCRs, and AISC equations used to calculate the capacities are given in Table 5.7.

5.8. Loading Rod Assembly

The forces to load the test specimen are provided by the jacks (Section 5.3), located within the loading rod assemblies (Figure 5.12). Figure 5.35 is a plan view of the west half of the test setup that shows the spacing between the ground anchor rods, the loading rod assemblies, and the centerline of the test specimen. Each loading fixture has to loading rod assemblies. In each loading rod assembly, a jack puts the main rod of the loading rod assembly into tension. The loading rod assembly transmits this load to the load transfer channels and the loading beam through a series of plates, rods, and half-rounds that make up the loading rod assembly.

The main rod of loading rod assembly is a 1 in diameter ASTM A193 grade B7 threaded rod with a nominal yield stress of 105 ksi and a nominal ultimate tensile stress of 125 ksi (Figure 5.12). The length is approximately 6.75 ft.

The tension demand in the main rod is equal to the factored load in the loading rod assembly (26.6 kip). A bending moment in the main rod may develop. The moment would be caused by an eccentricity of the force in the main rod due to θ_{LB} (see Figure 5.22). The flexural demand was calculated as an eccentricity multiplied by 26.6 kip. The eccentricity was calculated as the radius of the half-rounds multiplied by θ_{LB}. The eccentricity, which is equal to 0.21 in, is explained later in more detail with the discussion of the half-rounds. The flexural demand is 5.5 kip-in. It was assumed that no significant shear develops in the main rod and therefore, the moment is constant.

The capacity for tension of the main rod was calculated using AISC Section J3 and is 55.2 kip. The flexural capacity was calculated using AISC Section F11 and is 13.3 kip-in. The tension and flexural demands and capacities were used to evaluate the effect of the combined forces in the main rod. The DCR was determined using AISC Section H1.1. The required axial tensile strength, P_r, is the axial force (26.6 kip), and the required flexural strength, M_r, is the flexural demand (5.5 kip-in). The available axial tensile strength, P_c, is the design axial tensile strength (i.e., the factored axial capacity, which is equal to 55.2 kip). The available flexural strength, M_c, is the design flexural strength (i.e., the factored flexural capacity, which is equal to 13.3 kip-in). P_r divided by P_c is greater than 0.2, so Equation (H1-1a) was used to calculate the DCR for the combined forces. The DCR is 0.85. The demands, capacities, DCRs, and AISC equations used to calculate the capacities are listed in Table 5.6.

The main rod is put into tension when the jack pushes up against Plate C (PL_C), which is held down by a nut on the main rod (Figure 5.12). A plan view of PL_C is shown

in Figure 5.30 (c). A standard 1.0625 in diameter hole for a 1 in diameter bolt, is in the center. PL_C is 5 in wide, 5 in long, 0.75 in thick, and fabricated from ASTM A572 grade 50 steel. The width and length are designed to match Plate D (PL_D) and Plate F (PL_F) for simplicity. The thickness was selected so that PL_C would remain flat under bending and shear.

Flexure was not a concern for PL_C. The shear and bearing demands were taken as 26.6 kip. The area for the shear capacity was taken as a cylindrical area with a diameter equal to the outside diameter of the nut and a length equal to the thickness of the plate. The area for the bearing capacity was taken as a ring with an inner diameter equal to the diameter of the hole, and an outer diameter equal to the outer diameter of the nut. The demands, capacities, DCRs, and AISC equations used to calculate the capacities are given in Table 5.6.

Figure 5.12 shows that the force in the main rod is transferred to the load transfer channels by Plate F (PL_F). A plan view of PL_F is shown in Figure 5.30 (c). PL_F is fabricated from ASTM A572 grade 50 steel. A standard 1.0625 in diameter hole is in the center. The width and length of PL_F are 5 in long to match the dimensions of PL_C and PL_D. The thickness is 0.75 in, which is controlled by the flexural demand.

The demands and capacities of PL_F were calculated similarly to the demands and capacities of PL_A previously explained. The concentrated load for calculating the flexural demand was taken as 26.6 kip, which results in a flexural demand of 15.2 kip-in. The plastic section modulus used to calculate the flexural capacity was taken at the parallel

plane cross section at section A-A in Figure 5.30 (c). The flexural capacity is 24.9 kip-in, which results in a DCR of 0.61. The demands, capacities, DCRs, and AISC equations used to calculate the capacities for flexure, shear, and bearing are listed in Table 5.6.

The normal force between PL_F and the load transfer channels will result in frictional forces on the contact surfaces. The loading rod assemblies are designed assuming that they displace freely in the lateral direction in the parallel plane, and large frictional forces may prevent this. To decrease the frictional forces, Teflon is placed between the load transfer channels and PL_F. The static coefficient of friction of Teflon-on-Teflon is about 0.04 (Serway and Jewett, 2010) compared with 0.3 for steel-on-steel (AASHTO, 2005). The smaller static coefficient of friction reduces the maximum frictional force that can be developed before sliding occurs. The bottom of the load transfer channels is covered with a 10 in length piece of Teflon. The top of PL_F is covered with Teflon.

Bearing is a concern for the Teflon because of its low compressive strength. The bearing demand on the Teflon is 26.6 kip. The allowable bearing stress on unfilled Teflon PTFE is about 3.5 ksi (BPI, 2012). The bearing capacity was calculated as the allowable stress of the Teflon multiplied by the bearing area. This results in a capacity of 52.5 kip and a DCR of 0.51.

As the jack pushes up on PL_C, it pushes down on Plate D (PL_D). PL_D distributes the load to the top of the load cell (discussed later). A plan view of PL_D is shown in Figure 5.30 (d). An oversized 1.25 in diameter hole decreases the possibility of the main

rod bearing against the side of PL_D and affecting the load cell. The width and length of PL_D are 5 in to extend beyond the 4.5 in outer diameter of the jack (Figure 5.12). The thickness of 0.75 in was selected to keep the plate flat. PL_D is fabricated from ASTM A572 grade 50 steel. The side of PL_D that bears on the load cell is to be machined flat.

Flexure was not a concern for PL_D. The shear and bearing demands were taken as 26.6 kip. The area for the shear capacity was taken as a cylindrical area with a diameter equal to the inside diameter of the jack and a length equal to the thickness of the plate. The area for the bearing capacity was taken as the horizontal cross sectional area of the load cell. The demands, capacities, DCRs, and AISC equations used to calculate the capacities are given in Table 5.6.

A load cell is located under PL_D. The details and schematic of a typical load cell are shown in Figure 5.36. The load cell measures the applied load. The load cells are from equipment available at ATLSS. The load cells are 3.5 in diameter round bar fabricated from ASTM A193 grade B7 steel. A 2.5 in diameter hole was drilled through the center of the round bar.

As shown in Figure 5.12, the load cell bears on Plate E (PL_E). PL_E is supported by four small rods and nuts (explained later), one located at each corner, which transfer the load to the loading beam. A plan view of PL_E is shown in Figure 5.30 (e). The side of PL_E that the load cell bears on will be machined flat. PL_E has an oversized 1.25 in diameter hole for the main rod and oversized 0.625 in diameter holes for the small rods. PL_E is fabricated from ASTM A572 grade 50 steel and is 8.5 in wide and 10 in long to

match the dimensions of PL_B (discussed later). The thickness is 2 in to provide uniform compression on the load cell and prevent significant bending and shear deformations to keep the plate flat.

The flexural and shear capacities of PL_E were not calculated because the 2 in thickness provides sufficient flexural and shear strength and stiffness. The bearing demands on PL_E were checked at the location of the load cell (26.6 kip) and at the location of the small rods (6.7 kip).

At the load cell, the area for the bearing capacity was taken as the horizontal cross sectional area of the load cell. At the small rods, the area for the bearing capacity was taken as a ring with an inner diameter equal to the diameter of the hole and an outer diameter equal to the outer diameter of the nut. The bearing capacity is controlled by the small rod nuts. The demands, capacities, DCRs, and AISC equations used to calculate the capacities are given in Table 5.6.

The load is transferred from PL_E to PL_B by the four small rods and nuts (Figure 5.12). The small rods are 0.5 in diameter ASTM A193 grade B7 threaded rods with a nominal yield stress of 105 ksi and a nominal ultimate tensile stress of 125 ksi. Each small rod is about 3 ft long. It was assumed that each small rod supports $1/4^{th}$ of the factored load supplied by the jack (6.7 kip) and that no moment is developed in the small rods. An eccentricity of the force with respect to the vertical centerlines of the small rods would be small compared with the distance between the small rods (spaced 8.375 in apart in the parallel plane and 6.875 in apart in the longitudinal plane (see Figure 5.30 (b) and

(e))). The tensile capacity was calculated using AISC Equation (J3-1). The capacity of each small rod is 13.8 kip, which results in a DCR of 0.48.

The small rods transfer the load to PL_B (Figure 5.12), which bears on the round surface of the half-rounds (discussed later). A plan view of PL_B is shown in Figure 5.30 (b). PL_B is fabricated from ASTM A572 grade 50 steel and has an oversized 1.25 in diameter hole for the main rod and oversized 0.625 in diameter holes for the small rods. PL_B is 8.5 in wide, which is limited by the clear distance between the flanges of the loading beam. The length is 10 in, which is necessary to accommodate the dimensions of Plate H (discussed later). The thickness is 1 in and is controlled by the flexural demand. When the jacks are reset (explained in Section 4.3.3), a nut on the main rod above PL_B holds the loading fixture and test specimen in place.

The flexural demand on PL_B was calculated for bending in the parallel plane during loading of the test specimen and for bending in the longitudinal plane during the resetting of the jacks. The flexural demand in the parallel plane controlled. The flexural demand was calculated by treating PL_B as a simply supported beam loaded at mid-span by a 26.6 kip concentrated load. The length of the beam was taken as the distance between the centers of two of the small rods aligned in a parallel plane, 8.375 in. The flexural demand was taken as the maximum moment at mid-span of the simply supported beam, equal to 55.7 kip-in. The shear and bearing demands on PL_B were taken as 26.6 kip at the main rod, and 6.7 kip at each small rod.

The flexural capacity of PL_B calculated using AISC Equation (F11-1) is 81.6 kip-in. In this calculation, the plastic section modulus was determined for the longitudinal plane cross section at section A-A in Figure 5.30 (b). For shear, the location of the main rod controlled the capacity using a cylindrical area with a diameter equal to the outer diameter of the 1 in nut and a length equal to the thickness of PL_B. The bearing capacity at the main rod was calculated using a contact area of a ring with an outside diameter equal to the outside diameter of the 1 in nut and an inside diameter equal to the diameter of the hole. The bearing capacity at the small rods was calculated using a contact area of a ring with an outside diameter equal to the outside diameter of the 0.5 in nut and an inside diameter equal to the diameter of the hole. A summary of the demands, capacities, DCRs, and AISC equations used to calculate the capacities are given in Table 5.6.

PL_B pushes down on two half-round sections that rotate with the loading beam (see Figure 5.12 and Figure 5.22). The half-rounds enable the loading rod assembly to remain vertical while the loading beam rotates in the parallel plane. The half-rounds are half cylinders fabricated from 4 in diameter ASTM A193 grade B7 round bar with a nominal yield stress of 95 ksi and a nominal ultimate tensile stress of 115 ksi. Two 3 in long half-rounds are under PL_B with a space between them for the main rod. The longitudinal axis of these half-rounds is in the longitudinal plane.

The half-rounds will roll along the bottom of PL_B as the loading beam rotates in the parallel plane. Figure 5.22 shows the initial position and final position of these half-rounds. The loading beam is not shown for clarity, but the bottoms of the flanges of the loading beam are parallel to the top of PL_H. The rotation causes the point of contact to be

eccentric to the centerline of the main rod, which would induce a moment in the main rod as discussed previously. The eccentricity was calculated as the arc length that the half-round rolls through caused by θ_{LB}. The maximum eccentricity is equal to 0.21 in.

The half-rounds of the loading rod assembly support the load applied by the jack, which is less than the largest demand on the half-rounds of the load bearing assemblies. Therefore, the total demand on both half-rounds was taken as the factored load of the north load bearing assembly (27.2 kip) so the same size half-rounds can be used for both locations. Theoretically, the bearing stress on the half-rounds from PL_B is infinity because it is a flat surface bearing on a circular surface. However, to estimate the adequacy of the half-rounds, the bearing capacity was calculated using AISC Section J7 for a rocker with a diameter less than 25 in. The total capacity of both of the half-rounds is 88.6 kip, which results in a DCR of 0.31.

The loading rod assembly half-rounds bear on a 0.25 in thick neoprene pad as shown in Figure 5.12. This material is included to "soften" the contact between the half-rounds and Plate H. The neoprene is designed to permit a rotation in the longitudinal plane between the loading rod assemblies and loading beam. This rotation is discussed in Section 4.3.3.

The neoprene pad bears on Plate H (PL_H). PL_H transfers the load from the loading rod assembly to the loading beam through welds (discussed later) as shown in Figure 5.37. PL_H is fabricated from ASTM A572 grade 50 steel. A plan view of PL_H is shown in Figure 5.30 (f). Figure 5.38 shows a schematic of the top of the displaced loading rod

assembly. The position of the half-round, neoprene pad, and PL_H correspond to the displacements from the FE analysis for load step 50. The schematic shows the required minimum hole radius to prevent the main rod from bearing against PL_H. A diameter of 1.75 in should be sufficient for the extra-large hole. PL_H is 12 in wide, which is long enough to extend beyond the depth of the loading beam and provide enough length for the welds (Figure 5.37). PL_H is 6.5 in long to fit between the small rods in the parallel plane and not bear against the small rods when it rotates. PL_H is 1 in thick, which was controlled by the flexural demand.

The flexural demand on PL_H was determined by treating the plate as a simply supported beam in the longitudinal plane with two uniformly distributed loads at the locations of the half-rounds and neoprene pads as shown in Figure 5.39. In this figure, d is the depth of the loading beam (10 in), L_{HR} is the length of the half-round (3 in), $\varnothing_H$ is the diameter of the hole (1.75 in), and ω_{HR} is the distributed patch load applied by the half-rounds and neoprene pads. ω_{HR} was calculated as follows:

$$\omega_{HR} = \left(\frac{P_u}{2}\right)\left(\frac{1}{L_{HR}}\right) \qquad \textbf{(5.11)}$$

Where P_u is equal to 26.6 kip (the factored load applied by the loading rod assembly). The flexural demand was taken as the maximum moment at mid-span (see Figure 5.39), equal to 34.9 kip-in. The shear demand was taken as $P_u/2$. The bearing demand was taken as P_u. The flexural capacity was calculated with a plastic section modulus for the parallel plane cross section at section A-A in Figure 5.30 (f). The bearing capacity was calculated

using the area under the neoprene pads. The demands, capacities, DCRs, and AISC equations used to calculate the capacities are listed in Table 5.6.

PL_H is attached to the loading beam with 4 in long 1/4 in fillet welds, the minimum size weld required per AISC Table J2.4 (see Figure 5.37). The welds are on the outside of the flanges in the parallel plane. The demand on each weld is $P_u/2$ (13.3 kip; see Figure 5.39). The capacity of each weld was calculated using Equation (J2-3) and is equal to 22.3 kip. The DCR is 0.60.

5.9. Load Bearing Assemblies

The load bearing assemblies transmit the load from the loading beam to the test specimen. Full longitudinal plane cross section views of the load bearing assemblies at Section A, at Section B, and at Sections C and D are shown in Figure 5.13, Figure 5.14, and Figure 5.15, respectively. Figure 5.13 corresponds to section B-B of Figure 5.1, and Figure 5.14 and Figure 5.15 correspond to section C-C of Figure 5.1. Detailed longitudinal plane cross section views of the load bearing assemblies are given in Figure 5.9 at Section A (corresponding to Detail A in Figure 5.2), in Figure 5.10 at Section B (corresponding to Detail B in Figure 5.3), and in Figure 5.11 at Sections C and D (corresponding to Detail C in Figure 5.4 for Section C and corresponding to Detail D in Figure 5.5 for Section D). Figure 5.40 is a plan view of the west half of the test setup that shows the spacing of the load bearing assemblies, the loading rod assemblies, and the centerline of the test specimen. The load bearing assemblies at Section A are represented by an asterisk.

At each load bearing assembly (see Figure 5.6 through Figure 5.11), the load is transferred from the loading beam to one or two plates. These plates bear on a half-round. Below the half-round is a square bar and an HSS. A cap plate is between the half-round and the bar, and another cap plate is between the bar and the HSS. The HSS bears on a plate on top of the tube of the TFG (Plate G) or on top of the mid-span diaphragm (Plate K).

The load is transferred to the load bearing assembly through Plate J (PL_J). As shown in Figure 5.9, Figure 5.10, and Figure 5.11, PL_J is welded to the top of the flanges of the loading beam. Section A and Section B have one PL_J, and Section C and Section D have two PL_Js spaced 4 in apart on center. PL_J is a 2 in square bar fabricated from ASTM A572 grade 50 steel. It is cut to fit between the flanges of the loading beam. The dimensions were controlled by the flexural demands and welding requirements.

The flexural demand and shear demand on PL_J at Section A and at Section B (Figure 5.9 and Figure 5.10) controlled its design. The demands were calculated by treating PL_J as a simply supported beam with a uniformly distributed line load where PL_J bears on the half-round. The capacities were determined using AISC Section F11 and Section J4 for flexure and shear, respectively. A summary of the demands, capacities, DCRs, and AISC equations used to calculate the capacities are given in Table 5.6.

As shown in Figure 5.9, Figure 5.10, and Figure 5.11, the top and bottom edges of each end of PL_J are welded to the flanges of the loading beam. Each weld is a 1.375 in long 5/16 in fillet weld. The demand at each end of PL_J is 13.6 kip at Section A and at

Section B (the locations with the largest demand). The strength of the weld, rather than the base metal, determined the capacity of the welds. This was calculated using AISC Equation (J2-3). The capacity of the welds at each end of PL_J is 19.1 kip, which results in a DCR of 0.71.

At Section C and at Section D (Figure 5.8 and Figure 5.11), Plate I (PL_I) is between the two PL_Js and the half-round. PL_I transmits the load from the half-round to two PL_Js. PL_I is fabricated from ASTM A572 grade 50 steel, and is 2.5 in wide, 6 in long, and 0.75 in thick.

The flexural demand on PL_I was taken as the maximum moment calculated by treating PL_I as a 6 in long simply supported beam with a uniformly distributed load along the span. The shear demand was taken as half of the factored load applied at the load bearing assembly (27.2 kip). The flexural and shear capacities were determined from AISC Section F11 and Section J4, respectively. The demands, capacities, DCRs, and AISC equations used to calculate the capacities are listed in Table 5.6.

As shown in Figure 5.11, PL_I is welded to each PL_J with 1 in long 1/4 in fillet welds. Since PL_I bears against PL_J, these welds are only needed to keep the plates together. Therefore, the minimum weld size and the minimum weld length specified by AISC Section J2 are used.

PL_I at Section C and at Section D (Figure 5.11), and PL_J at Section A and at Section B (Figure 5.6 and Figure 5.7), bear on a half-round designed to enable the test specimen to respond independently from the loading fixture. The 6 in long half-rounds

are fabricated from 4 in diameter ASTM A193 grade B7 round bar with a nominal yield stress of 95 ksi and a nominal ultimate tensile stress of 115 ksi. At Section A and at Section B (Figure 5.9 and Figure 5.10), the half-round longitudinal axis is in the longitudinal plane because θ_{rel} is larger than the rotation about the parallel axis (in the longitudinal plane) of the test specimen (see Section 4.3.3). At Section C and at Section D (Figure 5.8), the half-round longitudinal axis is in the parallel plane because the rotation of the test specimen in the longitudinal plane is larger than θ_{rel}. The analysis for this half-round was the same as the analysis for the half-rounds at the loading rod assemblies explained in Section 5.8.

The half-round in the load bearing assembly bears on a cap plate (Figure 5.6, Figure 5.7, and Figure 5.11). A second cap plate is located under the 1 in square bar (between the two cap plates). The cap plates are designed to distribute the load to the bar and the HSS. The cap plates are fabricated from ASTM A572 grade 50 steel. They are 7 in wide and 7 in long to extend beyond the 6 in width of the HSS walls. They are 0.75 in thick, which was controlled by flexure in the bottom cap plate.

The flexural demand in the bottom cap plate (Figure 5.9) was taken as the maximum bending stress, σ_{max}, at the center of the plate. The bottom cap plate was analyzed as a 6 in by 6 in rectangular plate (equal to the width and length of the HSS) with simply supported edges and a uniform patch load applied over a central rectangular area (1 in by 6 in) equal to the square bar bearing on the bottom cap plate. σ_{max} is calculated as follows (Young and Budynas, 2002):

$$\sigma_{max} = \frac{\beta W}{t^2} \quad \textbf{(5.12)}$$

Where,

β is a parameter based on the dimensions of the plate and the dimensions of the rectangular patch load. Using Section 11.14 of Young and Budynas (2002) and linear interpolation, β is equal to 0.65.

W is the total applied load on the patch, which is equal to the factored load on the load bearing assembly (27.2 kip).

t is the thickness of the plate, 0.75 in.

σ_{max} in the bottom cap plate is 31.5 ksi. The factored flexural capacity of the cap plate was calculated as the nominal yield stress of the plate, 50 ksi, multiplied by the resistance factor for flexure, ϕ_b = 0.9, from AISC Section F1. The factored flexural capacity is 45 ksi, which results in a DCR of 0.70. The demands, capacities, DCRs, and AISC equations used to calculate the capacities for flexure, shear, and bearing are given in Table 5.6.

To prevent movement of the half-round, the top cap plate is welded to the half-round along two edges as shown in Figure 5.9 at Section A, in Figure 5.10 at Section B, and in Figure 5.8 at Sections C and D. Each 1/4 in fillet weld is 2.5 in long. The bottom cap plate is welded to the south and north walls of the HSS with a 2.5 in long 1/4 in fillet weld (Figure 5.6, Figure 5.7, and Figure 5.8).

The top cap plate bears on a 1 in square bar fabricated from ASTM A572 grade 50 steel (Figure 5.8, Figure 5.10, and Figure 5.9). The bar is designed to act as a rotational kinematic release. The longitudinal axis of the bar is perpendicular to the longitudinal axis of the half-round. The bar is 6 in long.

Bearing is the only concern for the square bar. The bearing demand is 27.2 kip. The bearing capacity was calculated using AISC Equation (J7-1). The bearing area was taken as the area equal to the width of the bar multiplied by the diameter of the half-round. The bearing capacity is 270 kip. The bearing DCR is 0.10.

To stabilize the square bar and cap plates during assembly of the loading fixture, crushable foam is used on both sides of the bar between the cap plates as shown in Figure 5.9, Figure 5.10, and Figure 5.8 at Section A, at Section B, and at Sections C and D, respectively. It is assumed that the foam does not carry any of the load. The foam is expected to crush to allow rotations in the plane perpendicular to the longitudinal axis of the bar. The foam can be replaced if needed.

The bottom cap plate under the square bar bears on an HSS (Figure 5.6 through Figure 5.11). The HSS is used to fill the distance between the bottom cap plate and the bearing plate (Plate G or Plate K) that loads the test specimen. The section is an HSS6x6x1/4 fabricated from ASTM A500 grade C steel. The length of the HSS is 14.75 in at Section A and 6.25 in at Section B, at Section C, and at Section D. The lengths are designed to allow a clear distance of 1.5 in between the TFGs and the bottom flange of the loading beam at Section A (Figure 5.6), and a clear distance of 1.5 in between the

bearing plate (Plate G) on the TFG and the bottom flange of the loading beam at Section B, Section C, and Section D (Figure 5.7, Figure 5.8, Figure 5.10, and Figure 5.11).

The north HSS at Section A and the north HSS at Section B were used to check the adequacy of the HSS because they have the largest rotations at load step 50 of the FE analysis (Section 4.3). The HSS were checked for combined flexure and axial force. The axial force was taken as 27.2 kip. The flexural demand was calculated as 27.2 kip multiplied by the eccentricity, e, between the centerline of the base of the HSS and the line of action of the vertical force acting on the half-round (shown in Figure 5.23 (b) and (c) for the HSS at Section A). The eccentricity was taken as H_i multiplied by $\tan(\theta_{TFG})$, where θ_{TFG} was taken from G2 and is the rotation of the tube in the parallel plane. The eccentricity at Section A is equal to 1.89 in and the eccentricity at Section B is equal to 0.51 in.

The adequacy of the HSS was determined using AISC Section H1.1. The required axial compressive strength, P_r, is the axial force (27.2kip), and the required flexural strength, M_r, is the flexural demand. M_r is equal to P_r multiplied by the eccentricity of P_r. M_r is 51.5 kip-in at Section A and 48.6 kip-in at Section B. The available axial compressive strength, P_c, is the design axial compressive strength (i.e., the factored axial capacity). P_c was calculated using AISC Equation (J4-6) (because KL/r of the HSS is less than 25) and is 236 kip. The available flexural strength, M_c, is the design flexural strength (i.e., the factored flexural capacity). M_c was calculated using AISC Equation (F7-1) and is 504 kip-in. For both HSS, P_r divided by P_c is less than 0.2, so Equation (H1-1b) was used to calculate the DCR of each HSS. The DCR of the HSS at Section A is 0.16 and the

DCR of the HSS at Section B is 0.15. The demands, capacities, DCRs, and AISC equations used to calculate the capacities are listed in Table 5.7.

The HSS and the bottom cap plate connection design was evaluated using AISC Section K1.1 for a concentrated axial force on the end of a rectangular HSS. The applied axial force is 27.2 kip. The two limit states of wall local yielding and wall local crippling are considered. The wall local yielding capacity was determined using Equation (K1-11) and the wall local crippling capacity was determined using Equation (K1-12). The demands, capacities, DCRs, and AISC equations used to calculate the capacities are listed in Table 5.7.

The top of the HSS is welded to the bottom cap plate as previously explained. As can be seen in Figure 5.6 at Section A, Figure 5.7 at Section B, and Figure 5.8 at Sections C and D, the base of the HSS is welded to a bearing plate with 2.5 in long 1/4 in fillet welds.

The bearing plates under the HSS are Plate G (PL_G) on top of the TFG tube at Section B, at Section C, and at Section D (Figure 5.7, Figure 5.8, Figure 5.10 and Figure 5.11), and Plate K (PL_K) on the top of the mid-span diaphragm at Section A (Figure 5.6 and Figure 5.9). Both plates are fabricated from ASTM A572 grade 50 steel.

PL_G is 12 in wide, 12 in long, and 1 in thick. The width was chosen to achieve the patch loading described in Section 4.2.3. The length was chosen to match the horizontal width of the tube. The thickness was selected to be stiff enough to distribute the load to

the TFG. PL_G is not attached to the tube of the TFG to avoid affecting the capacity of the tube.

PL_K is 8 in wide, 7 in long, and 0.75 in thick. As shown in Figure 5.9, the width extends beyond the edges of the flange of the mid-span diaphragm for welding. As shown in Figure 5.6, the length is short enough to avoid contact with the stiffener of the TFG, while the centerline of the load bearing assembly is 3 in away from the edge of the diaphragm. The length is long enough to extend beyond the walls of the HSS for welding. The thickness matches the cap plates. PL_K is welded to the edges of the flange of the diaphragm in the parallel plane with 2.5 in long 1/4 in fillet welds.

Bearing of the HSS on PL_G and PL_K is the only design consideration. The analysis used the maximum compressive force on the north wall of the HSS at Section B for PL_G and at Section A for PL_K. The maximum compressive force was determined from the stress analysis explained in Section 5.5.3 (Figure 5.23). The demands, capacities, DCRs, and AISC equations used to calculate the capacities are given in Table 5.6.

The space between the bearing plates (PL_G and PL_K) and the tops of the tubes (where PL_G is located) and the mid-span diaphragm (where PL_K is located) may need to be grouted or shimmed to create good contact conditions.

5.10. Diaphragm to TFG Connection Evaluation

The total load on the test specimen produces load effects in the connections between the diaphragms and the TFGs. The load effects are caused by the interaction

between the diaphragms and the TFGs. At Section A, there are additional load effects in the connections because the loads are applied to the diaphragm.

The loading fixture is designed for the maximum load of the test specimen. Initially, however, the connection between the diaphragm and the TFG was not designed for the loads applied to the diaphragm. The connection was designed for the scaled load effects from the full-scale two-TFG bridge under Strength I limit state loads (AASHTO, 2005) (the scaling process is explained in Section 3.3). Therefore, in the present study, the connection was evaluated for the maximum applied load. The connection between the diaphragm and G2 at Section A was evaluated because it has the largest load effects.

Figure 5.41 shows a fixed-ended beam model for the diaphragm, with two applied concentrated loads, R_{G1} and R_{G2}. This model was used to determine the additional shear, V_{add}, and additional moment, M_{add}, demand on the connection. Figure 5.41 shows the corresponding shear and moment diagrams. The length of the fixed-ended beam equals the length of the beam element used to model the diaphragm with the connection plates in the FE model (Section 4.3). R_{G1} and R_{G2} are applied at the locations of the centerline of the south load bearing assembly and the centerline of the north load bearing assembly, respectively. R_{G1} and R_{G2} were taken as the unfactored applied loads when the total applied load on the TFG test specimen equals the maximum load capacity. R_{G1} and R_{G2} have a load ratio of 1.05 (explained in Section 5.3). The shear, V_{G1} and V_{G2}, and moment, M_{G1} and M_{G2}, reactions were used to determine the additional load effects on the connections.

Figure 5.42 shows the shear and moment diagrams for the load effects at Section A from interaction between the diaphragm and the TFGs. The load effects are taken when the total applied load on the test specimen equals the maximum load capacity, and are unfactored. The shear, V_{int}, and moment, M_{int}, from the diaphragm-TFG interaction were obtained from the FE analysis at the ends of the beam elements at Section A (Point E in Figure 5.41 represents the north end of the beam elements).

The total shear, V_{total}, and the total moment, M_{total}, were used to evaluate the connection between the diaphragm and the TFG, and were calculated as follows:

$$V_{total} = V_{int} + V_{add} \quad \textbf{(5.13)}$$

$$M_{total} = M_{int} + M_{add} \quad \textbf{(5.14)}$$

As explained in Section 3.7, the connections consist of bolted connection plates used to attach the diaphragms to the TFG stiffeners. The welds between the TFG and the stiffener, and the bolted connections were evaluated.

5.10.1. Weld Design Evaluation

The existing welds (shown in Figure 5.43) were measured and used to determine the capacity of the welds between the stiffener and the TFG. The capacity based on the actual dimensions of the welds was compared to the expected demand at the time of the maximum applied load. Figure 5.43 is a schematic of the existing welds of the transverse stiffener at Section A to G2 (the connection with the largest demand). The existing welds

on both sides of the stiffener are typically 5/16 in fillet welds. However, the bottom welds contain locations where the weld is only 1/4 in.

Figure 5.44 is a schematic of the welds with the load effects, V_{total} and M_{total}, and the location of the center of gravity. Point E in Figure 5.44 is at the same location on the test specimen as Point E shown in Figure 5.41. The demand on the welds was calculated using the elastic (vector) method, for which the results are expected to be conservative. The unfactored moment, M_{weld}, acting on the weld configuration was calculated as follows:

$$M_{weld} = M_{total} + V_{total} e_w \quad \textbf{(5.15)}$$

Where e_w is the eccentricity of V_{total} from Point E to the center of gravity of the welds (see Figure 5.44). In all of the loading fixture design calculations, the load factor for the applied load (FS) is 1.3. The factored shear, V_u, therefore, was calculated as V_{total} multiplied by 1.3. The factored moment, M_{uweld}, equals M_{weld} multiplied by 1.3. M_{uweld} and V_u were divided by two and then used to find the resultant demand, R_u, on the welds on one side of the stiffener. R_u is largest at Point A in Figure 5.44, but the demand at Point B, at Point C, and at Point D were also evaluated. R_u at Point A is 8.76 kip/in; the other R_u values are given in Table 5.8.

The capacity of the configuration of the welds was calculated with AASHTO Equation (6.13.3.2.4b-1) for fillet welds in shear (AASHTO, 2005). The resistance factor,

ϕ_{e2}, equals 0.80 and the strength of the weld metal, F_{exx}, was taken as 70 ksi. The design capacity, R_r, of each existing weld configuration is 7.42 kip/in.

The DCR for Point A of the welds is 1.18, which indicates that the welds may be overloaded at Point A when the maximum applied load is reached. The DCRs for the other points are given in Table 5.8: Point B also has a DCR greater than 1.0, but Point C and Point D have DCRs less than 1.0.

The DCRs for these welds were accepted. Although the welds may start to yield at Point A and at Point B under the maximum applied load multiplied by 1.3, the other parts of the welds are able to carry additional load. These parts would also have to yield before the entire weld configuration fails.

In addition, the method for calculating the additional load effects on the welds are conservative. The analysis treated the diaphragms as a fixed-ended beam. If yielding occurs at the ends, the moment diagram of Figure 5.41 would change and the mid-span moment would increase, and the end moment would be limited by the weld yield moment.

The DCRs for the welds are computed with a 1.3 FS. To get another estimate of the possibility of overloading the welds as the test specimen reaches the maximum load capacity, the "actual" FS values were computed by dividing the factored capacity by the unfactored load effects. For Point A, the actual FS is 1.10, and for Point B, the actual FS is 1.14, which indicates that the welds should not yield when the applied load reaches the expected maximum load capacity of the test specimen.

5.10.2. Bolt Design Evaluation

The bolts and bolt holes of the connection between the diaphragm and the TFG were evaluated for the load effects when the applied load reaches the maximum load capacity of the test specimen. The connection plate with the bolts is shown in Figure 5.45. The bolt spacing and dimensions of the connection plate are given. The bolt group (the two rows of bolts to the right) consists of two rows of seven 0.75 in diameter ASTM A325 bolts that attach two connection plates to the TFG stiffener. The width of the connection was taken as the distance from the south edge of the stiffener to the north edge of the connection plates, which is the overlap between the connection plates and the stiffener.

Figure 5.45 shows the load effects on the right bolt group. Point E in Figure 5.45 is the same point on the test specimen as Point E in Figure 5.41 and Point E in Figure 5.44. Figure 5.46 is a schematic of the vertical and horizontal components of the demand on the bolts and bolt holes with the largest demands. An elastic (vector) analysis was used to find the demands. Bolt B1 and bolt hole BH1 have the largest demand, however, bolt B2 and bolt hole BH2 were also examined. The unfactored shear, V_{total}, and the factored shear, V_u, were the same as in the weld evaluation. The unfactored moment, M_{bolt}, acting on the bolt group was calculated as follows:

$$M_{bolt} = M_{total} - V_{total} e_b \qquad \textbf{(5.16)}$$

Where e_b is the eccentricity of V_{total} from Point E to the center of gravity of the bolt group (see Figure 5.45). The factored moment, M_{ubolt}, equals M_{bolt} multiplied by 1.3. The demands, R_u, on the bolts and bolt holes are given in Table 5.9.

The bolt capacities were evaluated for shear and slip resistance. The shear resistance of a single bolt was calculated using AASHTO Equation (6.13.2.7-2), which assumes that the threads of the bolt are included in the shear plane (2005). The slip resistance of a single bolt was calculated using AASHTO Equation (6.13.2.8-1) with a hole size factor for a standard hole, and a surface condition factor for a Class A surface. The factored capacities, R_r, of the bolts are given in Table 5.9.

The bolt hole capacity was evaluated for bearing resistance. The bearing resistance at a bolt hole was calculated using AASHTO Equation (6.13.2.9-2) because the clear end distance from the bolt hole to the edge of the material the bolt is connected to is less than two times the diameter of the bolt. The vertical and horizontal clear end distances are different, so both directions were checked. For the horizontal direction, the clear end distance is the same for the stiffener and the connection plates. Therefore, the bolt hole capacity in the horizontal direction is controlled by the 0.75 in thickness of the stiffener, which is less than twice the thickness of 0.5 in of each connection plate. For the vertical direction, the clear end distance is different for the stiffener and the connection plates because the stiffener extends beyond the edges of the connection plate. Therefore, the bolt hole capacity in the vertical direction is controlled by the connection plates. The factored capacities, R_r, of the bolt holes are given in Table 5.9.

The DCRs for the bolts and bolt holes are listed in Table 5.9. The DCRs for the slip of B1, shear of B1, and horizontal bearing at BH1 are larger than 1.0. Slip is not a major concern when the test specimen is at the maximum load. The shear of B1 and the bearing at BH1 are more critical. The DCRs for B2 and BH2 are less than 1.0 indicating that they are able to carry additional load. As the bolts and bolt holes begin to yield, the forces will be redistributed to the other bolts and bolt holes.

The yielding at the bolt holes in addition to the yielding in the bolts will cause the connection to deform, and as explained for the stiffener to TFG weld configuration, the analysis methods used for the bolt connection evaluation are conservative; deformation at the connection will redistribute the moment within the diaphragm. It was decided that the DCRs for B1 and BH1 are acceptable.

Similar to the weld analysis, the "actual" FS values were calculated for the shear resistance of the bolts and the bearing resistance of the bolt holes. The actual FS for the shear resistance of B1 is 0.90. However, the actual FS for the shear resistance of B2 is 1.31, so B2 will be able to carry additional load. The actual FS for the bearing resistance of BH1 and BH2 is 1.01 and 1.52, respectively.

5.10.3. Connection Plate and TFG Stiffener Design Evaluations

The connection plates and the stiffener between the diaphragm and the TFGs, shown in Figure 3.17, were evaluated for the load effects when the test specimen reaches the maximum applied load. The demands on the connection plates and stiffener were taken as the factored shear from the bolt design evaluation and the factored moment from

the bolt design evaluation. The demands, R_u, for the connection plate (CP) and stiffener (S) are given in Table 5.10.

The factored capacities of the connection plates and stiffener were calculated for block shear rupture, shear, and flexure. The block shear rupture capacity of the connection plates was calculated with AASHTO Equation (6.13.4-1) (2005). The block shear rupture of the stiffener was considered, but a block shear mechanism was not identified. The shear capacity of the connection plates and the stiffener was taken as the minimum of the shear yielding resistance calculated using AASHTO Equation (6.13.5.3-1), and the shear rupture resistance calculated using AASHTO Equation (6.13.5.3-2). The flexural capacity in the connection plates and the stiffener was based on the AASHTO LRFD Specification for a bolted splice plate in flexure. According to AASHTO Section 6.13.6.1.4, the gross section properties should be used to calculate the flexural stresses. The capacities, R_r, of the connection plates (CP) and stiffener (S) are listed in Table 5.10.

The DCRs for the connection plates and stiffener are given in Table 5.10. The DCR values are low, so the connection plates and the stiffener should be adequate to support the expected load capacity of the test specimen.

Table 5.1: Dimensions of plates and bars of loading fixture

Part	Width (in)	Length (in)	Thickness (in)
PL_A	8	5	1.5
PL_B	8.5	10	1
PL_C	5	5	0.75
PL_D	5	5	0.75
PL_E	8.5	10	2
PL_F	5	5	0.75
PL_G	12	12	1
PL_H	12	6.5	1
PL_I	2.5	6	0.75
PL_J	8.88	1.75	1.75
PL_K	8	7	0.75
1" Bar	1	6	1
Cap Plate	7	7	0.75
South End Tie Plate	4.5	4.5	0.25
Intermediate Tie Plate	4.5	2.75	0.25
North End Tie Plate	2	5	12
Stiffener	2.25	0.25	12

Table 5.2: Lengths of steel shapes of loading fixture

Part	Length (in)
HSS – Section A	14.75
HSS – Sections B, C, D	6.25
C12x20.7	240
W10x49	156
Loading Rod Assembly 4 in Diameter Half-Round	3
Load Bearing Assembly 4 in Diameter Half-Round	6

Table 5.3: Maximum moments for load transfer channels and loading beam

Section	Member	Nominal Maximum Moment (kip-ft)	Factored Maximum Moment (kip-ft)	Factored Maximum Moment (kip-in)
A	LTC	86.9	112.9	1355
	LB	51.8	67.4	809
B	LTC	84.6	110.0	1320
	LB	35.8	46.5	558
C	LTC	82.1	106.8	1281
	LB	35.8	46.5	558
D	LTC	70.4	91.6	1099
	LB	35.8	46.5	558

LTC = Load transfer channels of the loading fixture

LB = Loading beam of the loading fixture

Table 5.4: Ground anchor rod reactions and DCR

Section	Position	Nominal Reaction (kip)	Factored Reaction (kip)	Design Load (kip)	DCR
A	South	14.8	19.2	112.5	0.17
	North	26.1	34.0	112.5	0.30
B	South	15.0	19.5	112.5	0.17
	North	25.9	33.6	112.5	0.30
C	South	23.9	31.1	112.5	0.28
	North	17.0	22.0	112.5	0.20
D	South	19.9	25.8	112.5	0.23
	North	21.0	27.3	112.5	0.24

Table 5.5: Elastic deflection of built-up load transfer channels and loading beam at loading rod assemblies

	Built-Up Load Transfer Channels (in)				Loading Beam (in)	
	Step 35 (Maximum Load)		Step 50 (Beyond Maximum Load)		All Steps	
Section	South	North	South	North	South	North
A	0.66	0.13	0.66	0.11	0.48	0.53
B	0.64	0.15	0.63	0.10	0.26	0.31
C	0.60	0.26	0.61	0.24	0.26	0.31
D	0.47	0.43	0.48	0.42	0.26	0.31

Table 5.6: DCRs for loading fixture components

Part	Limit State	Unit	Demand	Capacity	DCR	AISC (Eq.)
PL_A	Flexure	kip-in	19.4	93.3	0.21	F11-1
	Shear	kip	17	161.8	0.11	G2-1
	Bearing	kip	34	1985	0.02	J7-1
PL_B	Flexure	kip-in	55.7	81.6	0.68	F11-1
	Shear	kip	26.6	137.8	0.19	J4-4
	Bearing	kip	26.6	36.4	0.73	J7-1
PL_C	Shear	kip	26.6	103.4	0.26	J4-4
	Bearing	kip	26.6	59.4	0.45	J7-1
PL_D	Shear	kip	26.6	90.3	0.29	J4-4
	Bearing	kip	26.6	207	0.13	J7-1
PL_E	Bearing	kip	6.65	9.1	0.73	J7-1
PL_F	Flexure	ksi	15.2	24.9	0.61	F11-1
	Shear	kip	26.6	86.4	0.31	J4-4
	Bearing	kip	26.6	59	0.45	J7-1
PL_G	Bearing	kip	10.3	94.4	0.11	J7-1
PL_H	Flexure	kip-in	34.9	53.4	0.65	F11-1
	Shear	kip	13.3	138.9	0.10	J4-4
	Bearing	kip	26.6	1620	0.02	J7-1
PL_H to LB Weld	Shear	Kip	13.3	22.3	0.60	J2-3
PL_I	Flexure	kip-in	6.8	15.8	0.43	F11-1
	Shear	kip	13.6	56.3	0.24	J4-3
	Bearing	kip	13.6	295	0.05	J7-1

LB = Loading beam of loading fixture

Table 5.6 (cont'd): DCRs for loading fixture components

Part	Limit State	Unit	Demand	Capacity	DCR	AISC (Eq.)
PL_J Sections A & B	Flexure	kip-in	40.0	90	0.44	F11-1
	Shear	kip	13.6	120	0.11	J4-3
PL_J Sections A & B Weld	Shear	kip	13.6	19.1	0.71	J2-3
PL_J Sections C & D Weld	Shear	kip	6.8	19.1	0.36	J2-3
PL_J Sections C & D	Flexure	kip-in	25.9	90	0.29	F11-1
	Shear	kip	6.8	120	0.06	J4-3
PL_K	Bearing	kip	10.6	94.4	0.11	J7-1
PL_K to HSS Weld	Shear	kip	27.2	27.8	0.98	J2-3
PL_K to Diaphragm Weld	Shear	kip	27.2	27.8	0.98	J2-3
1" Bar	Bearing	kip	27.2	270	0.10	J7-1
Cap Plate	Flexure	ksi	31.5	45.0	0.70	-
	Shear	kip	27.2	540	0.05	J4-3
	Bearing	kip	27.2	405	0.07	J7-1
Cap Plate to Half-Round Weld	Shear	kip	27.2	27.8	0.98	J2-3
Cap Plate to HSS Weld	Shear	kip	27.2	27.8	0.98	J2-3

Table 5.6 (cont'd): DCRs for loading fixture components

Part	Limit State		Unit	Demand	Capacity	DCR	AISC (Eq.)
LTC - South End & Intermediate Tie Plate	Shear		kip	7.7	33.8	0.23	G2-1
LTC - South End Tie Plate Weld	Shear		kip	7.7	36.2	0.21	J2-3
LTC - Intermediate Tie Plate Weld	Shear		kip	7.7	19.5	0.39	J2-3
LTC - North End Tie Plate	Shear		kip	7.7	720	0.01	G2-1
LTC - North End Tie Plate Bolts	Slip-Critical Connection		kip	7.7	9.4	0.82	J3-4
LTC - Bearing Stiffeners	Strength		kip	34.0	355	0.10	J4-6
	Bearing		kip	34.0	76	0.45	J7-1
LTC - Stiffener to Flange Weld	Shear		kip	17.0	22.3	0.76	J2-3
LTC - Stiffener to Web Weld	Shear		kip	13.0	19.5	0.67	J2-3
Teflon	Bearing		kip	26.6	52.5	0.51	-
Main Rod	Tension		kip	26.6	55.2	0.48	J3-1
	Flexure		kip-in	5.5	13.3	0.41	F11-1
	Tension & Flexure		-	-	-	0.85	H1-1a
Small Rod	Tension		kip	6.7	13.8	0.48	J3-1
Half-Rounds	Bearing		kip	27.2	88.6	0.31	J7-2
Concrete Block Bracing of LTC	Strength Torsional Bracing		kip-in	16.3	41.8	0.39	A-6-9
	Strength Lateral Nodal Bracing	Section A	kip	2.4	2.1	1.13	A-6-7
		Section D		2.4	1.9	0.92	

LTC = Load transfer channel of loading fixture

Table 5.7: DCRs for loading fixture steel sections

Steel Section	Limit State	Unit	Location	Demand	Capacity	DCR	AISC (Eq.)
Single Load Transfer Channel	Web Local Yielding (interior load)	kip	MR	13.3	79.3	0.17	J10-2
	Web Local Yielding (exterior load)	kip	GAR	17.0	39.7	0.43	J10-3
	Web Crippling	kip	MR & GAR	17.0	76.6	0.22	J10-4
	Web Sidesway Buckling (not restrained)	kip	GAR	17.0	4.0	4.23	J10-7
		kip	MR	13.3	4.0	3.31	
	Web Sidesway Buckling (restrained)	kip	GAR	17.0	100.5	0.17	J10-6
		kip	MR	13.3	100.5	0.13	
Built-Up Load Transfer Channels	Flexure	kip-in	MR	1355	1498	0.90	-
	Shear	kip	GAR	34	203	0.17	G2-1
Loading Beam	Flexure	kip-in	G2	809	1274	0.64	F6-1
	Shear	kip	MR	26.6	168	0.16	G2-1
HSS Section A	Wall Local Yielding	kip	G2	27.2	110.4	0.25	K1-11
	Wall Local Crippling	kip	G2	27.2	164.4	0.17	K1-12
	Compression	kip	G2	27.2	236	0.12	J4-6
	Flexure	kip-in	G2	51.5	504	0.10	F7-1
	Compression & Flexure	-	-	-	-	0.16	H1-1b
HSS Section B	Compression	kip	G2	27.2	236	0.12	J4-6
	Flexure	kip-in	G2	48.6	504	0.10	F7-1
	Compression & Flexure	-	-	-	-	0.15	H1-1b

GAR = Ground anchor rod MR = Main rod of the loading rod assembly

Table 5.8: Stiffener to G2 weld connection check

Weld Point	R_u (kip/in)	R_r (kip/in)	DCR
A	8.76	7.42	1.18
B	8.49	7.42	1.14
C	6.74	7.42	0.91
D	6.22	7.42	0.84

Table 5.9: Diaphragm to TFG bolt check

Limit State	Part	Unit	R_u	R_r	DCR
Shear	B1	kip	46.3	32.2	1.44
	B2	kip	32.0	32.2	0.99
Slip	B1	kip	46.3	18.5	2.51
	B2	kip	32.0	18.5	1.73
Horizontal Bearing	BH1	kip	45.0	35.1	1.28
	BH2	kip	30.0	35.1	0.86
Vertical Bearing	BH1	kip	11.0	39.0	0.28

B1, B2, BH1, and BH2 are shown in Figure 5.46

Table 5.10: Diaphragm to TFG connection plate and stiffener check

Limit State	Part	Unit	R_u	R_r	DCR
Block Shear Rupture	CP	kip	57.5	406.6	0.14
Shear	CP	kip	57.5	388.5	0.15
	S	kip	57.5	423.7	0.14
Flexure	CP	ksi	39.8	50.0	0.80
	S	ksi	30.2	50.0	0.60

CP = Connection plate S = Stiffener

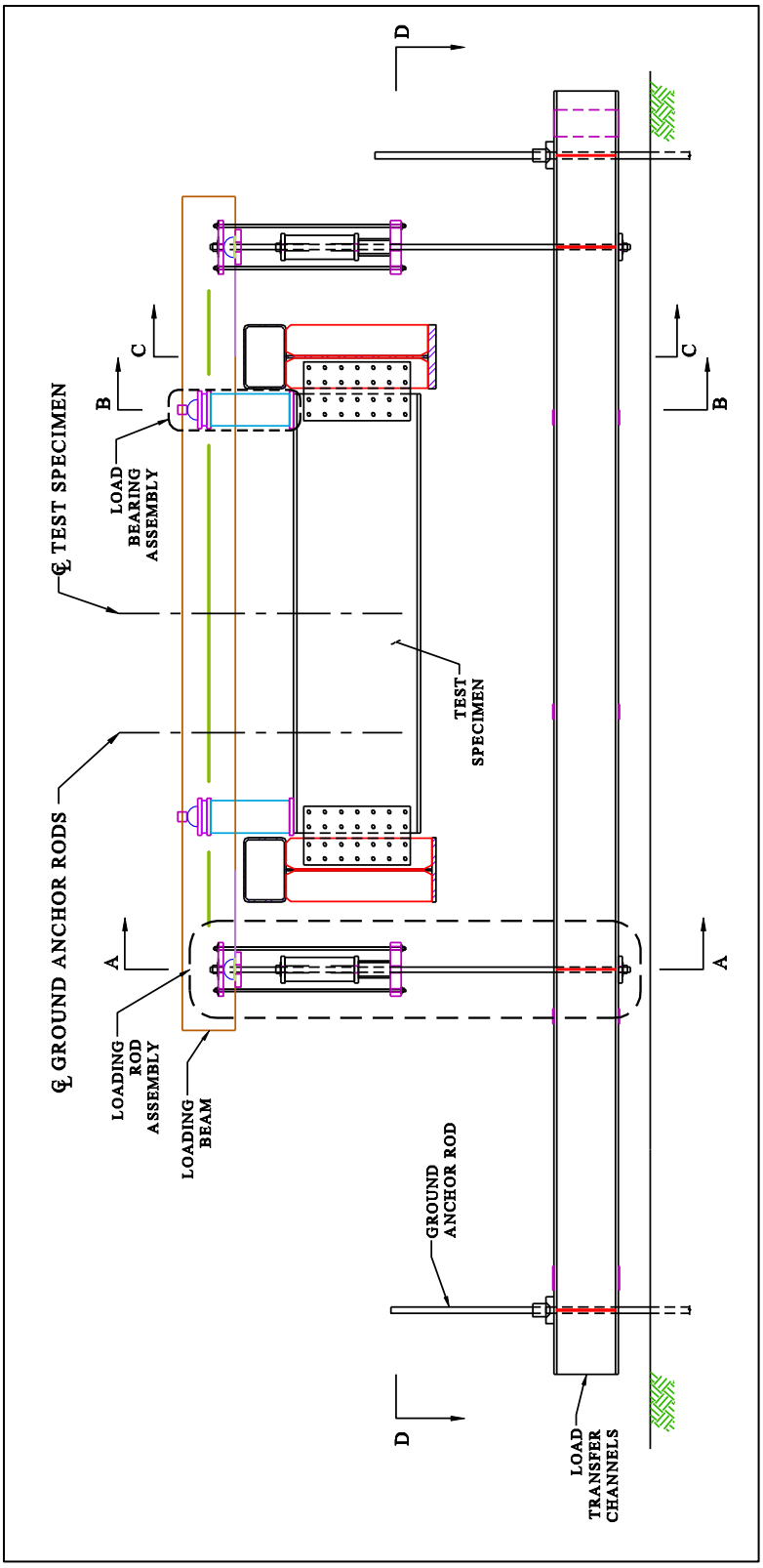

Figure 5.1: Parallel plane cross section view of test specimen and loading fixture

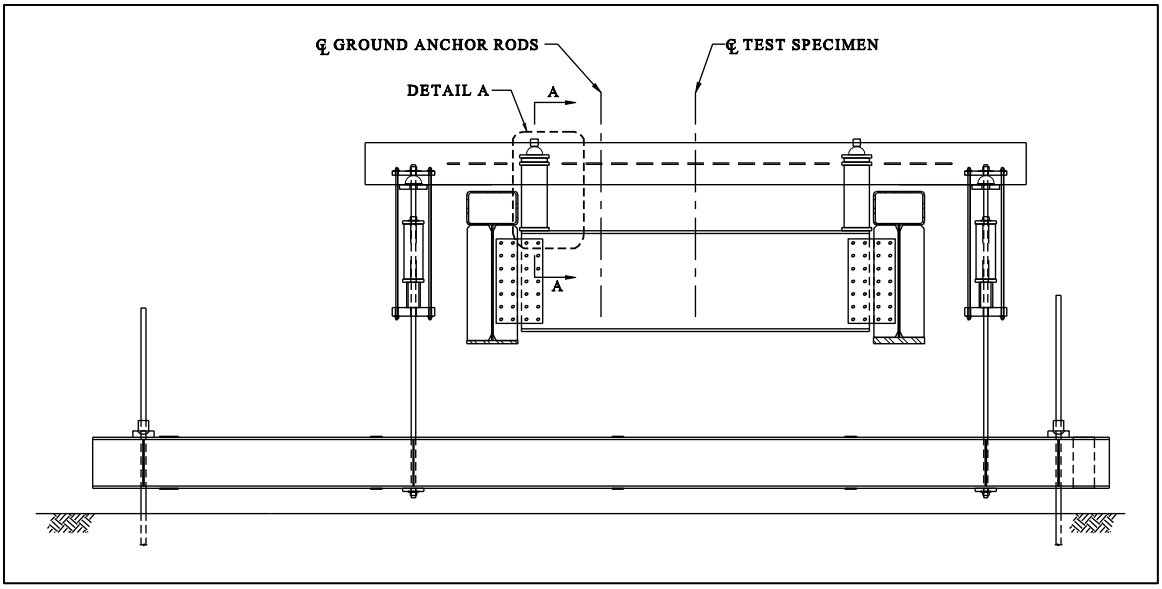

Figure 5.2: Parallel plane cross section view at Section A

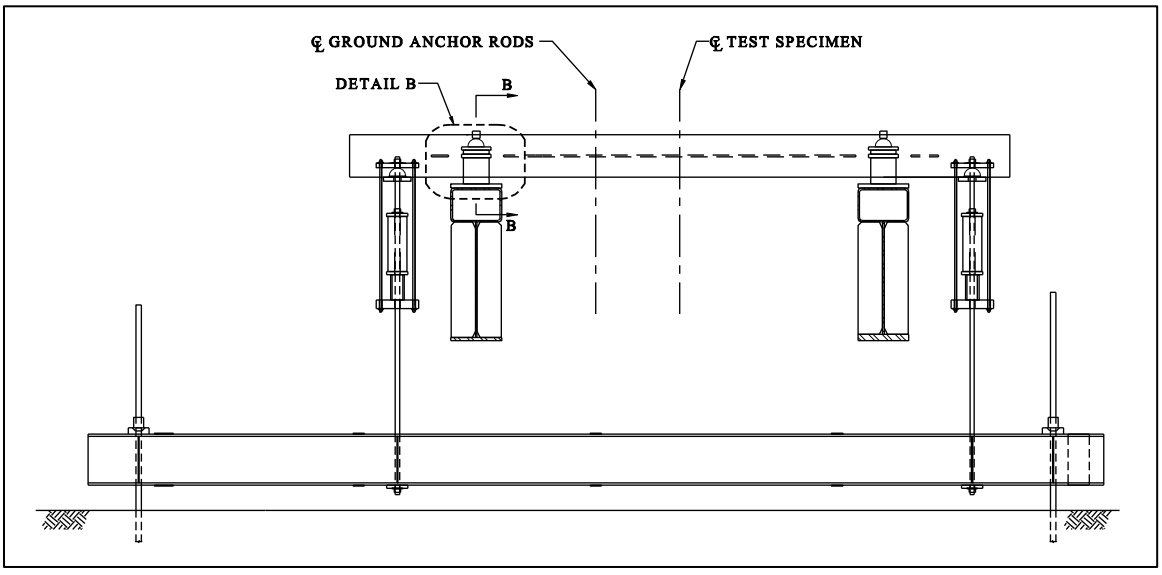

Figure 5.3: Parallel plane cross section view at Section B

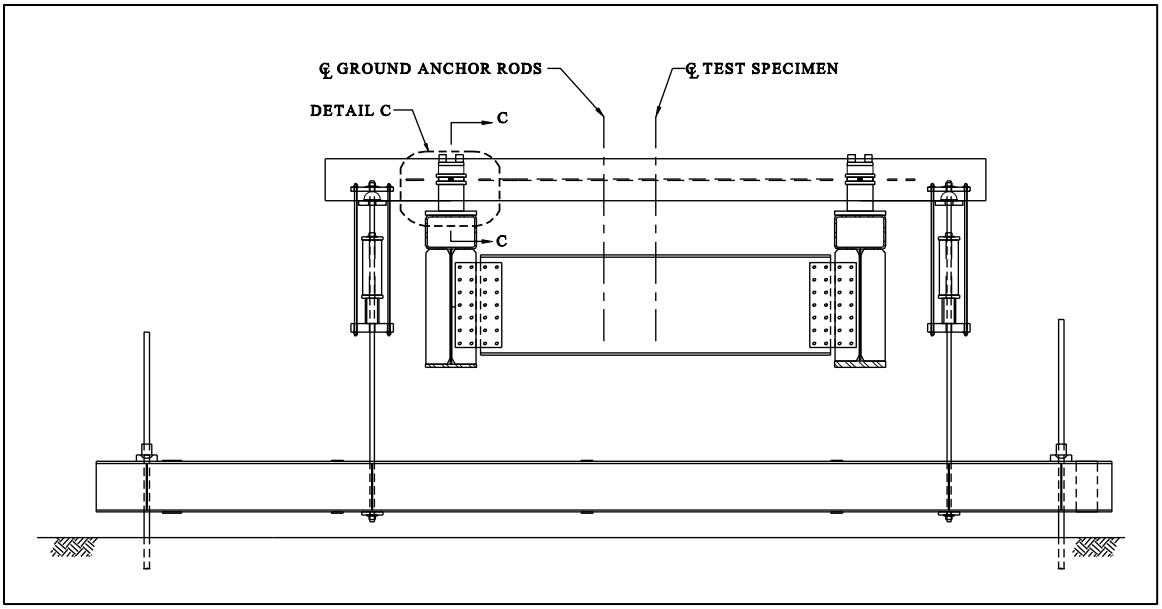

Figure 5.4: Parallel plane cross section view at Section C

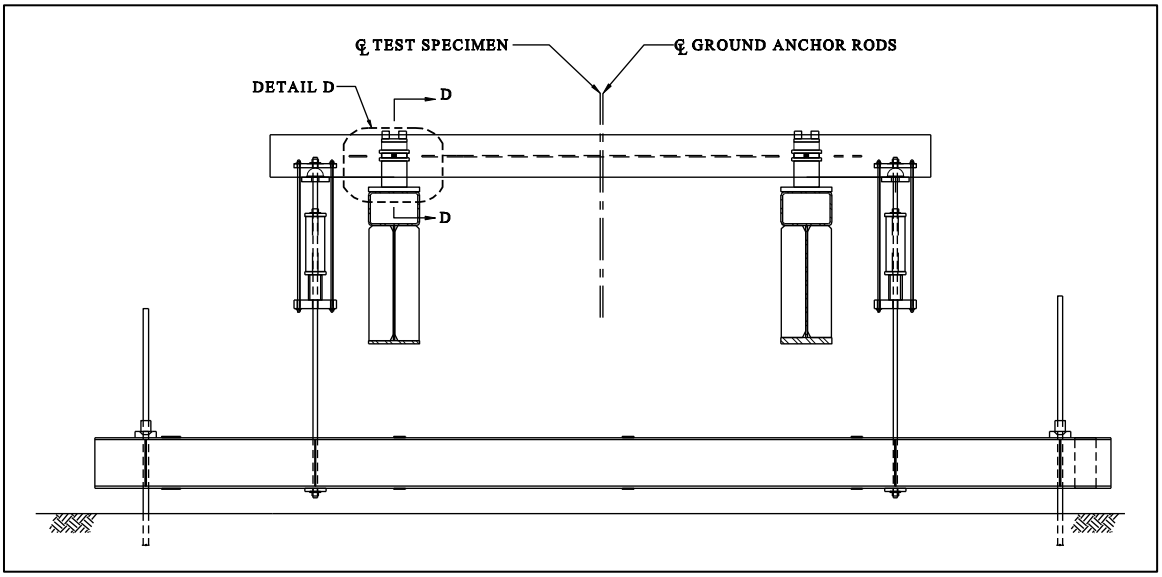

Figure 5.5: Parallel plane cross section view at Section D

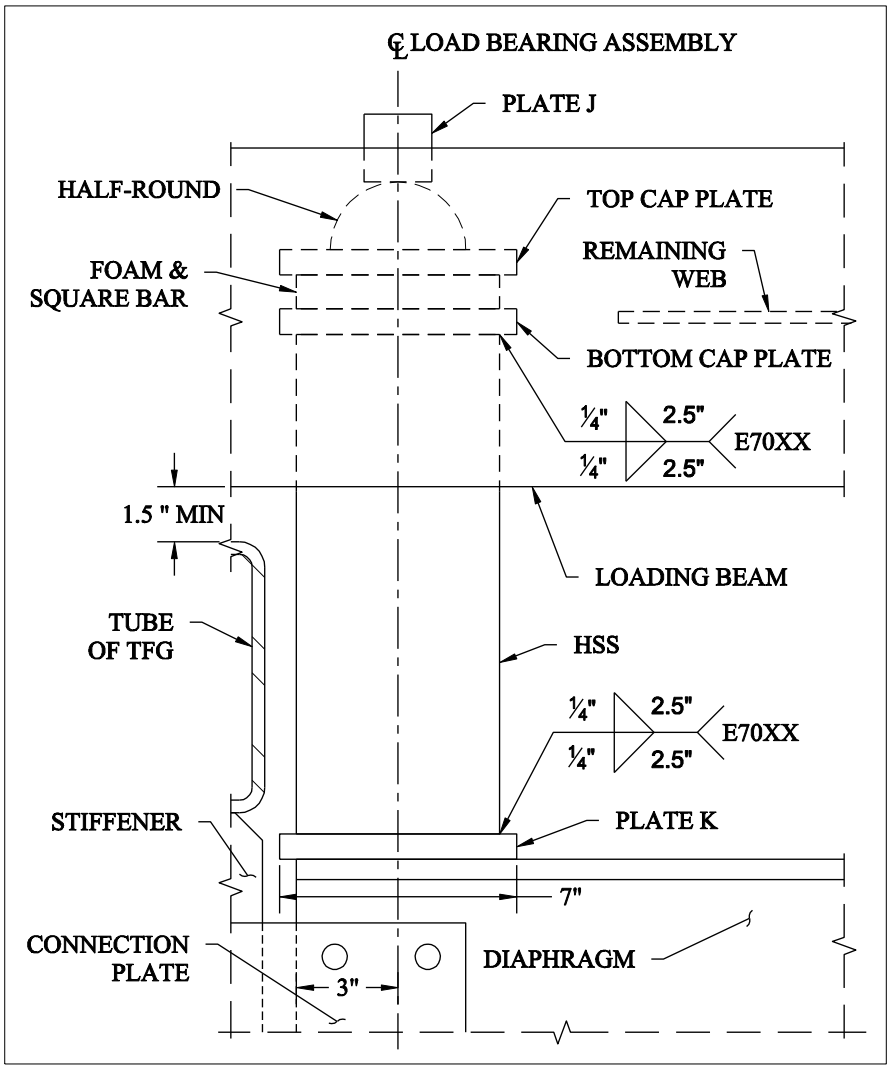

Figure 5.6: Detail A of Figure 5.2 - parallel plane cross section view of load bearing assembly at Section A

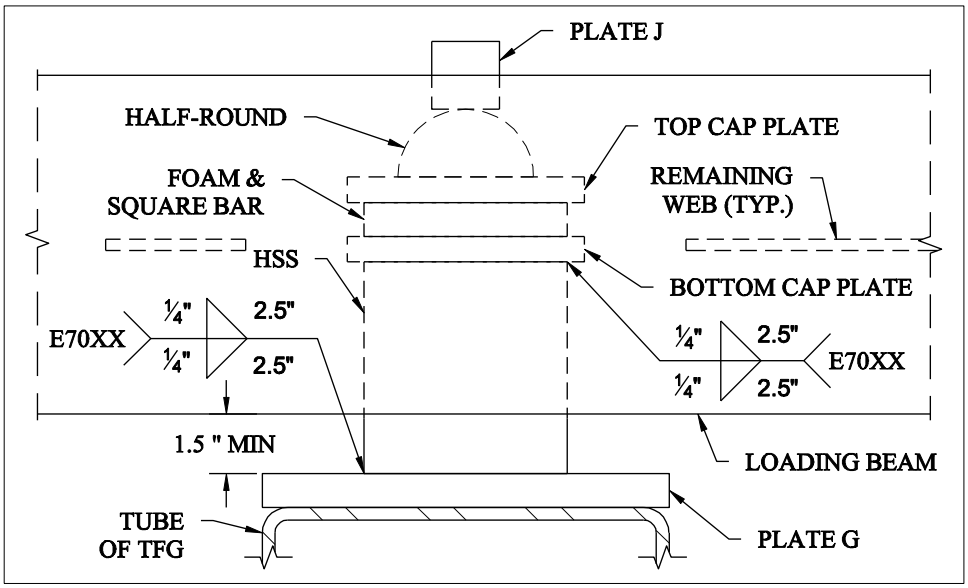

Figure 5.7: Detail B of Figure 5.3 - parallel plane cross section view of load bearing assembly at Section B

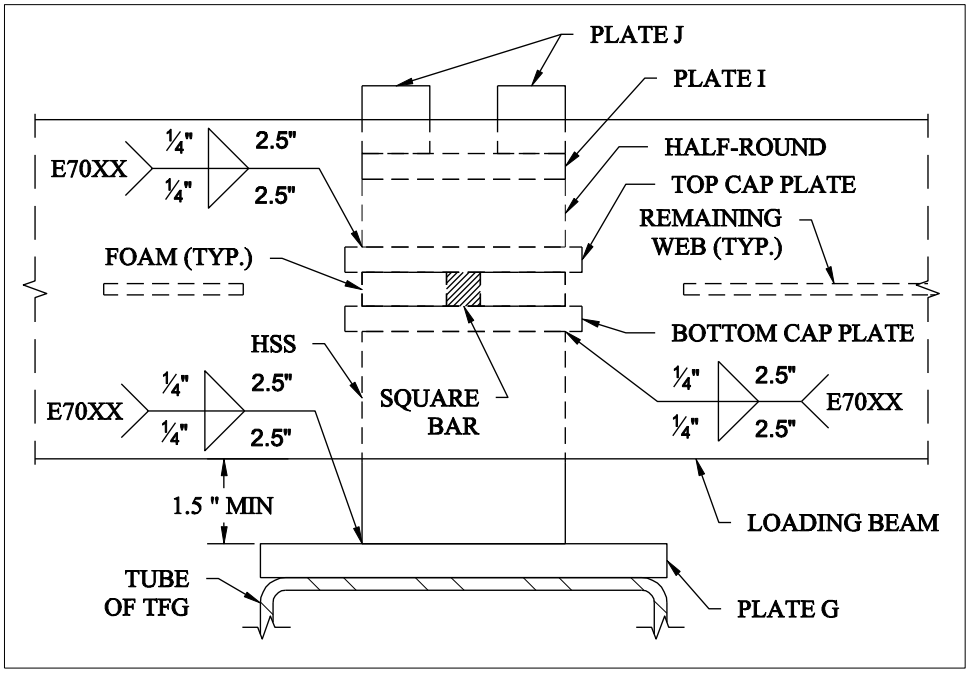

Figure 5.8: Detail C of Figure 5.4 and Detail D of Figure 5.5 - parallel plane cross section view of load bearing assembly at Section C and at Section D

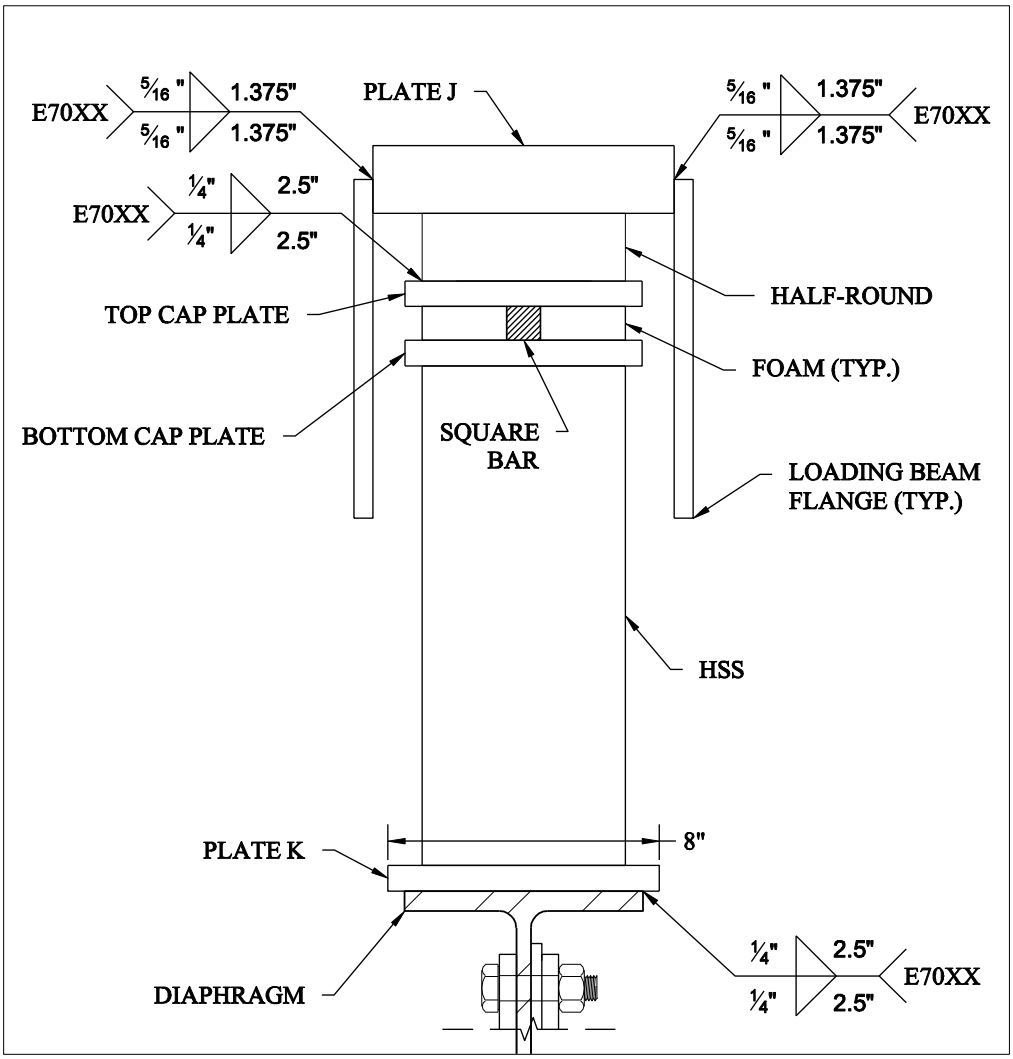

Figure 5.9: Section A-A of Figure 5.2 - longitudinal plane cross section view of load bearing assembly at Section A

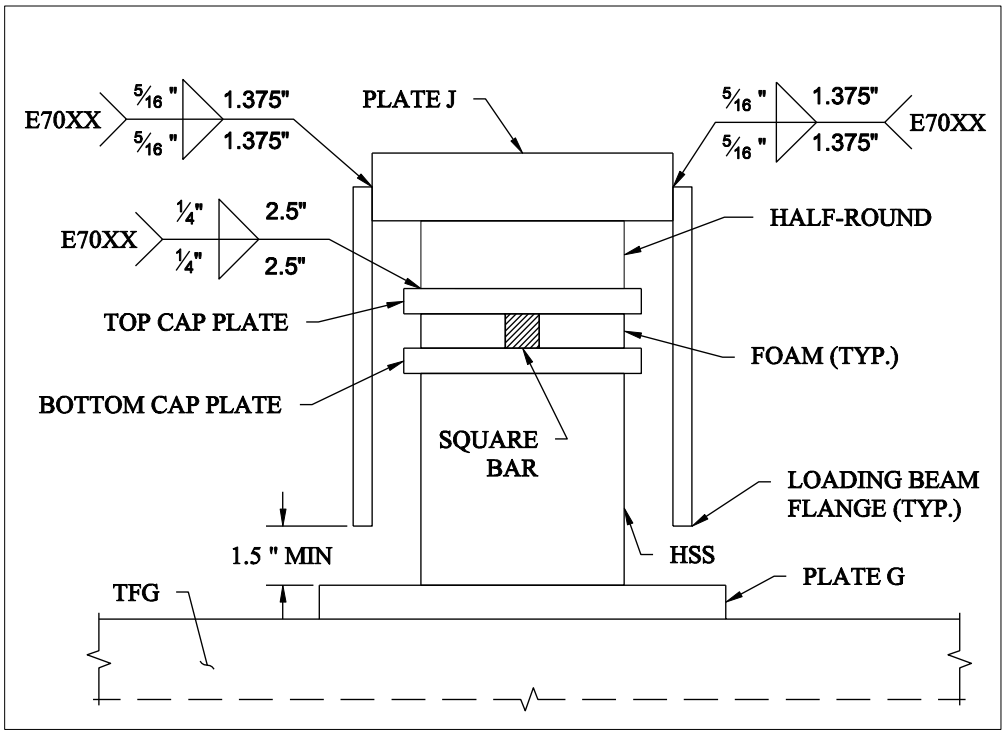

Figure 5.10: Section B-B of Figure 5.3 - longitudinal plane cross section view of load bearing assembly at Section B

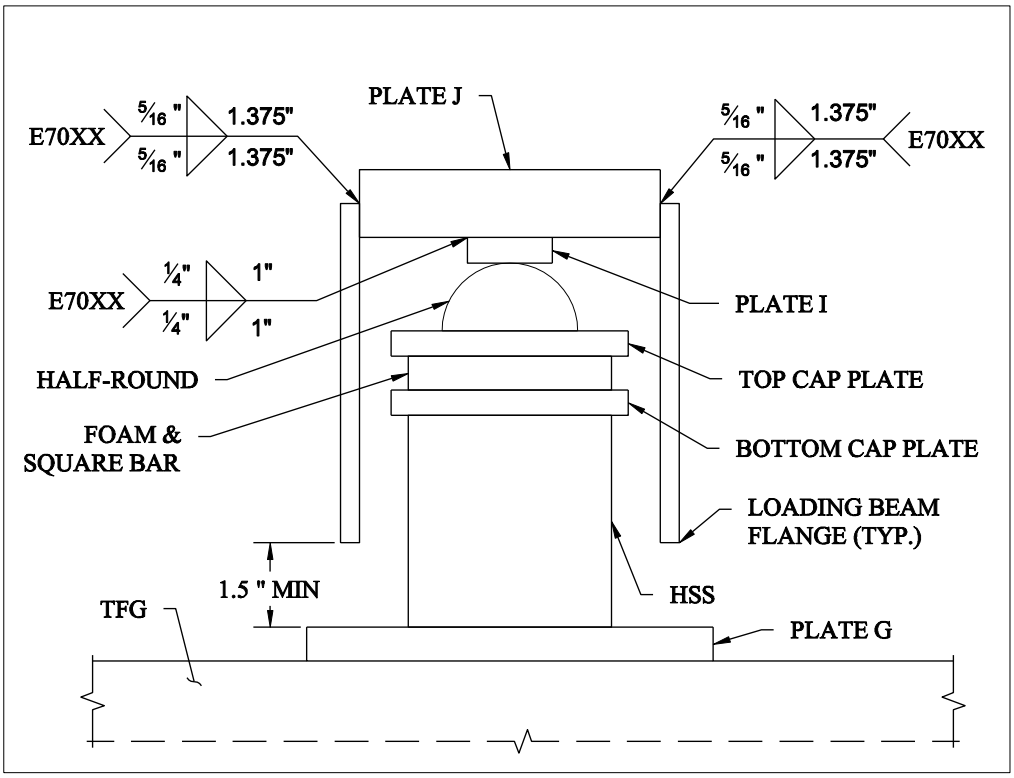

Figure 5.11: Section C-C of Figure 5.4 and section D-D of Figure 5.5 - longitudinal plane cross section view of load bearing assembly at Section C and at Section D

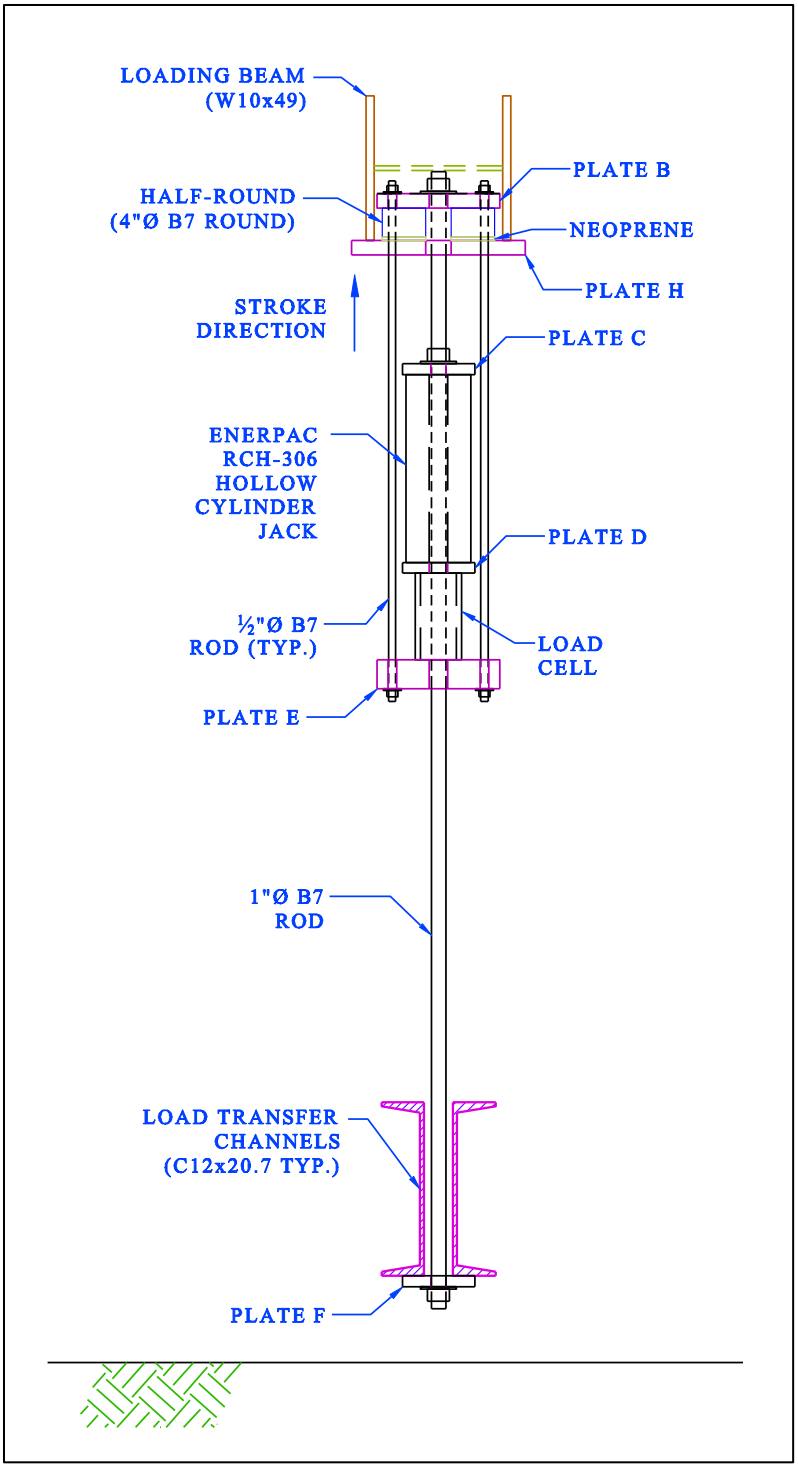

Figure 5.12: Longitudinal plane cross section view of loading rod assembly

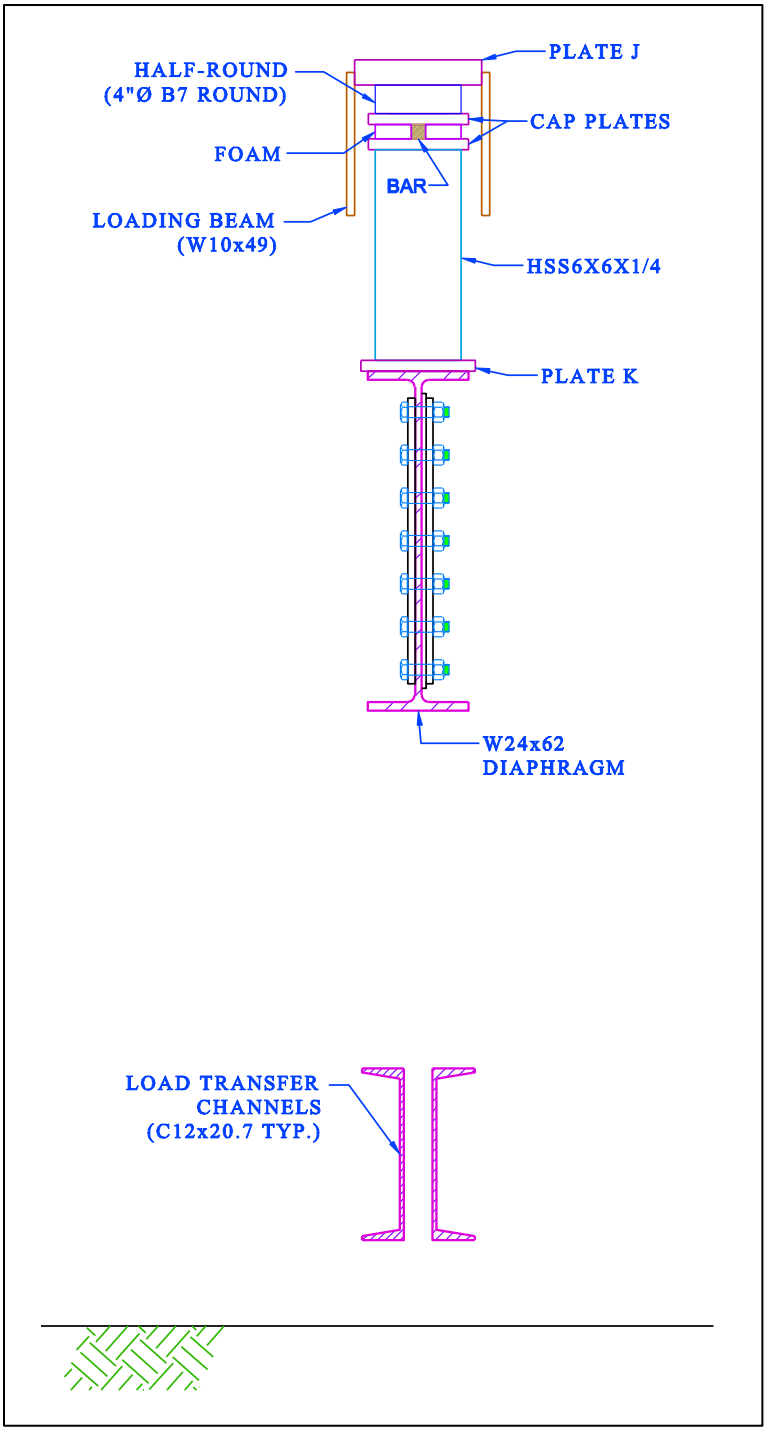

Figure 5.13: Longitudinal plane cross section view of load bearing assembly at Section A

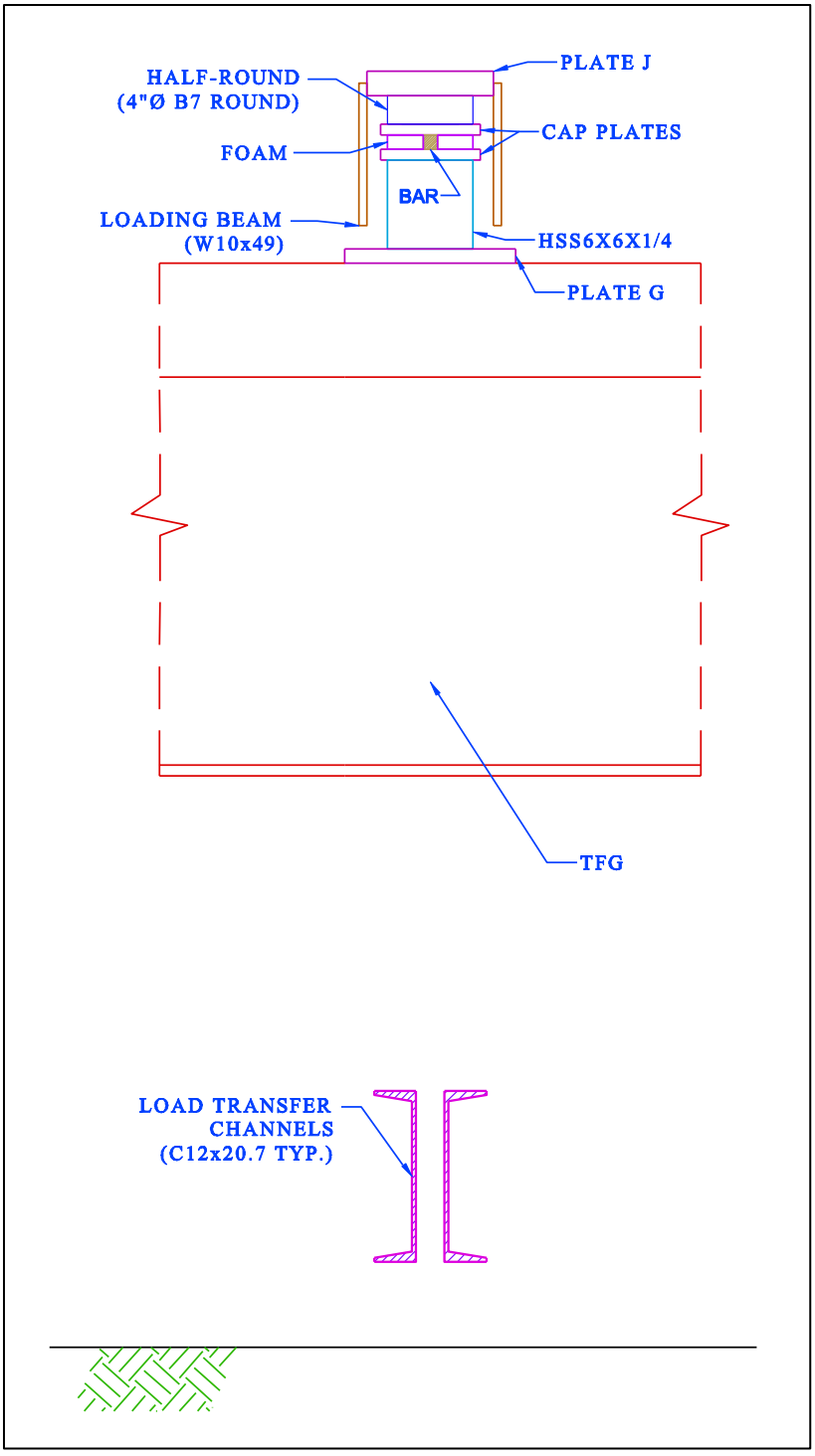

Figure 5.14: Longitudinal plane cross section view of load bearing assembly at Section B

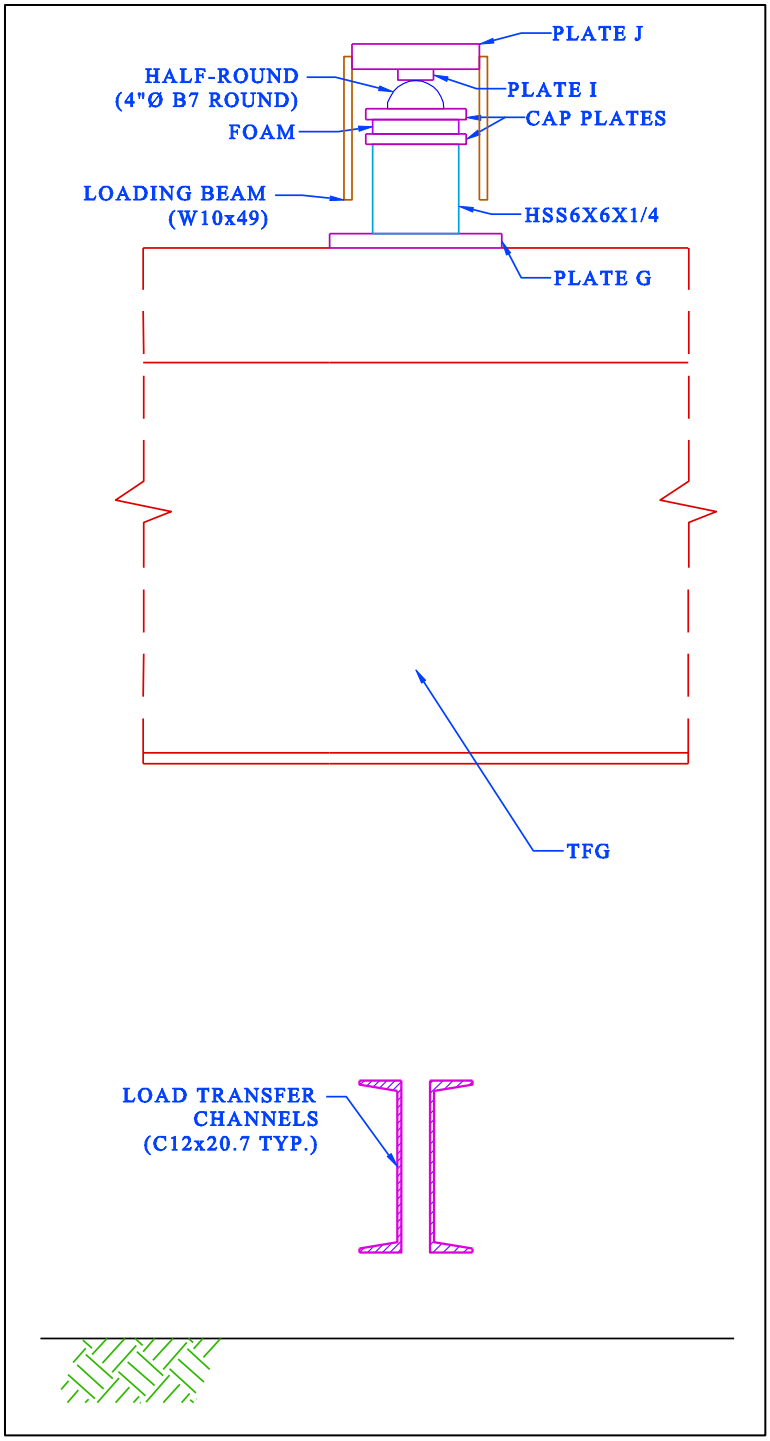

Figure 5.15: Longitudinal plane cross section view of load bearing assembly at Section C and at Section D

Figure 5.16: Enerpac RCH-326 hollow plunger cylinder (ENERPAC, 2012)

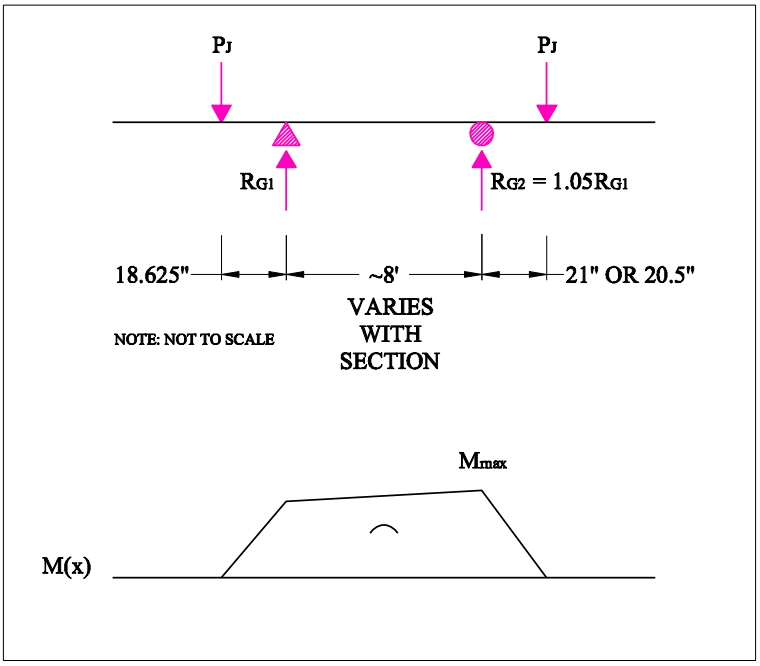

Top loading beam

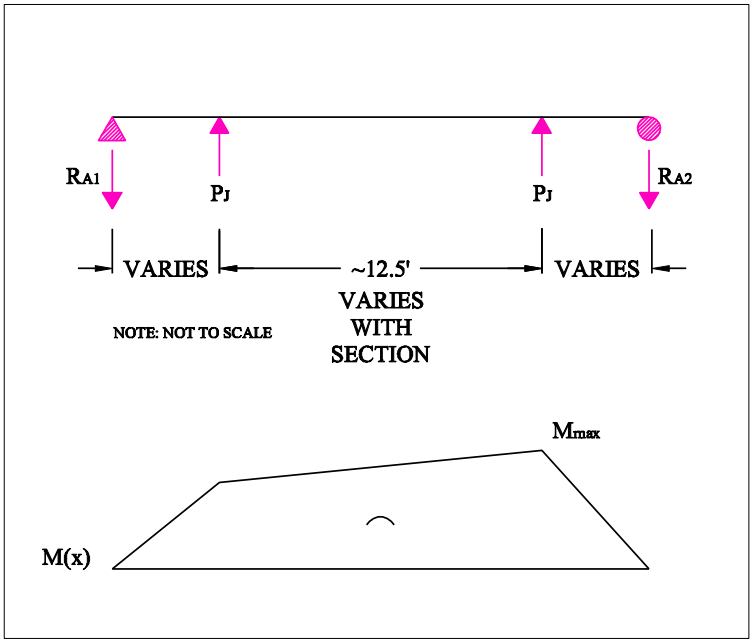

(b) Bottom load transfer channels

Figure 5.17: Simply supported beam and corresponding moment diagram for loading beam and load transfer channels

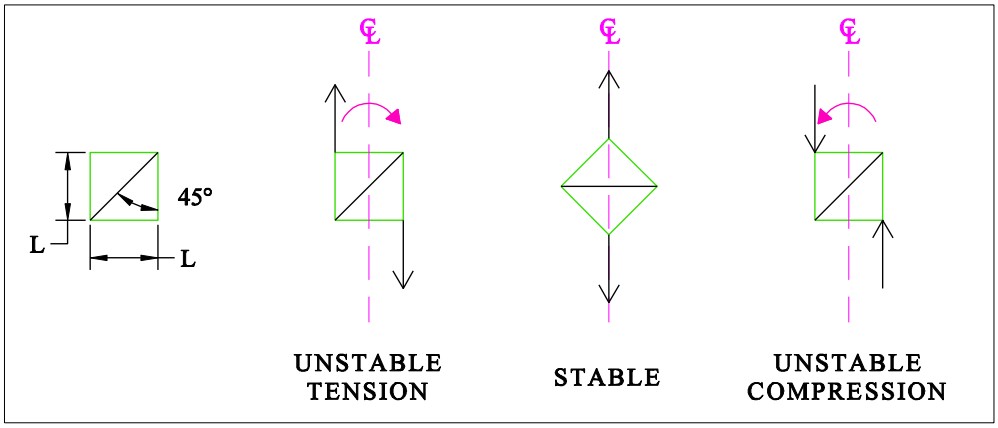

(a) Short rectangle

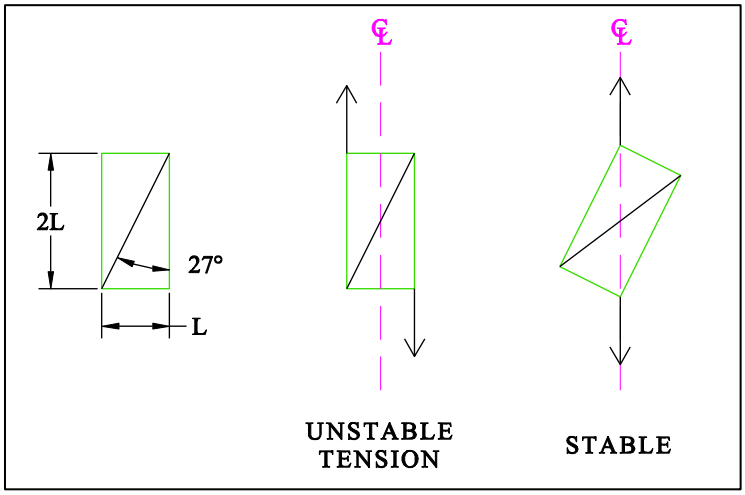

(b) Tall rectangle

Figure 5.18: Simple model for load height effects on stability

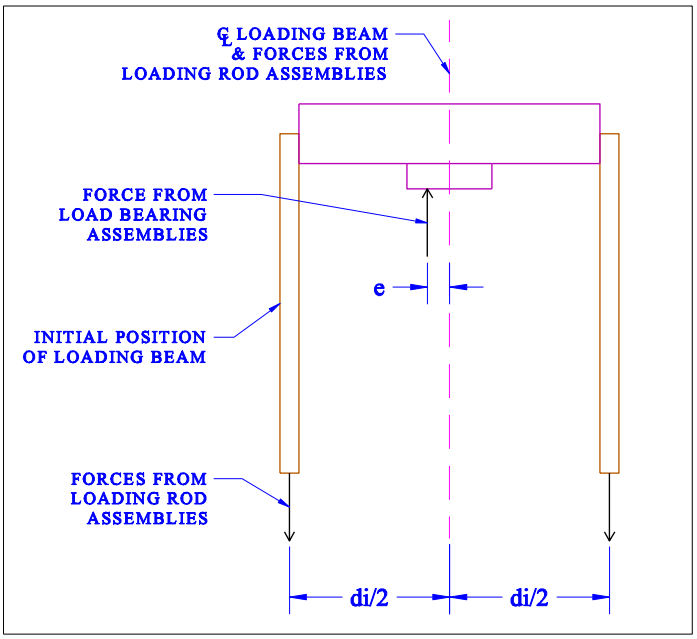

(a) Initial unstable position

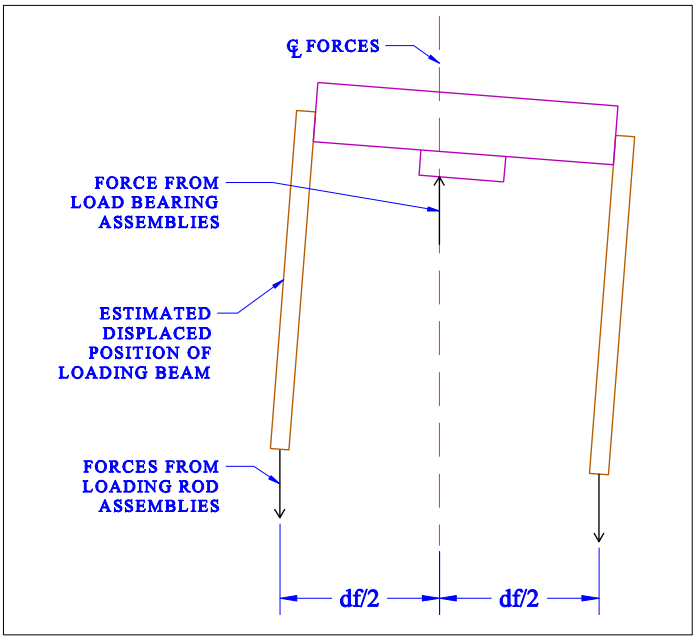

(b) Final stable position

Figure 5.19: Stability of loading beam

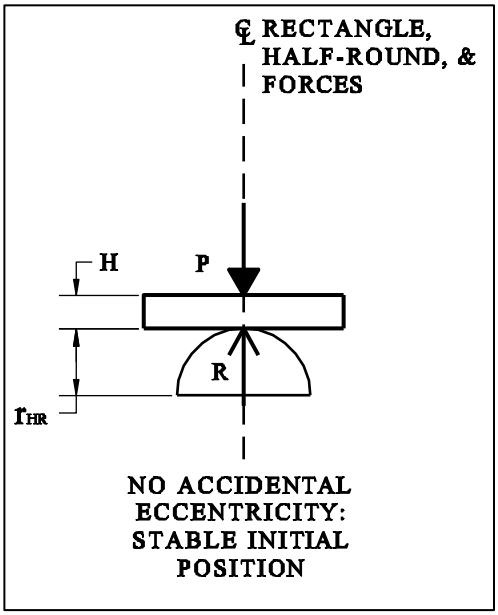

(a) Initial stable position

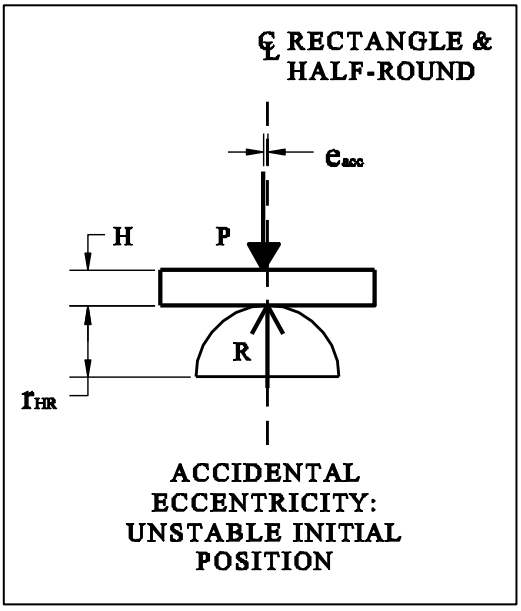

(b) Initial unstable position

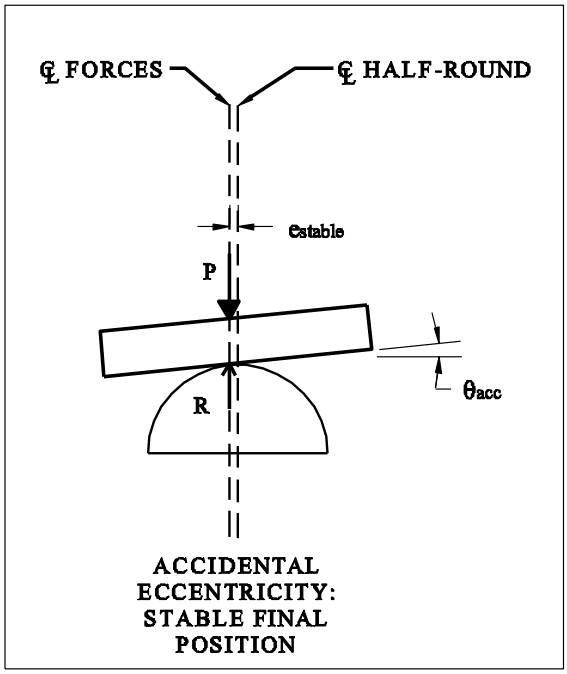

(c) Final stable position due to accidental eccentricity

Figure 5.20: Stability analysis with thin plate

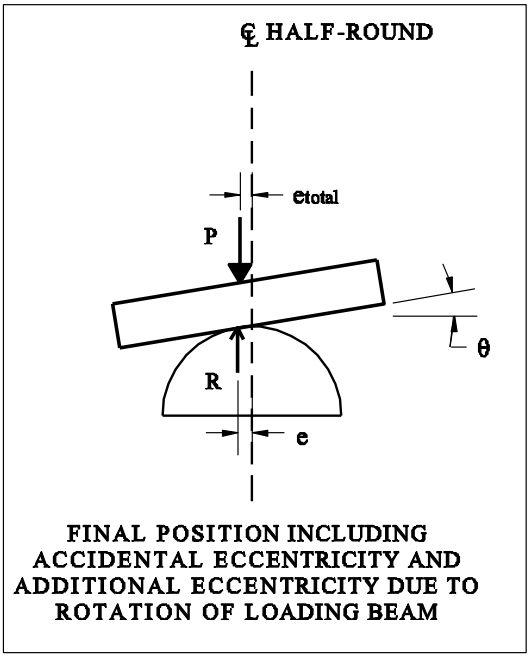

(d) Final position including accidential eccentricity and rotation during tests

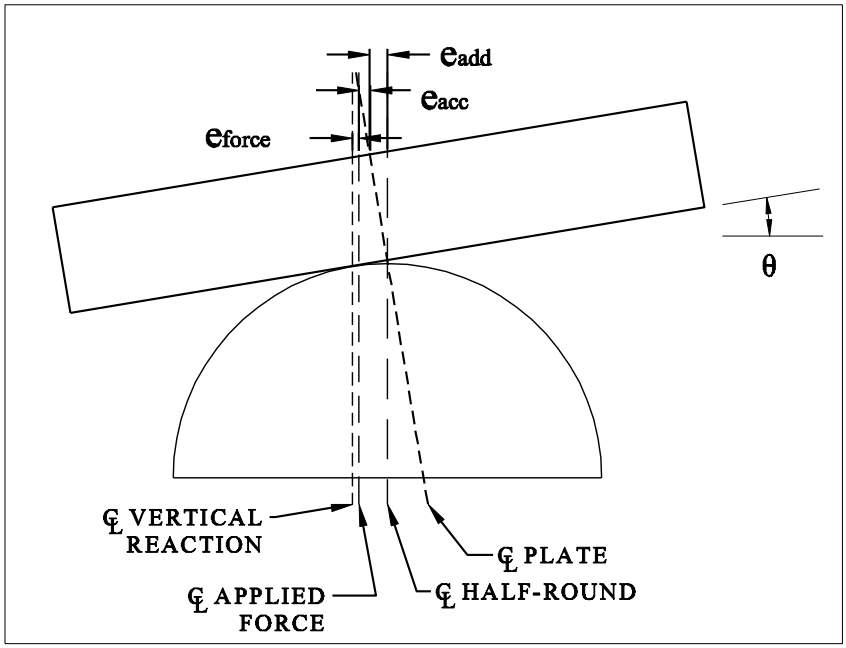

(e) Centerlines and eccentricities for final position

Figure 5.20 (cont'd): Stability analysis with thin plate

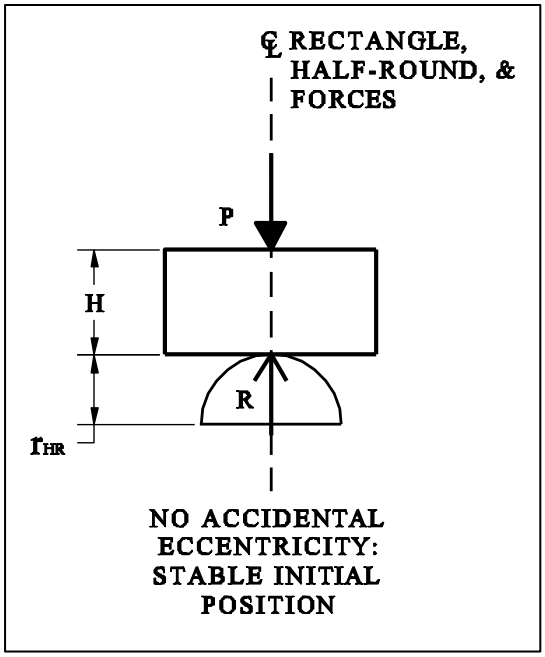

(a) Initial stable position

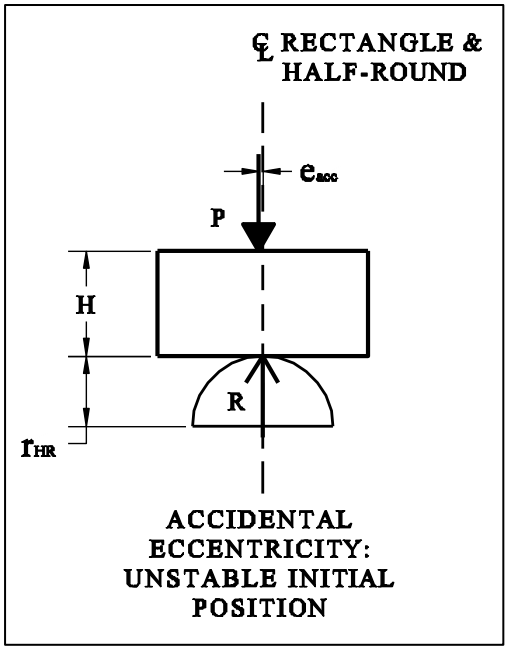

(b) Initial unstable position

N/A

(c) Final stable position due to accidental eccentricity

Figure 5.21: Stability analysis with thick plate

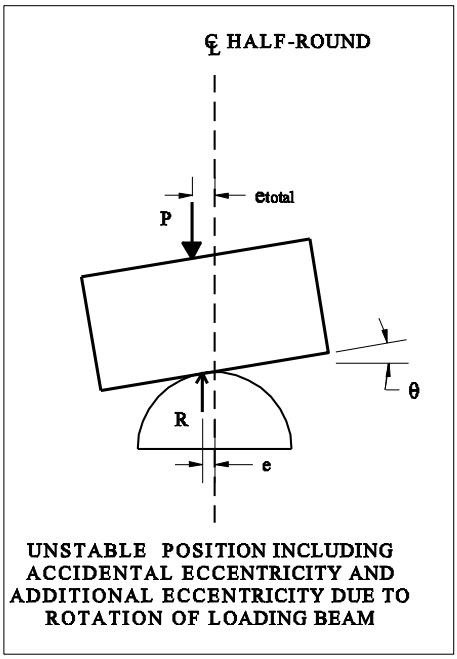

(d) Final position including accidential eccentricity and rotation during tests

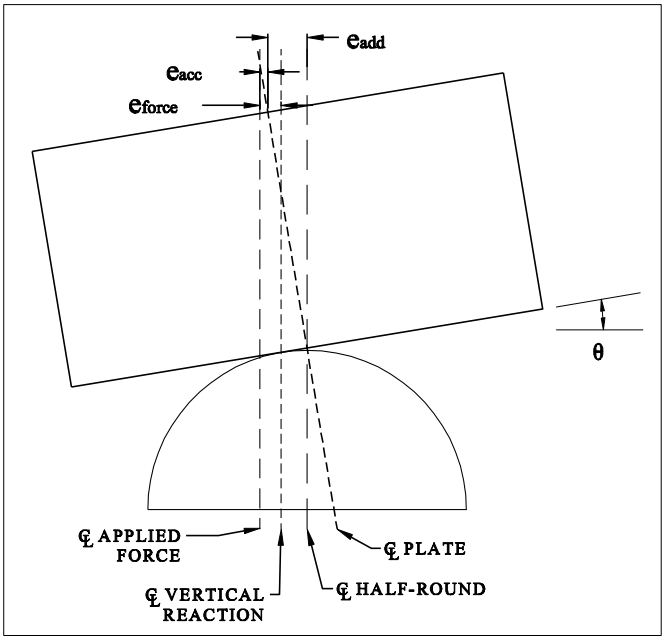

(e) Centerlines and eccentricities for final position

Figure 5.21 (cont'd): Stability analysis with thick plate

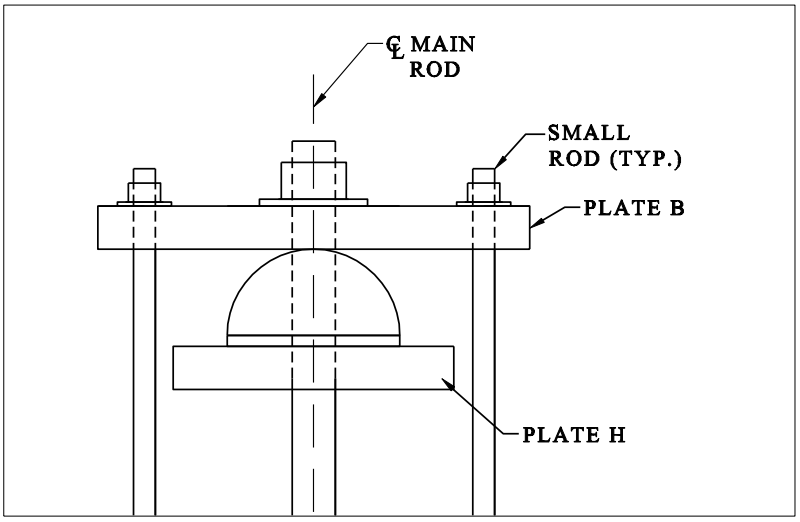

(a) Initial position

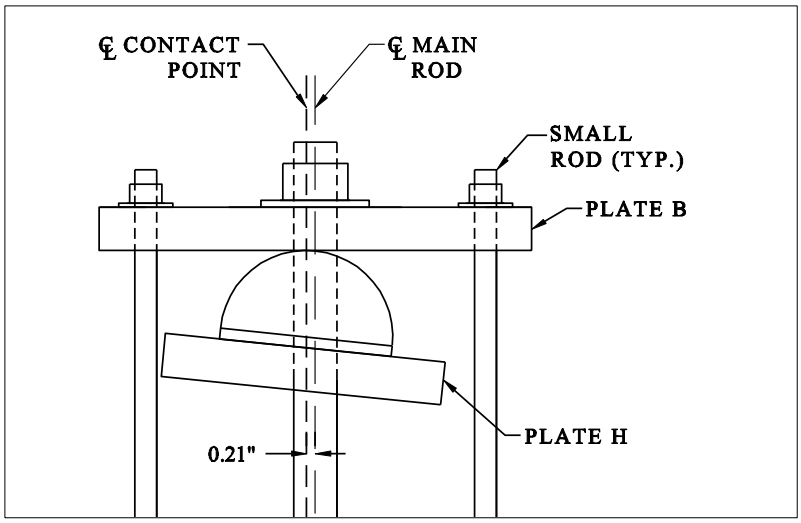

(b) Final position

Figure 5.22: Half-round rotation in parallel plane at loading rod assemblies

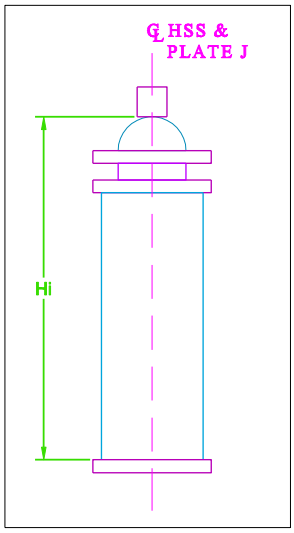

(a) Initial position

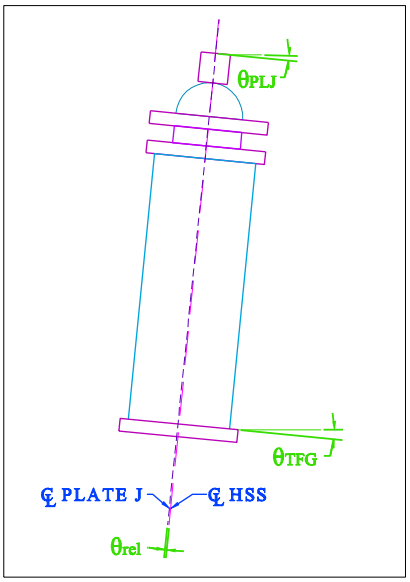

(b) Final position

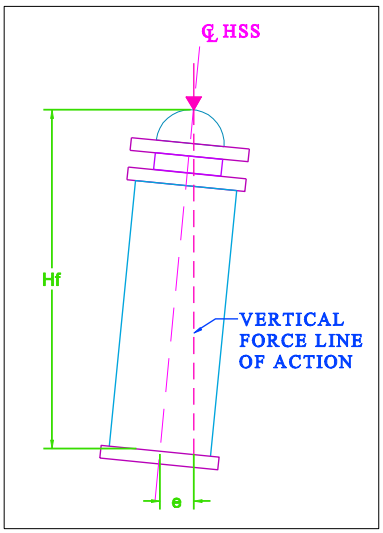

(c) Force on section

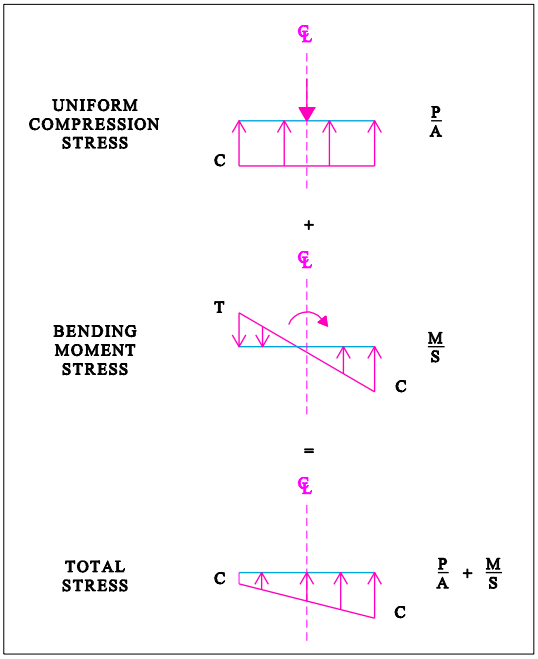

(d) Stresses on bottom of HSS

Figure 5.23: Analysis of Section A HSS stability

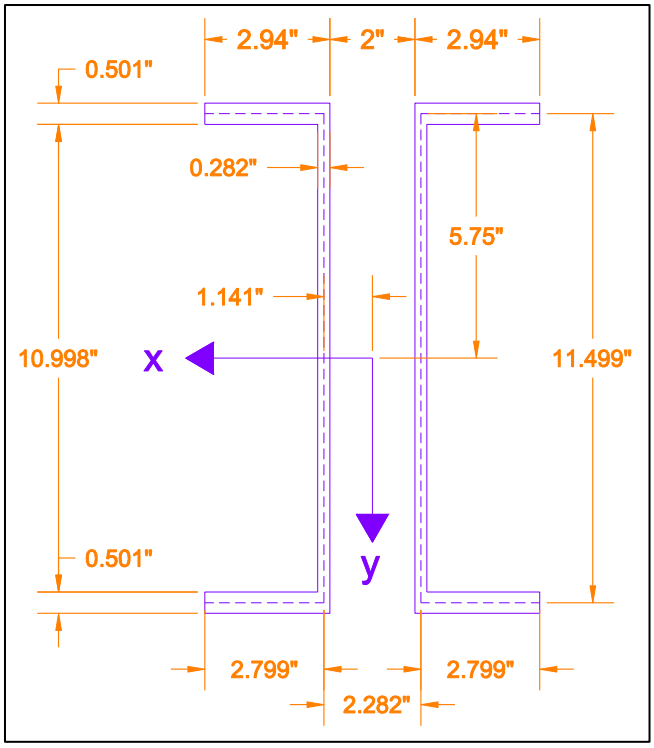

Figure 5.24: Longitudinal plane cross section view of built-up load transfer channels

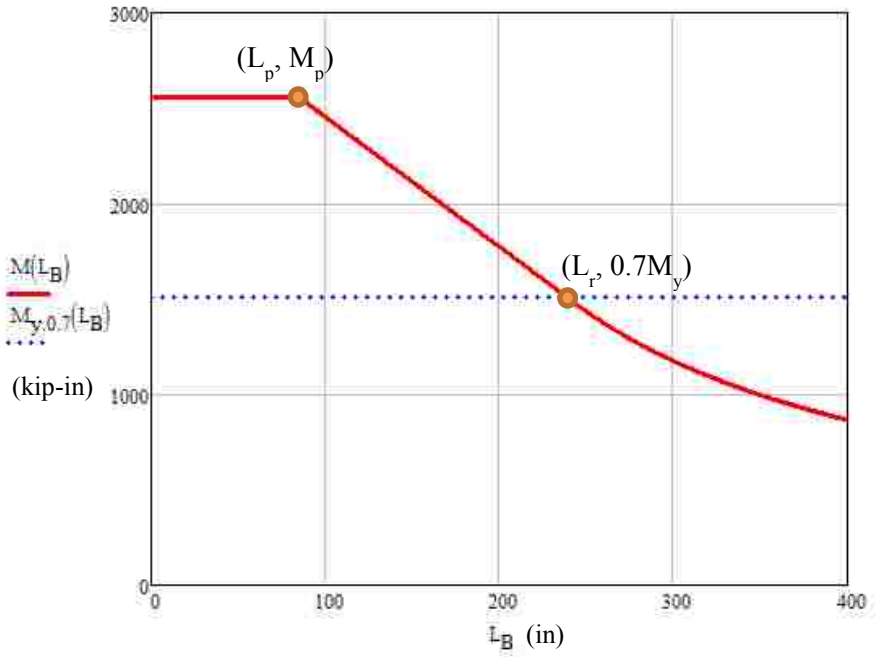

Figure 5.25: Nominal flexural strength as function of unbraced length of built-up load transfer channels

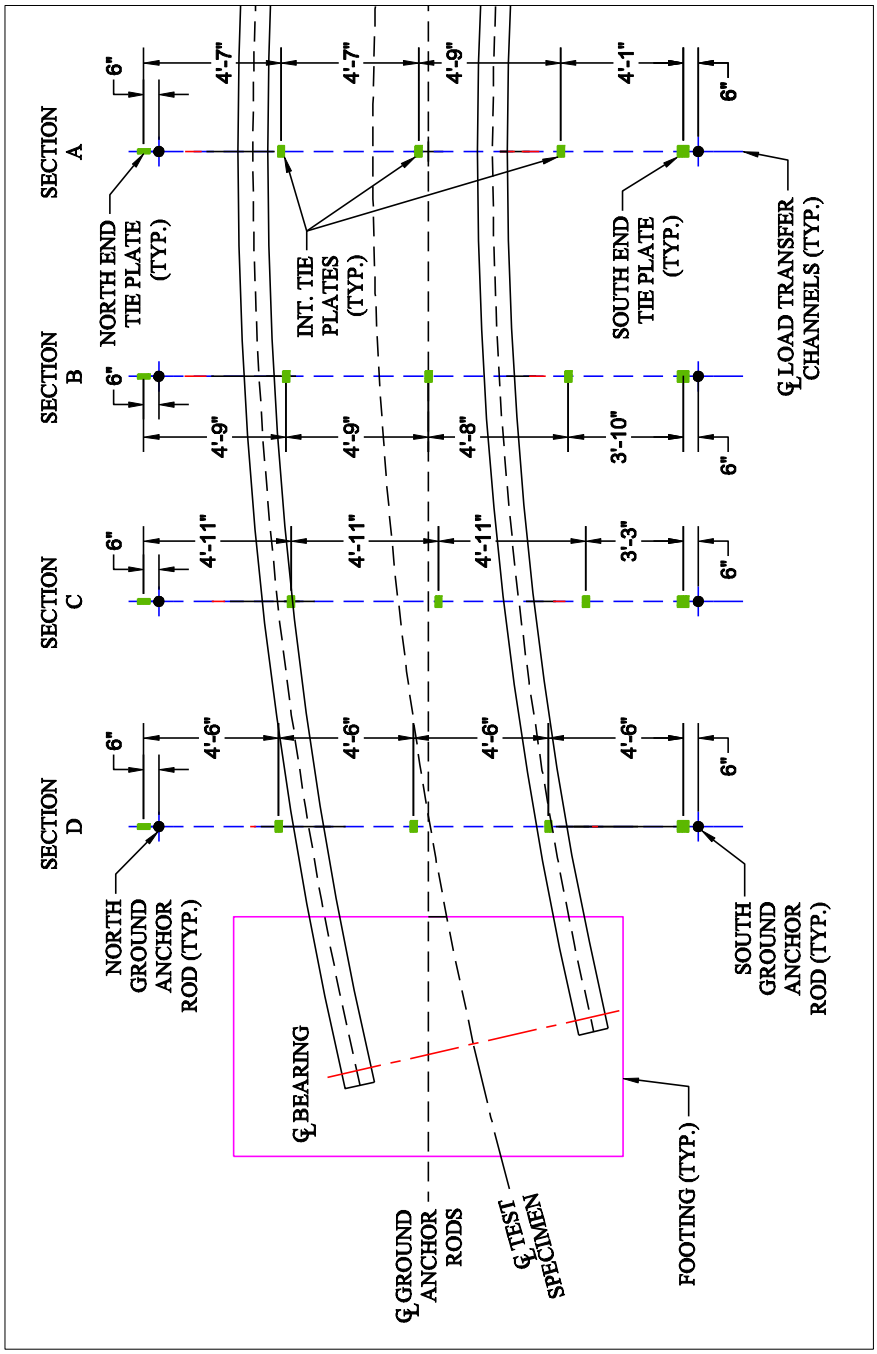

Figure 5.26: Tie plate arrangement

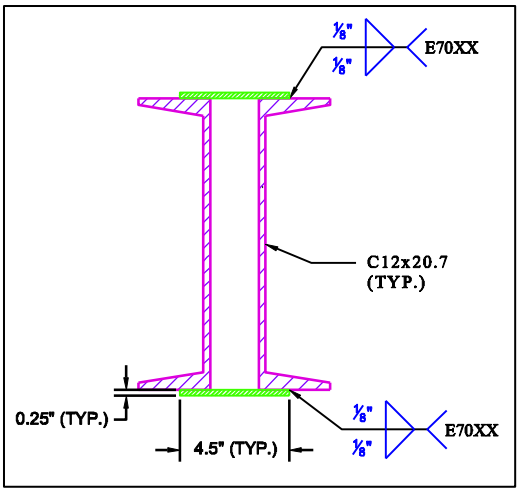

(a) Longitudinal cross section view of south end tie plate and intermediate tie plates

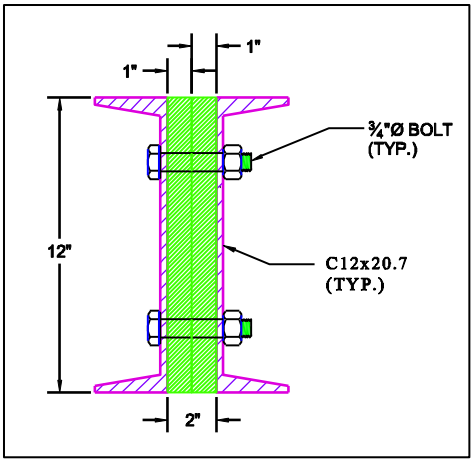

(b) Longitudinal cross section view of north end tie plate

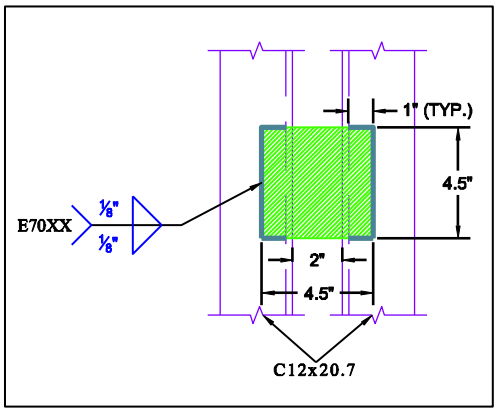

(c) Plan view of south end tie plate

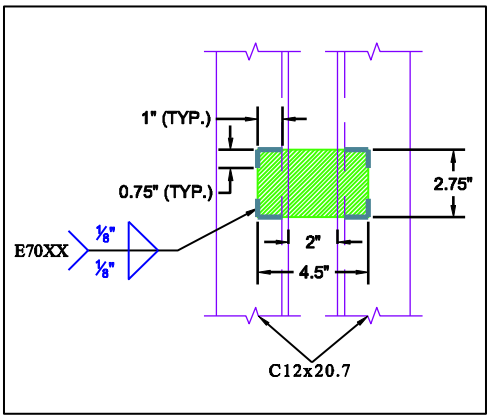

(d) Plan view of intermediate tie plates

Figure 5.27: Tie plate designs

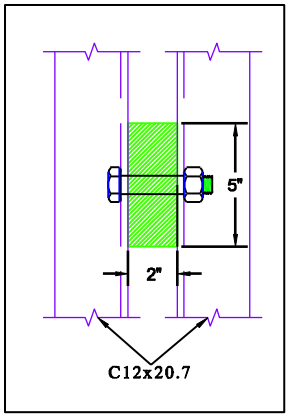

(e) Plan view of north end tie plate

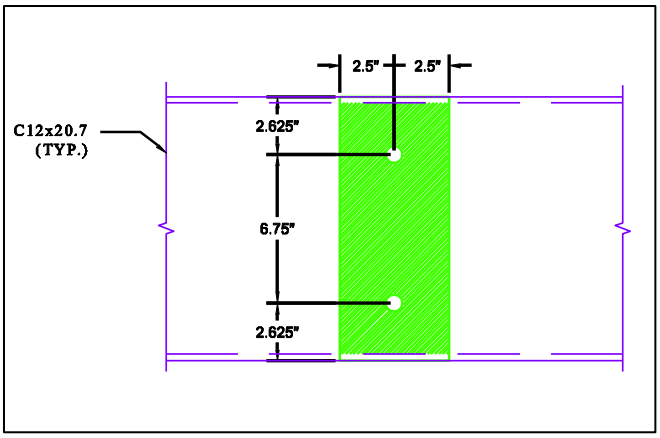

(f) Parallel plane cross section view of north end tie plate

Figure 5.27 (cont'd): Tie plate designs

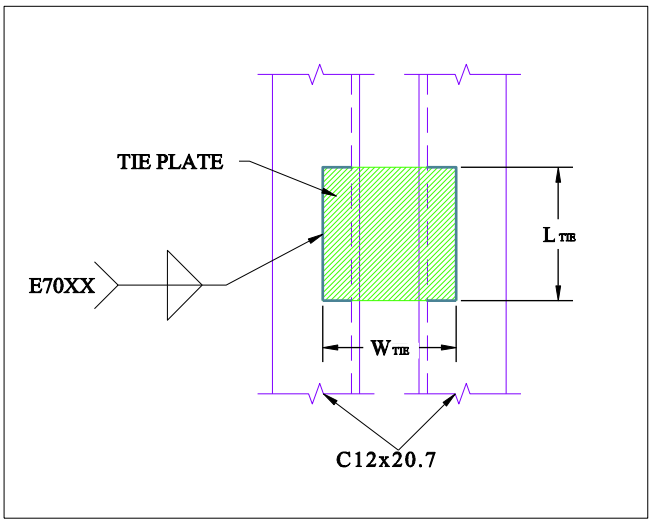

Figure 5.28: General plan view of welded tie plate

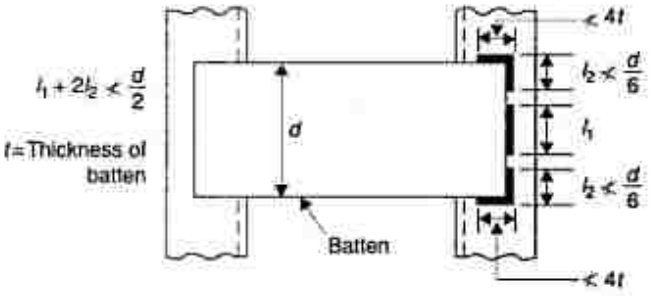

Figure 5.29: IS 800:2007 weld guidelines for battens (tie plates) (Sai, 2008)

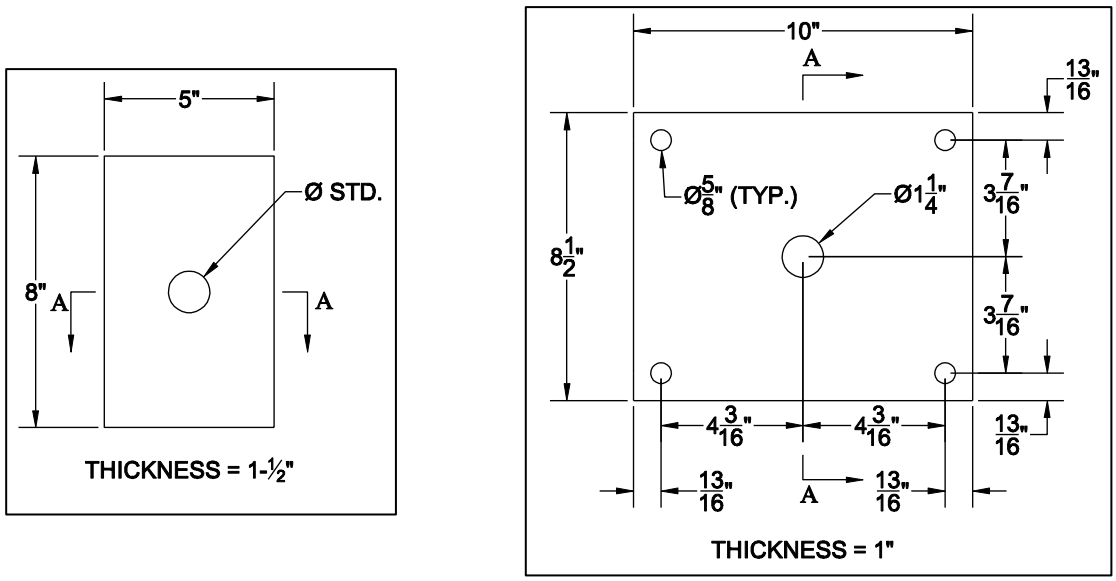

(a) Plate A

(b) Plate B

Figure 5.30: Plan view with dimensions of loading fixture plates with holes

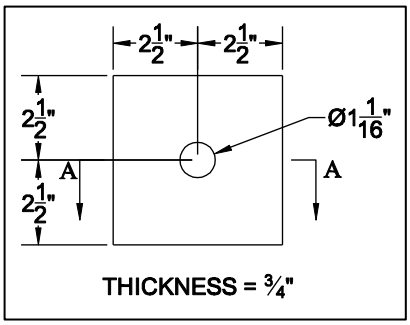

(c) Plate C and Plate F

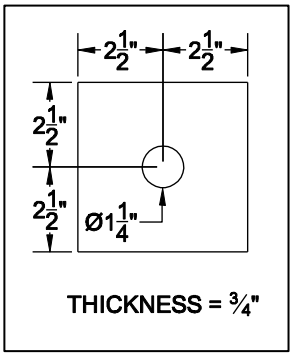

(d) Plate D

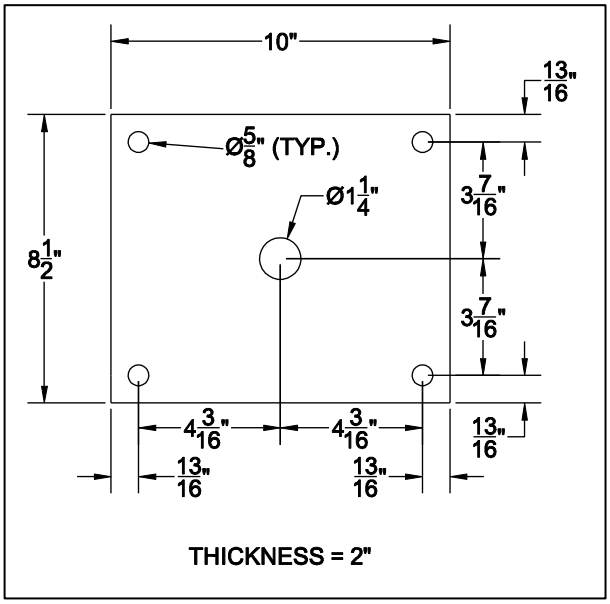

(e) Plate E

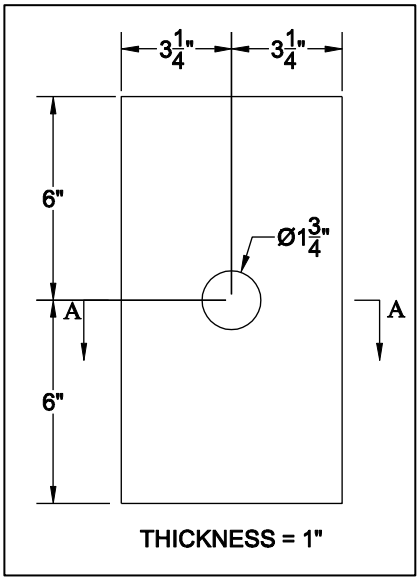

(f) Plate H

Figure 5.30 (cont'd): Plan view with dimensions of loading fixture plates with holes

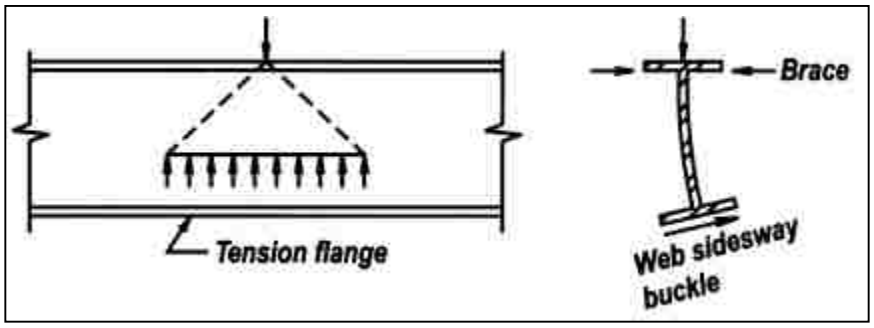

Figure 5.31: Web sidesway buckling (AISC, 2005)

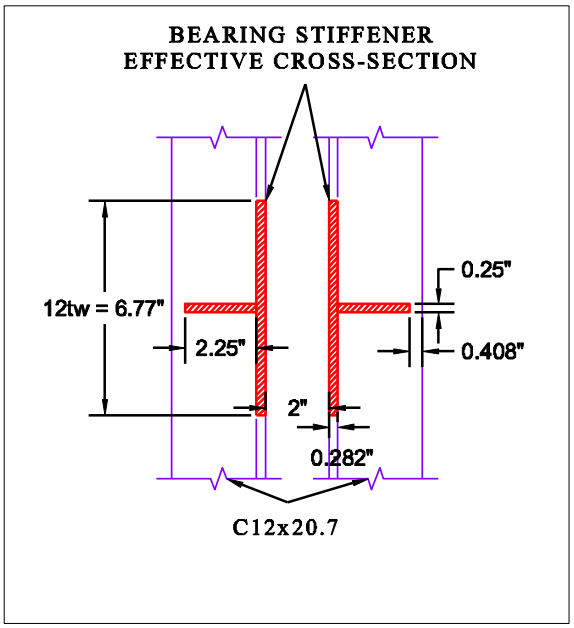

(a) Plan view

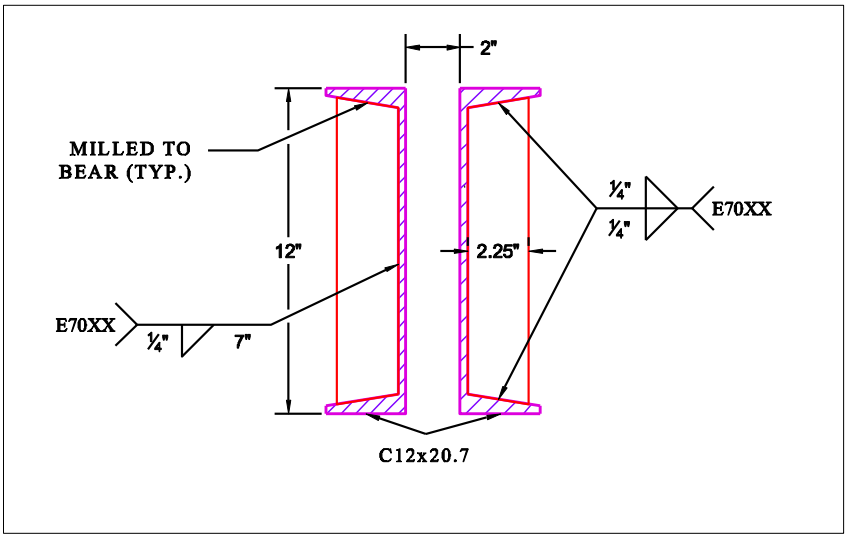

(b) Parallel plane cross section view

Figure 5.32: Load transfer channel bearing stiffeners

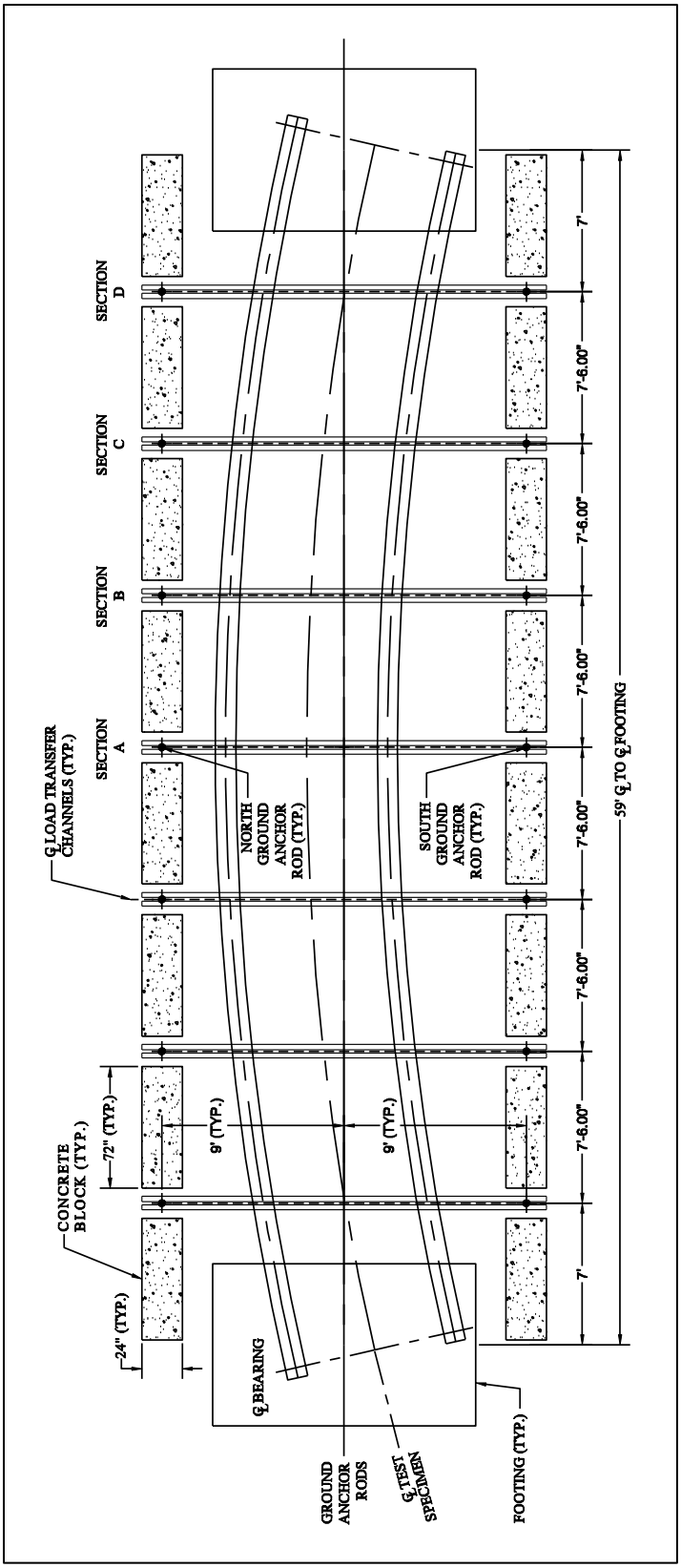

Figure 5.33: Bracing plan view

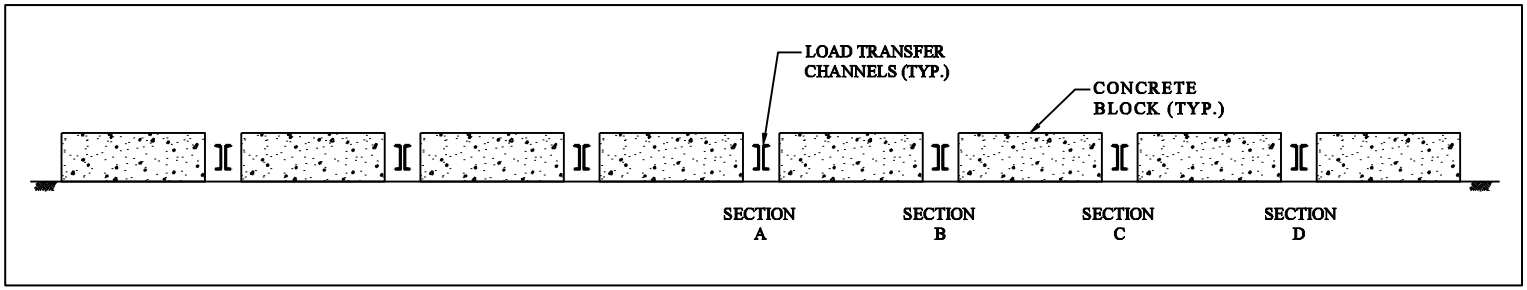

(a) Full cross section view

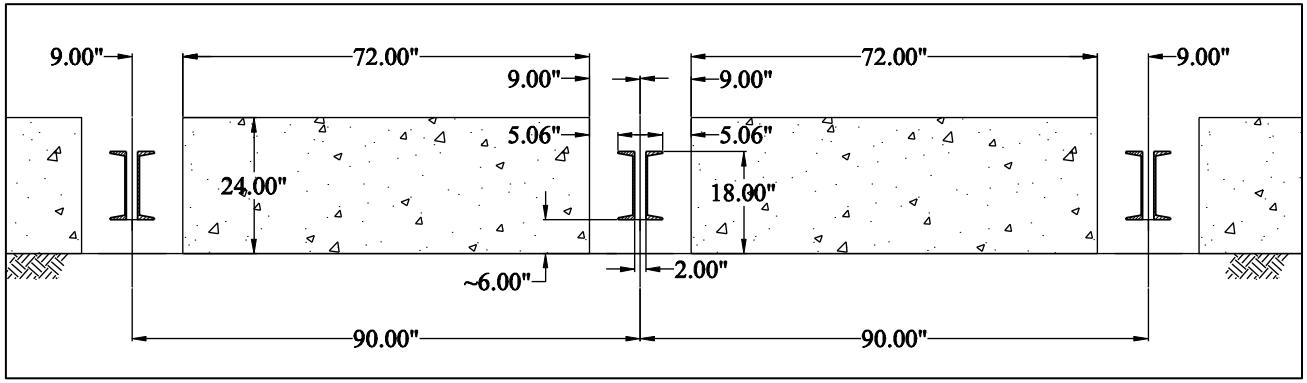

(b) Typical dimensions

Figure 5.34: Bracing longitudinal cross section view

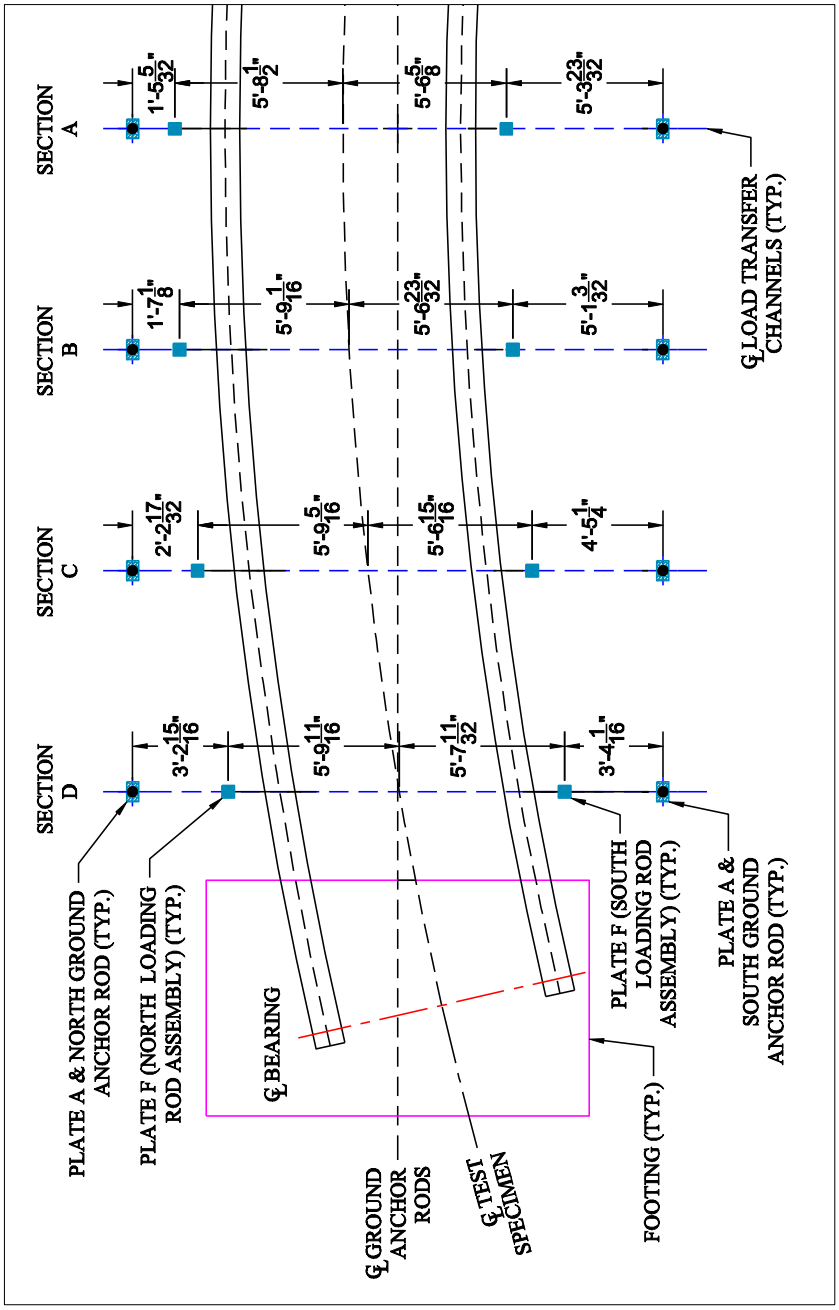

Figure 5.35: Loading rod assembly arrangement

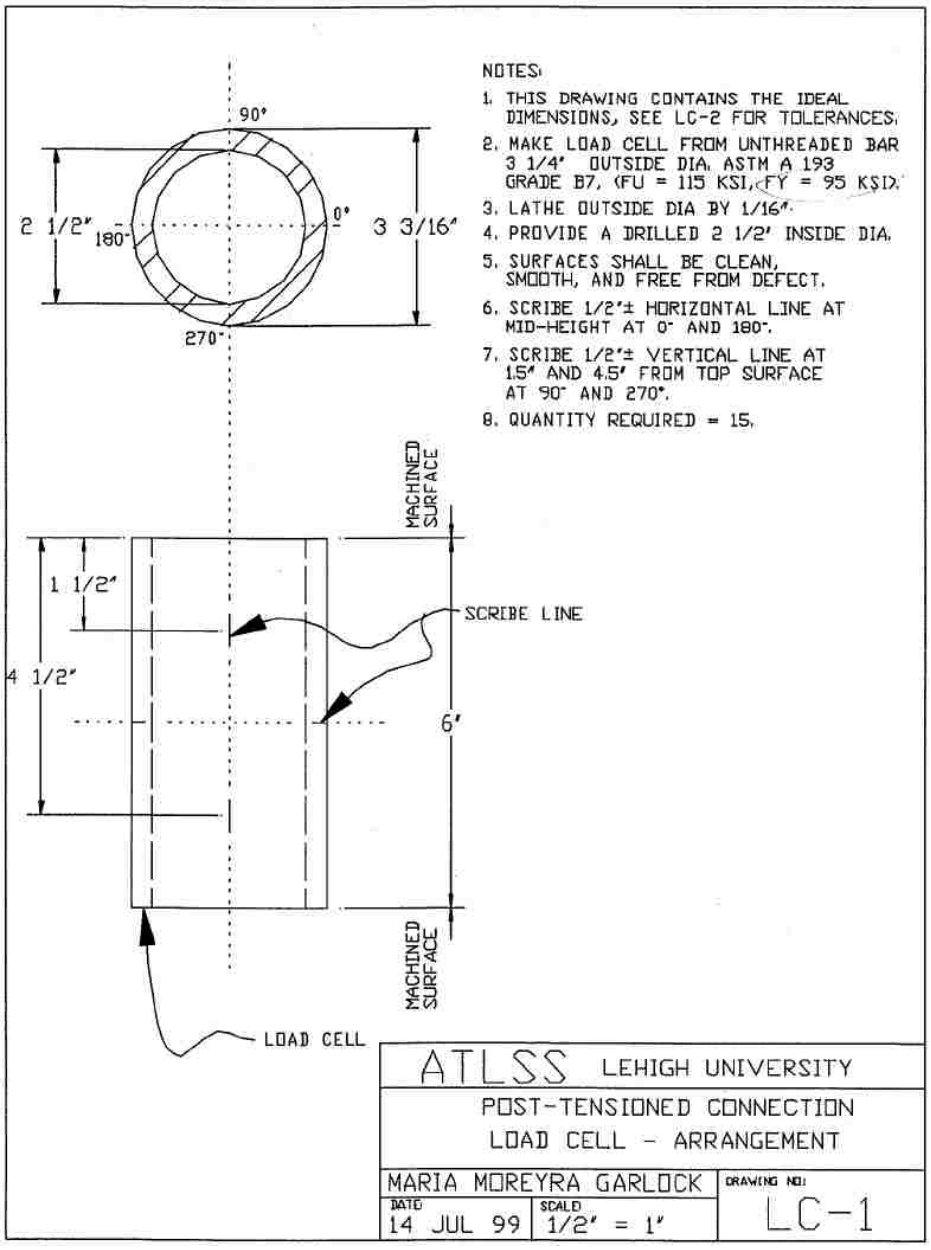

Figure 5.36: Load cell details (Garlock, 1999)

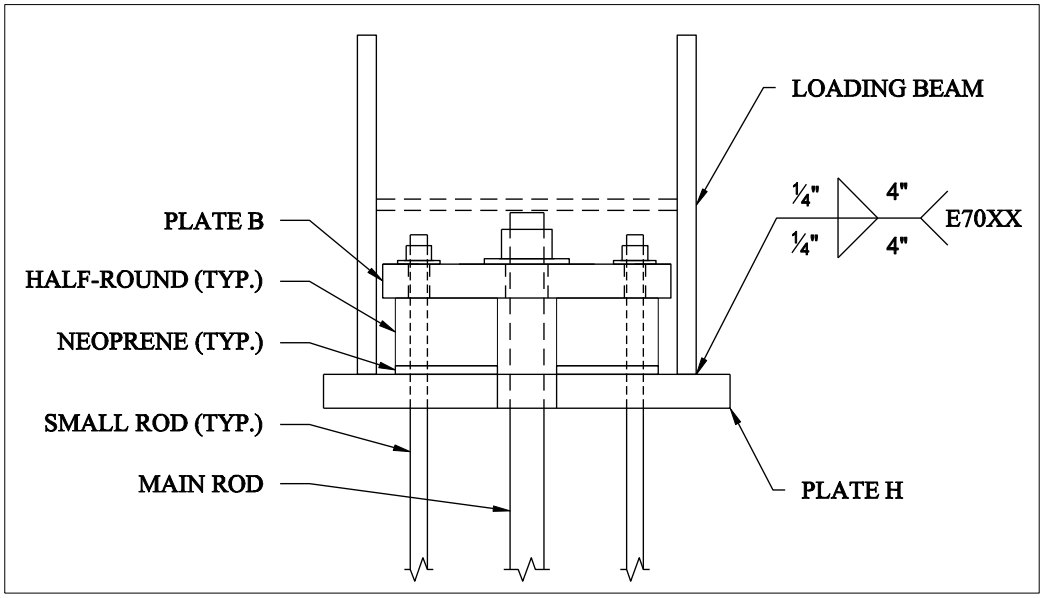

Figure 5.37: Plate H to loading beam welds (longitudinal plane cross section view of top of loading rod assembly)

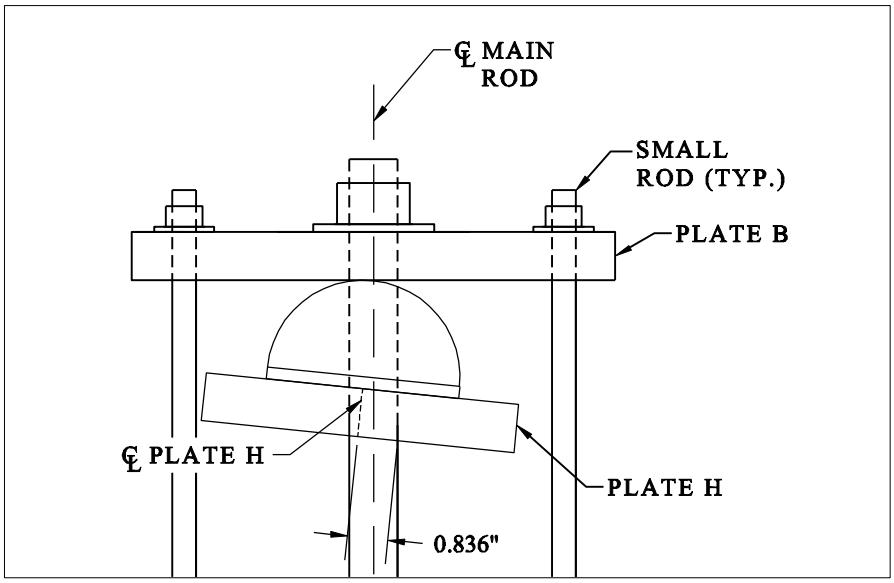

Figure 5.38: Half-round rotation to determine PL_H hole size

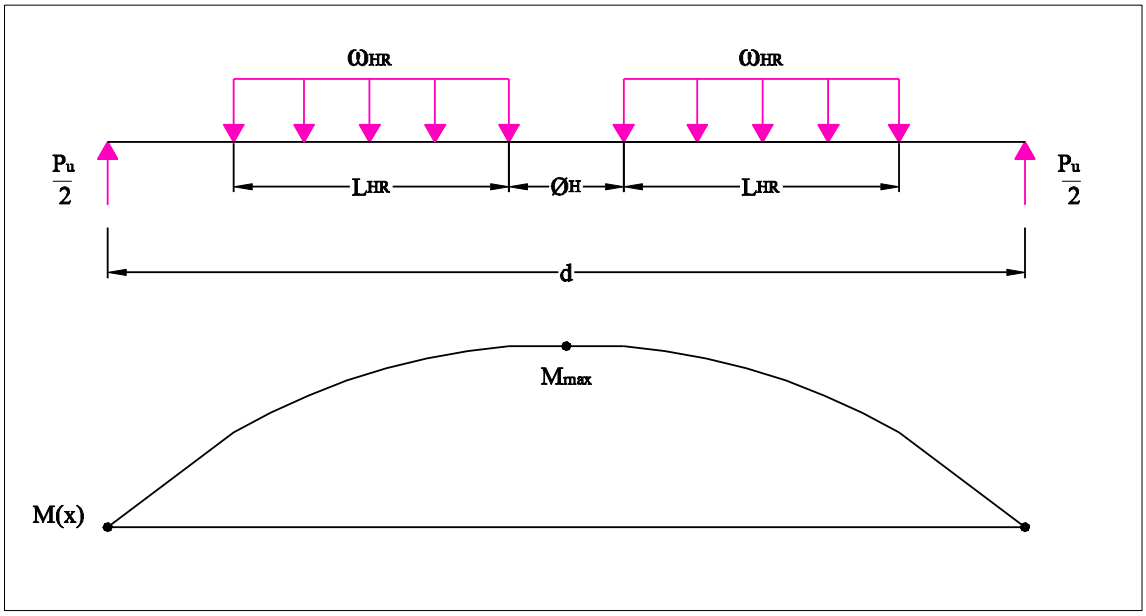

Figure 5.39: FBD and corresponding moment diagram for analysis of PL_H

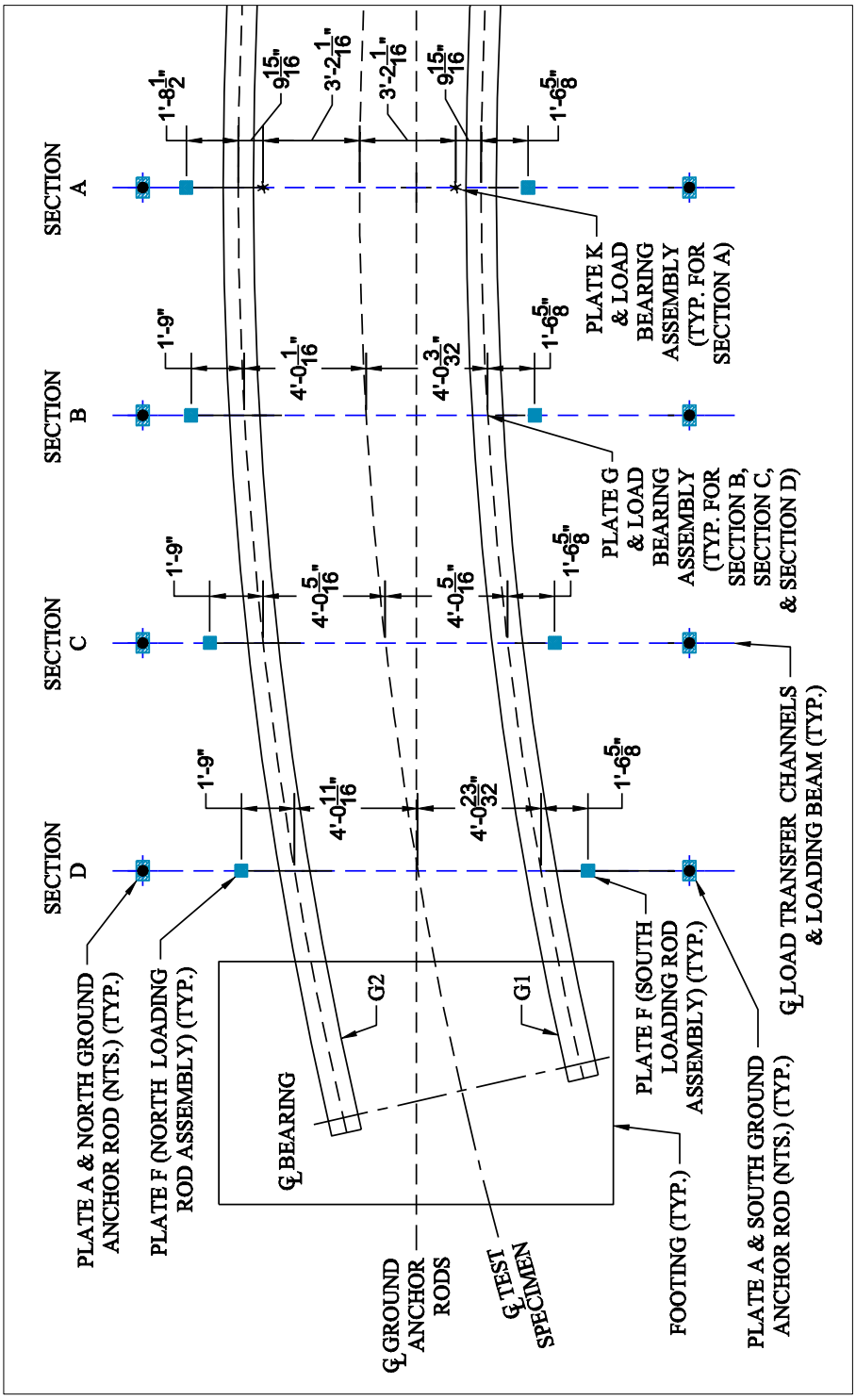

Figure 5.40: Load bearing assembly arrangement

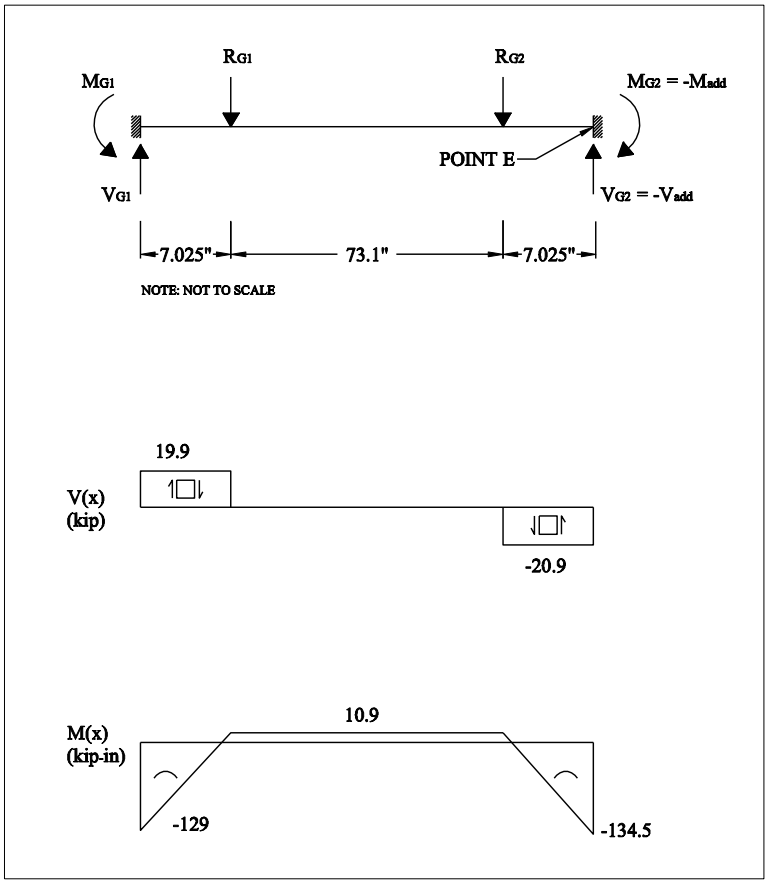

Figure 5.41: Diaphragm under applied loads, shear, and moment diagrams

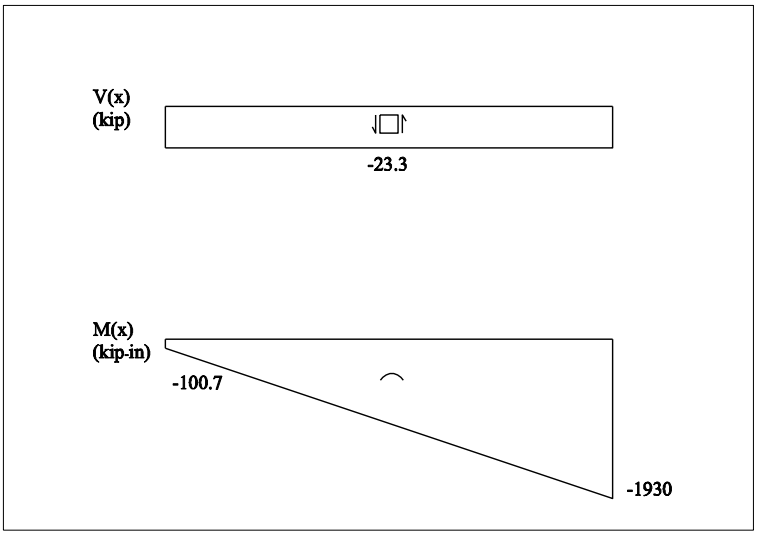

Figure 5.42: Diaphragm-TFG interaction shear and moment diagrams

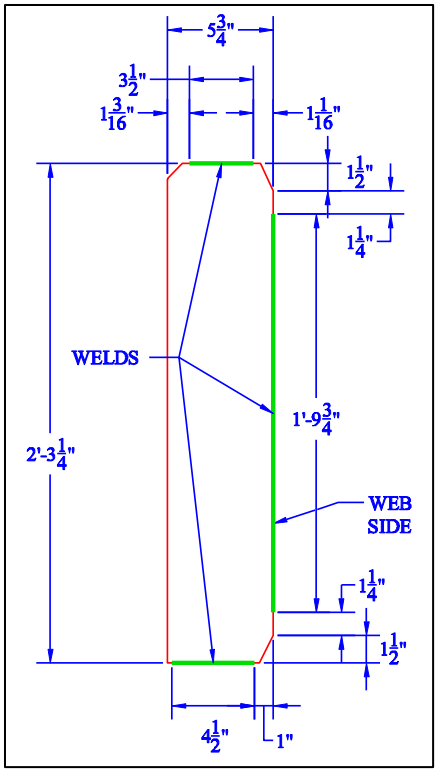

Figure 5.43: Existing welds of transverse stiffener to G2 at Section A

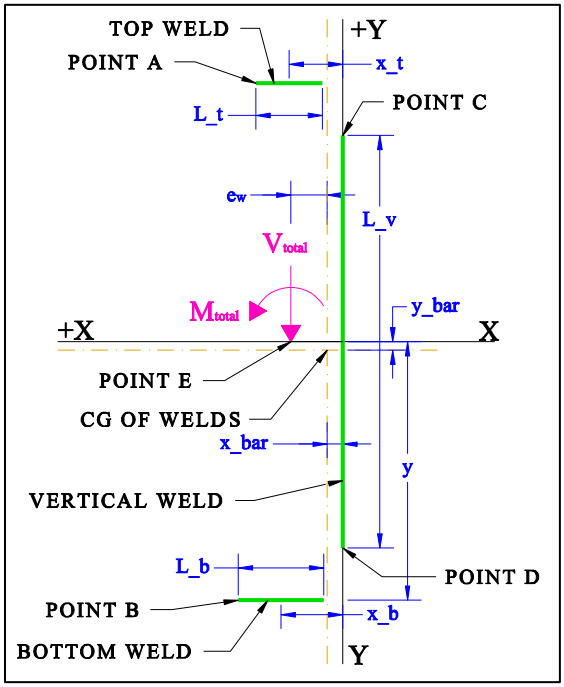

Figure 5.44: Forces on welds of transverse stiffener to G2 at Section A

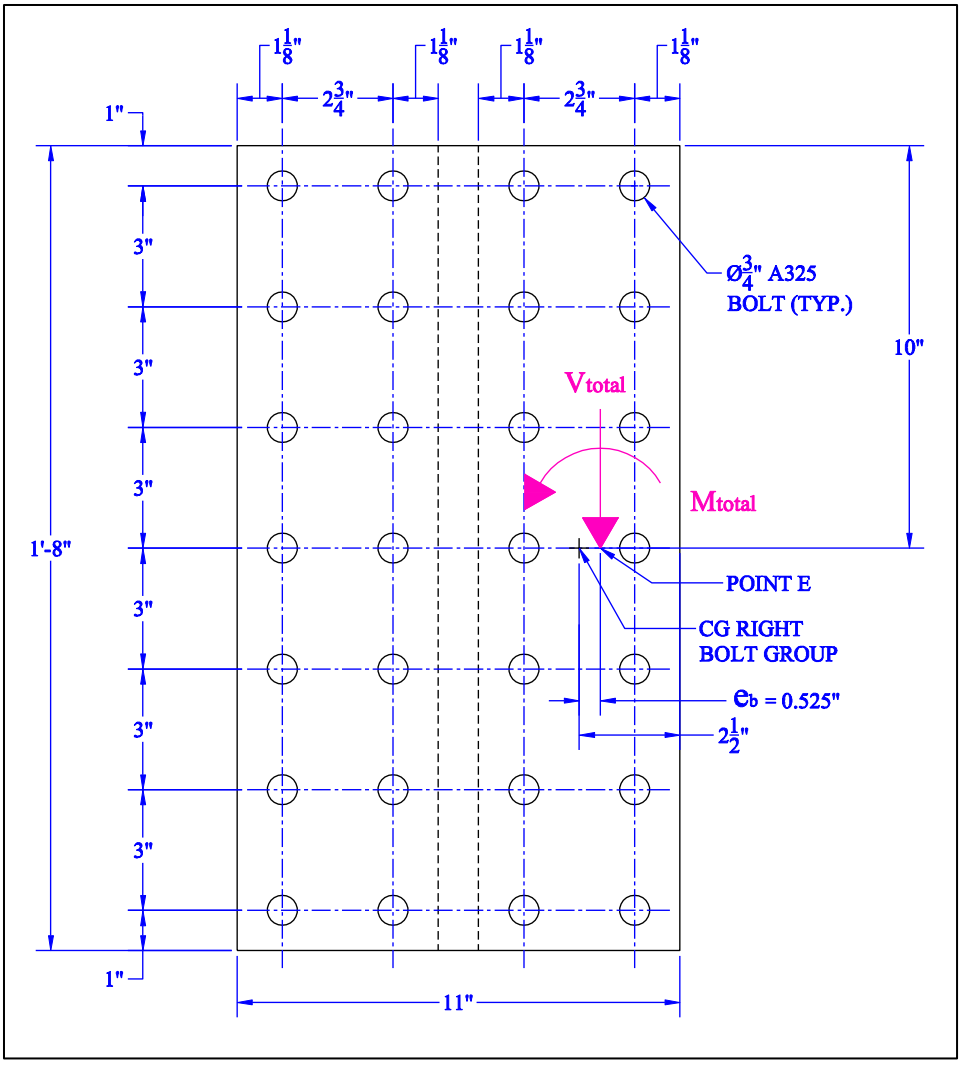

Figure 5.45: Connection plate with applied forces acting on right bolt group

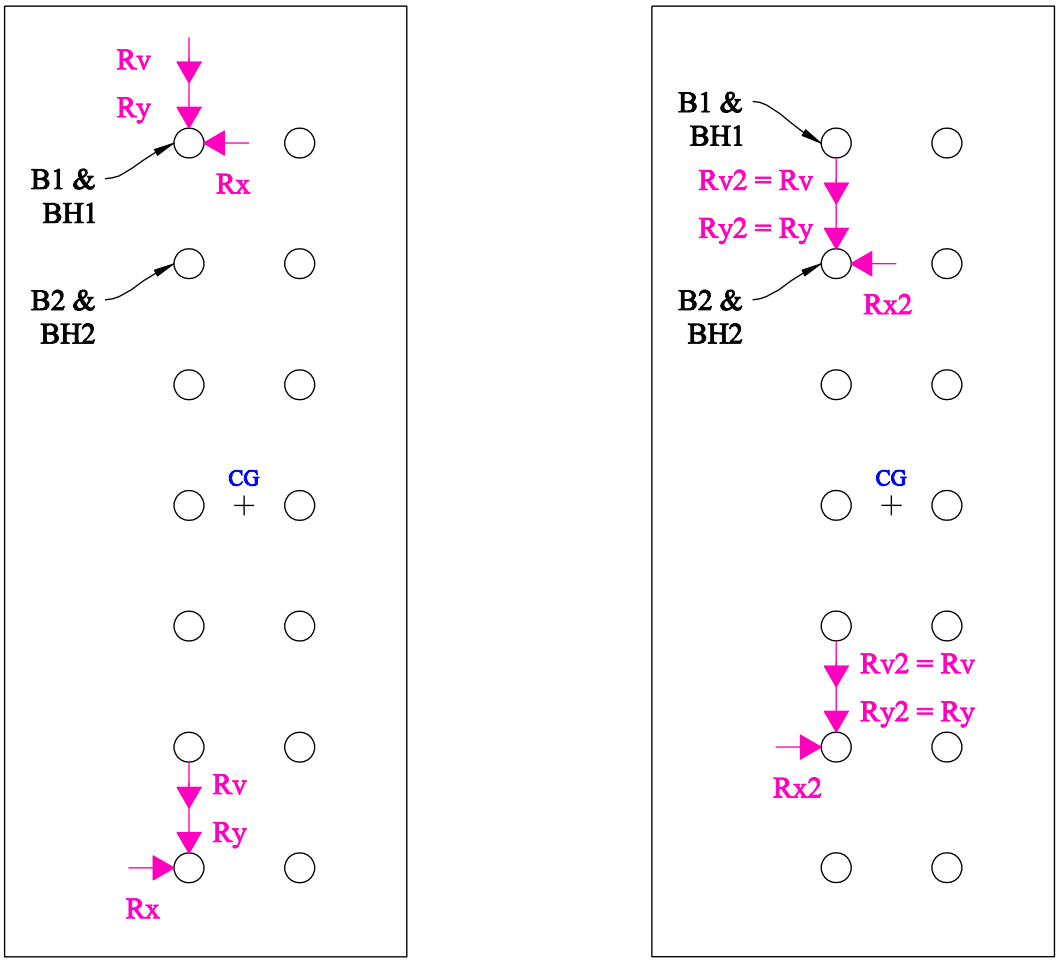

(a) Demand on B1 and BH1

(b) Demand on B2 and BH2

Figure 5.46: Demand on bolts and bolt holes

CHAPTER 6: SUMMARY, CONCLUSIONS, AND FUTURE WORK

6.1. Summary

An innovative curved steel bridge girder, called a curved tubular flange girder (TFG), is being studied. The I-shaped TFG has a cross section with a rectangular hollow steel tube as the top flange and a flat steel plate as the bottom flange. The closed cross section of the tube greatly increases the torsional stiffness of the girder and the I-shape is efficient in flexure and allows for easy fabrication and erection. A 2/3-scale test specimen with two horizontally curved TFGs braced by three internal diaphragms and two end diaphragms has been designed, fabricated, and erected. The test specimen was designed using the AASHTO Load and Resistance Factor Design (LRFD) Bridge Design Specifications (2005) and design recommendations by Dong (2008) for TFGs. This thesis presents the test setup and the FE analyses of the loading and the kinematics of the test specimen response. This thesis also describes how the FE results were used to design the loading fixtures for the test.

First, information was presented on the test setup. The location and layout of the test setup were described and the geometry of the test specimen was described. The design of the two-girder test specimen was discussed. Information was provided on the design of the TFGs, the TFG stiffeners, the diaphragms, the connections of the diaphragms to the TFGs, the bearing and the footings, and the ground anchor rods of the test setup.

Second, a study of load patterns applied to the test specimen and the resulting displacements was completed. FE models were used to study various load cases to verify that 14 concentrated loads arranged in pairs (one on each girder) could produce similar load effects at mid-span as a uniformly distributed load over the span. This study varied the load pattern using combinations of distributed pressure loads, distributed line loads, patch pressure loads, and point loads. The effect of boundary conditions on the FE results was studied. The displacements and rotations of the test specimen and the loading fixtures required for the design of the loading fixtures were discussed.

Third, the design of the loading fixtures was discussed. The connections between the diaphragms and the TFGs were evaluated for the expected maximum load capacity of the test specimen. The loading fixtures were designed to simulate deck placement loading conditions and to account for the expected displacements of the test specimen and the loading fixtures. Four different loading fixture types were designed to accommodate the geometry of the test setup and the expected displacements of the test specimen. The designs satisfied the maximum load capacity of the test specimen, and specifications from the AISC Steel Construction Manual (2005) and AASHTO LRFD Bridge Design Specifications (2005).

The loading fixtures use hydraulic jacks to pull up on a pair of channels laced together with tie plates and to pull down on a wide flange beam bent about its weak axis to load the test specimen. This is done using a series of steel rods, plates, half-rounds, and other parts. The loads applied to the load transfer channels are resisted by ground anchor rods. The load transfer channels are braced at the ends by concrete blocks.

The loading fixtures are designed to be stronger than the required loads and to maintain stability of the loads. In addition, the loading fixtures are designed to not restrain the response of the test specimen as it deflects under load. The half-rounds, neoprene pads, and other details of the loading fixture should act as kinematic releases to allow the test specimen to rotate independently from the loading fixtures. Teflon between the load transfer channels and the bottom plate of the loading rod assemblies should enable the loading rod assemblies to displace laterally. The loading fixtures are designed to displace laterally in the parallel plane and not collide with the north ground anchor rods.

6.2. Conclusions

The following conclusions can be made from the studies of the FE models of the test specimen, and the design calculations:

- Fourteen concentrated loads can be used to simulate the effects of a uniformly distributed load over the span of the test specimen. The relationship between the total applied load and the flexural capacity at mid-span will be maintained and the displacements of the test specimen should be similar.
- Changing the boundary conditions at one end of the FE model from two pins (one for each girder) to a pin and a roller had a small influence on the FE results.

- The test to determine the load capacity of the test specimen will not be artificially restrained by the loading fixtures.
- The components of the loading fixtures will be able to support the applied loads and move through the required displacements required to push the test specimen beyond the maximum load capacity.
- The concrete blocks will properly brace the ends of the built-up load transfer channels of the loading fixture.
- The connections between the diaphragms and the TFGs will not fail before the maximum load capacity of the test specimen is reached.

6.3. Future Work

The remaining work for the tests is as follows:

- Fabrication and assembly of the loading fixtures is needed.
- A final plan for the hydraulics of the loading fixtures is needed.
- An instrumentation plan for the tests is needed. This plan should include the type (e.g., strain gauges, inclinometers), the number, and the location of the instruments that will be used to monitor the responses of the test specimen and the loading fixtures.
- The test specimen needs to be tested for the Constructability limit state load and the maximum load capacity.

- The displacements of the loading fixtures during the tests should be observed and noted to determine how they compare with the expected displacements.
- The displacements of the loading rod assemblies need to be noted during the tests, especially the circumferential displacements and rotations in the circumferential plane at Section D. The loading rod assemblies should remain vertical; any inclination should be documented.
- Any lateral displacement in the parallel plane of the load transfer channels should be recorded.
- Validation of the FE model results with the responses of the test specimen should be completed after the tests.

The following recommendations are made for future TFG research:

- Tests and comparisons with FE analyses of curved TFG systems for the Strength I and Service II limit states should be made.
- Studies of TFGs should be made for other limit states identified in the AASHTO LRFD Bridge Design Specifications (2005).

REFERENCES

AASHTO (1995). *Guide Design Specifications for Bridge Temporary Works*. American Association of State Highway Transportation Officials, Washington, D.C.

AASHTO (1998). *AASHTO LRFD Bridge Design Specifications.* American Association of State Highway and Transportation Officials, Washington, D.C.

AASHTO (2003). *Guide Specifications for Horizontally Curved Steel Girder Highway Bridges.* American Association of State Highway Transportation Officials, Washington, D.C.

AASHTO (2005). *AASHTO LRFD Bridge Design Specifications.* American Association of State Highway and Transportation Officials, Washington, D.C.

ABAQUS (2011). *ABAQUS/Standard User's Manual: Volume I – III, Version 6.11*. Hibbitt, Karlsson, and Sorenson, Inc., Pawtucket, RI.

ACI (2011). *Building Code Requirements for Structural Concrete (ACI 318-11) and Commentary.* American Concrete Institute, Farmington Hills, MI.

AISC (2005). *Steel Construction Manual, 13th Edition*. American Institute of Steel Construction, Inc., Chicago, IL.

AWS (1988). *Bridge Welding Code D1.5-88.* American Welding Society, Miami, FL.

BPI (2012). "DuPont Teflon PTFE Specifications." Boedeker Plastics, Inc., Shiner, TX. <http://www.boedeker.com/teflon_p.htm> (accessed July 2012).

Dabrowski R. (1968). *Curved Thin Walled Girders, Theory and Analysis*. Cement and Concrete Association, London, England. (Translated from German by C.V. Amerongen).

Dong J. (2008). "Analytical Study of Horizontally Curved Hollow Tubular Flange Girders." Ph.D. Dissertation, Department of Civil and Environmental Engineering, Lehigh University, Bethlehem, PA.

Dong J., Sause R. (2009). "Flexural strength of tubular flange girders." *Journal of Constructional Steel Research* 65(3): 622-630.

Dong J., Sause R. (2010a). "Finite element analysis of curved tubular flange girders." *Engineering Structures* 32(1): 319-327.

Dong J., Sause R. (2010b). "Behavior of hollow tubular flange girder systems for curved bridges." *Journal of Structural Engineering* 136(2): 174-182.

ENERPAC (2011). "RCH-Series, Hollow Plunger Cylinders." Enerpac, Milwaukee, WI. <http://www.enerpac.com/sites/default/files/rch_e327_us.pdf> (accessed April 2012).

ES (2009). "Earthcore Services Boring Log." Earthcore Services, LLC., Pottstown, PA.

Fan Z. (2007). "Behavior of Horizontally Curved Steel Tubular-Flange Bridge Girders." Ph.D. Dissertation, Department of Civil and Environmental Engineering, Lehigh University, Bethlehem, PA.

Garlock M. E. M. (1999). "Design, analysis, and experimental behavior of seismic resistant post-tensioned steel moment resisting frames." Ph.D. Dissertation, Department of Civil and Environmental Engineering, Lehigh University, Bethlehem, PA.

Google (2012). *Google Maps*. Google, Inc., Mountain View, CA: <https://maps.google.com/> (accessed May 2012).

ITC (2008). "Test Certificate." Independence Tube Corporation, Chicago, IL. 24 June 2008.

Kim B. G. (2005). "High Performance Steel Girders with Tubular Flanges." Ph.D. Dissertation, Department of Civil and Environmental Engineering, Lehigh University, Bethlehem, PA.

Kim B.G., Sause R. (2005a). "High Performance Steel Girders with Tubular Flanges." ATLSS Report 05-15, ATLSS Engineering Research Center, Lehigh University, Bethlehem, PA.

Kim B.G., Sause R. (2005b). "High Performance Steel Girders with Tubular Flanges." *International Journal of Steel Structures*, vol. 5, No. 3, pp. 253-263.

Ma H. (2012). "High Performance Steel Girders with Tubular Flanges." Ph.D. Dissertation (in progress), Department of Civil and Environmental Engineering, Lehigh University, Bethlehem, PA.

Nucor (2009). "Mill Test Report." Nucor, Winton, NC. 17 July 2009.

PE (2009a). "ATLSS Engineering Research Center Curved Tubular Flange Girder Project 112.5 Kip Tiedown Anchors Plan, Procedure & Section." Peirce Engineering, Inc., Phoenixville, PA. 1 July 2009.

PE (2009b). "Observation Report." Peirce Engineering, Inc., Phoenixville, PA. 27 July 2009.

Putnam E. (2010). "Design, Experimental, and Analytical Study of a Horizontally Curved Tubular Flange Girder." M.S. Thesis, Department of Civil and Environmental Engineering, Lehigh University, Bethlehem, PA.

Putnam E. (2011). Drawings of test setup. Feb. 2011.

Sai Ram K. S. (2010). *Design of Steel Structures.* Dorling Kindersley (India) Pvt. Ltd, licenses of Pearson Education in South Asia, New Delhi, India.

Salmon C. G., Johnson J. E., Malhas F. A. (2009). *Steel Structures: Design and Behavior: Emphasizing Load and Resistance Factor Design, 5th Edition*. Prentice Hall, Upper Saddle River, NJ.

Sause R. (2012). "Innovative Steel Bridge Girders with Tubular Flanges." IABMAS 2012, Proceedings of the 6th International Conference on Bridge Maintenance, Safety, and Management, Stresa, Lake Maggiore, Italy, July 8-12, 2012.

Sause R., Dong J. (2008). "Finite-element analysis of curved hollow tubular flange girders." Proceedings, 25th Annual International Bridge Conference, Pittsburgh, PA, USA.

Sause R., Ma H., Putnam E., Dong J. (2009). "Update on Curved Girders with Tubular Flanges." Summer Meeting of the American Iron and Steel Institute Bridge Task Force, Baltimore, MD, August 12-14, 2009.

Sause R., Kim B.G., Wimer M.R. (2008). "Experimental Study of Tubular Flange Girders." *Journal of Structural Engineering*, ASCE, vol. 134, No. 3, pp. 384-392.

SDI (2008). "Certified Mill Test Report." Steel Dynamics, Inc. Structural and Rail Division, Columbia City, IN. 9 Oct. 2008.

Serway R. A., Jewett J. W. (2010). *Physics for Scientists and Engineers, Volume 1, 8th Edition.* Cengage Learning, Belmont, CA.

Wassef W.G., Ritchie P.A., and Kulicki J.M. (1997). "Girders with Corrugated Webs and Tubular Flanges – An Innovative Bridge System." Proceedings, 14th International Bridge Conference, Pittsburgh, PA, pp. 425-432.

Wimer M.R., Sause R. (2004). "Rectangular Tubular Flange Girders with Corrugated and Flat Webs." ATLSS Report 04-18, ATLSS Engineering Research Center, Lehigh University, Bethlehem, PA.

Young W., Budynas R. (2002). *Roark's Formulas for Stress and Strain, 7th Edition*. McGraw-Hill, Boston, MA.

VITA

Kayla Marie Hampe was born on November 4, 1987 in Exeter, New Hampshire to Edward and Lisa Hampe. She studied Civil Engineering at the University of New Hampshire in Durham, NH and participated in UNH's honors program. In 2008, she was inducted to Tau Beta Pi, the national engineering honor society. She graduated Summa Cum Laude in May 2010 from UNH with a Bachelor of Science in Civil Engineering and a minor in Spanish.

Kayla decided to continue her education at Lehigh University in Bethlehem, Pennsylvania. She began her studies in August 2010 with the department of Civil and Environmental Engineering. During her time as a graduate student, she was a teaching assistant for undergraduate classes in Structural Analysis I, Hydraulic Engineering, and Bridge Systems Design. She expects to receive her Master of Science in Structural Engineering in September 2012 and pursue a career as a bridge engineer.